University of Alberta

Novel Spectroscopic Probes of Sunscreens, Initial Excited-state Structural Dynamics and DNA Photodamage

by

Sulayman Adeyemi Oladepo

A thesis submitted to the Faculty of Graduate Studies and Research
in partial fulfillment of the requirements for the degree of

Doctor of Philosophy

Department of Chemistry

Spring 2010
Edmonton, Alberta

Examining Committee

Dr. Glen Loppnow, Chemistry

Dr. Mark McDermott, Chemistry

Dr. John Klassen, Chemistry

Dr. Charles Lucy, Chemistry

Dr. Phillip Choi, Chemical and Materials Engineering

Dr. Ricardo Aroca, Chemistry and Biochemistry, University of Windsor

Dedication

Dedicated to my wife Bilqees Abimbola Oladepo, my daughter Asmah Temidola Oladepo and my son Farhan Folaranmi Oladepo for their unflinching support and understanding during my PhD

Abstract

This thesis discusses developing new tools to probe DNA damage resulting from photoinduced chemical processes and probing the initial excited-state structural dynamics of nucleic acids and sunscreen agents. The results of this thesis show that UV resonance Raman spectroscopy (UVRRS) is an information-rich probe of chemical compositions in *in situ* analysis of sunscreen formulations. The results indicate that 244-nm excited UV resonance Raman spectra can provide a limit of detection of 0.23% w/w of sunscreen active ingredients (AIs), far below typical active ingredient (AI) concentrations in sunscreen formulations.

UVRRS was used to probe the photostability of sunscreens, by determining the initial excited-state structural dynamics of Benzophenone-3 (BZ3), a common sunscreen active ingredient. Only minor excited-state structural distortions were obtained, based on the low displacement values, suggesting an inherently stable molecule. The largest structural change occurs along the carbonyl stretch, suggesting a strong interaction with the methanol solvent and a dissipative decay path for the molecule. Similarly, to gain an insight into how the structure of nucleic acids determine their photochemistry, UVRRS was used to probe the initial excited-state structural dynamics of 9-methyladenine (9-MeA). As for BZ3, the initial excited-state structural dynamics obtained for 9-MeA, are low, and much lower than for pyrimidine bases, providing a strong evidence for the photochemical stability of this purine base analog, compared to pyrimidines.

Since DNA does not exist in isolation in cells, the role of a UV-absorbing amino acid, tryptophan, in UV-induced DNA photodamage was explored using molecular beacons (MBs) to detect the damage. The results indicate that tryptophan protective effects on DNA far outweighs their photodamage potential.

However, MBs are expensive and they have some technical limitations, despite their exquisite sensitivity. Therefore, a new DNA damage detection method was developed based on smart probes (SPs). These probes are shown to be sensitive and sequence specific for detecting DNA photodamage.

Acknowledgements

All thanks and praises are due to Allah (SWT) who has made this PhD degree a reality. He has granted me success in what initially seemed an insurmountable task. The significance of the divine role Allah has played in seeing me through yet another graduate degree cannot be overstressed. To Him and Him alone will I forever be grateful! I seek His abundant blessings on the gentle soul of the noble prophet Muhammad (SAW), and those who follow him till the day of recompense.

Let me start by expressing my profound and unreserved gratitude to my PhD research advisor, Prof. Glen Loppnow for his thorough supervision, guidance and selfless service towards my development as a scientist. I am also grateful to Glen for being a true friend, who listens and shows concern on all matters – chemistry and non-chemistry alike. I must also say that his cordial but thorough supervisory style is exemplary, and it goes a long way in quickly making people feel comfortable to work with him. By and large, the good memories of the last 3.5 years in his research group will stay with me forever, and he will always be remembered in a very special way! My PhD examining committee members also deserve my appreciation. I thank all of them for their time and suggestions.

My special thanks also go to members of Loppnow's research group, both past and present. I thank Dr. Brant Billinghurst, who first gave me a hands-on training on Raman spectroscopy, Dr. Lal Mohan Kundu, for assistance with DNA and molecular beacons, and Christine Pinnock for training with fluorimeter. I also give special thanks to Amira El Yazbi for her support and concern always. I thank her for being a concerned friend and colleague that I can always count on. I equally thank Swaroop Sasidharanpillai for his help in various ways. I am also grateful for the concern shown by Zahra Shire, Faranak Teimoory and Sindhu Nair. I wish all them a highly rewarding graduate experience.

In a very special way, I would like to thank my dear wife, Bilqees, for her support, patience, concern, understanding and love. Similarly, I thank my two wonderful kids of graduate school, Asmah and Farhan. I thank Allah for giving them both to us. Their being troubleless kids indeed made the rather difficult PhD work an “easy ride” for me. The smiles and the “welcome daddy” chorus that I would hear when I returned after long and frustrating hours in the lab cannot be easily forgotten. I pray Allah to bless and preserve them both, and make them sources of pride for us and Al-Islam.

At this juncture, I wish to thank my dear parents from whom this whole story began, Mallam Imran Alao Oladepo and Madam Nimotallahi Abike Oladepo. I thank them for their parental support, concern, understanding and prayers. I also thank Allah for their kind of parents. I ask Allah to preserve them both in good health so they can patiently reap the fruits of their hard labour. I am particularly grateful to my brother, Musodiq Oladepo, for his concern, support, understanding and prayers. May Allah reward him in abundance and bless his family. In the same vein, I thank my other brother and sisters, Mr. Qazeem Oladepo, Mrs. Monsurat Hammed and family, Basirat Oladepo and Sakirat and her family. My uncles, Mr. Kuzamat Oladepo and Mr. Rufus Olatunji also deserve my special thanks, may God bless them and their families. I equally thank my cousins, Mr. Rasheed Alimi and Mrs. Modinat Moshood for their concern and support.

I give special thanks to my very good friends, Mr. ‘Wale Yussuff and Mr. Waheed Oredola. My appreciation also goes to many people who also showed concern during my PhD program. These include Mr. Ismail Adedigba, Mr. Sulayman Adedigba, Mr. Tunde Mustapha, Habeeb Abdul Salaam, Mallam Audu (UK), Dr. Dhikrullahi Amidu, Mallam. Rasheed Lawal, Mr. Lateef Lawal, Mallam Abdul Ganiyy Shittu and Mr. Oyetoso. I also thank Saeed Mohammed and family, Nirala Jagnarian and family, Kamaldeen Yusuf and family, as well as Khadijah Saliu and family. In addition, I thank Dr. Francis Nsiah for his advice, support and concern. I wish him God guidance in all his future endeavours as he prepares to finally return home. I also acknowledge

the support and concern of Kunle Elegbede, Morolake Kuteyi, George (Josh) Ebesoh, Amr Elhawiet and Mahmoud Bahnasy.

I am grateful to Wayne Moffat of Spectral Services Laboratory for his ever-friendly services and assistance. Same goes to other staff of the lab. I also thank the Department of Chemistry, Faculty of Graduate Studies and Research, University of Alberta, Natural Sciences and Engineering Research Council of Canada (NSERC), Alberta Cancer Board (ACB), Alberta Heritage Foundation for Medical Research (AHFMR) and Canada Foundation for Innovation (CFI) for various forms of funding.

Finally, I acknowledge the support and concern of all others whose names are inadvertently left out. To all of them I say thanks a lot!

Sulayman A. Oladepo

March 2010.

Table of Contents

Chapter 1: Introduction

Chapter 2: UV Resonance Raman Spectroscopy as a Robust Spectroscopic Tool for *in situ* Sunscreen Analysis

Chapter 5: The Effect of Tryptophan on UV-induced DNA Photodamage

List of Tables

List of Figures

List of Abbreviations

Abbreviation	Full Name
A	absorption or adenine
Ade	adenosine
AIs	active ingredients
AMP	adenosine monophosphate
β-BBO	β-barium borate
BZ3	benzophenone-3
C	cytosine
CCD	charge coupled device
CPDs	cyclobutane pyrimidine dimers
dApdA	adenine deoxyribodinucleotide
DNA	deoxyribonucleic acid
Dabcyl	4-(4’-dimethylaminophenylazo)-benzoic acid
5-FU	5-fluorouracil
EDTA	ethylenediaminetetraacetic acid
F	fluorescence
FAM	6-carboxyfluorescein
FRET	Förster or fluorescence resonance energy transfer
FTIR	Fourier transform infrared spectroscopy
G	guanine
GC	gas chromatography
HPLC	high performance liquid chromatography
IC	internal conversion
IR	infrared
ISC	intersystem crossing
LBO	lithium triborate
LNA-MB	locked nucleic acid molecular beacon
LOD	limit of detection

LOQ	limit of quantitation
9-MeA	9-methyladenine
MB	molecular beacon
MEKC	micellar electrokinetic chromatography
MeOH	methanol
MS	mass spectrometry
NIR	near infrared
NMR	nuclear magnetic resonance
OCS	octyl salicylate
OCT	octisalate
OCY	octocrylene
OMC	octyl methoxycinnamate
ppb	part per billion
P	phosphorescence
PABA	para-amino benzoic acid
PAHs	polyaromatic hydrocarbons
PCR	polymerase chain reaction
PED	potential energy distribution
Ph	photochemical reaction
Q	quenching
ROS	reactive oxygen species
RREPs	resonance Raman excitation profiles
RRS	resonance Raman spectroscopy
Samp	sample
S/N	signal-to-noise ratio
SPF	sun protection factor
SP	smart probe
sr	steradian
Std	internal standard
TLC	thin layer chromatography
Trp	tryptophan
UV	ultraviolet

UVA	ultraviolet A (320-400 nm)
UVB	ultraviolet B (280-320 nm)
UVC	ultraviolet C (100-280 nm)
UVRR	UV resonance Raman
UVRRS	UV resonance Raman spectroscopy
UV-Vis	UV-Visible

List of Symbols

α	polarizability
α	absorptivity
α_0	equilibrium value of polarizability
β	hyperpolarizability
γ	second hyperpolarizability
Δ	delta (displacement)
μ	dipole moment
υ	scattered photon energy
υ_e	resonant electronic transition energy
υ_0	incident photon energy
$\tilde{\nu}_k$	vibrational wavenumber
$\tilde{\nu}_0$	incident laser wavenumber
ε	molar absorptivity
ε_v	energy of the intermediate vibrational state
ε_i	energy of the initial vibrational state
□	quantum yield
$\|f\rangle$	final vibrational state
$\|v\rangle$	intermediate vibrational state
$\|i\rangle$	initial vibrational state
σ_A	absolute absorption cross-section
σ_R	absolute resonance Raman cross-section
$\frac{d\sigma}{d\Omega}$	differential cross-section
k_x	rate constants of a deactivation process
l	pathlength
ρ	depolarization ratio
τ_x	lifetime of process x
Γ	homogeneous line width

Θ	standard deviation of the inhomogeneous line width
Å	Angstrom (a unit of length equivalent to 10^{-10} m)
c	speed of light
C	absorbing species concentration
d	Raman sample pathlength
n	refractive index
C_i	molar concentration of species i
D	coupling strength between the electronic transition and the solvent coordinate
E	electric field vector or spectrometer efficiency
E_L	incident photon energy
E_s	scattered photon energy
E_o	electric field amplitude of photon or the zero-zero energy between the lowest vibrational levels of the ground and excited electronic states
$<E_o>$	average energy
G(t)	homogeneous shape function
h	Planck's constant
$\hbar$	Planck's constant divided by 6.284
H	inhomogeneous line width or Hamiltonian
I	transmitted or resonance Raman intensity
I_o	incident light intensity
k	Boltzmann constant
K	scaling constant
L	internal field correction
M	transition length
Q_k	the kth normal mode of vibration
Q_{k0}	the normal coordinate amplitude
T	temperature

Chapter 1

Introduction*

Spectroscopy is a unique scientific tool for investigating many chemical systems in order to answer a number of important fundamental questions. With advances in laser technology and optics fabrication, different spectroscopic techniques are now sufficiently developed to a level that advanced forms of a given spectroscopic technique are now possible. These techniques come with the added advantage of enhanced capabilities which enable scientists to conduct more advanced experiments that were originally deemed impossible and which may answer new questions. For example, UV resonance Raman spectroscopy (UVRRS) which is one major spectroscopic technique discussed in this thesis evolved from traditional Raman spectroscopy, and it is now a well-established technique with a myriad of applications, to which traditional Raman cannot be put to use. The unique capabilities of UVRRS at selectively exciting chromophores in complex mixtures[1,2] and in probing the initial excited-state structural dynamics of molecules[3-8] are harnessed in some of the research work described in this thesis. Similarly, molecular beacon-based fluorescence and smart probe-based fluorescence spectroscopy are used for the detection of DNA photodamage. The capability of UVRRS for the exploration of the structure and dynamics of excited-states of molecules[9] makes the technique well-suited for studying the excited-state structural dynamics of nucleic acids.

Deoxyribonucleic acids (DNA) constitute the genetic basis of life and

---

* A version of sections 1.1.4, 1.1.7, 1.2.1, 1.2.3 and 1.2.4 has been published. Loppnow, G. R., Billinghurst, B. E., Oladepo, S. A. In *Radiation Induced Molecular Phenomena in Nucleic Acids. A Comprehensive Theoretical and Experimental Analysis Series: Challenges and Advances in Computational Chemistry and Physics.* Shukla, M. K., Leszczynski, J., Eds.; Springer: Netherlands, 2008; pp 237-263.

carry all the developmental potential of an organism within its genes.[7] The very small size of nucleic acids makes them vulnerable to an array of environmental insults.[7] Principal among these is UV radiation, which has deleterious effects on DNA causing various forms of damage. Thus, a good understanding of the molecular mechanisms of DNA damage and protection is essential for human health. Part of the work presented in this thesis is aimed at understanding the mechanism of DNA damage and protection. Depending on the type of irradiation, and whether or not oxygen is present, different photoproducts may be formed.[7] For instance, ionizing radiation also causes damage to DNA (A. Mah, S. Sparling and G. R. Loppnow, manuscript in preparation). Hence, investigations of the photochemistry of nucleic acids will aid our understanding of the molecular basis for DNA photodamage.

Photochemical reactions are one of the deactivation pathways through which an excited molecule can lose its excess energy. However, these reactions mostly result in unwanted structural changes in DNA. This structural change leads to mutation and cancer. The excitation of DNA molecules is a result of their exposure to harmful UV radiation. Because the nucleobases which are the chromophores in DNA absorb in the UV region, their exposure to UV radiation is dangerous and it is their photochemical reaction that forms the basis for DNA photochemistry. As subsequently indicated in this thesis, sensitive probes are required to monitor DNA damage. Molecular beacons and smart probes, both of which constitute powerful tools for probing DNA damage, are based on fluorescence spectroscopy and were selected for use as probes of DNA damage in our experiments.

1.1 Raman Spectroscopy

The main spectroscopies employed to detect vibrations in molecules involve the processes of IR absorption and Raman scattering.[10] They are widely used to provide information on chemical structures and dynamics. Vibrational transitions in molecules can be detected by absorption of infrared (IR) radiation, inelastic scattering of radiation (Raman) and fluorescence.[11]

Specific selection rules apply in each case. In particular, IR and Raman are complementary techniques and both are required to provide a full vibrational picture. Since the interaction of electromagnetic radiation with matter is based on a set of selection rules; not all vibrations can give rise to absorptions in the IR spectrum. In order for a molecule to give rise to IR bands, there has to be a change in its dipole moment during a given vibration. Consequently, homonuclear diatomics such as H_2, O_2, Cl_2 etc. do not give stretching vibrations in the IR. The same applies to totally symmetric vibrations of larger molecules with centres of symmetry, as well as any vibration that does not generate an electric dipole during its normal mode of vibration.[11]

The phenomenon of inelastic scattering of light was first postulated in 1923 by Smekal,[12] followed by the experimental observation in 1928 by C. V. Raman and K. S. Krishnan,[10,13,14] and the first comprehensive treatment of the underlying theory of Raman spectroscopy was offered by Placzek in 1934.[11] In order to observe such IR-inactive vibrations, it is necessary to consider the inelastic scattering of light – a phenomenon referred to as Raman scattering, which is governed by different selection rules compared to IR spectroscopy.[7,11] It is similar to IR spectroscopy in that it provides vibrational information, but the Raman light is neither absorbed nor emitted.[7] Raman scattering is less widely used than IR absorption, due to problems with sample degradation, signal strength, and fluorescence. However, recent advances in technology and the ability of Raman spectroscopy to probe aqueous solution, samples inside glass containers and samples without any preparations have led to a rapid growth in the application of the technique.[10] For instance, lasers are now available as powerful and monochromatic light sources, making the technique of Raman spectroscopy the method of choice for many applications.[15,16] Also, the use of cooled charge coupled device (CCD) array detectors which are more sensitive with high quantum efficiency and low noise and the availability of volume holographic filters and gratings to provide improved overall throughput and Rayleigh light rejection make Raman spectroscopy a general-purpose analytical technique.[15]

If a transparent sample is illuminated with a beam of monochromatic, polarized light, a vast majority of the light is transmitted through the sample without change.[7,11] An additional fraction is scattered, but the wavelength remains unchanged. This light is referred to as Rayleigh scattering and it is the elastic component of the scattered light. This form of scattering carries no molecular information.[7] The amount of Rayleigh scattered light depends on the excitation wavelength and the relative size of the scatterers compared to the wavelength of the excitation light, but does not depend on the molecular vibrations of the sample.[7] Typically, the Rayleigh scattered light is the most intense since most photons scatter this way.[10]

Apart from the Rayleigh line, there is a very tiny fraction that exits the sample as inelastically scattered light, i.e. the Raman scattered light.[7,11] Generally, the Raman scattered light can be of either higher or lower energy, depending on whether the molecule is initially vibrationally excited or not. If so, the molecule may give up some energy to the electromagnetic field, resulting in scattered light at higher energy (lower wavelength) than the exciting light. This type of Raman scattering is called anti-Stokes scattering. In this form of scattering, the Raman intensities depend on the population in the higher-lying vibrational levels, and other factors on which Stokes scattering depend, such as the laser wavelength and Raman cross-section. The population in the higher-lying vibrational levels usually decreases with a Boltzmann dependence for vibrations significantly greater than the approximately 200 cm^{-1} of thermal energy available at room temperature. In practice, anti-Stokes-shifted Raman bands are usually only seen below 1000 cm^{-1}, because only for these bands is the Boltzmann distribution of the excited vibrational state populated to greater than 1% at ambient temperatures.[17] If the molecular vibrations are all predominantly in their lowest level, the electromagnetic field transfers energy to excite the molecule to a higher-lying vibrational level and the scattered light is at lower energy (higher wavelength) than the excited light (Figure 1.1). This latter case is called Stokes scattering and is more typically measured in a Raman spectroscopy experiment. [7] Raman scattering is inherently a weak process in that only one in every 10^6-10^8

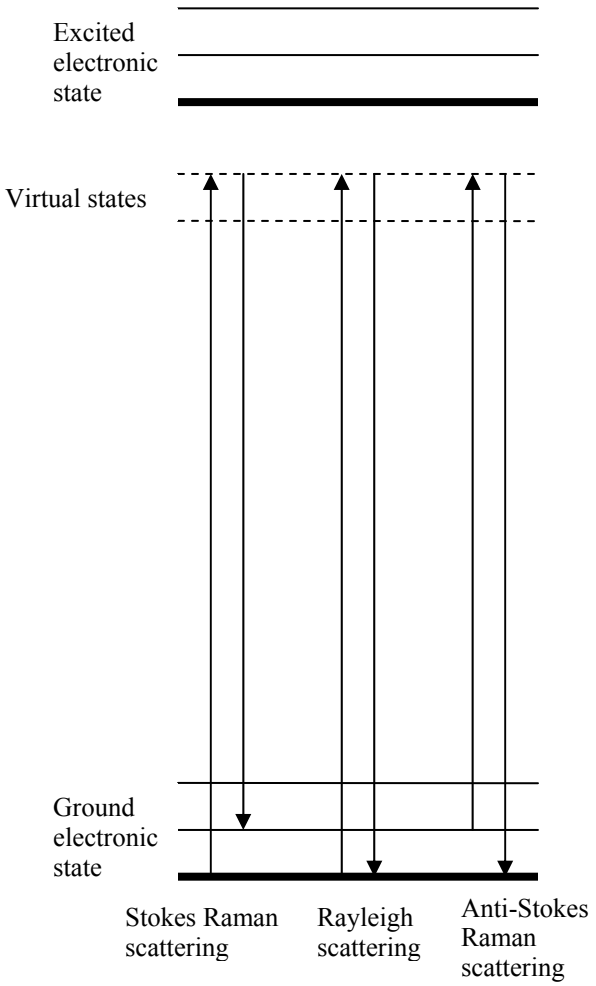

Figure 1.1. Stokes Raman scattering, Rayleigh scattering and anti-Stokes Raman scattering processes. In the Stokes scattering process, the molecule is initially in its ground vibrational level of the ground electronic state. An excitation photon (*up arrow*) carries the molecule to a virtual level (*dashed line*) from which it immediately scatters inelastically (*down arrow*), leaving the molecule in an excited vibrational level of the ground state. In the Rayleigh scattering process, the molecule is initially in its ground vibrational level of the ground electronic state. An excitation photon (*up arrow*) carries the molecule to a virtual level (*dashed line*) from which it immediately scatters elastically (*down arrow*), leaving the molecule back in its original ground vibrational level of the ground state. In the anti-Stokes scattering process, the molecule is initially in an excited vibrational level of the ground electronic state. An excitation photon (*up arrow*) carries the molecule to a virtual level (*dashed line*) from which it immediately scatters inelastically (*down arrow*), leaving the molecule in a ground vibrational level of the ground state. Note that the excitation and scattering processes are instantaneous and simultaneous. The excited electronic state is also shown, but it is not involved in the process since the energy of excitation is not sufficient to take the molecule up to the excited electronic energy state. However in resonance Raman scattering, the excitation brings the molecule to this electronic state (see Figure 1.2).

photons which scatter is Raman scattered.[10] It should be noted however that this weakness in itself does not make the process insensitive, since with modern lasers and microscopes, very high power densities can be delivered to small samples.

1.1.1 Vibrational spectroscopy

The complete vibrational spectrum of diatomic or polyatomic molecules can be obtained using IR absorption and inelastic scattering (Raman) of electromagnetic radiation. Both are usually presented as complementary vibrational techniques, but the processes are different; absorption for infrared and scattering for Raman. This difference in process has important consequences that reinforce the idea that infrared and Raman are complementary spectroscopies. The gross selection rules are different. Infrared intensities are dependent on a change in permanent dipole moment with the vibration, while Raman intensities depend on a change in the polarizability with the vibration. Thus, water is a strong infrared absorber but is a weak Raman scatterer, making Raman spectroscopy much more useful for aqueous and biological samples. In addition, many bands that are weak in the IR spectrum are among the strongest bands in Raman spectrum. For instance, S-S and C=C stretching bands are often so weak as to be unrecognizable in the IR but are very strong in the Raman spectrum. Also, low frequency bands are far more easily measured by Raman spectroscopy than by IR, as most spectrometers readily measure down to 100 cm^{-1} or less.[17] Most functional groups are dipolar, making infrared spectroscopy a very useful technique for the identification of unknown compounds. In fact, this difference results from the gross selection rules, which lead to symmetry considerations, yielding the mutual exclusivity principle which states that if a molecule contains a center of symmetry, the vibrations that are infrared allowed are Raman forbidden by symmetry and vice versa.[7]

Before the mid-1980s, Raman spectroscopy was often considered a less desirable technique than IR absorption spectroscopy. This was due to the fact that only one in about 10^8 photons undergoes Raman scattering. The weakness

of the Raman signal has been ameliorated by the advent of multiplex and multichannel techniques, which have greatly increased the sensitivity of modern Raman spectrometry. Additionally, many compounds fluoresce when illuminated by visible lasers. The fluorescence signal can in some cases far exceed and thus swamp the Raman signal. Fluorescence can be a significant interference in Raman spectroscopy, since it occurs in the same spectral region and can be much more intense than the Raman signal. Thus, a judicious choice of excitation wavelength will ensure that the Raman intensities are optimized. Near IR (NIR) and UV lasers have been used for sample illumination to eliminate fluorescence interference. Lasers are typically used to provide the excitation in a Raman spectroscopy experiment, as they are highly collimated, powerful, monochromatic, polarized sources, ideal for Raman spectroscopy. Since Raman intensity is proportional to $(\tilde{\nu}_0 - \tilde{\nu}_i)^4$, a lower excitation wavelength is useful in most cases, and UV Raman measurements have a greater intrinsic sensitivity than the corresponding measurements made with a NIR or visible laser of the same power.[7,10,17]

Although both infrared and Raman spectroscopy equipment share the general characteristics of having a light source, wavelength dispersion device and detector, the specific equipment used for infrared and Raman spectroscopy differs. Infrared spectroscopy is an absorption technique, and therefore requires a light source operating in the infrared region of the spectrum, typically between 15000 and 10 cm^{-1} (667 nm to 1000 μm).

1.1.2 Resonance Raman spectroscopy (RRS)

The resonance Raman effect comes into play when the frequency of the incident radiation falls within an electronic absorption band.[18,19] Resonance Raman scattering refers to a phenomenon in which the Raman line intensities are greatly enhanced by excitation with wavelengths that closely match that of an electronic absorption band of an analyte (Figure 1.2).[20,21] When the frequency of the excitation laser beam is close to the frequency of an electronic transition, intensity enhancements of some normal modes of as large as 10^8 have been observed.[22] This is an important aspect of resonance

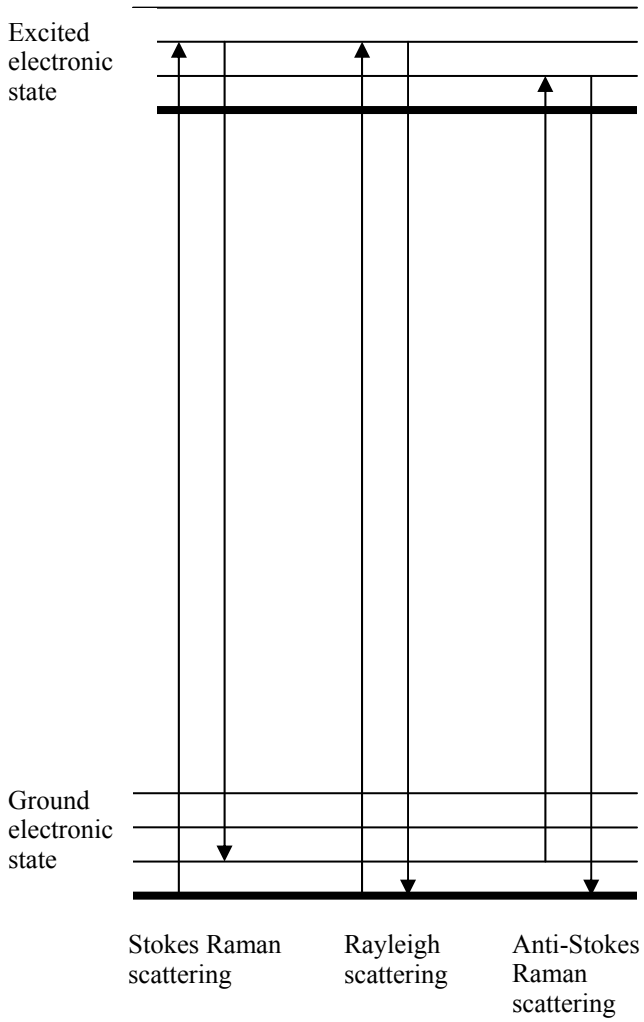

Figure 1.2. The resonance Raman scattering process. All the three processes of Stokes, Rayleigh, and anti-Stokes scattering are shown. Resonance Raman scattering follows the same process as for off-resonance Raman, except that the virtual level (shown as dashed lines in Figure 1.1) is coincident with real excited vibronic level of the molecule. Again, the difference between the excitation and scattered photon wavelength or energy is measured.

Raman spectroscopy.[10,18,22] This means that Raman spectroscopy becomes a much more sensitive technique, and since only the chromophore gives the more efficient scattering, it is also selective for that part of the molecule involving the chromophore. When the resonance condition occurs, it is possible to get both electronic and vibrational information from the sample.[10] When the exciting radiation is resonant with an electronic transition, Raman spectra are dominated by totally symmetric vibrations which mimic the change in molecular geometry that accompanies electronic excitation.[18] In some cases, non-totally symmetric vibrations are also enhanced as a result of symmetry changes which accompany the electronic transition, or by means of vibronic coupling of excited electronic states. Resonance enhancement presents the opportunity for increased sensitivity and selectivity in the detection of dilute components of mixtures.[10,18,22] Conventional Raman instrumentation supplemented by tunable lasers can be employed in analytical and biochemical applications in which the vibrational spectrum of a chromophore is enhanced relative to its non-absorbing surroundings. One key reason this technique has become important is that molecules that give good resonance Raman spectra may not be plagued by fluorescence interferences, if the excitation wavelength is in the UV range.[10,22] It should be noted that, depending on the absorption band of the sample, RRS experiments can be performed with NIR, visible and UV excitation wavelengths.

There are particular excitation frequencies that are natural frequencies of oscillation of specific electron oscillators of the molecular electron cloud. These natural frequencies are the molecular electronic absorption band frequencies. Excitation at these frequencies is said to be in "resonance" with the electronic transition (Figure 1.2). Therefore, the Raman scattering process is said to be "resonance Raman" scattering.[22] This resonance excitation at the natural frequency of electron cloud oscillation results in an increased oscillating charge displacement and a corresponding increase in the induced dipole moment. This in turn results directly in an increased scattering or reradiation efficiency for Raman scattering.[22] We can change the part of the molecule studied by changing excitation wavelengths, if the absorption bands

derive from different chromophoric segments of the molecule. However, if the two absorption bands derive from the same chromophoric segment of a single molecule, the spectra will differ because of differences in the structure of the excited-states associated with the two electronic transitions; the different excited-states couple differently with the ground state vibrational motion.[22]

The resonance Raman spectrum, like the ordinary Raman spectrum, is recorded as a function of the frequency shift between the incident and scattered radiation, where peaks are observed at the vibrational frequencies of the molecule.[18] Although the selection rules for resonance and off-resonance Raman are different, the peak frequencies in either case are those for the molecule in its ground state. However, the intensities of the resonance Raman-active vibrational modes depend on the nature of the resonant excited electronic state.

1.1.3 UV resonance Raman spectroscopy (UVRRS)

UV Raman spectroscopy uses selective excitation in the UV absorption bands of molecules to produce spectra of particular analytes and chromophoric segments of macromolecules. The rapid advancements in the 1980s led to extensions into spectral regions away from the visible, and this has dramatically increased the utility and applicability of Raman spectroscopy.[22] The fact that many biological samples absorb in the UV region makes this technique particularly suited for biochemical applications.[1,9,16,22-24] In addition, UV resonance Raman measurements can show little fluorescence interference compared to conventional visible-wavelength Raman measurements.[2,22,25] However, due to the high energy of UV radiation, sample degradation and photodecomposition can result. To minimize this effect in practice, the laser is detuned to lower the power at the small sample area being probed, so that exposure of the sample for an extended period of time will not cause any significant sample damage. In addition, the sample, if in solution form, can be flowed, or if contained in an NMR tube can be spun. All of these minimize the effect of sample degradation as caused by the high energy laser.

UV excitation is more sensitive, compared to traditional Raman spectroscopy. This is not surprising, considering the inverse fourth-power relation between Raman intensity and excitation wavelength. This sensitivity adds to the advantage of UVRRS. Thus, UVRRS can be said to be composed of two-part sensitivity factors – the inverse fourth-power relation between intensity and wavelength, and the resonance enhancement. The latter factor is also responsible for the selectivity of UVRRS, since absorption in the UV could be characteristic of the analyte to be probed by this technique.

1.1.4 Theory

According to classical theory, Raman scattering by a molecule arises from an induced electric dipole, which results from the interaction of an electromagnetic field with a vibrating molecule. Electric dipoles may be induced in a molecule by static or alternating external electric fields.[7,11] An incident electromagnetic field drives the electron cloud of the molecule at the incident frequency. An oscillating dipole moment is created by the resulting displacement of electronic charge. Because the charge is accelerating, it radiates energy in the form of electromagnetic radiation. The radiated frequency is identical to the excitation frequency; light is scattered elastically. Because charge acceleration induces the radiation, the Rayleigh scattering efficiency increases with the fourth power of the excitation frequency. Those oscillations that most efficiently Raman scatter are those that couple most effectively to the oscillating electric dipole moment induced by the excitation electromagnetic field.[22] The relation between the induced dipole moment vector $\boldsymbol{\mu}$ and the electric field vector E can be written in the form of the following power series:[26]

$$\boldsymbol{\mu} = \boldsymbol{\alpha}E + \frac{1}{2}\boldsymbol{\beta}E^2 + \frac{1}{6}\boldsymbol{\gamma}E^3 + \ldots\ldots \qquad (1.1)$$

where $\boldsymbol{\alpha}$ is the polarizability, $\boldsymbol{\beta}$ is the hyperpolarizability, and $\boldsymbol{\gamma}$ is the second hyperpolarizability of the molecule. The induced dipole moment $\boldsymbol{\mu}$ is a first rank tensor, while the polarizabilities $\boldsymbol{\alpha}$, $\boldsymbol{\beta}$, $\boldsymbol{\gamma}$ are tensors of rank 2, 3, and 4, respectively. Tensors are operators describing physical properties responsible

for the connection between vectorial quantities.[11] Polarizability can be defined as the measure of the flexibility of the electron cloud, i.e. the ease with which the electron cloud of a molecule can be deformed or displaced to produce an electric dipole under the influence of an external electric field. The non-linear terms of Eq. 1.1 are usually very small compared to the linear term, so they do not play a role in normal, linear Raman scattering. Considering only the linear term, Eq. 1.1 becomes

$$\boldsymbol{\mu} = \boldsymbol{\alpha}\mathrm{E} \tag{1.2}$$

i.e. the product of the molecular polarizability and the oscillating electric field.[7,11]

When the time dependence of the induced dipole moment is considered, the polarizability tensor may be modulated by the normal vibrations. In this case, assuming a harmonic potential for the molecular vibration, and that the polarizability does not deviate significantly from its equilibrium value (α_0) as a result of the vibration, the dependence of the molecular polarizability on the normal coordinates is given by:[26]

$$\alpha_k = \alpha_0 + \left(\frac{\partial \alpha}{\partial Q_k}\right)_0 Q_{k0} \cos 2\pi c \tilde{\nu}_k t \tag{1.3}$$

where Q_k is the kth normal mode of vibration, Q_{k0} is the normal coordinate amplitude and $\tilde{\nu}_k$ is the vibrational wavenumber. The variation of the electric field strength with time is given by:

$$E = E_0 \cos 2\pi c \tilde{\nu}_0 t \tag{1.4}$$

where E_0 is the electric field amplitude of the photon, c is the speed of light, t is time and $\tilde{\nu}_0$ is the incident laser wavenumber. Solving for the induced dipole yields

$$\mu = \alpha_0 E_0 \cos 2\pi c \tilde{\nu}_0 t + \frac{1}{2}\left(\frac{\partial \alpha}{\partial Q_k}\right)_0 Q_{k0} E_0 \left[\cos 2\pi c(\tilde{\nu}_0 - \tilde{\nu}_k)t + \cos 2\pi c(\tilde{\nu}_0 + \tilde{\nu}_k)t\right] \quad (1.5)$$

The three cosine functions in Eq. 1.5 indicate that the induced dipole oscillates with three distinct frequencies simultaneously. The first term describes Rayleigh scattering at the incident laser wavenumber $\tilde{\nu}_0$, the second term is Stokes Raman scattering at wavenumber $\tilde{\nu}_0 - \tilde{\nu}_k$ and the third term is anti-Stokes Raman scattering at wavenumber $\tilde{\nu}_0 + \tilde{\nu}_k$. These so-called beat frequencies are produced when the dipole oscillating at $\tilde{\nu}_0$ is modulated by the molecular vibration oscillating at $\tilde{\nu}_k$. The classical theory can be said to successfully describe the frequency relationships of Raman scattering. It shows that Raman shift is independent of the frequency of the incident radiation. Thus, whether a molecule is excited with a blue or green laser, the same wavenumber pattern will be obtained, with the Raman shifts characteristic of the scattering molecule.[11]

1.1.5 Resonance Raman spectrum and the absorption spectrum

The processes of resonance Raman and absorption are separated clearly by time. Figure 1.3 is used to explain the nature of the absorption process in electronic absorption spectroscopy. The absorption process is the transition from the ground state to an excited-state as shown. This process is different from resonance Raman scattering. The resonance Raman scattering process is not deemed to involve transition from the ground to the excited-state. In the absence of any other effects, when light of the correct frequency is absorbed, one would observe a spectrum that is composed of a huge number of closely spaced sharp spectral bands whose individual intensities depend on the magnitude of the transition dipole.[27] In practice, each of these spectral bands is so broad that one observes only a relatively smooth spectral envelope. Often, the most intense transition is to one of higher vibronic states. The causes of band broadening include environmental heterogeneity, Doppler

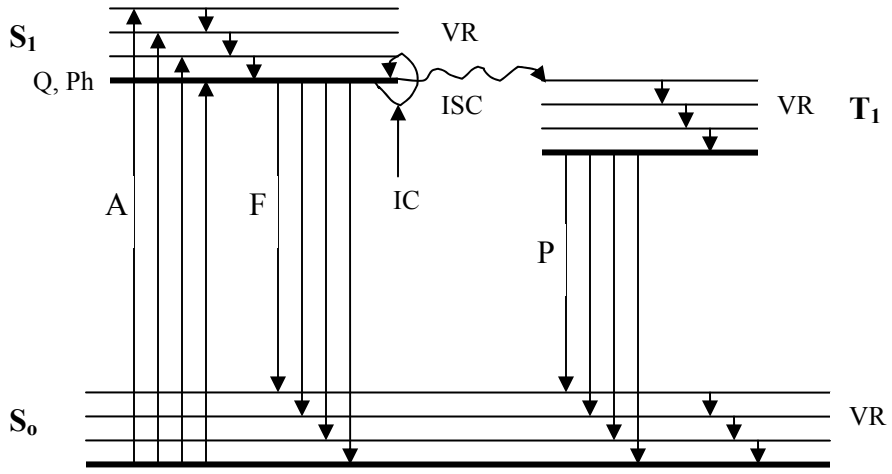

Figure 1.3. Jablonski diagram showing the absorption of light (A) by a molecule and its excitation from the ground state (S_o) to the excited-state (S_1). In the excited-state, the different relaxation processes that take place are indicated (F = fluorescence, P = phosphorescence, IC = internal conversion, ISC = intersystem crossing, VR = vibrational relaxation, Q = quenching and Ph = photochemical reaction). Note that P is from a different state (T_1) compared to F which originates from S_1.

shifts, contributions from a number of levels and the presence of hot bands arising from electrons present in the excited-states. The result of all this is that a potentially complex and very informative spectrum is reduced to a very simple one.[10,27] The most intense resonance Raman scattering in some cases will come mainly from the first two vibronic levels. Therefore, it is not necessarily the case that the maximum absorbance of a UV/Visible transition is the energy at which the greatest resonance Raman scattering will occur.[10]

1.1.6 Experimental considerations

Basically, the instrumentation for RRS is not fundamentally different from that for off-resonance Raman spectroscopy. Additional sample handling constraints may apply for RRS in order to minimize the deleterious effects of absorption, such as sample heating and photochemical decomposition. In addition, the intrinsic fluorescence of the sample may be unavoidable and require instrumental or chemical approaches to fluorescence rejection.[18] The frequency of the excitation source has to fall within the electronic absorption band. This requirement necessitates the use of tunable lasers, which can give excitation wavelengths in the UV-Visible region to suitably match the absorption bands of many molecules.[18,22] Another advantage of using tunable lasers is that in favourable cases the excitation frequency can be chosen to minimize interference from fluorescence emission. Electronic transitions typically span the UV, visible, and NIR regions of the spectrum.[18] The samples of interest will dictate the nature of the source required. While tunable lasers give rise to a significant improvement in the signal-to-noise ratio (S/N), a major problem with them is that they are large and expensive.[22] However, a new hollow cathode UV laser has been introduced that utilizes sputtered silver or copper in a noble gas to give rise to 244 and 248 nm excitation wavelengths.[22,28] This laser is small and inexpensive, it is air-cooled and has a low power consumption. Other UV lasers include double Ar^+ lasers, UV diode lasers and excimer laser.

Laser tunability imposes additional considerations when employing single monochromators with array detectors.[14,18] Such an experimental arrangement

requires notch filters to reject the strong Rayleigh scattering at the laser frequency. If unrejected, high levels of stray light obscure the Raman signal from lower frequency Raman bands. Each excitation frequency requires its own filter. This consideration is however obviated when using polychromators with higher stray light rejection, but also lower throughput.[18]

Prism and grating monochromators, wavelength dispersion devices for infrared spectroscopy, have been largely supplanted by interferometers and Fourier transform infrared spectroscopy (FT-IR) is commonplace. Raman vibrational spectroscopy is performed in the visible and near-infrared regions of the spectrum. The frequency shifts in the Stokes and anti-Stokes Raman spectra usually corresponds to the frequencies of the normal modes of molecular vibrations, only the frequency shift of the scattered light from the excitation frequency (wavelength) is measured; thus the shift values are more convenient for characterizing the band positions than absolute wavenumbers. Grating-based monochromators are used almost exclusively in Raman spectroscopy, usually with one or more filters to remove the higher-intensity Rayleigh scattering. The most popular detectors are CCD detectors, but photomultiplier tubes and photodiode arrays are still used. In addition, UV detectors are more sensitive than NIR detectors.[7,17] FT Raman is used in some systems, but usually only for off-resonance Raman as the excitation wavelength is 1064 nm.

1.1.7 Initial excited-state structural dynamics

An advantage of the resonance condition is that the Raman signal is significantly enhanced compared to that of unenhanced Raman scattering. It was noticed early on that the relative intensities may also be significantly different in a resonance Raman experiment compared to those obtained off-resonance.[7] RRS yields the initial excited-state structural dynamics of molecules from the intensities of the Raman bands that are observed, which are in resonance with the electronic excitation, since the excitation wavelength falls within the absorption band of the molecule being probed. The intensities are converted to relative Raman cross-sections, usually by using an internal

standard to normalize the intensities. Cross-sections, which are typically reported as an area/molecule (cm^2/molecule) can be thought of as a measure of the efficiency of a given molecule at capturing photons, i.e. it is a measure of how much of the incident light is scattered by the molecule. Quantum mechanically, resonance Raman cross-sections can be calculated by the following sum-over-states expression which is derived from second-order perturbation theory within the adiabatic, Born-Oppenheimer and harmonic approximations:

$$\sigma_R = \frac{8\pi e^4 M^4 E_s^3 E_L}{9\hbar^4 c^4} \int_0^\infty dE_0 H(E_0) \left| \sum_v \frac{< f \mid v >< v \mid i >}{\varepsilon_v - \varepsilon_i + E_0 - E_L - i\Gamma} \right|^2 \qquad (1.6)$$

where the resonance Raman cross-section, σ_R, is directly proportional to the absolute measured resonance Raman intensity. In this expression, M is the transition length, E_s and E_L are the scattered and incident photon energies, respectively, $|f>$, $|v>$ and $|i>$ are the final, intermediate, and initial vibrational states, respectively, ε_v and ε_i are the energies of the intermediate and initial vibrational states, E_o is the zero-zero energy between the lowest vibrational levels of the ground and excited electronic states, and Γ is the homogeneous line width.[7] Here,

$$H(E_o) = (2\pi\Theta)^{-1/2} \exp\{-(< E_o > - E_o)^2 / 2\Theta^2\} \qquad (1.7)$$

$H(E_o)$ is the inhomogeneous line width function with standard deviation Θ and average energy $<E_o>$. While theoretically elegant, Eq. 1.6 is computationally intensive to evaluate in practice. Of more utility is the time-dependent analog of it, shown in Eqs. 1.8 – 1.9 below.

$$\sigma_R = \frac{8\pi E_s^3 E_L e^4 M^4}{9\hbar^6 c^4} \int_0^\infty dE_0 H(E_0) \left| \int_0^\infty < f \mid i(t) > \exp\{i(E_L + \varepsilon_i)t / \hbar\} G(t) dt \right|^2 \qquad (1.8)$$

$$\mid i(t) >= \exp^{-2\pi H t / h} \mid i > \qquad (1.9)$$

In these equations, G(t) is a homogeneous line width function, and |i(t)> is the initial vibrational wavefunction propagated on the excited-state potential energy surface. For molecules interacting with a solvent bath, G(t) represents the dynamics of the chromophore-solvent coupling and takes the form $e^{-g_R(t)-ig_I(t)}$, where $g_R(t) = D^2[e^{-2\pi\Lambda t/h}-1+2\pi\Lambda t/h]/\Lambda^2$, and $g_I(t) = \pi D^2 t/kTh$ in the strongly overdamped, high temperature limit. D is the coupling strength between the electronic transition and the solvent coordinate, k is the Boltzmann constant, h is Planck's constant, T is the temperature, and $h/2\pi\Lambda$ is the characteristic solvent time scale. The inhomogeneous line width function is simply a Gaussian distribution of zero-zero energies and assumes the electronic zero-zero energy is more susceptible to solvent interactions.[7]

The absorption cross-section, directly proportional to the molar extinction coefficient ε, is given by:

$$\sigma_A = \frac{4\pi E_L e^2 M^2}{6\hbar^2 cn} \int_0^\infty dE_0 H(E_0) \int_{-\infty}^{\infty} dt < i \mid i(t) > \exp\{i(E_L + \varepsilon_i)t/\hbar\} G(t) \quad (1.10)$$

Within the separable harmonic approximation, the <*f*|*i(t)*> and <*i*|*i(t)*> overlaps are dependent on the semi-classical force the molecule experiences along this vibrational normal mode coordinate in the excited electronic state, i.e. the slope of the excited electronic state potential energy surface along this vibrational normal mode coordinate. Thus, the resonance Raman and absorption cross-sections depend directly on the initial excited-state structural dynamics, but in different ways mathematically. It is this complementarity between resonance Raman and absorption cross-sections that allows us to extract the initial structural dynamics from a quantitative measure of the absorption spectrum and resonance Raman cross-sections.

The resonance Raman cross-section, σ_R, can be measured experimentally from the resonance Raman intensity by the following equation

$$\sigma_{Samp} = \sigma_{Std} \frac{I_{Samp}[Std] E_{Std} L_{Samp} n_{Samp} \left(\frac{1+2\rho}{1+\rho} \right)_{Samp}}{I_{Std}[Samp] E_{Samp} L_{Std} n_{Std} \left(\frac{1+2\rho}{1+\rho} \right)_{Std}} 10^{dC(\varepsilon_{Samp} - \varepsilon_{Std})} \quad (1.11)$$

where σ is the absolute Raman cross-section, I is the resonance Raman intensity, E is the spectrometer efficiency, $L = [(n^2 + 3)/3]^4$ is the internal field correction, n is the refractive index, ρ is the depolarization ratio, d is the Raman sample pathlength, C is the absorbing species concentration, and ε is the molar extinction coefficient. The subscripts Samp and Std refer to the sample and intensity standard, respectively, present in solution at concentrations [Samp] and [Std]. If an internal intensity standard is used, $L_{Samp} = L_{Std}$ and $n_{Samp} = n_{Std}$. The way we carry out this procedure in our group is we use an internal standard whose cross-section would have been measured previously. Typical internal standards used include cyclohexane, benzene, acetonitrile, cacodylate, sulphate and nitrate. The $10^{dc(\varepsilon_{Samp} - \varepsilon_{Std})}$ aspect of Eq. 1.11 represents the correction for the differential self-absorption by the sample and d is the path length for the incident laser power to decrease by half ($d = -(\log 0.5/c\varepsilon_{laser})$), where ε_{laser} is the extinction coefficient at the laser frequency.

The absolute Raman cross-section σ_R, is related to the differential cross-section $\frac{d\sigma}{d\Omega}$ as follows:

$$\sigma_R = \frac{8\pi(1+2\rho)d\sigma}{3(1+\rho)d\Omega} \quad (1.12)$$

If an internal standard of known differential cross-section is used, the differential cross-section of the sample can be determined from the measured relative intensities:[18]

$$\frac{I_1}{I_2} = \frac{C_1 d\sigma_1 / d\Omega}{C_2 d\sigma_2 / d\Omega} \quad (1.13)$$

where C_i is the molar concentration of species I and $\frac{d\sigma_i}{d\Omega}$ its differential cross-section for a particular Raman band. The intensities in Eq. 1.13 are determined from the area under the band rather than the peak intensity. Sample values of differential cross-sections of some of the molecules used in this thesis are shown in Table 1.1.

A critical pre-requisite to using Raman and resonance Raman spectroscopy to examine the initial excited-state structural dynamics of molecules is the determination of the normal modes of vibration for the molecule of interest. The most definitive method for determining the normal modes is exhaustive isotopic substitution, subsequent measurement of the IR and Raman spectra, and computational analysis with the Wilson FG method.[7] Such an analysis is rarely performed presently because of the improvements in accuracy of *ab initio* and semi-empirical calculations. *Ab initio* computations have been applied to most simple molecules, resulting in relatively consistent descriptions of the normal modes for such molecules.

1.1.8 Applications of RRS

Intensities in RRS reveal structural information about the excited electronic state. Resonance enhancement also depends on the dynamics in the excited electronic state.[18] As a result, resonance Raman spectra can provide subpicosecond time-domain information about the excited chromophore and the solvent motion which couples to the electronic transition. Resonance Raman spectroscopy is a powerful tool for probing excited-state structure and dynamics.[29] By tuning the exciting laser wavelength into the absorption band of a given molecule, resonant enhancement of those vibrational modes coupled to the molecular electronic excitation occurs. The selective excitation of chromophores lead to increased sensitivity in mixtures. The resonance Raman vibrational band intensity is directly proportional to the slope of the excited-state potential energy surface along that vibrational coordinate – the greater the change in molecular structure along the vibrational coordinate, the more intense the resulting resonance Raman band. Thus, the intensities of the

Table 1.1. Typical values of differential cross-sections of some of the molecules used in this thesis

Sample	Typical values of differential cross-sections (x 10^{-14} $Å^2$/(molecule sr)
Benzophenone-3 (BZ3)	4.1 x 10^3 – 18.4 x 10^4
9-Methyladenine (9-MeA)	18.2 x 10^4 – 14.5 x 10^6
Sodium nitrate	5.8 x 10^3 – 1.9 x 10^4
Methanol	2.0 - 19.2

resonance Raman bands reflect the conformational distortion of the molecule along each normal mode upon excitation to an electronic excited-state,[2,4-6,30,31] and the initial excited-state structural dynamics of any given molecule can be probed by RRS. There is a large number of published papers on the application of UVRRS in determining the excited-state structure and dynamics of nucleic acids and their components.[7] Our group has also begun to extend this to a number of common sunscreen active ingredients (AIs) (see Chapter 3), with a view to elucidating their excited-state structure and dynamics as they relate to their photochemistry and photostability.

Another important application of RRS is the measurement of resonance Raman excitation profiles (RREPs). Since absolute and relative intensities of the bands in a resonant spectrum are dependent on the separation between the excitation and resonance frequencies and on the nature of the electronic transitions, it can be useful to plot the intensity of selected bands against the frequency of the laser.[10] The intensities of resonance Raman-active vibrational modes depend on the nature of the resonant excited vibronic state. RREP is the variation of Raman intensity of one of these modes as a function of excitation frequency.[18] As stated above, this profile can be analyzed to determine the change in geometry of the molecule along the normal coordinate on going from the ground state to the excited electronic state. RRS is essentially a two-dimensional experiment, where the intensity is recorded as a function of frequency shift (for fixed excitation frequency) to obtain the resonance Raman spectrum, and as a function of excitation frequency to obtain RREPs for the various modes (at fixed frequency shifts).[18] RREPs are closely connected to electronic absorption spectra and they provide additional information which cannot be obtained from the absorption spectrum alone. To do this effectively, a tunable laser is usually used so that the Raman spectrum can be recorded at different laser frequencies. In the simplest RREP, the maximum intensity of the band produced will be the point at which maximum resonance occurs. RRS has also been used to elucidate the A-term resonance enhancement from a small molecule such as iodine.[10] Perhaps the most widespread use of RRS is for the study of heme-containing proteins.[10,32,33] The

resonance Raman scattering obtained with visible excitation of these proteins is due to an interaction with the π-π* transitions from the porphyrins ring of the heme group.

In addition to the two important applications just mentioned, UVRRS has a number of other unique applications. The ability of UVRRS to selectively examine the vibrational spectra of particular species in complex mixtures makes the technique uniquely important for many analytical applications.[22] Selectivity is determined by the relative Raman cross-sections of the analyte compared with other species present in the sample. Sensitivity depends on the magnitude of the analyte's Raman cross-sections compared with those of overlapping, interfering Raman bands and emission from the sample.[22] Fluorescence interference does not normally occur in condensed phases with UV excitation below 260 nm. Thus, species with lowest singlet states below 260 nm may have vanishingly low fluorescence quantum yields because they may be flexible and return to the ground state through non-radiative processes,[22,25] though this may not be generally true.

To demonstrate the selectivity and sensitivity that can be achieved with UVRRS, structurally similar polyaromatic hydrocarbons (PAHs) such as naphthalenes, substituted anthracenes and pyrene have been analyzed. These compounds were monitored down to 200 parts per billion (ppb), and the spectra differentiated between species as similar as 2-methyl- and 9-methylanthracene.[22,25,34-36] PAHs are the most intense Raman scatterers[22] and the vibrations that are enhanced are mostly symmetric in-plane ring-breathing modes. The UV resonance Raman spectra of these PAHs, though similar, are different enough to identify the ring system. The selectivity of UVRRS has also been exploited by our research group to probe the active ingredients (AIs) in sunscreen formulations, as will be discussed in Chapter 2.[2,32] We proved that even though the sunscreen AIs are structurally similar, (just like the PAHs mentioned above), UVRRS can discriminate between them, especially, when 244 nm excitation is used. Also, despite the complex matrix in which the AIs are present, UVRRS has the capability to analyze the AIs with minimal perturbations from the matrix. In addition, UVRRS has been used by our

group for the direct detection of oxidative product of guanine (8-oxo-deoxyguanine).[37] Current methods being used are indirect and thus the direct detection of the oxidative lesion by UVRRS is highly desirable.

Major advances have also occurred in the UVRRS measurements of biologically important molecules and for biological assemblies such as viruses, bacteria and algae.[22] The resonance Raman enhancement profiles have been almost completely characterized for aromatic amino acids, peptide and protein amide vibrations, nucleic acids, DNA and visual pigments.[4,5,7,10,22] Protein dynamics and early stages of protein and peptide unfolding have been extensively studied. UVRRS is now arguably the most sensitive method for determining dilute solution secondary structure.[22]

With the availability of UV lasers, excitation in the UV region (below 260 nm) is also an excellent way of avoiding fluorescence. Thus, for Raman measurements that are greatly perturbed by fluorescence in the visible region, UV excitation may reduce such interference significantly. This explains why the PAHs which are normally fluorescent in the visible region gave intense Raman signal in the UV, and why the sunscreen AIs which are subtly fluorescent above 300 nm gave high-quality UVRR spectra at 244 nm.[2,22,32]

1.2 DNA Damage and Protection

1.2.1 DNA structure and their components

Nucleic acids are the very essence of life, and contain the genetic information of all organisms.[7] DNA carries all of the developmental potential of an organism within its genes. RNA possesses catalytic and self-catalytic properties, plays a role in gene expression, and is the intermediary between DNA and proteins.[7,38,39] The structures of the nucleic acid bases are shown in Figure 1.4. Both DNA and RNA are polymers consisting of an alternating sugar/phosphate backbone and a nucleobase attached to each sugar.[7] The sugar in RNA is ribose and the one in DNA is 2'-deoxyribose. These sugars are connected via phosphate groups bonded to the 3' carbon of one sugar and the 5' carbon of an adjacent one. Both DNA and RNA carry a significant

Pyrimidines

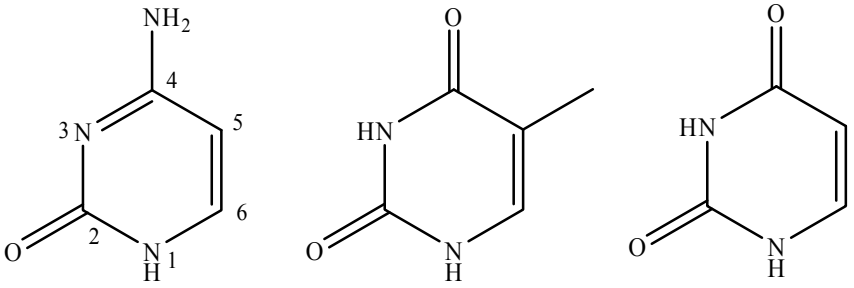

Purines

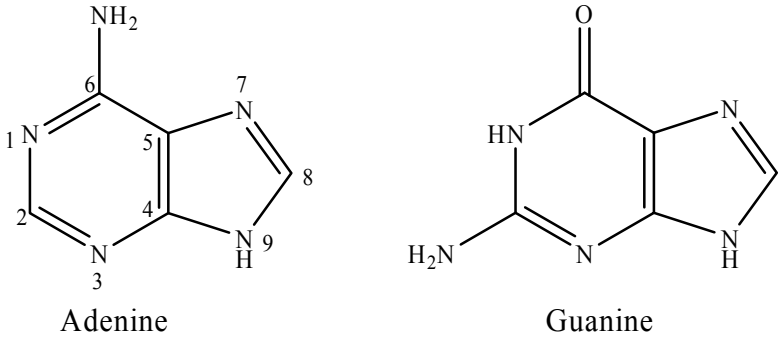

Figure 1.4. Structures of the five nucleobases. The atomic numbering scheme for the ring atoms is shown on the first member of each group.

negative charge because each phosphate group has a single negative charge.[7] The nucleobases are grouped into the purines (adenine and guanine) and the pyrimidines (cytosine, thymine and uracil), based on their parent structures. Both nucleic acids contain the same purines, adenine and guanine. Both also contain cytosine. But thymine is almost exclusively found in DNA, while uracil is almost exclusively found in RNA.

1.2.2 UV radiation and DNA damage

The alarming increase in the incidence of skin cancer is a major cause of concern and the centre of much research. The causes of skin cancer are complex and are not well understood. However, for both malignant and non-malignant melanoma, exposure to solar UV radiation has been implicated.[40,41] Of the UV-IR energy reaching the earth's surface, 15% is in the UV region, 60% is in the visible region and the remaining 25% is in the IR region.[42,43] The UV region is the most energetic despite the fact that it accounts for the smallest fraction of terrestrial solar energy. It is therefore most likely to induce biological damage. Other wavelengths outside this region can also induce damage.

The UV radiation is divided into three regions according to the resultant biological effects.[41] The UVC region comprises 100 – 280 nm, but this region of the solar spectrum is absorbed mainly by ozone and oxygen in the atmosphere and therefore does not significantly reach the earth's surface.[41] The intermediate range is the UVB region from 280 – 320 nm, a portion of which does not reach the earth's surface because it is absorbed by stratospheric ozone. The shortest measurable solar wavelength at sea level is 290 nm,[41] i.e. wavelengths below 290 nm do not reach the earth's surface. However, this wavelength cut-off is markedly dependent on the atmospheric ozone concentration and any depletion of the ozone layer will allow wavelengths shorter than 290 nm to penetrate to the terrestrial environment. Under normal condition of solar UV exposure, the UVB is most significant in the induction of skin cancers.[42,44] UVB is also the principal cause of erythema and it is implicated in structural and cellular skin damage such as elastosis,

actinic keratosis and talengiectasis.[41,45] The longer wavelength region called UVA is from 320 – 400 nm and was originally thought to be harmless because of its low energy. It is now known to cause wrinkling, photoaging of the skin, dermatological photosensitivity, some erythema, and has recently been shown to contribute to melanoma induction.[41,46] Recently, this region of the UV has been shown to induce single strand breaks and DNA-protein crosslinks in a manner similar to ionizing radiation.[41,47] Since the absorption of DNA spans both the UVC and UVB regions, it is these wavelengths that are most destructive to living organisms.

1.2.3 DNA photochemistry

Although the photochemical quantum yields are low, nucleic acids and their components exhibit a variety of photochemistry.[7] Different photoproducts are formed, depending on whether the nucleic acid is irradiated with UV light or ionizing radiation, and whether the irradiation occurs in the presence or absence of oxygen.[7] When DNA is exposed to UV radiation, photochemical products such as cyclobutane pyrimidine dimers (CPDs), [6-4] pyrimidine-pyrimidinone and photohydrates are formed.[7,37,48] The formation of these photoproducts ultimately leads to cancer. In order to understand the molecular basis for such photodamage, the photochemistry of the nucleobases have been extensively explored (Figures 1.5 – 1.9).[7,37,49-51] In addition, our group has done a lot of work on the initial excited-state structural dynamics of nucleobases and their analogs.[4-7] This work allows us to draw a link between the structural distortions that take place in the excited-state of these molecules and photochemistry.

Figures 1.5 – 1.9 show most of the primary photoproducts formed in DNA from each of the pyrimidine and purine nucleobases. It should be noted that most of the photochemical mechanisms and quantum yields are dependent on the size of oligonucleotide[7]. For example, thymine cyclobutyl photodimer formation proceeds from the monomeric nucleobase with a very low quantum yield via the singlet state in dilute solution, while the quantum yield increases

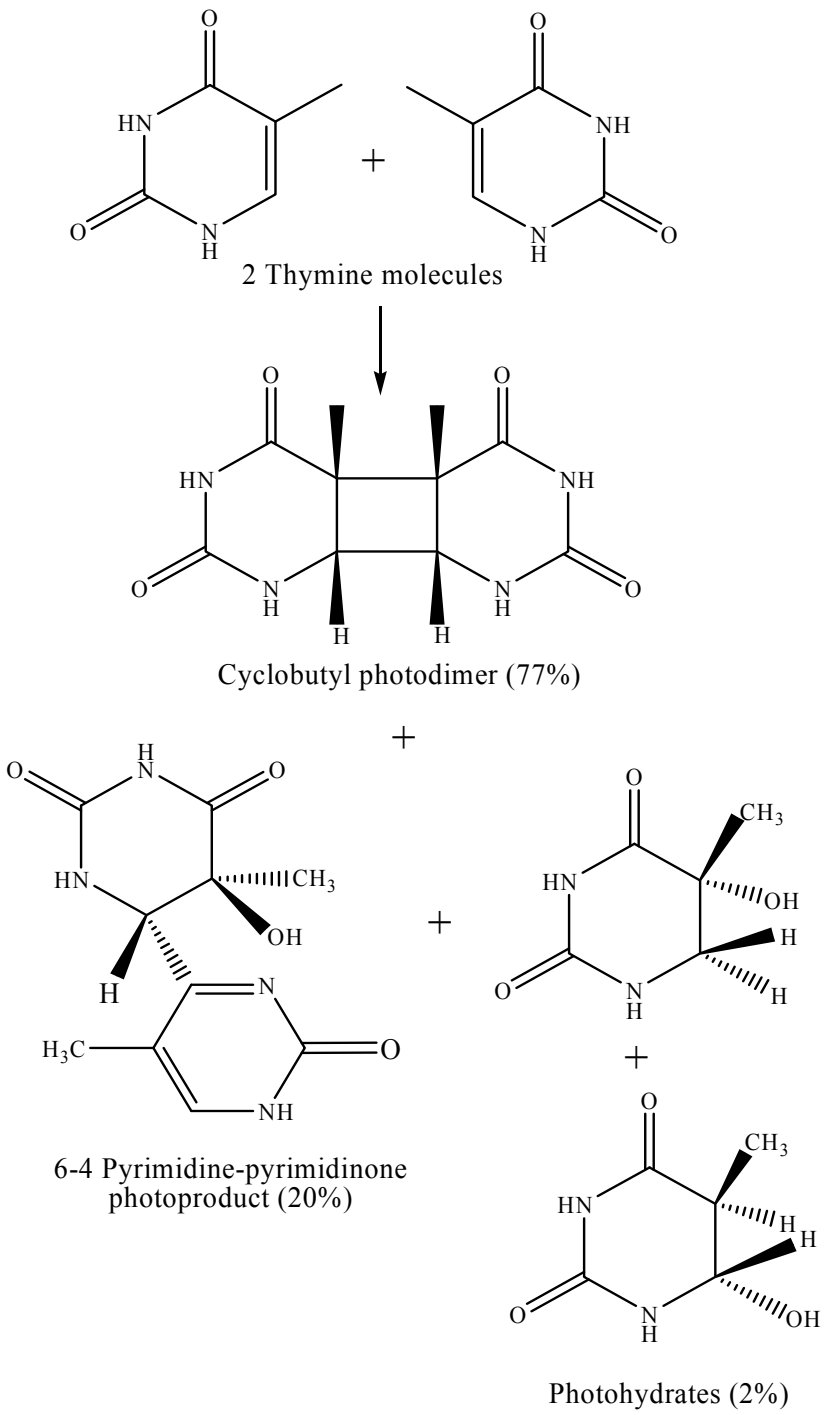

Figure 1.5. Chemical structures of the photoproducts formed from thymine as a result of UVB/UVC radiation. The percentage yield of each product is indicated. Only the cis-syn CPD (T<>T), the most biologically relevant isomer in DNA, is shown.

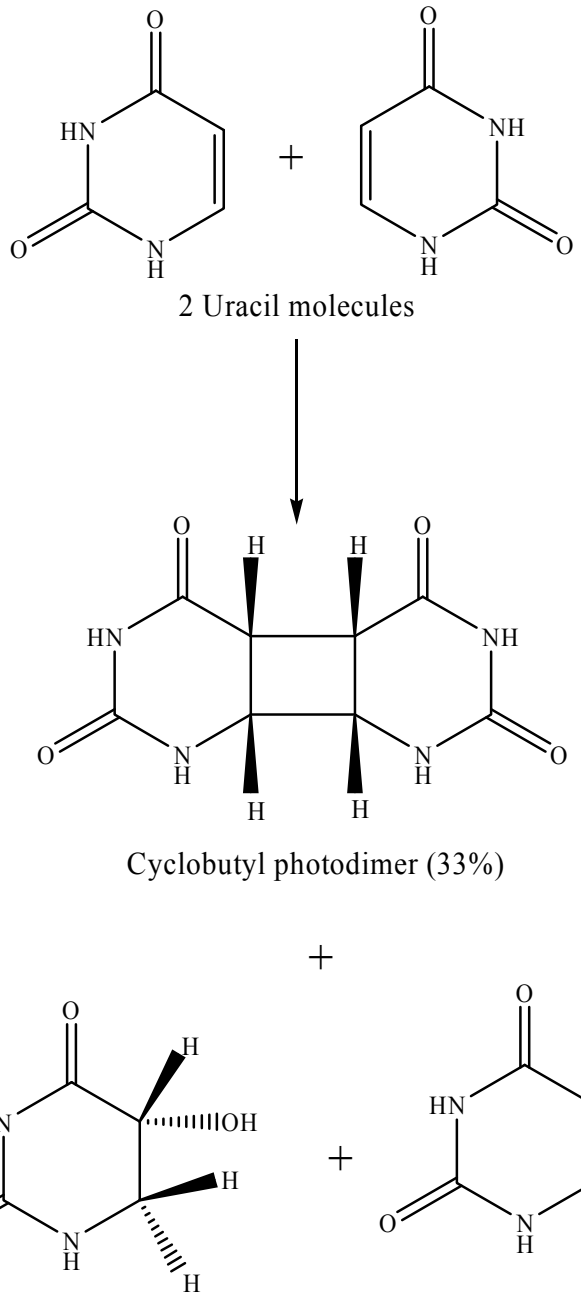

Figure 1.6. Chemical structures of the photoproducts formed from uracil as a result of UVB/UVC radiation. The percentage yield of each product is indicated. Only the cis-syn CPD, the most biologically relevant isomer in DNA, is shown.

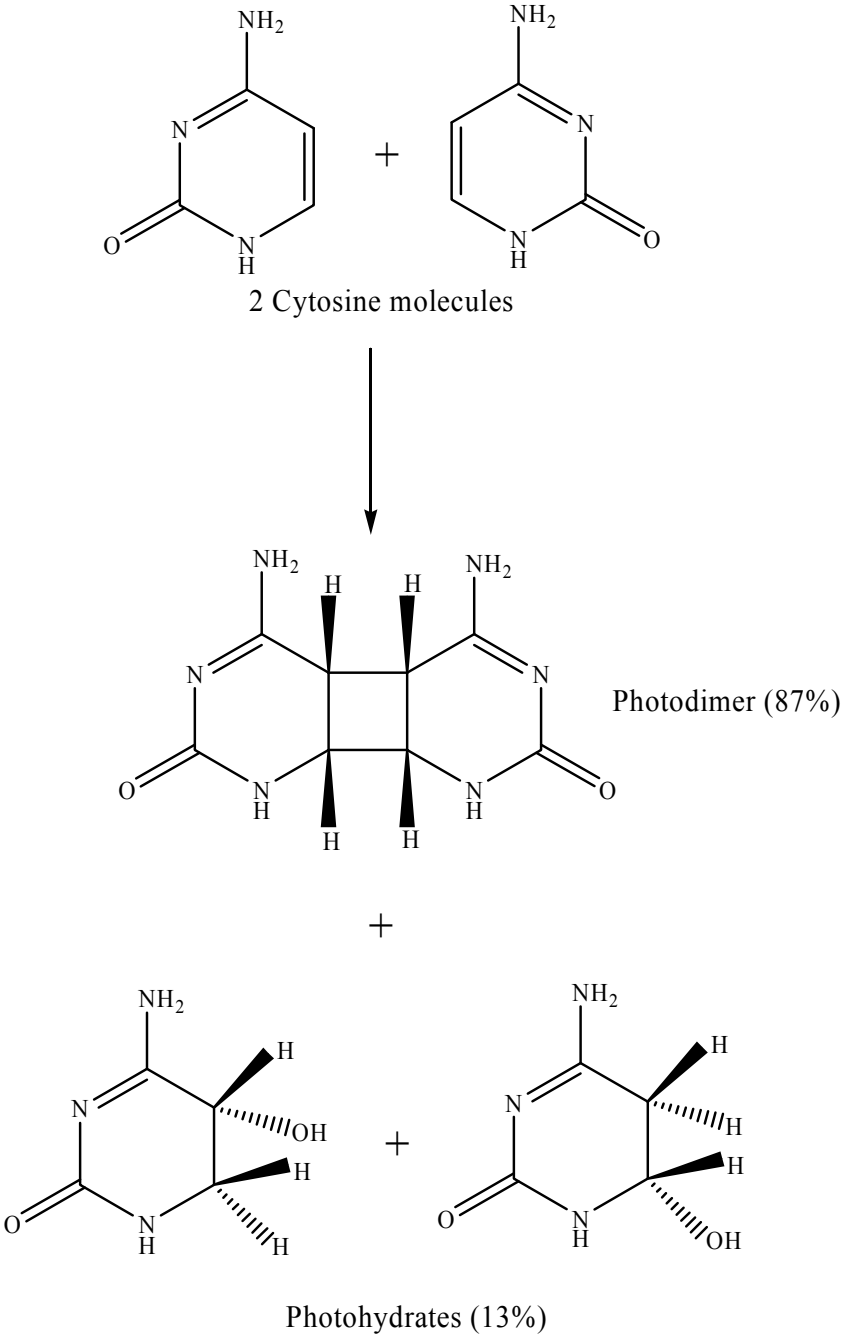

Figure 1.7. Chemical structures of the photoproducts formed from cytosine as a result of UVB/UVC radiation. The photochemical quantum yield are shown in brackets. Only the cis-syn CPD, the most biologically relevant isomer in DNA, is shown.

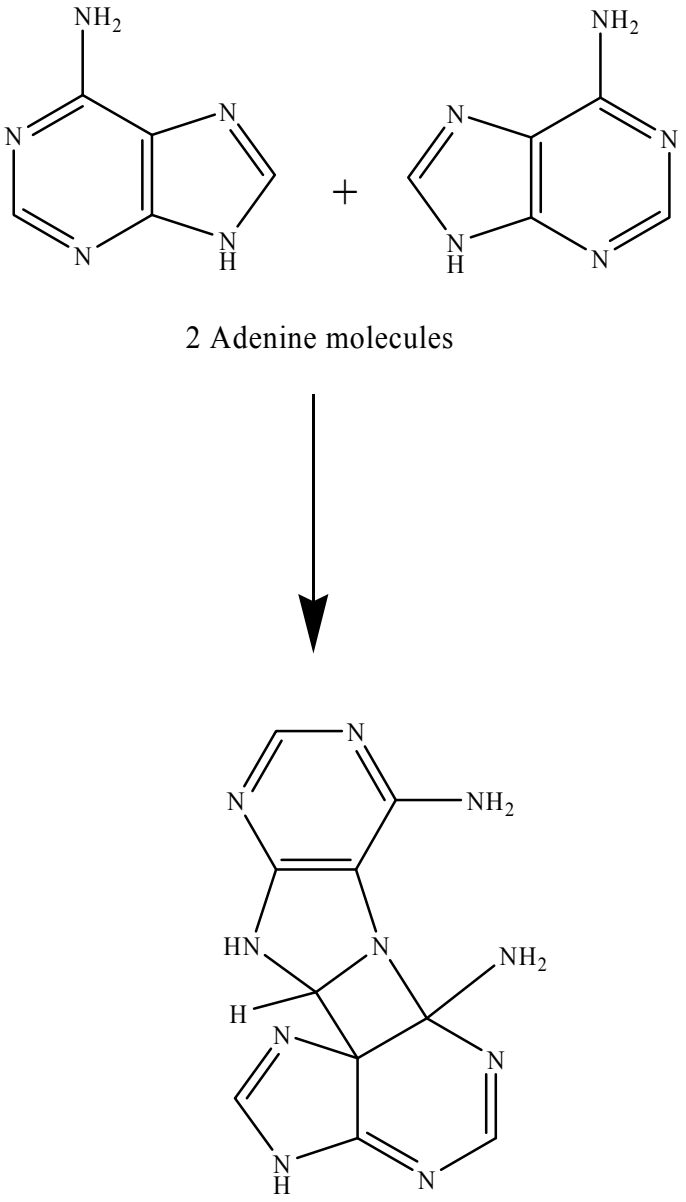

Figure 1.8. Chemical structure of the photoproduct formed from adenine as a result of UVB/UVC radiation.

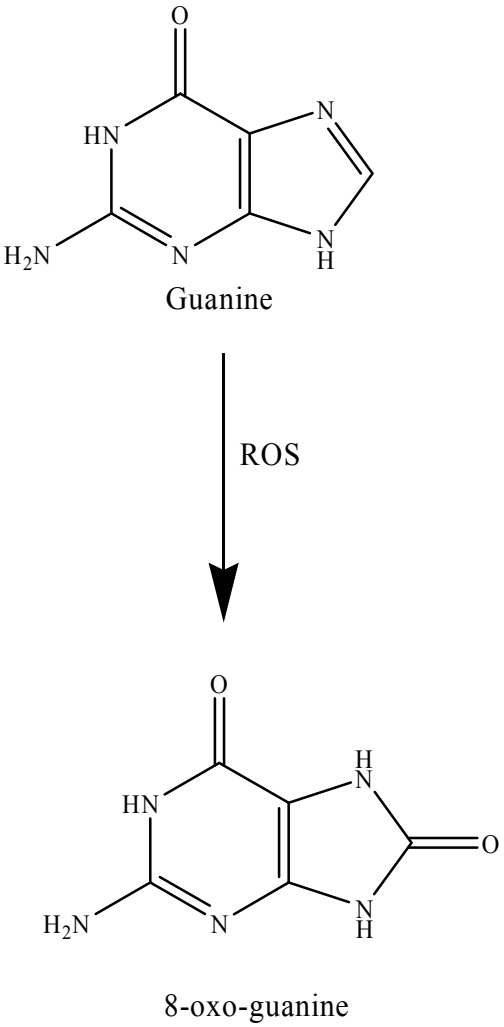

Figure 1.9. Chemical structure of the oxidative photoproduct formed from guanine as a result of UVB/UVC radiation in the presence of reactive oxygen species (ROS).

to 0.065 and the mechanism is thought to proceed via the singlet state for 1,3-dimethylthymine in stacked aggregates in more concentrated solutions.

The pyrimidine nucleobases have the highest quantum yields for photoreactivity, with thymine ~ uracil > cytosine. The purine nucleobases are relatively photostable compared to the pyrimidine. Thus, they have much lower quantum yields for photochemistry. However, they can be quite reactive in the presence of oxygen[7] (Figure 1.9). As can be seen from Figure 1.5, thymine forms primarily cyclobutyl photodimers (T<>T) via a [2π+2π] cycloaddition, with the *cis-syn* photodimer most prevalent in DNA. This is the lesion which is found most often in DNA and has been directly linked to the suntan response in humans.[7] A [2π+2π] cycloaddition reaction between the double bond in thymine and the carbonyl or the imino of an adjacent pyrimidine nucleobase can eventually yield the pyrimidine pyrimidinone [6-4]-photoproduct via spontaneous rearrangement of the initially formed oxetane or azetidine. This photoproduct has a much lower quantum yield than the photodimer in both dinucleoside monophosphates and in DNA. Finally, thymine can also form the photohydrate photoproducts via photocatalytic addition of water across the C_5=C_6 bond.

Uracil, which is found in RNA but not in DNA, has a similar photoreactivity to thymine. Although the rate of photoreaction is similar, the photoproduct partitioning is different. While uracil forms the cyclobutyl photodimer and photohydrate, there is no evidence that it forms the pyrimidine-pyrimidinone [6-4] photoproduct. Also, the major photoproduct in uracil is the photohydrate, not the cyclobutyl dimer as in thymine. The photohydrate has been predicted to form from a zwitterionic excited-state structure.[7,52] Thus, it is even more surprising that the photohydrate is the major photoproduct in uracil, as the tertiary carbon at C_5 in thymine is expected to better stabilize a carbocation in the zwitterionic excited-state. The origin of these differences in photochemistry remains largely unsolved, although recent UVRRS of both show a difference in the initial excited-state dynamics in the 10 fs time scale, which may account for some of the photochemical differences.[8]

Finally, cytosine is the least reactive of the pyrimidine nucleobases. It also forms the cyclobutyl photodimer and the photohydrate, but no evidence of the pyrimidine-pyrimidinone [6-4]-photoproduct has been found. Cytosine, uracil, and thymine can form heterophotodimers (e.g. T<>C and U<>C) in addition to the homophotodimers. The purines can also participate in photochemical reactions. Some evidence has been found that adenine and thymine can form a heterophotodimer.[7] However, the purines appear to be more susceptible to oxidative damage as a result of their much lower oxidation potentials.[7,53] Of the purines, guanine is most susceptible and forms primarily 8-oxo-guanine. However, 8-oxo-guanine is somewhat unstable and can rearrange to a number of different products.[7] Adenine forms a photodimer via a primary event which involves the cycloaddition of the N7C8 double bond of the 5'-A with the C6C5 single bond of the 3'-A[54] (Figure 1.8)

For all of these type of DNA damage, the initial step in the photochemical reaction is absorption of an ultraviolet photon. The lowest-lying, allowed state is thought to have primarily ($\pi\pi^*$) character for all of the nucleobases,[7,55] although there is thought to be one or more ($n\pi^*$) states which are nearly degenerate with the initially excited ($\pi\pi^*$) state.

1.2.4 Initial excited-state structural dynamics of nucleobases

The initial excited-state structural dynamics of nucleic acid bases have also been extensively studied.[4-7] Generally speaking, purines are more photochemically stable than the pyrimidines,[7,56] due to their ultrafast electronic relaxation dynamics.[57-59] Since the chromophores in nucleic acids are the bases (Figure 1.4), and it is their photophysics and photochemistry that govern the intrinsic stability of DNA,[57] most excited-state dynamics studies have focused on the bases and their analogs. An extensive review of the initial excited-state structural dynamics of DNA and their components was published recently.[7]

After excitation, an incompletely understood combination of electronic and structural dynamics occurs on the excited-state. While significant progress has been made in understanding the electronic dynamics of the

excited-states, primarily through ultrafast time-resolved absorption and fluorescence spectroscopy, very little is known about the structural dynamics. There are several reasons for this. As mentioned above, the excited-state lifetimes of the nucleobases are quite short, typically on the order of a picosecond or less. This short lifetime makes it difficult to resolve the vibrational dynamics before relaxation. Finally, the difficulty of working in the ultraviolet region with ultrafast lasers provides a significant technical challenge in measuring the initial excited-state structural dynamics. Nevertheless, ultraviolet resonance Raman spectroscopy has provided recent insight into the initial excited-state structural dynamics and the factors which affect them.

1.2.5 Sunscreens

Sunscreens are chemicals used to protect the skin from the harmful effects of UV radiation. Sunscreen chemicals may be classified according to the type of protection they offer as either physical blockers or chemical absorbers.[32,42,60] The physical blockers are chemicals that reflect the UV radiation. Examples include zinc oxide, titanium dioxide, red petrolatum and more recently, cerium-titanium phosphates.[32,60] These blockers, if present in sufficient quantities will reflect all the UV, visible and IR rays. They can be used in conjunction with chemical absorbers to achieve high sun protection factors. New forms of the metal oxides are currently being introduced that claim to enhance the sun protection without imparting the traditional opaqueness that is aesthetically unappealing in cosmetic formulations.[60] Of the available physical blockers, zinc oxide and titanium dioxide have been used in a number of particle sizes and suspensions and are widely used in cosmetic formulations.

Chemical absorbers absorb the harmful UV radiation. They are classified into either UVA or UVB absorbers, depending on which region of UV the active ingredients absorb at.[60] UVA absorbers are chemicals that tend to absorb in the 320 – 360 nm region of the UV, while UVB ones absorb in the 280 – 320 nm range. Examples of UVA absorbers are benzophenones, the

anthranilates and the dibenzoyl methanes. UVB absorbers include cinnamates, salicylates and camphor derivatives.[42,60] The best classification of UV absorbers is the one based on the chemical properties of the sunscreens. Hence most sunscreens available on the market can be one of cinnamate derivatives, salicylate derivatives, benzophenone derivatives, camphor derivatives, dibenzoyl methane derivatives and anthranilate derivatives. Other miscellaneous compounds such as digalloyl trioleate and lawsone are also found.[42,60] The general chemical structures of the common sunscreen AIs classes are shown in Figure 1.10. Structurally, these compounds are generally aromatic compounds conjugated to a carbonyl group, usually, with an ortho or para electron-donating group.

1.2.5.1 Mechanism of sunscreen action

Sunscreens shown in Figure 1.10 absorb the harmful short wavelength, high energy UV rays (250-340 nm) and convert it into innocuous longer wavelength, lower energy radiation.[60] The sunscreen chemical is excited to a higher energy state (π^*) from its ground state. As the excited molecule returns to the ground state, energy is emitted which is lower than the energy initially absorbed.

The energy is emitted in the form of longer wavelengths and lower energy. The longer wavelength radiation is emitted in one of several ways as shown in Figure 1.11. The energy emitted may be in the IR region. Although, this energy may be perceived as a mild heat on the skin, this minuscule heat effect is usually undetected since the skin receives much larger heat by being directly exposed to the sun's heat.[60] If the emitted energy lies in the visible region, it may be perceived as either a fluorescence or a phosphorescence effect. This type of effect is common in the imidazoline type sunscreens where a slight bluish haze may be seen on the skin or in formulations.[60] A fraction of the sunscreen molecules may also react photochemically. In the ground state, cis-trans or keto-enol photoisomerization has been observed in some organic molecules causing a mild shift in the lambda max of the chemical.[60]

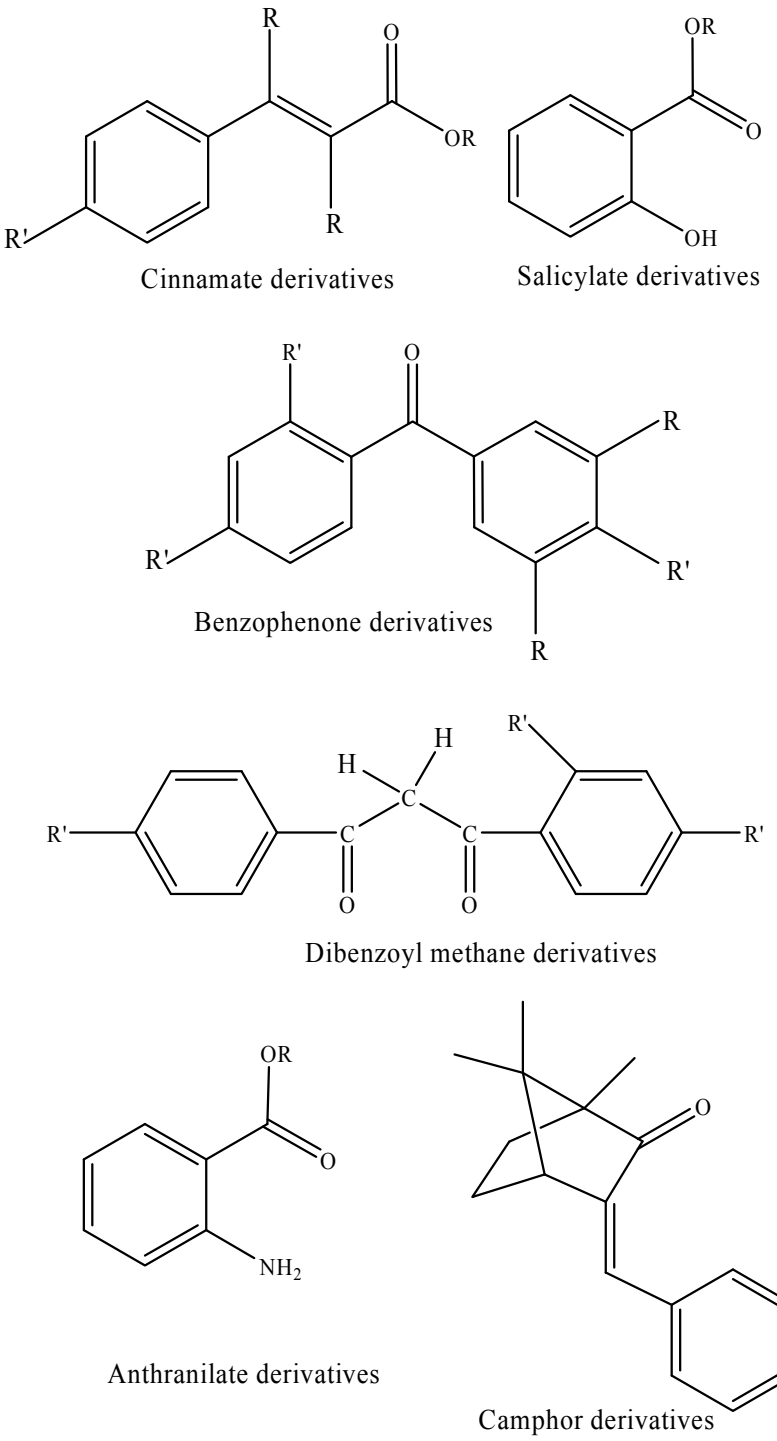

Figure 1.10. Chemical structures of different classes of sunscreens (R = hydroxyl, alkyl or alkoxy group; R' = OH, OCH_3, NH_2 or $N(CH_3)_2$ group).

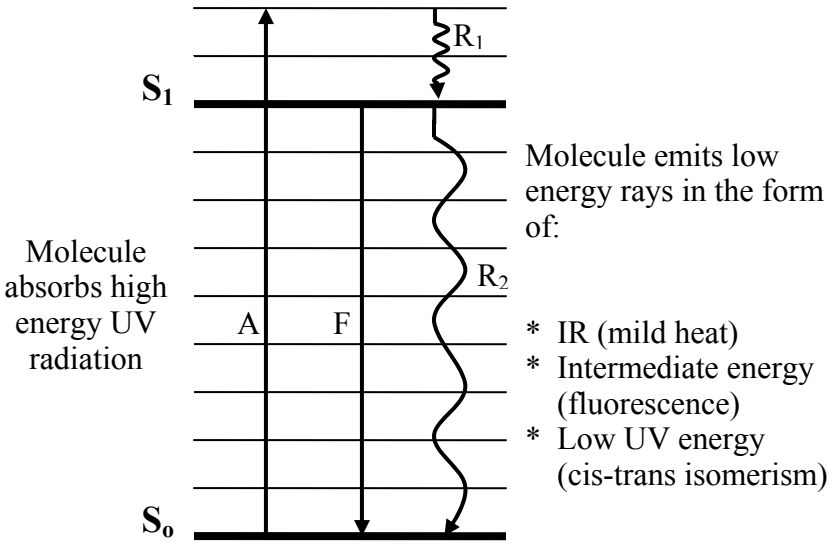

Figure 1.11. A depiction of the mechanism of sunscreen action. The upward vertical arrow represents absorption of harmful UV radiation, while the downward arrow represents fluorescence emission. The downward curly arrows depict vibrational relaxation which appears in form of mild heat. More details are given in the text about the underlying processes. A = absorbance; F = fluorescence; R_1 and R_2 are the vibrational relaxations to S1 and So states, respectively.

1.2.5.2 Factors that influence sunscreen performance

Two major factors profoundly affect the effectiveness of sunscreen chemicals. These are solvent effects and the effect of extinction coefficient. pH may also play a role in the effectiveness of sunscreens, but this factor is less important because the complex sunscreen formulations usually have an overall pH that is compatible with the skin. Thus, it is not usually a subject of concern for sunscreen manufacturers. Both solvent and pH effects will shift the absorption band of a given sunscreen molecule, thereby affecting its effectiveness.

1.2.5.3 Solvent effects

Most sunscreen formulations are creams, lotions or gels, with the AIs dissolved in solvents of different polarities and properties, such as water, glycerine, mineral oil and alcohol solvents.[61] Since sunscreens function by absorbing the harmful UV radiation, their effectiveness may be influenced by the solvents in which they are dissolved. Solvents are known to cause shifts in the absorption bands of sunscreen chemicals (solvatochromism).[60,61] The observed shifts in the absorption bands are due to the relative degrees of solvation of the ground state and the excited-state of the sunscreen molecule.[60] Therefore, to predict the effect of a given solvent on a particular sunscreen AI, the electronic structure of the molecule must be understood, as well as the interaction between the solvent and the AI.[60,61]

The solvation of polar sunscreens (e.g. banned sunscreen AI, para amino benzoic acid) by a polar solvent such as water and ethanol will be quite extensive. This extensive solvation stabilizes the ground state and destabilizes the excited-state. The net result of this is a hypsochromic shift to a shorter wavelength. For less polar sunscreens, such as cinnamate derivatives, the solvent-sunscreen AI interaction is different, because the excited-state is more polar than the ground state, leading to a net stabilization of the excited-state by polar solvents. This lowers the energy requirements for the electronic transition, and hence a bathochromic shift to a longer wavelength is observed.

The interaction of polar solvents with ortho-substituted sunscreen AI classes such as salicylate and anthranilate derivatives are uniquely different. Most of the available lone pair electrons in these sunscreen AIs are not available for interaction with the solvent molecules, but are used in the formation of an intramolecular hydrogen bond as shown in Figure 1.12. These molecules are subject to an "ortho effect" by forming a hydrogen bond between the H and O (Figure 1.12). This ortho effect tends to supersede the resonance delocalization effect. Consequently, salicylates and anthranilates do not exhibit any significant solvent-dependent shifts.[60,61] The solvent-dependent shifts observed for various sunscreens in different types of solvents, which are in perfect agreement with the above explanations have been documented.[60,61]

1.2.5.4 Effects of extinction coefficient

Since sunscreen AIs are chemical absorbers, the effectiveness of a typical sunscreen molecule is based on its extinction coefficient. Chemicals with high extinction coefficient are more efficient absorbers than those with lower coefficients. The more efficient the electron delocalization in a molecule, the higher its extinction coefficient.[60] All the electronic transitions in a molecule can be either symmetry allowed or symmetry forbidden. Symmetry allowed transitions generally lead to higher extinction coefficients and vice versa. Thus, trends in extinction coefficient of sunscreen AIs can be qualitatively predicted based on the spatial orientation and the electronic transition responsible for the observed UV spectrum.[60] For example, the extinction coefficient of para- and ortho-disubstituted aromatic compounds can be compared (cinnamate for para- and salicylate for ortho-disubstituted aromatic compounds). In the cinnamate, the two substituents on the benzene ring are in a para relationship, whereas in the case of salicylate, the two substituents are in a sterically hindered ortho relationship (see Figure 1.10). In the salicylate, the two substituents are close to each other causing a deviation from planarity. Any slightest deviation from coplanarity will reduce the resonance delocalization significantly, and hence a lower extinction

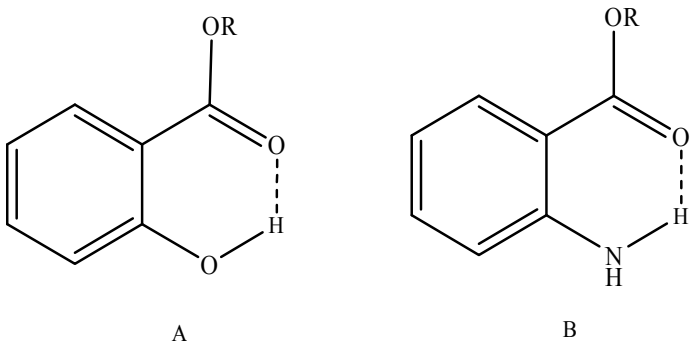

Figure 1.12. Intramolecular hydrogen bonding ("through space") interaction in salicylate (A) and anthranilate derivatives (B).

coefficient is observed in salicylate compared to cinnamate.[60] Increased conjugation, which leads to increased resonance delocalization will also result in higher extinction coefficient. This explains why the extinction coefficient of ethylene, 1,3-butadiene and 1,3,5- hexatriene are 15,000, 21,000 and152,000 $M^{-1}cm^{-1}$, respectively.[60] Looking at the structures of cinnamate and salicylate in Figure 1.10, this latter fact may also explain why salicylate, which is less conjugated than cinnamate, has a lower extinction coefficient.

1.2.5.5 pH effects

Alkaline pHs (pH > 9) will assist in the formation of anions that tend to increase delocalization of electrons. This electron delocalization would decrease the energy required for electronic transition in the UV, and hence a bathochromic shift to longer wavelength is observed. Conversely, acidic conditions (pH < 4) will assist in the formation of cationic aromatic sunscreen molecules, which will cause a hypsochromic shift to lower wavelengths since the protonation of the lone pair of electrons with acid would prevent resonance delocalization.[60] Basically, the effects are as a result of the change in the overall electronic structure of the sunscreen molecule when the pH condition is changed. However, as said above, this effect is less of a concern as pH is not expected to dramatically change when the various constituents are mixed, or when the sunscreen is actually being used.

1.2.6 Excited-state structural dynamics of sunscreen AIs

The photostability properties of sunscreen AIs affect their performance.[62] The AIs present in sunscreen formulations are expected to be photostable with minimal potential to form photoproducts in the excited-state after they absorb the harmful UV radiation. This is a desirable characteristic of a good sunscreen agent. However, sunscreen AIs may not be photochemically stable and they may form photochemical products on absorption of light, instead of efficiently dissipating the absorbed energy. The resulting photochemical products may not be good absorbers of UV light and this would lead to loss of effectiveness of the sunscreen formulation. The photochemical instability of

the sunscreen AIs may be inherent in the chemical absorbers themselves or it may result from chemical interactions of different AIs or between AIs and the matrix components. In addition, there is increasing evidence that in trying to dissipate the absorbed UV radiation, sunscreens may stimulate damage to human skin cells.[41] This is harmful to the skin rather than protective. Thus, it is crucial to probe the photostability and the potential harmful chemical side effects of the sunscreens. These possible photochemical interactions of sunscreen AIs and the sunscreen matrix deserve a thorough investigation of the underlying mechanisms, in order to better design sunscreen AIs which are photostable and formulate effective sunscreen lotions. To understand the photochemical reactions of the sunscreen AIs, an exploration of the initial excited-state structural dynamics is required so as to obtain information on the molecular structural changes that take place along the photochemical coordinate of the potential energy surface. To this end, our group has begun to use UVRRS to probe the initial excited-state structural dynamics of sunscreen AIs. This will enable us to gain insight into their excited-state deactivation pathways and correlate these with the photostability and photochemistry of the sunscreen AIs (Chapter 3).

1.3 Fluorescence Spectroscopy

Luminescence is the emission of light from any substance and occurs from electronically excited-states,[21,63] following the absorption of usually shorter wavelength radiation. Luminescence is divided into three categories: fluorescence, phosphorescence and chemiluminescence. Both fluorescence and phosphorescence are alike in that in both, excitation is brought about by absorption of photons. However, they differ because fluorescence takes place between levels of the same electronic spin, while phosphorescence occurs between states of different electronic spin. Transitions to the ground state is spin allowed for fluorescence, hence its lifetimes are in the order of 10^{-9} s. For phosphorescence, transitions to the ground state are spin forbidden.Therefore, the lifetimes are much longer, often on the order of seconds or even minutes.[21]

Chemiluminescence is based on the emission of radiation by an excited species formed from a chemical reaction. One of the attractive features of fluorescence spectroscopy is its inherent sensitivity due to its zero background. It also has a large linear range. For selected species under controlled conditions, single molecules can be detected with this technique.

1.3.1 Theory

When a molecule is excited by absorption of light, it can return to its ground state by a combination of several processes. The simple Jablonski diagram of Figure 1.3 can be used to explain fluorescence. As shown in the figure, fluorescence and phosphorescence involve the emission of radiation. Usually, the most favourable path to the ground state is the one that minimizes the lifetime of the excited-state.[21] Following absorption, the excited molecule has to get rid of its excess energy by one or more deactivation pathways. With a few rare exceptions, molecules populating the different vibrational levels of the excited-state will relax to the lowest vibrational level of this state. This process is called vibrational relaxation and its lifetime is on the order of 10^{-14} - 10^{-12} s. From the lowest vibrational level of the excited-state, several other deactivation processes can then intervene to bring the molecule to its ground state. There could be direct vibrational coupling between the ground and excited electronic states (vibronic level overlap) and quantum mechanical tunnelling (no direct vibronic overlap but a small energy gap), these are called internal conversion (IC) processes. It is usually a rapid process (on the order of 10^{-12} s) and therefore effectively competes with fluorescence. If the energy of the singlet spin state overlap those of the triplet state (Figure 1.3), there could be vibrational coupling occurring between these two states. If this happens, molecules in the singlet state can cross over to the triplet state. This is called intersystem crossing (ISC). This process is characteristic of high spin-orbit coupling molecules. In the presence of other species called quenchers, there could also be bimolecular interaction, electron transfer and energy transfer processes taking place. This is called quenching. In addition, unimolecular or bimolecular photochemical reaction can occur. The

fluorescence process corresponds to the relaxation of the molecule from the singlet excited-state to the singlet ground state with the emission of light. Its relatively short lifetime of ~10^{-9} s means that it can favourably compete with intersystem crossing and phosphorescence. The wavelength of the emitted light is longer than that absorbed, hence its energy is always less than that absorbed. The fluorescence spectrum is usually a mirror image of the excitation spectrum.[63] Phosphorescence is the relaxation of the molecule from the triplet excited-state to the singlet ground state with the emission of light. Because this is a classically forbidden transition, it has a long lifetime and a slow rate (10^{-2} – 100 s).[21]

1.3.2 Factors affecting fluorescence

There are basically two factors which influence fluorescence: chemical structure and environment. A good fluorophore should have a rigid flat structure, a high extinction coefficient and a high fluorescence quantum yield. A rigid structure would mean that the molecule cannot readily undergo internal conversion, which competes with its fluorescence. Most intense fluorescence is found in compounds containing aromatic rings with low energy $\pi\pi^*$ transitions. Usually, conjugated aromatic hydrocarbons fluoresce, with the efficiency increasing with the number of rings and degree of condensation.[21] Fused ring structures also make good fluorophores. In addition, a good fluorophore will have a low tendency to undergo intersystem crossing. Usually, molecules with no heavy atoms and no lone pairs of electrons are better fluorophores than those with these characteristics. Fluorescence is also sensitive to solvent environment, since this determines how flexible the fluorophore can be. Part of this is the pH of the environment. Both the protonated and deprotonated forms of a given fluorophore will cause a shift in the wavelength and a change in intensity. Also affecting fluorescence is the presence of species in the environment which can quench the fluorescence signal. For instance, the presence of molecular oxygen is known to reduce fluorescence intensity. Due to its paramagnetic properties,

oxygen promotes intersystem crossing and conversion of molecules to the triplet state.[21]

1.3.3 Quantum yield (□)

The quantum yield (also called quantum efficiency) is the ratio of the number of molecules that fluoresce to the total number of excited molecules. It is also the ratio of the number of emitted photons to the number absorbed. This value can approach unity for highly fluorescent molecules. It is close to zero for nonfluorescent species. The quantum yield can be determined from the relative rates for the other competing deactivation processes.

$$\phi = \frac{k_f}{k_f + k_{ic} + k_{isc} + k_P + k_Q[Q] + k_{Ph}[A]} \tag{1.14}$$

In the above Equation, the *k* terms are the respective rate constants for fluorescence (F), internal conversion (IC), intersystem crossing (ISC), phosphorescence (P), quenching (Q) and photochemical reaction (Ph). [Q] and [A] are the concentrations of the quencher and the 2nd photochemical reactant, respectively. Note that k_Q and k_{Ph} may be 2nd order processes. The quantum yield for all these processes should equal unity.

$$\phi_f + \phi_{ic} + \phi_{isc} + \phi_P + \phi_Q + \phi_{Ph} = 1 \tag{1.15}$$

The fluorescence lifetime τ_f can be obtained by simply taking the inverse of k_D, the denominator in Eq. 1.14. Similarly, the lifetimes of the other deactivation processes can be obtained as shown in Eq. 1.16.

$$\tau_x = \frac{1}{k_x} \tag{1.16}$$

τ_x is the lifetime for the process and k_x stands for the rate constants for the respective deactivation processes.

1.3.4 Fluorescence-based detection of DNA damage

The sensitive and precise measurement of DNA damage and repair are essential for understanding the lethal and mutagenic effects of UV-induced DNA photoproducts.[64] Various strategies have been used to measure the damage caused by chemical agents, UV radiation and γ-radiation. These include gel electrophoresis,[65] capillary electrophoresis,[66,67] electrochemical,[66,68] HPLC,[69] mass spectrometric[70-72] and polymerase chain reaction (PCR) amplification[73] methods. All these methods have their advantages and disadvantages. For instance, electrophoretic and chromatographical techniques need to isolate the probe–target hybrids from an excess of unhybridized probes, which itself may introduce lesions.[64] Also, all the aforementioned techniques are invasive and therefore cannot be adapted for *in situ* or *in vivo* use.[64]

A number of fluorescence methods for probing DNA damage have been proposed. Typically, fluorescent methods offer enhanced sensitivity and the potential for use *in situ* or *in vivo*.[64] One such method uses fluorescence detection based on molecular beacons (MB). The utility of this new class of sensitive and specific fluorescent probes has been demonstrated for the detection of DNA damage by our group.[64] Also, we recently demonstrated the applicability of smart probes (SP), which are similar in structure to molecular beacons but do not have quenchers. These two probes are discussed below.

1.3.4.1 Molecular Beacons (MBs)

MBs are oligonucleotide probes with a stem-loop structure (Figure 1.13), containing a fluorescent dye on one end and a quencher on the other.[74-77] In the absence of target DNA, the fluorophore and the quencher are in close proximity, so there is minimal fluorescence due to fluorescence resonance energy transfer (FRET), or some other quenching mechanism, from the fluorophore (donor) to the quencher (acceptor). However, in the presence of

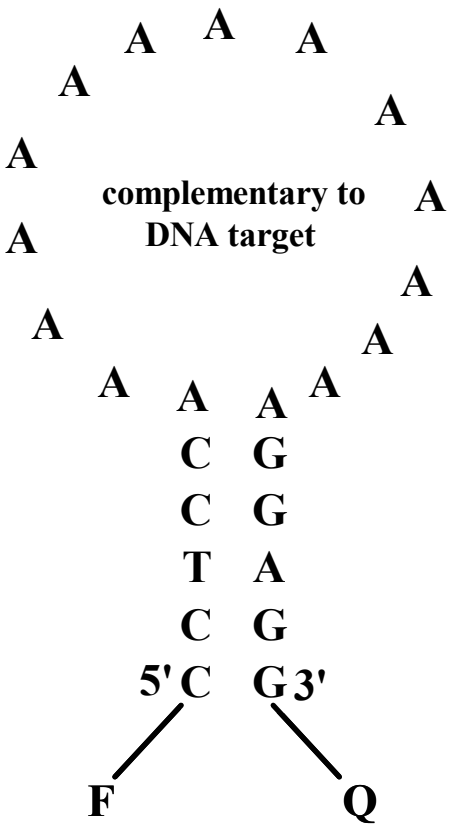

Figure 1.13. Structure of a molecular beacon. F = fluorophore; Q = quencher.

the complementary target sequence, the MB hybridizes with the target, resulting in a significant increase in fluorescence. If the target sequence is damaged, say it contains thymine dimers for example, the hybrid formed between the MB and the damaged DNA is less stable since the DNA target is no longer perfectly complementary to the loop of the MB. Thus, the fluorescence is lower for this hybrid compared to that formed between the undamaged DNA and the MB. The difference in fluorescence intensity in these two cases is observable for a single base mismatch in the DNA.[75] These inherent properties make the MBs highly sensitive and very selective probes for DNA damage.

1.3.4.2 Limitations of MBs

Despite the exquisite sensitivity of MBs, they have some limitations.[78-83] First, they require site-specific labelling of both termini of the hairpin with a fluorophore and a quencher. This dual labelling makes their synthesis difficult and expensive.[78,79,81,83] Secondly, since the two termini of the hairpin are already occupied by the donor and acceptor, any further modification, for example for attachment to a solid support would require the incorporation of an additional modified nucleotide into the stem.[78,81] This may deteriorate the stability of the hairpin probe.[78] Thirdly, if due to ineffective coupling, the hairpin is only labelled with the fluorophore, highly sensitive assays are interfered with by a high background due to unquenched probe molecules.[78,79] To address these problems, self-quenching smart probes (vide infra), which lack these shortcomings were developed.

Other problems associated with MBs such as endogenous nuclease degradation, non-specific binding by DNA/RNA binding proteins[84] and stem disruption[82] have been identified. The proposed solutions to these problems involve the use of locked nucleic acid molecular beacons (LNA-M Bs)[84] and hairpin stem containing unnatural enantiomeric L-DNA.[82] However, these proposed probes still retain all three limitations of MBs identified above and so may not find extensive applications.

Dimer probes, a class of fluorescent hairpin probes that are labelled on both termini with fluorophores have also been used as DNA probes.[85-88] These probes are based on the formation of non-fluorescent dye dimers caused by dye aggregation.[85,88] The phenomenon of aggregation and dimerization of fluorescent dyes in aqueous solutions has been shown for a number of fluorescent dyes.[85-88] Similarly, pyrene excimer signalling molecular beacons, which contain two pyrene monomers as fluorophores on one end and a quencher on the other end of a hairpin oligonucleotide has been used for DNA detection.[89] Also, low-noise stemless peptide nucleic acid beacons, which consist of an intercalator dye surrogate in the middle of the oligonucleotide strand, acting as a donor and another dye attached to one end of the probe acting as the acceptor have been used for DNA and RNA detection.[90] However, all these probes suffer from the same set of limitations as MBs, so they are not discussed further in this thesis.

1.3.4.3 Smart Probes (SPs)

Instead of using donor-acceptor interactions between two extrinsic labels, interactions of fluorophores with nucleobases or amino acids can be used for the specific detection of DNA or RNA sequences.[81] Recently, hairpin probes that take advantage of the selective fluorescence quenching of fluorophores by neighbouring guanosine residues were introduced.[78-81,83,91,92] This quenching, which occurs via photoinduced intramolecular electron transfer, can also be achieved using tryptophan residues.[81,91] Usually, the probes use the differences in specific properties of naturally occurring nucleotides, in particular, the low oxidation potential of guanosine.[78,81,93,94]

SPs (Figure 1.14) are hairpin oligonucleotide probe molecules just like MBs. They exist in the stem-loop structure in the absence of complementary target sequence. In this form, the fluorescence is quenched by the guanosine residues. However, in the presence of the complementary target sequence, the stem unwinds forcing the fluorophore and the guanosine residues far apart, thereby restoring fluorescence. Thus, these novel probes are similar in structure and properties to the MBs described above, but they are only

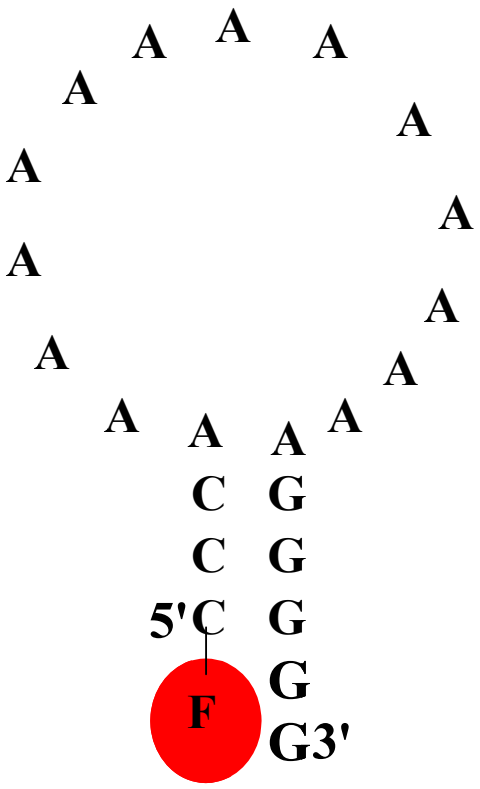

Figure 1.14. Structure of a smart probe. The fluorophore (F) is also shown.

labelled at one end with a fluorophore (without the extrinsic quencher). Hence, unlabelled oligonucleotides do not contribute to the measured signal. These probes are capable of single-molecule level detection.[79] By careful design and selection of appropriate fluorophore, these probes can give a fluorescence increase of up to 20-fold upon hybridization to the target sequence.[78,80,81] This increase can be achieved by careful balance of different factors that influence the quenching efficiency. These factors include use of suitable fluorophores, guanosine position in the complementary stem, the attachment of additional overhanging guanosine residues in the complementary stem, and the replacement of guanosine with stronger electron-donating nucleotides such as 7-deazaguanosine residues.[81] The smart probe shown in Figure 1.14 has two guanosine residues as overhangs in addition to the three guanosine residues in the complementary stem. In contrast to MBs, smart probes are relatively easy to synthesize (single labelling step), they are cheaper and they have free terminus at the unlabelled end for further modifications.[78] These excellent properties make these probes suitable for DNA damage detection and all other applications involving DNA sequence assay.

1.4 Research Outline

UV resonance Raman spectroscopy is a powerful spectroscopic technique which allows the analysis of complex samples as well as the exploration of the initial excited-state structural dynamics of molecules. In the same vein, fluorescence-based molecular beacon detection method and smart probe-based fluorescence spectroscopy were used to probe DNA photodamage. The unique capabilities of each of these techniques are exploited in the research work presented in the following five chapters.

In Chapter 2, the selectivity of UVRRS was used for the direct *in situ* analysis of sunscreen formulations. Current HPLC methods are time-consuming, less universal and unable to be used for online quality control analysis. We therefore harnessed UVRRS and we were able to analyze several

sunscreen formulations directly, without any sample pretreatment or separation. The technique is fast, robust, environmentally-friendly and adaptable for online quality control in the sunscreen industry.

Chapters 3 and 4 deal with the exploration of the initial excited-state structural dynamics of Benzophenone-3 (BZ3) and 9-methyladenine (9-MeA), respectively. Chapter 3 presents the photostability and photochemistry studies of a sunscreen AI. To be every effective, sunscreens need to be photostable with a very low photochemical quantum yield. This very important information is currently lacking. Thus, UVRRS was used to probe the initial excited-state structural dynamics of a common sunscreen AI, BZ3, with a view to gaining a fundamental understanding of its initial excited-state structural dynamics. Our knowledge of the excited-state structural dynamics might enable the design of better and more stable sunscreening agents and understand their reactivity. The initial excited-state structural dynamics 9-MeA are the subject of Chapter 4. The work is unique in that there has been no report on the initial excited-state structural dynamics of this molecule. Earlier work have explored its electronic dynamics. But in order to fully understand the excited-state dynamics and photochemistry of this molecule, the molecular distortions that take place must be known. This information is obtained from the initial excited-state structural dynamics.

In Chapter 5, a molecular beacon-based fluorescence technique was used to explore the kinetics of DNA photodamage in the presence of tryptophan (Trp), as well as the mechanism of possible protective interaction between DNA and Trp. Understanding the molecular mechanism for DNA damage is important for human health. In addition, the possible protective effect of Trp on DNA and the kinetics were explored, since Trp also absorb in roughly the same region as DNA, and it is present together with DNA in cells.

The capability of fluorescently-labelled self-quenching smart probes (SPs) for multiplex homogeneous and heterogeneous detection of DNA sequence analysis, as well as UV-induced DNA photodamage is explored in Chapter 6. SPs constitute a cheaper alternative to MBs. To that end, their suitability for multiplex homogeneous and heterogeneous detection of DNA sequence

analysis, as well as UV-induced DNA photodamage was explored. This research opens up a new route for multiplex detection of specific DNA sequences. Because the approach developed in this work gives very fast results, DNA damage analysis on microarrays can be more rapidly done, and cheaply too. All the results of Chapters 2 – 6 are summarized in Chapter 7, while future direction and outlook are also presented.

1.5 References

(1) Asher, S. A. *Anal. Chem.* **1993**, *65*, 201A-210A.

(2) Oladepo, S. A.; Loppnow, G. R. *Anal. Chim. Acta* **2008**, *628*, 57-66.

(3) Loppnow, G. R.; Mathies, R. A. *Biophys. J.* **1988**, *54*, 35-43.

(4) Billinghurst, B. E.; Loppnow, G. R. *J. Phys. Chem. A* **2006**, *110*, 2353-2359.

(5) Billinghurst, B. E.; Yeung, R.; Loppnow, G. R. *J. Phys. Chem. A* **2006**, *110*, 6185-6191.

(6) Yarasi, S.; Brost, P.; Loppnow, G. R. *J. Phys. Chem. A.* **2007**, *111*, 5130-5135.

(7) Loppnow, G. R.; Billinghurst, B. E.; Oladepo, S. A. In *Radiation Induced Molecular Phenomena in Nucleic Acids – A Comprehensive Theoretical and Experimental Analysis Series: Challenges and Advances in Computational Chemistry and Physics;* Shukla, M. K. Leszczynski, J., Ed.; Springer: Netherlands, 2008; Vol. 5, pp 237-263.

(8) Yarasi, S.; Ng, S.; Loppnow, G. R. *J. Phys. Chem. B* **2009**, *113*, 14336-14342.

(9) Asher, S. A. *Anal. Chem.* **1993**, *65*, 59A-66A.

(10) Smith, E.; Dent, G. In *Modern Raman Spectroscopy - A Practical Approach;* John Wiley & Sons, Ltd.: Chichester, England, 2005; pp 1-210.

(11) Keresztury, G. In *Handbook of Vibrational Spectroscopy;* Chalmers, J. M., Griffiths, P. R., Eds.; John-Wiley & Sons Ltd.: Chichester, UK, 2002; Vol. 1, pp 71-87.

(12) Smekal, A. G. *Naturwissenschften* 1923, 11, 873-

(13) Raman, C. V.; Kriahnan, K. S. *Nature* **1928**, *121*, 501-502.

(14) Pelletier, M. J. In *Analytical Applications of Raman Spectroscopy;* Pelletier, M. J., Ed.; Blackwell Science Ltd: Oxford, 1999; pp 1-478.

(15) Pan, M.-W.; Benner, R. E.; Smith, L. M. In *Handbook of Vibrational Spectroscopy;* Chalmers, J. M., Griffiths, P. R., Eds.; John-Wiley & Sons Ltd.: Chichester, UK, 2002; Vol. 1, pp 491-506.

(16) Asher, S. A.; Johnson, C. R.; Murtaugh, J. *Rev. Sci. Instrum.* **1983**, *54*, 1657-1662.

(17) Griffiths, P. R. In *Handbook of Vibrational Spectroscopy;* Chalmers, J. M., Griffiths, P. R., Eds.; John-Wiley & Sons Ltd.: Chichester, UK, 2002; Vol. 1, pp 33-43.

(18) McHale, J. L. In *Handbook of Vibrational Spectroscopy;* Chalmers, J. M., Griffiths, P. R., Eds.; John-Wiley & Sons Ltd.: Chichester UK, 2002; Vol. 1, pp 534-556.

(19) Myers, A. B.; Mathies, R. A. In *Biological Applications of Raman Spectroscopy*; Spiro, T. G., Ed.; Wiley: New York, 1988; Vol. 1, pp 1-58.

(20) Clark, R. J. H.; Dines, J. J. *Angew. Chem. Int. Ed. Engl.* **1986**, 25, 131-158.

(21) Skoog, D. A.; Holler, F. J.; Crouch, S. R. In *Principles of Instrumental Analysis;* Thomson Brooks/Cole: CA, 2007; 6th edition, pp 1039.

(22) Asher, S. A. In *Handbook of Vibrational Spectroscopy;* Chalmers, J. M., Griffiths, P. R., Eds.; John-Wiley & Sons Ltd.: Chichester UK, 2002; pp 557-571.

(23) Harada, I.; Sugawara, Y.; Matsuura, H.; Shimanouchi, T. *J. Raman Spectrosc.* **1975**, *4*, 91-98.

(24) Pezolet, M.; Yu, T.-J.; Peticolas, W. L. *J. Raman Spectrosc.* **1975**, *3*, 55-64.

(25) Asher, S. A.; Johnson, C. R. *Science* **1984**, *225*, 311-313.

(26) Long, D. A. In The *Raman Effect: A Unified Treatment of the Theory of Raman Scattering by Molecules;* John-Wiley & Sons Ltd.: Chichester UK, 2002; pp 1-597.

(27) Cantor, C. R.; Schimmel, P. R. In *Biophysical Chemistry Part II: Techniques for the study of biological structure and function;* W. H. Freeman and Company: New York, 1980; Vol. 2, pp 548.

(28) Sparrow, M. C.; Jackovitz, J.; Munro, C. H.; Hug, W.; Asher, S. A. *Appl. Spectrosc.* **2001**, *55*, 66.

(29) Myers, A. B.; Mathies, R. A. In *Biological Applications of Raman Spectroscopy*; Spiro, T. G., Ed.; Wiley-Interscience: New York, 1987; Vol. 2, pp 1-58.

(30) Billinghurst, B. E.; Oladepo, S. A.; Loppnow, G. R. *J. Phys. Chem. B* **2009**, *113*, 7392-7397.

(31) Fraga, E.; Webb, M. A.; Loppnow, G. R. *J. Phys. Chem.* **1996**, *100*, 3278-3287.

(32) Oladepo, S. A.; Loppnow, G. R. In *UV resonance Raman spectroscopy as a tool for probing complex samples;* Withnall, R., Chowdhry, B. Z., Eds.; Proceedings of the 21st international conference on Raman spectroscopy (ICORS); IMPublications: Chichester, UK, 2008; pp 1028-1029.

(33) Hu, S. Z.; Smith, K. M.; Spiro, T. G. *J. Am. Chem. Soc.* **1996**, *118*, 12638-12646.

(34) Asher, S. A. *Anal. Chem.* **1984**, *56*, 720-724.

(35) Johnson, C. R.; Asher, S. A. *Anal. Chem.* **1984**, *56*, 2258-2261.

(36) Rummelfanger, R.; Asher, S. A.; Perry, M. B. *Appl. Spectrosc.* **1988**, *42*, 267-272.

(37) Kundu, L. M.; Loppnow, G. R. *Photochem. Photobiol.* **2007**, *83*, 600-602.

(38) Zaug, A. J.; Been, M. D.; Cech, T. R. *Nature* **1986**, *324*, 429-433.

(39) Chakraborty, C. *Curr. Drug Targets* **2007**, *8*, 469-482.

(40) De Gruijl, F. R.; Van der Leun, J. C. *Health Phys.* **1994**, *67*, 319-325.

(41) Knowland, J.; McHugh, P. J.; Dunford, R. In *Sunscreen Photobiology. Molecular, Cellular and Physiological Aspects;* Gasparo, F. P., Ed.; Springer: New York, 1997; pp 47-62.

(42) Martincigh, B. S.; Allen, J. M.; Allen, S. K. In *Sunscreen Photobiology. Molecular, Cellular and Physiological Aspects;* Gasparro, F. P., Ed.; Springer-Verlag: New York, 1997; pp 11-45.

(43) Sayre, R. M. *Cosmet. Toiletries* **1992**, *107*, 105-109.

(44) Urbach, F. *Photochem. Photobiol.* **1989**, *50*, 507-513.

(45) Brown, M. W.; Galley, E. *Cosmet. Toiletries* **1990**, *105*, 69-73.

(46) Drobetsky, E. A.; Turcotre, J., Chateauneuf, A. *Proc. Natl. Acad. Sci. USA* **1995**, *92*, 2350-2354.

(47) Peak, J. G.; Peak M. J. *Mutation Res.* **1991**, *246*, 187-191.

(48) Faichuk, M.; Mah, A.; Loppnow, G. R. *Photochem. Photobiol.* **2007**, *83*, 1491-1496.

(49) Ruzsicska, B. P.; Lemaire, D. G. E. In *CRC Handbook of Organic Photochemistry and Photobiology;* Horspool, W. M., Song, P.-S., Ed.; CRC Press: New York, 1995; pp 1289-1317.

(50) Weimann, A.; Belling, D.; Poulsen, H. E. *Nucleic Acids Res.* **2002**, *30*, e7-e7.

(51) Hsu, G. W.; Ober, M.; Carell, T., Beese; L. S. *Nature* **2004**, *431*, 217-221.

(52) Gorner, H. *J. Photochem. Photobiol. B-Biol.* **1991**, *10*, 91-110.

(53) Baik, M. H.; Silverman, J. S.; Yang, I. V.; Ropp, P. A.; Szalai, V. A.; Yang, W. T.; Thorp, H. H. *J. Phys. Chem. B* **2001**, *105*, 6437-6444.

(54) Clingen, P. H.; Davies, R. J. H. *J. Photochem. Photobiol. B* **1997**, *38*, 81-87.

(55) Crespo-Hernandez, C. E.; Cohen, B.; Hare, P. M.; Kohler, B. *Chem. Rev.* **2004**, *104*, 1977-2019.

(56) Poerschke, D. *J. Am. Chem. Soc.* **1973**, *95*, 8440-8446.

(57) Satzger, H.; Townsend, D.; Zgierski, M. Z.; Patchkovskii, S.; Ullrich, S; Stolow, A. *Proc. Natl. Acad. Sci. USA* **2006**, *103*, 10196-10201.

(58) Serrano-Andres, L.; Merchan, M.; Borin, A. C. *Proc. Natl. Acad. Sci. USA* **2006**, *103*, 8691-8696.

(59) Bisgaard, C. Z.; Satzger, H.; Ullrich, S.; Stolow, A. *ChemPhysChem* **2009**, *10*, 101-110.

(60) Shaath, N. A. In *Sunscreens Development, Evaluation and Regulatory Aspects. Cosmetic Science and Technology Series;* Lowe, N. J., Pathak, M. A., Eds.; Marcel Dekker: New York, 1990; Vol. 10, pp 211-233.

(61) Beyere, L.; Yarasi, S.; Loppnow, G. R. *J. Raman Spectrosc.* **2003**, *34*, 743-750.

(62) Herzog, B.; Wehrle, M.; Quass, K. *Photochem. Photobiol.* **2009**, *85*, 869-878.

(63) Lakowicz, J. R. In *Principles of Fluorescence Spectroscopy;* 2006; Vol. 3, pp 954.

(64) Yarasi, S.; McConachie, C.; Loppnow, G. R. *Photochem. Photobiol.* **2005**, *81*, 467-473.

(65) Weinfeld, M; Soderlind, K.-J. M. *Biochemistry* **1991**, *30*, 1091-1097.

(66) Haab, B. B; Mathies, R. A. *Anal. Chem.* **1995**, *67*, 3253-3260.

(67) Le, X. C.; Xing, J. Z.; Lee, J.; Leadon, S. A.; Weinfeld, M. *Science* **1998**, *280*, 1066-1069.

(68) Wang, J.; Rivas, G.; Ozsoz, M.; Grant, D. H.; Cai, X.; Parrado, C. *Anal. Chem.* **1997**, *69*, 1457-1460.

(69) Kaur, H.; Halliwell, B. *Biochem. J.* **1996**, *318*, 21-23.

(70) Douki, T.; Court, M.; Sauvaigo, S.; Odin, F.; Cadet, J. *J. Biol. Chem.* **2000**, *275*, 11678-11685.

(71) Douki, T.; Cadet, J. *Biochemistry* **2001**, *40*, 2495-2501.

(72) Ravanat, J.-L.; Douki, T.; Cadet, J. *J. Photochem. Photobiol. B: Biol.* **2001**, *63*, 88-102.

(73) Kumar, A.; Tyagi, M. B.; Jha, P. N. *Biochem. Biophys. Res. Commun.* **2004**, *318*, 1025-1030.

(74) Sokol, D. L.; Zhang, X.; Lu, P.; Gewirtz, A. M. *Proc. Natl. Acad. Sci. USA* **1998**, *95*, 11538-11543.

(75) Bonnet, G.; Tyagi, S.; Libchaber, A.; Kramer, F. R. *Proc. Natl. Acad. Sci. USA* **1999**, *96*, 6171-6176.

(76) Leone, G.; van Schijndel, H.; van Gemen, B.; Kramer, F. R.; Schoen, S. D. *Nucleic Acids Res.* **1998**, *26*, 2150-2155.

(77) Tyagi, S.; Kramer, F. R. *Nature Biotechnol.* **1996**, *14*, 303-308.

(78) Stohr, K.; Hafner, B.; Nolte, O.; Wolfrum, J.; Sauer, M.; Herten, D.-P *Anal. Chem.* **2005**, *77*, 7195-7203.

(79) Knemeyer, J. P.; Marme, N.; Sauer, M. *Anal. Chem.* **2000**, *72*, 3717-3724.

(80) Misra, A.; Kumar, P.; Gupta, K. C. *Anal. Biochem.* **2007**, *364*, 86-88.

(81) Heinlein, T.; Knemeyer, J.-P.; Piestert, O.; Sauer, M. *J. Phys. Chem. B* **2003**, *107*, 7957-7964.

(82) Kim., Y., Yang, C. J., Tan, W. *Nucleic Acids Res.* **2007**, *35*, 7279-7287.

(83) Misra, A.; Shahid, M. *Bioorg. Med. Chem.* **2009**, *17*, 5826-5833.

(84) Wang, L.; Yang, C. J.; Medley, C. D.; Benner, S. A.; Tan, W. *J. Am. Chem. Soc.* **2005**, *127*, 15664-15665.

(85) Marme, N.; Habl, J.; Knemeyer, J.-P. *Chem. Phys. Lett.* **2005**, *408*, 221-225.

(86) Knemeyer, J.-P.; Marme, N.; Häfner, B.; Habl, G.; Schafer, G.; Müller, M.; Nolte, O.; Sauer, M.; Wolfrum, J. *Int. J. Environ. Anal. Chem.* **2005**, *85*, 625-637.

(87) Marme, N.; Friedrich, A.; Denapaite, D.; Hakenbeck, R.; Knemeyer, J.-P. *Chem. Phys. Lett.* **2006**, *428*, 440-445.

(88) Friedrich, A.; Habl, G.; Sauer, M.; Wolfrum, J.; Hoheisel, J.; Marme, N.; Knemeyer, J.-P. *Proc. of SPIE* **2007**, *6444*, 64440M-1-64440M-7.

(89) Conlon, P.; Yang, C. J.; Wu, Y.; Chen, Y.; Martinez, K.; Kim, Y.; Stevens, N.; Marti, A. A.; Jockusch, S.; Turro, N. J.; Tan, W. *J. Am. Chem. Soc.* **2008**, *130*, 336-342.

(90) Socher, E.; Bethge, L.; Knoll, A.; Jungnick, N.; Herrmann, A.; Seitz, O. *Angew. Chem. Int. Ed.* **2008**, *47*, 9555-9559.

(91) Marme, N.; Knemeyer, J.-P. *Anal. Bioanal. Chem.* **2007**, *388*, 1075-1085.

(92) Nazarenko, I.; Pires, R.; Lowe, B.; Obaidy, M.; Rashtchian, A. *Nucleic Acids Res.* **2002**, *30*, 2089-2195.

(93) Steeken, S.; Jovanovic, S. V. *J. Am. Chem. Soc.* **1997**, *119*, 617-618.

(94) Seidel, C. A. M.; Schulz, A.; Sauer, M. *J. Phys. Chem.* **1996**, *100*, 5541-5553.

Chapter 2

Ultraviolet Resonance Raman Spectroscopy as a Robust Spectroscopic Tool for *in situ* Sunscreen Analysis*

2.1 Introduction

Sunscreens are chemicals used to protect the skin from the deleterious effects of ultraviolet (UV) radiation. Exposure to UV radiation can lead to such harmful effects as carcinogenesis, actinic keratosis, skin aging and immunosuppression.[1-5] Sunscreen formulations employ a variety of active ingredients (AIs) which are typically strong absorbers, reflectors or scatterers of UV radiation as one means to protect against such UV-induced damage.[6,7] These AIs are usually present in sunscreen products in varying amounts from 0.1 - 10% w/w,[8] depending on the desired level of protection, and they are incorporated into a variety of other cosmetic products.[6] Different countries have different legislations permitting the use of different sunscreen AIs as well as their concentration levels.[6,8-11] Thus, the identities and concentration levels of the AIs in various sunscreen products must be monitored to ensure compliance with set regulatory standards.

Sunscreen AIs can be classified as either physical blockers or chemical absorbers.[1-6] The physical blockers reflect or scatter the harmful UV radiation, while the chemical absorbers absorb the harmful UV radiation.[1-6] Common physical blockers include zinc oxide (ZnO), titanium dioxide (TiO_2) and more recently, amorphous cerium-titanium phosphates (Ce_{1-x}-$Ti_xP_2O_7$).[12]. Common

---

* Versions of this chapter have been published. Oladepo, S. A., Loppnow, G. R., *Anal. Chim. Acta.,* **2008,** 628, 57-66.; Oladepo, S. A., Loppnow, G. R., *Proceedings of The 21st International Conference on Raman Spectroscopy (ICORS),* **2008,** 1027-1028.

chemical absorbers include derivatives of cinnamate, crylene, salicylate, benzophenone, camphor and anthranilate.[6] Benzophenones and anthranilates absorb in the UVA region (320-400 nm), while all absorb in the UVB region (280-320 nm). Sunscreen formulations contain AIs which absorb in both regions of UV radiation for adequate protection. Structurally, chemical absorbers are generally aromatic compounds conjugated directly or indirectly to a carbonyl group, usually with an *ortho* or *para* electron donating group (such as amine, hydroxyl or methoxy) substituted to the carbonyl.[6,7] The chemical structures of the sunscreen AIs used in this study are shown in Figure 2.1.

The analytical control of sunscreen formulations is necessary since the concentrations of the AIs in the products are related to their efficacy, usually reflected in the sun protection factor (SPF) indicated on the label of the products.[8] Chromatographic techniques are currently the most commonly used for sunscreen analysis,[6,8-10,13-29] with high performance liquid chromatography (HPLC) being the preferred method.[8-10,21,25] Gas chromatography (GC),[6,10,27,29] thin layer chromatography (TLC)[10,24,29,30] and micellar electrokinetic chromatography (MEKC)[9,21] have also been used to analyze sunscreen compositions. One unique feature of HPLC is its ability to separate most sunscreen AIs,[8-10] even salts, without the need for derivatization.[25] In addition, actual sample separation can be achieved in a reasonable amount of time for HPLC,[9] following a rigorous sample pretreatment. Finally, non-toxic and environment-friendly "green" reagents can be used for HPLC separations.[9] All other separation techniques that are currently used for sunscreen analysis lack these attractive features. However, HPLC also has some shortcomings. HPLC involves rigorous, laborious and time-consuming sample pretreatment, making the method unattractive for fast and routine online quality control. In some instances, the method may not achieve complete separation of analytes in one run.[25] The separation methods may also have to undergo significant modifications if a new set of sunscreen formulations have to be accommodated. Hence, it would be desirable to have a general analytical technique capable of analyzing sunscreen formulations

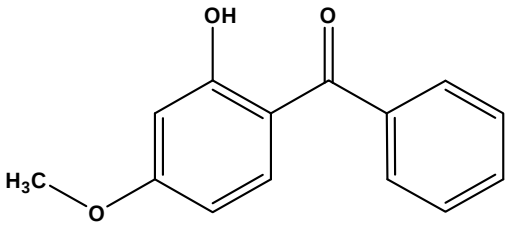

Benzophenone-3 (BZ3)

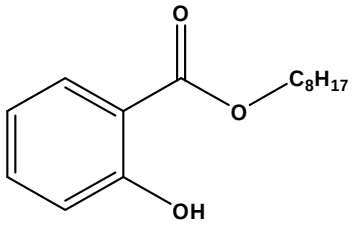

Octyl salicylate (OCS)

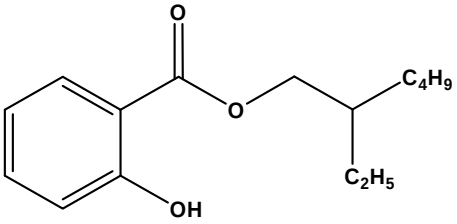

2-Ethylhexyl salicylate (Octisalate, OCT)

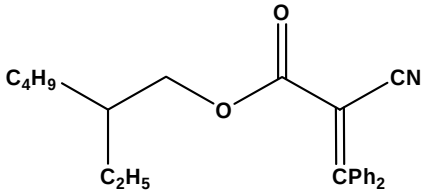

Octocrylene (OCY)

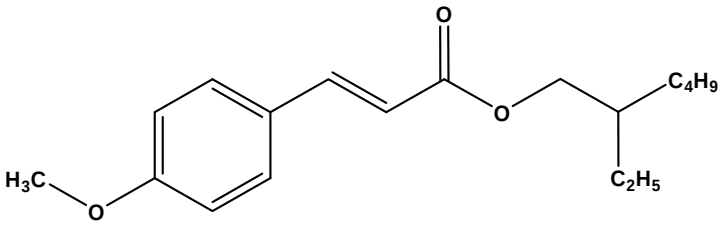

Octyl methoxycinnamate (OMC)

Figure 2.1. Molecular structures of the sunscreen AIs used in this work.

without the laborious and time-consuming sample pretreatment, and which is easily adapted to online quality control.

Attempts have also been made to analyze sunscreen samples using various spectroscopic techniques such as UV-Vis absorption spectroscopy,[6,9-11,27,31-32] nuclear magnetic resonance (NMR),[6,8-10,29,33-34] infrared spectroscopy (IR),[6,8,13] mass spectrometry (MS),[6,13,34] and Raman spectroscopy.[7,9,10,26,35-37] Since the sunscreen AIs are usually present in complex matrices, direct spectroscopic analysis of these compounds is difficult. Thus, most of these spectroscopic techniques cannot be used for direct *in situ* analysis of sunscreens without sample pretreatment and separation. There is currently no spectroscopic technique which has been reported to be capable of independent, direct and routine analysis of sunscreens.

Ultraviolet resonance Raman spectroscopy (UVRRS) is an information-rich probe of chemical composition in complex samples[38] and can be easily adapted for process control, quality control and quality assurance. It is capable of analyzing different analytes in complex matrices with unique spectral signatures of the analytes and essentially no interference from other components. In this technique, the excitation wavelength is chosen such that it falls within the UV absorption band of the analyte of interest. This resonance gives rise to enhancement of those vibrational modes coupled to the electronic excitation,[39,40] leading to a significant increase in Raman signal compared to normal Raman spectroscopy. Since the excitation wavelength only corresponds to the absorption band of a particular analyte, that species can be selectively probed with minimal interference from other components in the same mixture. Thus, this technique is sensitive based on the signal enhancement and it is selective because the excitation wavelength is chosen to match the absorption band of the analyte of interest, so there is little or no interference from the bulk sample matrix. Thus, there is no need for sample pretreatment or separation.

In this chapter, it is shown that UVRRS can be used for direct *in situ* analysis of sunscreen formulations, and overcomes many of the limitations of currently used techniques. UVRRS gave distinct spectral features for each

sunscreen AI probed as well as mixtures of the AIs. UVRRS was able to discriminate the AIs present in actual sunscreen formulations with little interference from fluorescence and the wide variety of other ingredients present in the complex sunscreen matrix. The technique was also used to quantify the amount of octyl methoxycinnamate (OMC) a common AI used in typical sunscreen formulations. In the sunscreen matrix, a limit of detection (LOD) and limit of quantitation (LOQ) that are far below the concentrations typically used in sunscreens were found. The dynamic range is about two orders of magnitude. Thus, the UVRRS-based method is capable of detecting this, and possibly other AIs, even when they are present in the lowest amounts typically used. This is the first report of the direct application of UV resonance Raman spectroscopy for routine sunscreen analysis.

2.2 Experimental

2.2.1 Materials and methods

Benzophenone-3 (BZ3), octyl methoxycinnamate (OMC) and octyl salicylate (OCS) were generously donated by ISP Van Dyk (Belleville, NJ, USA). 2-ethylhexyl salicylate (OCT) and 2-ethylhexyl-2-cyano-3,3-diphenyl-2-propenoate (OCY) were obtained from Sigma-Aldrich Canada (Oakville, ON, Canada). Six sunscreen formulations were obtained from a local store and used as received. ACS grade methanol was obtained from Fisher Scientific (Ottawa, ON, Canada). All solutions were prepared in methanol except for the LOD and LOQ determinations in sunscreen matrix. Methanol and all the AIs were used as received without further purification.

2.2.2 Spectroscopy

Absorption spectra of sunscreen AI solutions (20-100 μM) were measured using a Hewlett-Packard (Sunnyvale, CA USA) 8452A diode array spectrophotometer. The absorbance of a methanol blank was automatically

subtracted from that of the sample. Fluorescence emission spectra of the sunscreen AIs (100 μM in methanol) were measured using a Photon Technologies International (Birmingham, NJ, USA) fluorescence system. An excitation wavelength corresponding to the absorption maximum of each sample was used. Excitation at 244 nm was also used. Emission spectra were acquired from about 5-10 nm higher than the excitation wavelength to 800 nm.

Laser excitation for the resonance Raman experiments was obtained from a Coherent (Santa Clara, CA, USA) picosecond mode-locked Ti:sapphire laser pumped with a doubled, solid-state, diode-pumped continuous wave Nd: YVO_4 laser. In order to obtain 244, 257, 266 and 275 nm excitation wavelengths, the output of the Ti:sapphire was doubled using a lithium triborate (LBO) crystal followed by third harmonic generation in a β-barium borate (β-BBO) crystal in an Inrad (Northvale, NJ, USA) harmonic generator. Typical UV laser powers were 2-15 mW at the sample. Multichannel detection of the resonance Raman scattering was obtained with a water-cooled diode array detector (Princeton Instruments, Trenton, NJ, USA) connected to a model 5222 double-grating spectrometer (Spex Industries, Metuchen, NJ, USA) with 3600 g/mm gratings. Spectral slit widths were 5-7 cm^{-1}. For each spectrum, the total accumulation time was 15 minutes. For qualitative experiments, the collection of the resonance Raman spectra were repeated on three fresh samples at each wavelength. For the sunscreen AIs and AI mixtures, the laser beam was spherically focused on an open stream of flowing solution. For the sunscreen formulations, the laser was focused on the formulation coating the outer walls of a spinning 5 mm o.d. NMR tube. Excitation wavelengths of 244, 257, 266 and 275 nm were used. Resonance Raman spectra were obtained of sunscreen AIs (10 mM in methanol), bulk sunscreen formulations and mixtures of AIs in which the AIs are present in the same concentrations as they are in the sunscreen formulations (2 - 10% w/w). For quantitation experiments, concentrations between 0.0004% w/w and 1.5% w/w were used for OMC in methanol, while concentrations between 0% w/w and 30% w/w were used for OMC in a sunscreen matrix. The

excitation wavelength for this set of experiments was 244 nm and at least two replicates were carried out for each sample. At 244 nm excitation, four repeated spectral acquisitions were carried out on the sunscreen formulations and the mixtures of AIs to ensure reproducibility. Spectral acquisitions were made on four fresh samples of sunscreen formulations and two fresh samples for the mixtures. No evidence of sample photodecomposition was observed for any sample. Frequency calibration was performed by measuring the Raman scattering of organic solvents for which the peak positions are known (*n*-pentane, cyclohexane, dimethylformamide, methanol, acetonitrile and acetic acid). Wavenumbers are accurate to ±2 cm^{-1}.

2.2.3 Data analysis

All UV-Vis and resonance Raman spectra were processed using Thermo Electron Corporation (Woburn, MA, USA) GRAMS/AI. The UV-Vis spectral baselines were offset to zero. The resonance Raman spectra were analyzed by first correcting the spectra for the wavelength dependence of the spectrometer efficiency by dividing these spectra by the measured spectrum of a standard lamp (Oriel Corporation, Stanford, CT, USA). The spectral baselines were leveled by subtracting multiple joined line segments from each spectrum. After baseline levelling, each spectrum was offset to yield a baseline of zero. Methanol solvent peaks were not subtracted from the spectra and no smoothing was performed on the spectra. Deconvolution was used to separate overlapping peaks by fitting regions of the spectra to sums of Gaussian (or Gaussian/Lorentzian) peaks. The amount of Lorentzian was never greater than 10% of the total line shape. Fluorescence emission spectra were processed with Microcal Origin 6.1 (Northampton, MA, USA).

2.3 Results and Discussion

2.3.1 UV-Vis absorbance of sunscreen AIs

The absorption spectra of the sunscreen AIs should be known to choose the appropriate excitation wavelength for UVRRS effectively. Figure 2.2A shows the absorption spectra of the five sunscreen active ingredients considered in this work. Above 250 nm, OCY has maximum absorbance at 304 nm, OCS and OCT both have absorbance maxima at 306 nm, OMC has a peak at 310 nm with a shoulder at about 295 nm, and BZ3 has two bands with peaks at 288 nm and 326 nm. These results are in agreement with those previously reported for these compounds.[6,7,41] Thus, appropriate Raman excitation wavelengths should lie in the 260-300 nm region in order to achieve resonance with these low-lying excited-states. In the high energy region (below 250 nm), each AI has two absorption bands in the 210–245 nm region.[6] The band around 210 nm is common to all AIs with different intensities (Figure 2.2A). OCY has another band at 225 nm, while both OCS and OCT have a band at 240 nm. The band for OMC in this region occurs at 227 nm, while BZ3 has a band at 242 nm. All these absorption band characteristics have been previously observed.[6] The absorption spectrum of one of the sunscreen formulations (L-DT) was also acquired and it was found that this formulation contains many more UV-absorbing species other than just the AI (Figure 2.2B). Thus, a judicious choice of excitation wavelength is necessary to distinguish the ultraviolet resonance Raman (UVRR) spectrum of the AI from that of the sample matrix.

2.3.2 Fluorescence emission measurements

Fluorescence emission can be a major interference in resonance Raman experiments, as the fluorescence signal can completely swamp the weak Raman signal.[42] Figure 2.3A shows the fluorescence spectra of the sunscreen AIs excited at wavelengths corresponding to the absorption maximum of each sample. OCS, OCT and OMC exhibit some fluorescence, BZ3 at 324 nm excitation shows low but measurable fluorescence, but OCY and BZ3 at 288 nm excitation show no fluorescence. OCS and OMC have been shown

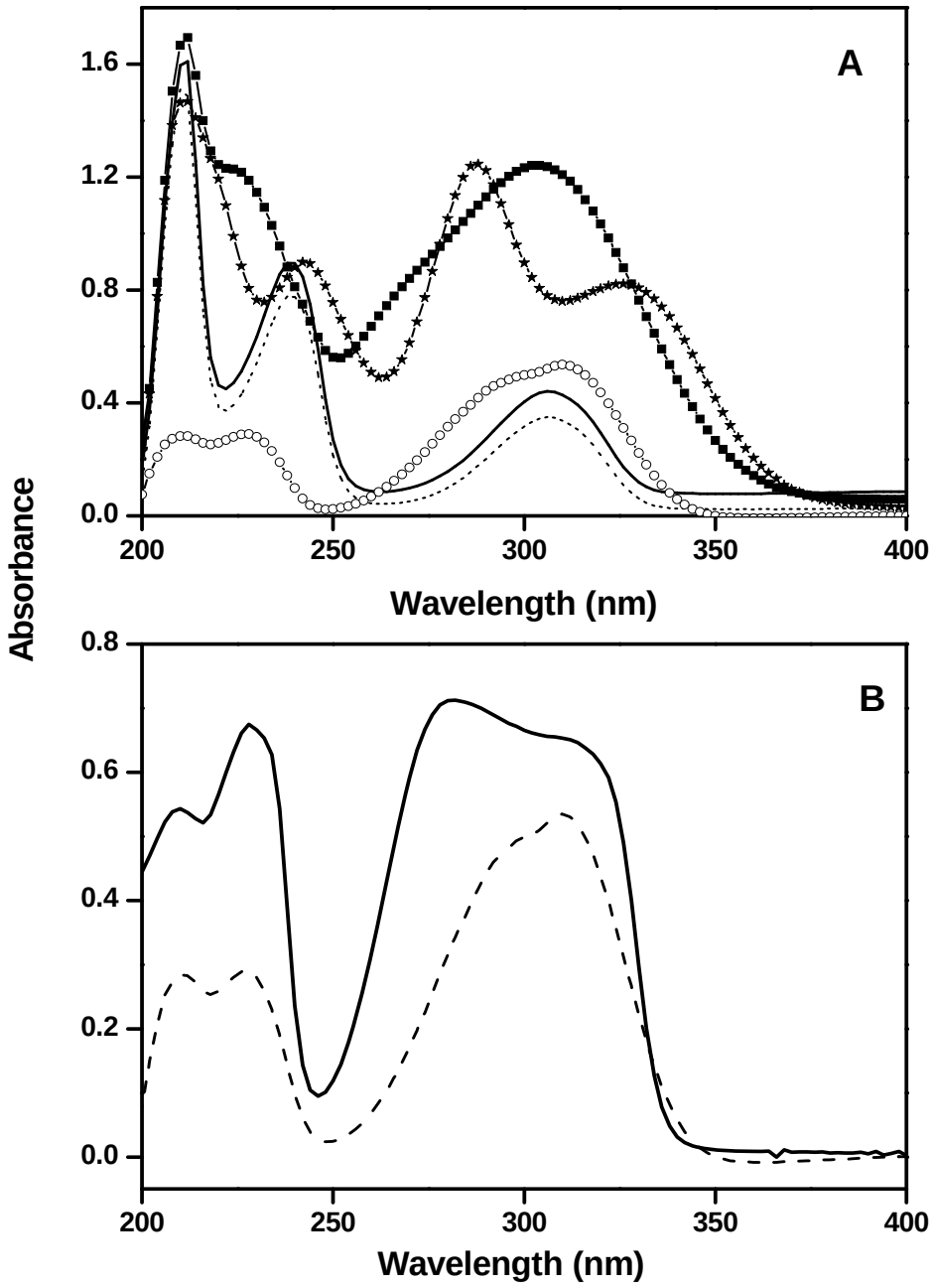

Figure 2.2. (A) UV-Vis absorption spectra of sunscreen AIs in methanol. All samples are 100 μM concentrations except OMC which is 20 μM. The sunscreens are OCT (solid line), OCY (filled squares), OCS (dashed line), BZ3 (filled stars), and OMC (open circles). The OCT spectrum has been slightly offset along the ordinate for clarity. (B) UV-Vis absorption spectra of 20 μM OMC in methanol (dashed line) and a sunscreen lotion formulation L-DT containing only OMC as the active ingredient (solid line). The spectrum of the lotion indicates that components of the matrix other than the active ingredients are also absorbing in the wavelength region shown. The path lengths used are 1 cm and 0.1 cm for pure OMC and L-DT respectively.

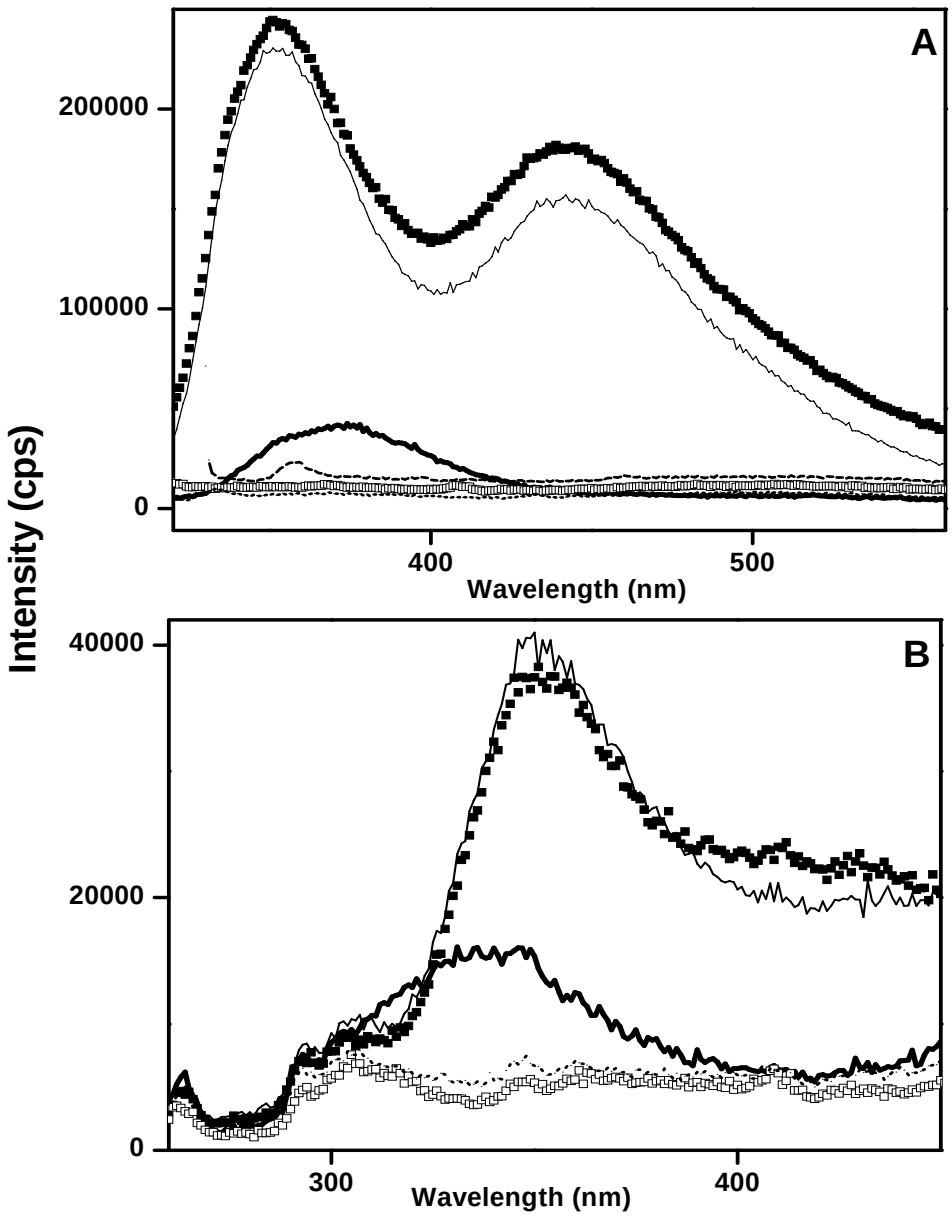

Figure 2.3. (A) Fluorescence spectra of 100 μM of sunscreen AIs in methanol excited at wavelengths corresponding to the absorption maximum of each sample. The sunscreens are OMC (excited at 310 nm, thick line), OCS (excited at 306 nm, thin line), OCT (excited at 306 nm, solid rectangle), BZ3 (excited at 288 nm, open rectangle), BZ3 (excited at 324 nm, dashed line), and OCY (excited at 304 nm, dotted line). The spectra of OCT and BZ3 have been slightly offset along the ordinate for clarity. (B) Fluorescence spectra of 100 μM sunscreen AIs in methanol excited at 244 nm. OMC (thick line), OCS (thin line), OCT (solid rectangle), BZ3 (open rectangle), and OCY (dotted line). The spectrum of BZ3 has been slightly offset along the ordinate for clarity.

previously to be fluorescent.[43] OCT is expected to be fluorescent, since it has an identical chromophore to OCS (Figure 2.1). The fluorescence emission was also measured by using 244 nm as the excitation wavelength, which is the UVRRS excitation wavelength that gave optimal discrimination between the AIs in the resonance Raman experiments (see section 2.3.4). As shown in Figure 2.3B, the overall fluorescence intensity decreased significantly, as expected from lower absorption at this wavelength, and the pattern of fluorescence for OCS, OCT and OMC is similar to those of Figure 2.3A. Both BZ3 and OCY show very low fluorescence, as observed with excitation at their absorption maxima. Thus, fluorescence interference, if present at excitation wavelengths above 300 nm, may be expected to be absent or very minimal below this wavelength.

2.3.3 UVRRS of sunscreen AIs

The Raman spectra of the AIs must be acquired with multiple excitation wavelengths to optimally develop UVRRS as an analytical tool for probing sunscreen AIs in real samples. The results for these excitation wavelengths are shown in Figures 2.4-2.7. As shown in these figures, the spectral patterns of the AIs are different from one another, particularly at 244 nm, except for OCS and OCT. The similarity in these two latter spectra is to be expected, since these two compounds are structural isomers and their chromophores are identical. This result indicates that we are indeed in resonance at all excitation wavelengths used in this study. The similarity in the spectra of OCS and OCT should not cause problems in the analysis, since only one or the other is used in every sunscreen formulation known. Thus, this method should be capable of complete analysis of the sunscreen AIs present in any given sample.

Based on the spectral patterns of Figures 2.4-2.7 and previous assignments,[7,44] the band around 1610 cm^{-1} in BZ3 is ascribed to a C=O stretch mixed with C=C stretches. For OCS and OCT, the intense bands at 1688 cm^{-1}, 1625 cm^{-1} and 1248 cm^{-1} are assigned to the C=O stretch, C=C stretch and C-O salicylate stretch, respectively.[7,44] In the case of OCY, the rather broad band around 1606 cm^{-1} is ascribed to the C=O stretch mixed with

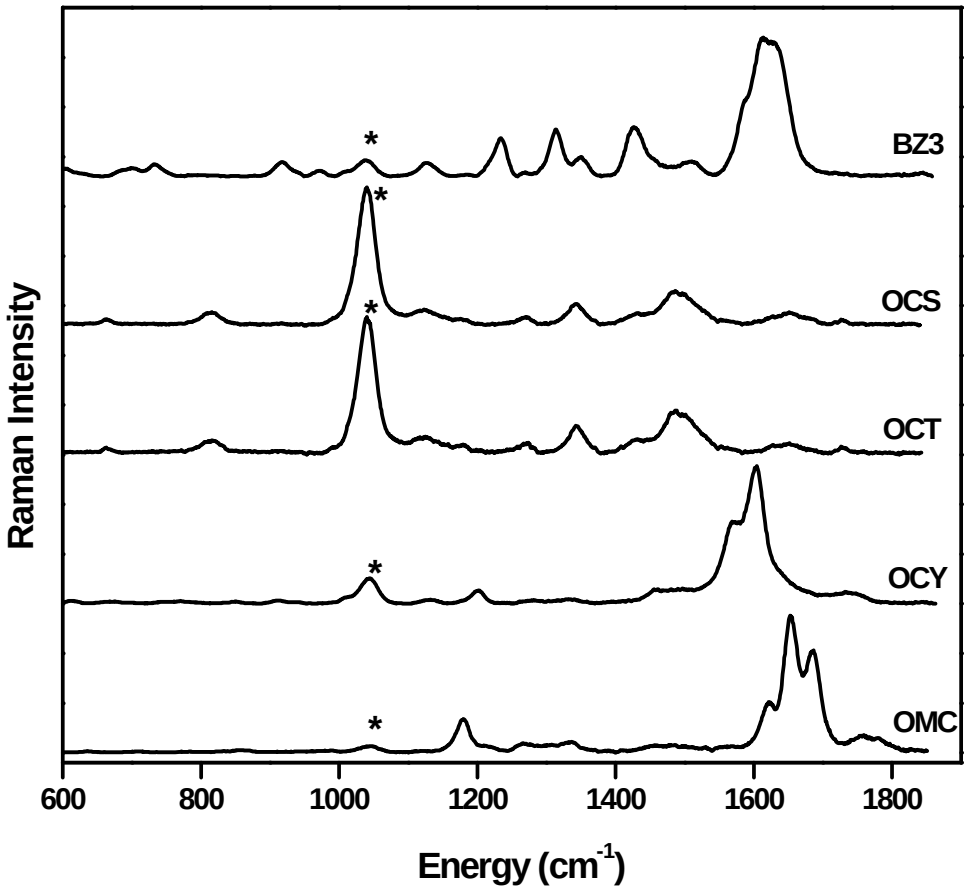

Figure 2.4. UVRR spectra of 10 mM sunscreen AIs in methanol excited at 275 nm. Structures and abbreviations are given in Figure 2.1. The bands due to methanol are indicated by asterisks (*). Spectra have been scaled to the height of the largest peak in each spectrum and offset along the ordinate for clarity.

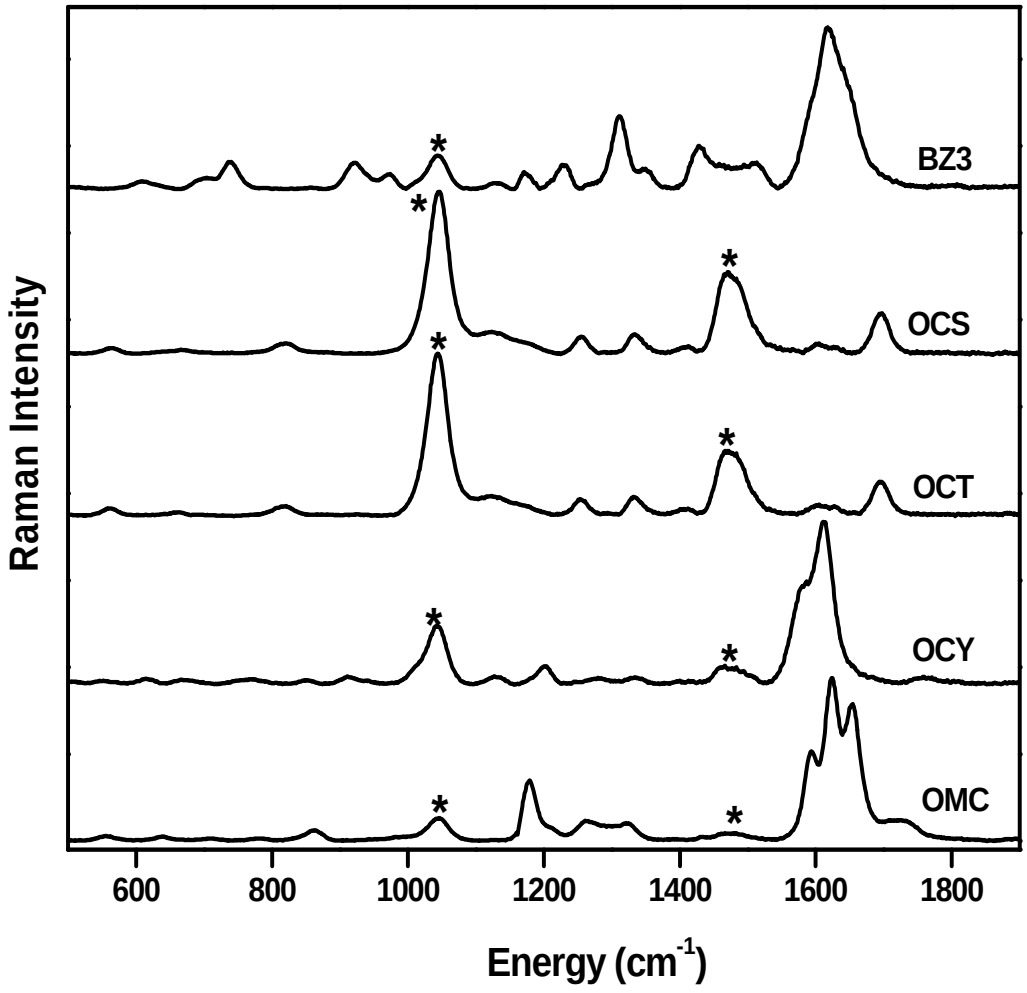

Figure 2.5. UVRR spectra of 10 mM sunscreen AIs in methanol excited at 266 nm. Structures and abbreviations are given in Figure 2.1. The bands due to methanol are indicated by asterisks (*). Spectra have been scaled to the height of the largest peak in each spectrum and offset along the ordinate for clarity.

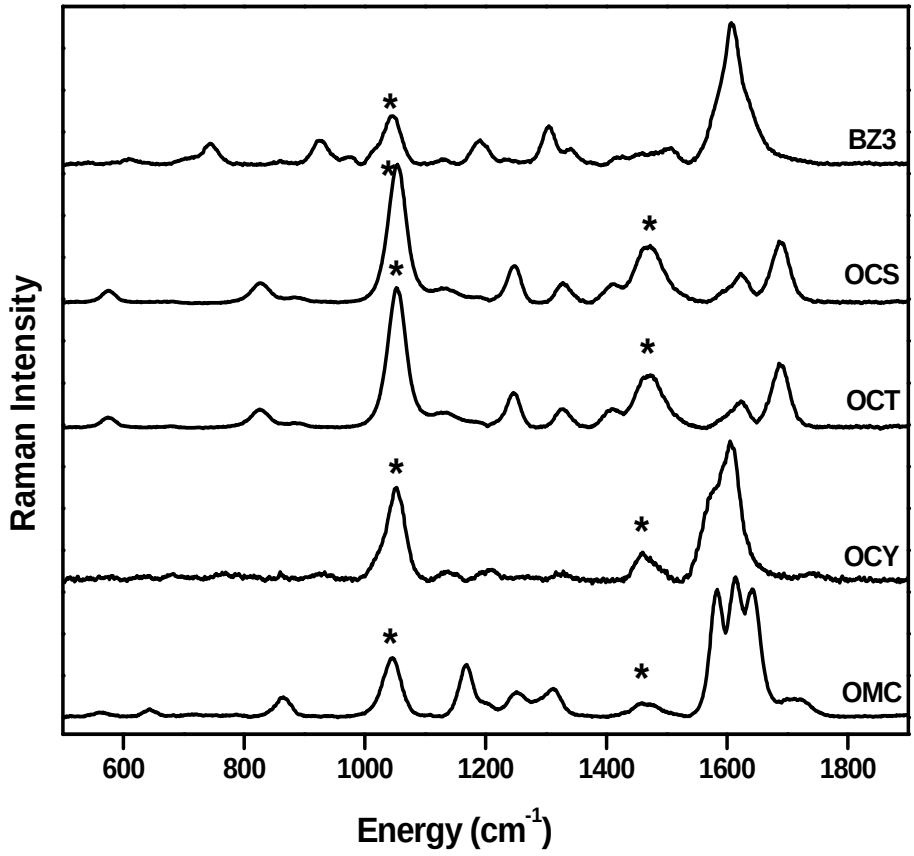

Figure 2.6. UVRR spectra of 10 mM sunscreen AIs in methanol excited at 257 nm. Structures and abbreviations are given in Figure 2.1. The bands due to methanol are indicated by asterisks (*). Spectra have been scaled to the height of the largest peak in each spectrum and offset along the ordinate for clarity.

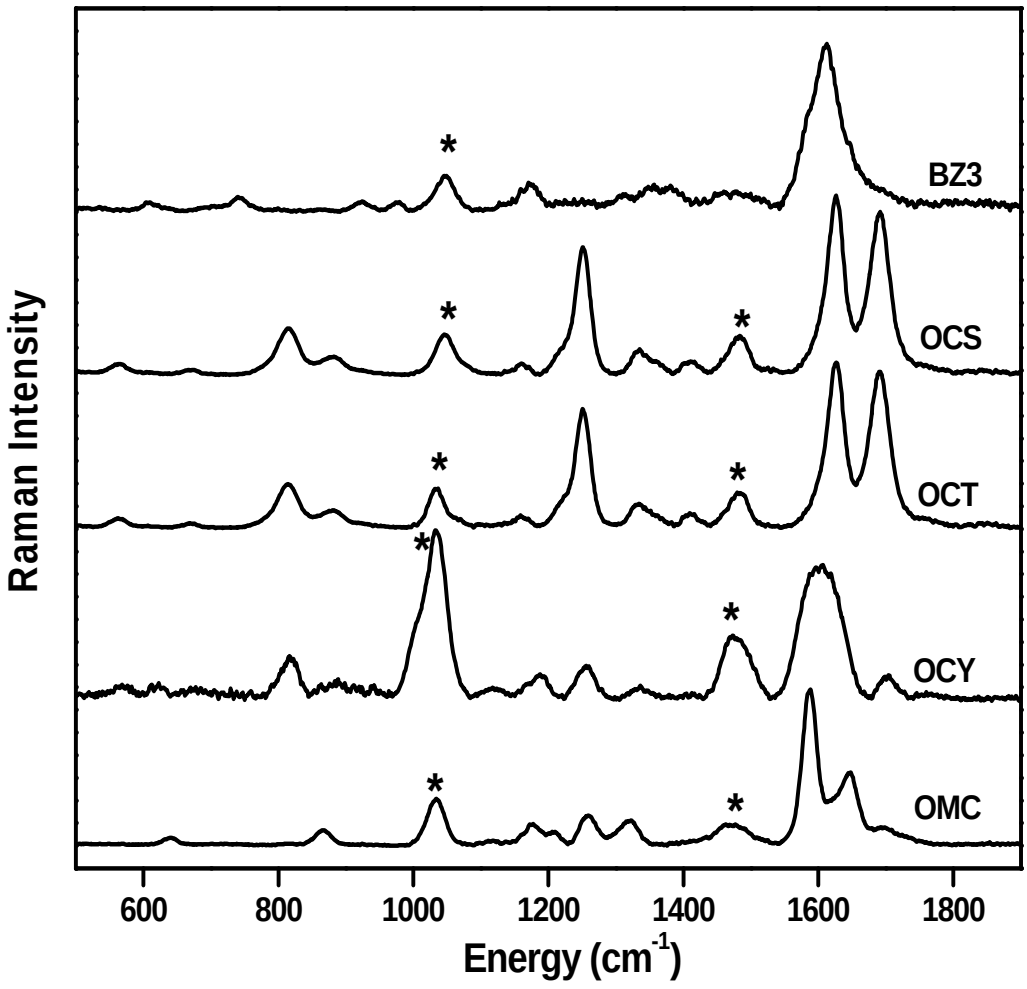

Figure 2.7. UVRR spectra of 10 mM sunscreen AIs in methanol excited at 244 nm. Structures and abbreviations are given in Figure 2.1. The bands due to methanol are indicated by asterisks (*). Spectra have been scaled to the height of the largest peak in each spectrum and offset along the ordinate for clarity.

one or more C=C stretches. For OMC, the bands at 1646 cm^{-1} and 1586 cm^{-1} are ascribed to an exocyclic C=C stretch and aromatic ring vibration, respectively, while the broad, weak high energy band around 1700 cm^{-1} is ascribed to the conjugated C=O stretch.[7,44]

The UVRRS spectra of all five sunscreen AIs, as a function of excitation wavelength for all wavelengths used in this study are shown in Figure 2.8-2.12. From each of these figures, one can see that the spectral signatures for a given sunscreen AI at 244 nm are distinct from the signatures at 257, 266 and 275 nm, providing for easier discrimination of the sunscreen AIs at 244 nm. Also, it can be seen that the resonance enhancement of some vibrational modes change as a function of excitation wavelength. For example, for OCS and OCT (Figures 2.9 and 2.10), the C=C stretch band around 1620 cm^{-1} which is barely visible at 275 nm excitation, is a strong signal at 244 nm, while the aromatic C=O stretch band around 1690 cm^{-1} also increases in intensity on going from 275 to 244 nm excitation. When compared to methanol solvent bands, the relative intensities of these bands also increase significantly from 275 nm to 244 nm. In the case of BZ3 (Figure 2.8), some of the bands between 1345 cm^{-1} and 600 cm^{-1} which are present at 275 nm disappear completely at 244 nm. However, the intensity of the major band around 1610 cm^{-1} relative to that of methanol essentially stays the same from 275 nm through to 244 nm. As shown in Figure 2.11, the low energy weak intensity shoulder at 1583 cm^{-1} corresponding to the aromatic ring vibrations in OCY at 275 nm excitation is no longer visible at 244 nm, but a rather broad band is observed. In addition, compared to the methanol bands, the relative intensity of the band around 1605 cm^{-1} is somewhat reduced on going from 275 nm to 244 nm. For OMC (Figure 2.12), the three bands centered around 1620 cm^{-1} at 275 nm excitation, change in intensity at 257 nm, and coalesce into two bands at 244 nm, while the relative intensities of the bands compared to methanol is somewhat reduced at 244 nm excitation. In all these cases, different signal enhancements are obtained at different excitation wavelengths because the vibrational modes are moving from resonance with one excited-

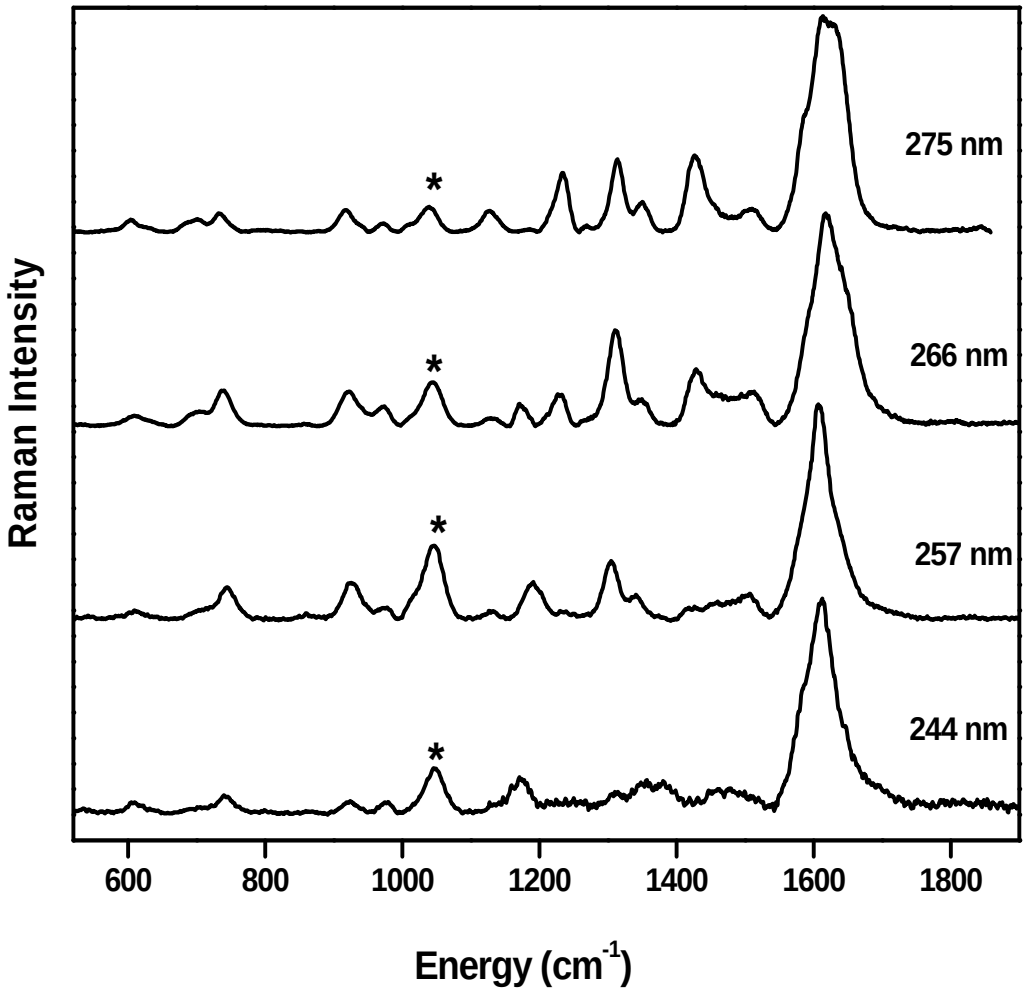

Figure 2.8. UVRR spectra of Benzophenone-3 (BZ3) in methanol excited at different excitation wavelengths. The bands due to methanol are indicated by asterisks (*). Spectra have been scaled to the height of the largest peak in each spectrum and offset along the ordinate for clarity.

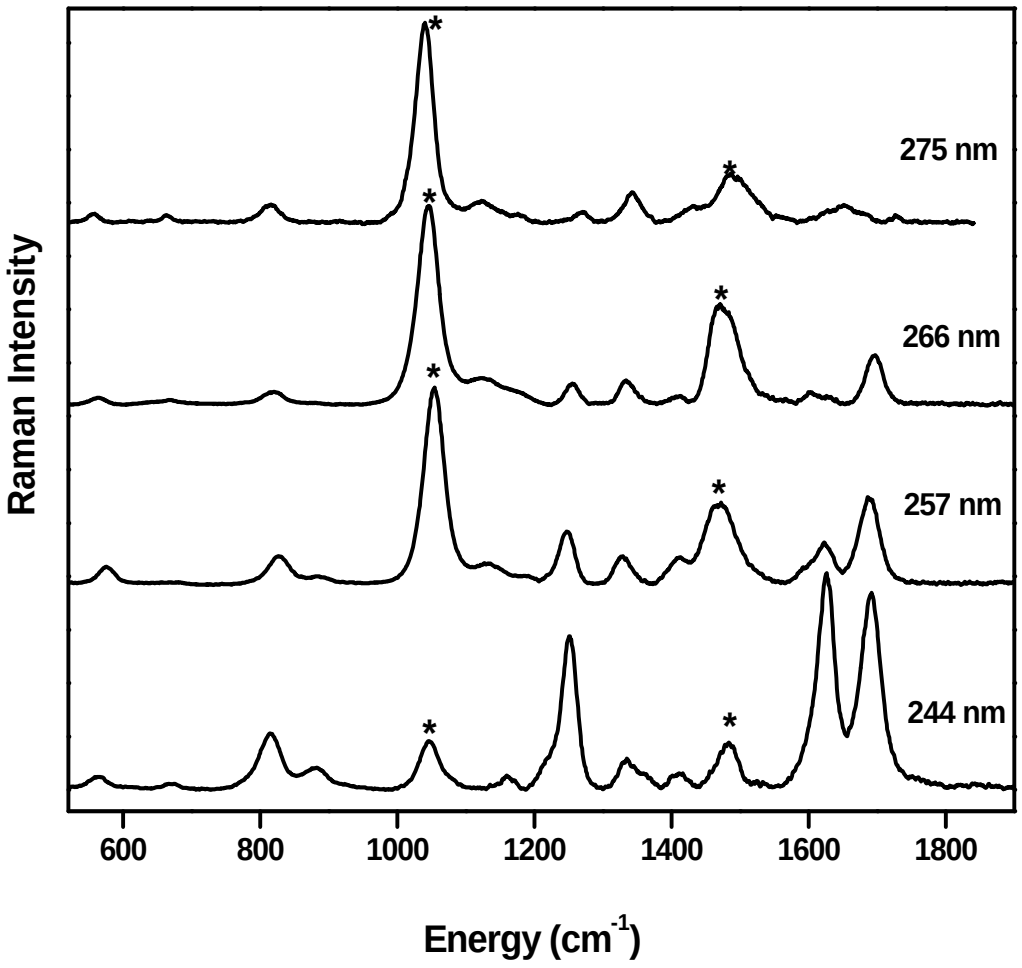

Figure 2.9. UVRR spectra of Octyl salicylate (OCS) in methanol excited at different excitation wavelengths. The bands due to methanol are indicated by asterisks (*). Spectra have been scaled to the height of the largest peak in each spectrum and offset along the ordinate for clarity.

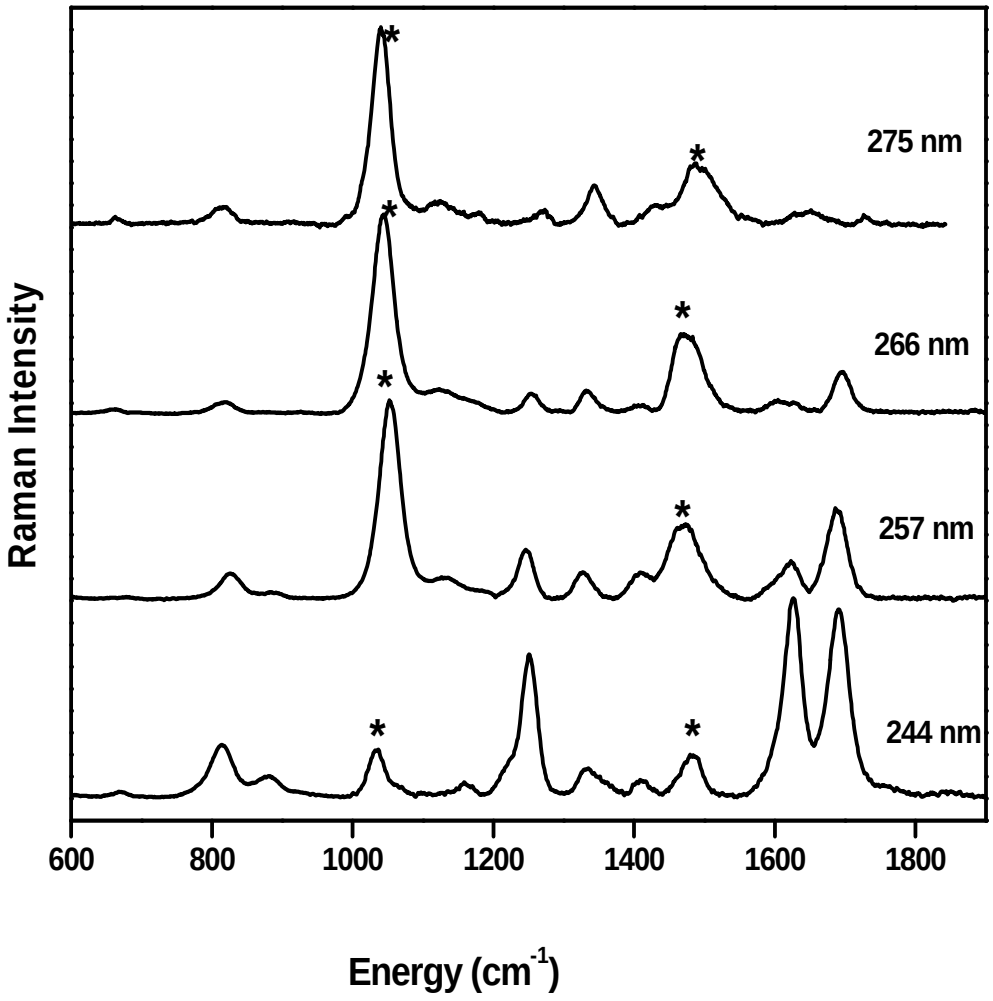

Figure 2.10. UVRR spectra of 2-Ethylhexyl salicylate (OCT) in methanol excited at different excitation wavelengths. The bands due to methanol are indicated by asterisks (*). Spectra have been scaled to the height of the largest peak in each spectrum and offset along the ordinate for clarity. Note that the spectral signatures here are similar to those in Figure 2.9 above, since OCT has the same chromophore as OCS shown in Figure 2.9.

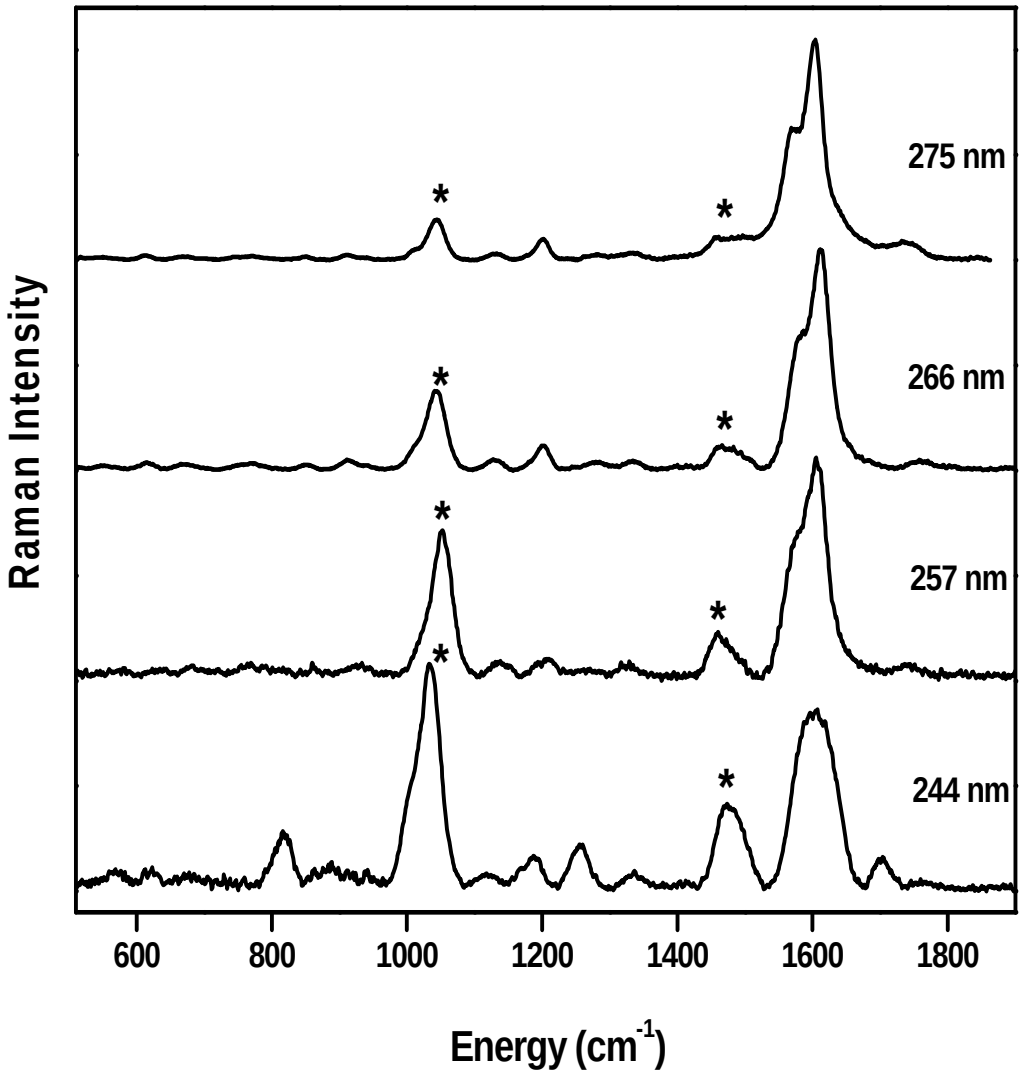

Figure 2.11. UVRR spectra of 2-Ethylhexyl-cyano-3,3-diphenyl-2-propenoate (Octocrylene, OCY) in methanol excited at different excitation wavelengths. The bands due to methanol are indicated by asterisks (*). Spectra have been scaled to the height of the largest peak in each spectrum and offset along the ordinate for clarity.

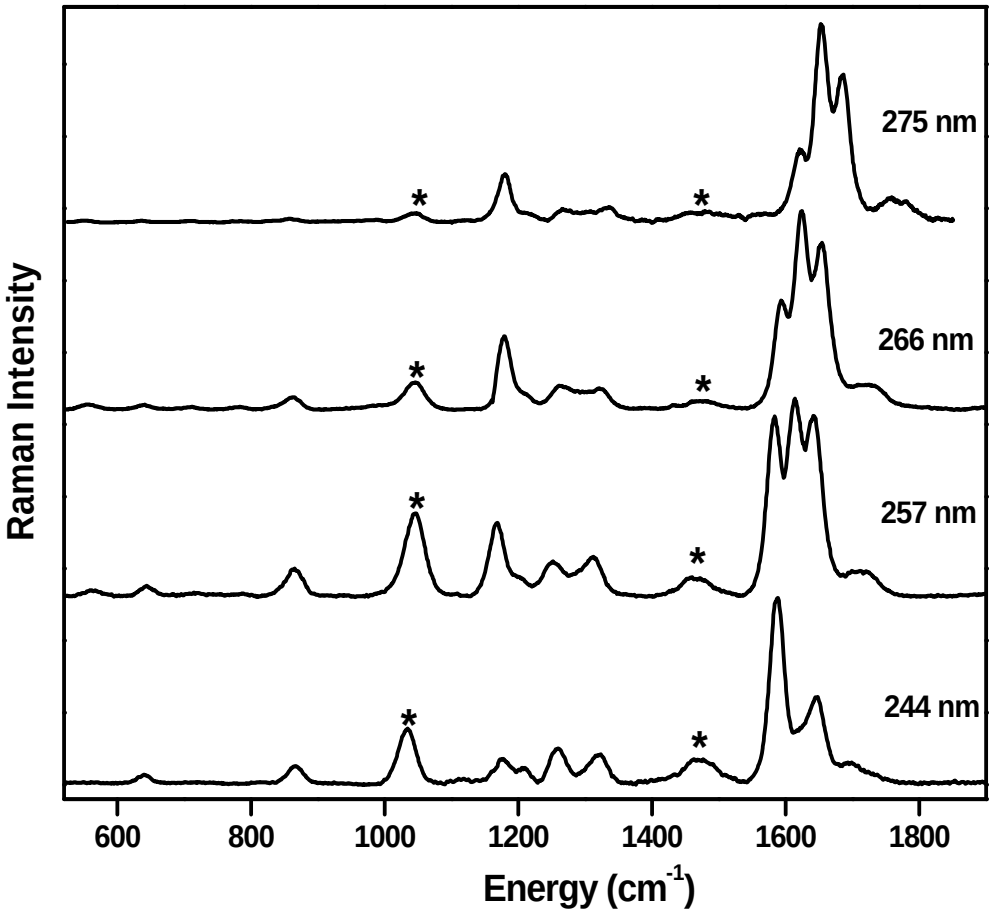

Figure 2.12. UVRR spectra of Octyl methoxycinnamate (OMC) in methanol excited at different excitation wavelengths. The bands due to methanol are indicated by asterisks (*). Spectra have been scaled to the height of the largest peak in each spectrum and offset along the ordinate for clarity.

state to another, as reflected in the different absorption bands at different wavelengths in the spectra of Figure 2.2A.

The similarity in the spectra observed for all five AIs at 275, 266 and 257 nm (Figures 2.8-2.12) demonstrates that we are observing resonance enhancement from the ca. 300 nm excited-state. The figures demonstrate the differential signal enhancement capability of UVRRS. It should be noted that the differential enhancement of signal observed for the AIs here, are of similar quality as those shown in the next two sections for the AI mixtures and real sunscreen formulations. In all of the different samples measured here, the spectral patterns change as the wavelength is tuned. This effect provides a powerful analytical tool for discriminating various species in complex mixtures. The differences in spectral signatures observed in Figures 2.8-2.12 can be rationalized based on the absorption spectra of the AIs shown in Figure 2.2A. The best discrimination between the AIs was achieved at 244 nm, in resonance with high-lying excited-states of the sunscreen AIs (Figure 2.2A). It has been established that signal enhancement in UVRRS is related to changes in molecular structure.[39-40] An earlier report has also shown that higher excited-states might be more sensitive to the electronic structures of substituents than do lower-lying excited-states.[45] Similarly, differences in molecular structures of lower-lying and higher-lying excited-states in substituted benzenes lead to different dipole moments and aromatic character of these molecules.[46] It is therefore rationalized that at 244 nm (higher energy excited-state) the molecules exhibit different spectral patterns because the excited-state is sensitive to both the phenyl rings and the substituents, compared to those of lower energy excited-states where the excited-state is sensitive to only the phenyl rings, hence the similarity in their spectral patterns at longer excitation wavelengths. Better discrimination can therefore be made between the sunscreen AIs at this lower wavelength (higher energy excited-state) due to the sensitivity of this excited-state to both the phenyl rings and the substituents of the AIs.

2.3.4 UVRRS of sunscreen AI mixtures

All of the sunscreen formulations have one or more AIs as shown in Table 2.1. A methanol binary mixture of the AIs corresponding to each sunscreen formulation was prepared to develop a library of reference spectra and to see if the UVRRS technique is capable of discriminating between AIs in a mixture. This step will also make it possible to monitor any contribution or interference that might come from the sunscreen matrix when the spectra of the sunscreen formulations are recorded. The results for four of the sunscreens at all excitation wavelengths used are shown in Figures 2.13-2.16. As the figures show, the spectra of the mixtures are indistinguishable at 275, 266 and 257 nm. Indeed, it can be said that at all excitation wavelengths longer than 244 nm, the spectral signatures of the AI mixtures are indistinguishable. The UVRR spectra excited at the longer wavelengths are all similar to that of M-DT, which contains only OMC. Thus, it may be rationalized that the vibrational modes of OMC are swamping out the contributions of the other components in each of the other three mixtures. This is consistent with Figures 2.3-2.7, which show OMC to have the highest intensity relative to methanol of all the sunscreen AIs at all wavelengths, all other parameters being the same. The fact that other AIs (except OCY) are usually present at lower concentrations than OMC in actual sunscreen formulations (Table 2.1) may also play a role in this observation.

At 244 nm excitation however, the mixtures give more distinct spectral signatures (Figure 2.16), consistent with the explanation that the excited-state is sensitive to both the phenyl rings and the substituents at the higher-energy excited-state corresponding to this excitation wavelength, while the excited-state is sensitive to only the phenyl rings at the lower-lying excited-state corresponding to 257 to 275 nm. Based on the spectra of the constituent AIs shown in Figure 2.7, one can identify the AIs in the mixtures of Figure 2.16. The four spectra shown in this figure may be seen to fall into two classes based on the similarity of the spectral patterns. M-BS, M-CT and M-DT form one class, containing either OMC only, or OMC and either OCY or BZ3 (see Table 2.1). M-HT constitutes the second class, and contains OMC and OCT.

Table 2.1. Sunscreen formulations analyzed with UVRRS

		Active Ingredients[a]				
Sample	SPF[b]	BZ3	OCS	OCT	OCY	OMC
L-BZ	45	6	5	-	2	7.5
L-HT	45	-	-	5	-	7.5
L-BS	50	-	-	-	10	7.5
L-CT	15	4	-	-	-	7.5
L-DT	4	-	-	-	-	3
L-OB[c]	30	-	-	-	-	-

[a]The different active ingredients in each formulation and their respective compositions (in % w/w) reported on their respective labels. [b]Sun Protection Factor (SPF), is defined as the ratio of minimal erythema dose for protected skin to that of unprotected skin. It is a measure of the effectiveness of the sunscreen formulation. [c]This formulation contains none of the five AIs considered in this work, it was only used to model a real sunscreen matrix for LOD determination of OMC. It however contains titanium dioxide (10.5% w/w) and terephthalylidene dicamphor sulfonic acid (1% w/w) as active ingredients. The SPF values and the %w/w concentration of the AIs shown here are as indicated on the packaging of each lotion.

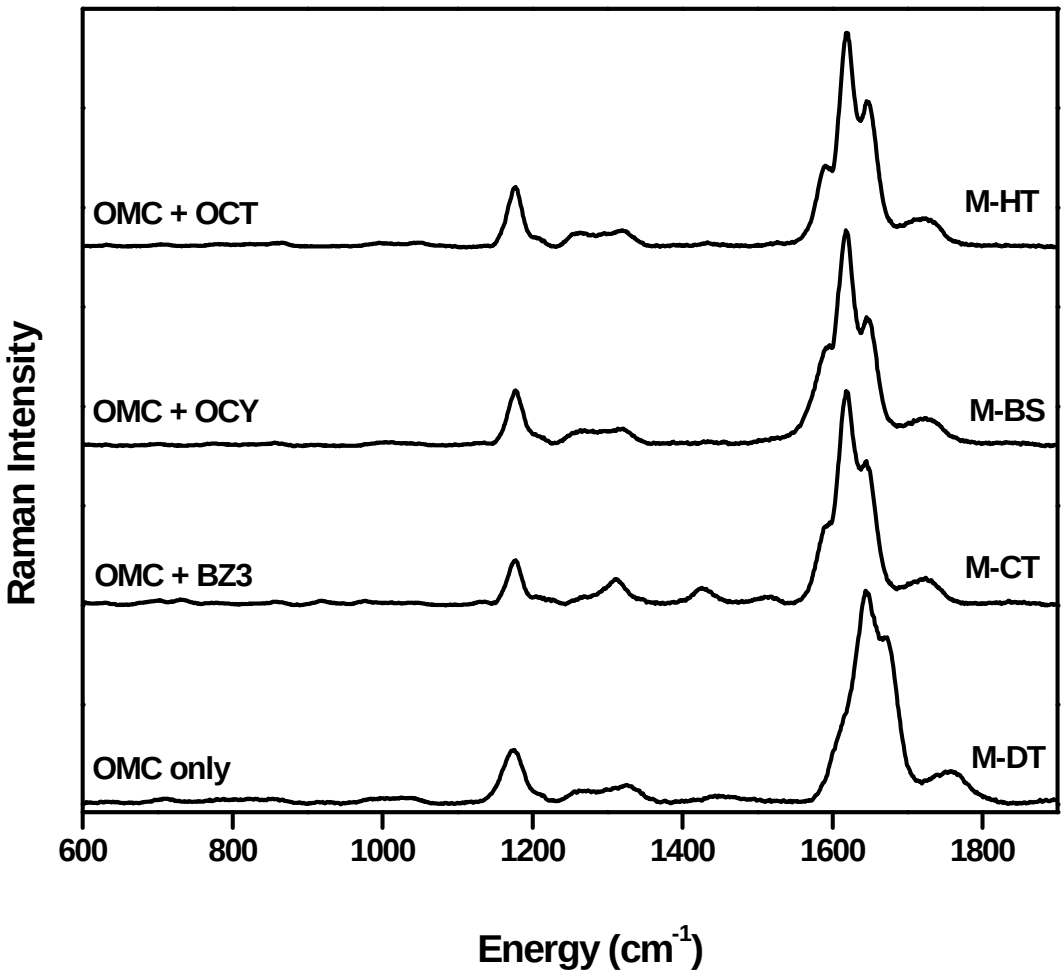

Figure 2.13: UVRR spectra of sunscreen AI mixtures in methanol excited at 275 nm. For these mixtures the compositions of Table 1 in methanol were used. Spectra have been scaled to the height of the largest peak in each spectrum and offset along the ordinate for clarity. The "M" prefix means that the samples here are mixtures of the AIs corresponding to the sunscreen formulations shown in Table 2.1. The constituent AIs in each mixture are also shown on the left of each spectrum.

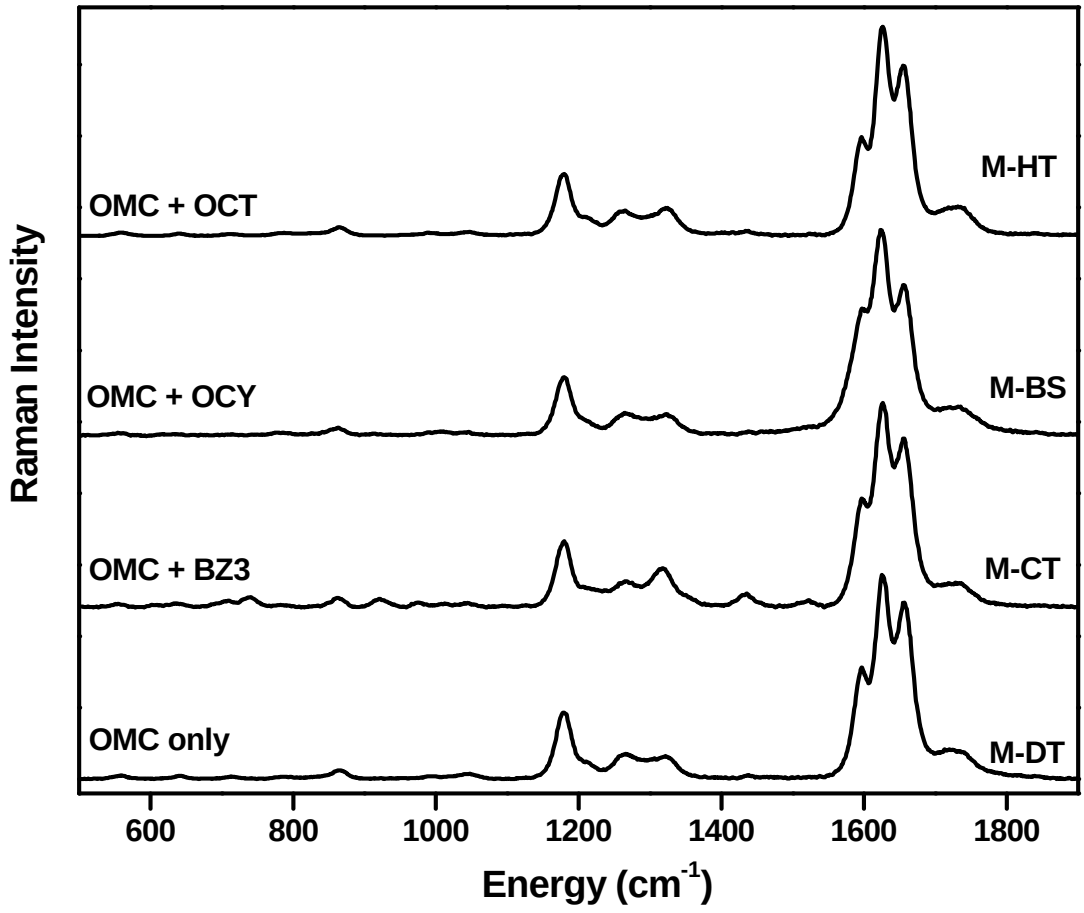

Figure 2.14: UVRR spectra of sunscreen AI mixtures in methanol excited at 266 nm. For these mixtures the compositions of Table 1 in methanol were used. Spectra have been scaled to the height of the largest peak in each spectrum and offset along the ordinate for clarity. The "M" prefix means that the samples here are mixtures of the AIs corresponding to the sunscreen formulations shown in Table 2.1. The constituent AIs in each mixture are also shown on the left of each spectrum.

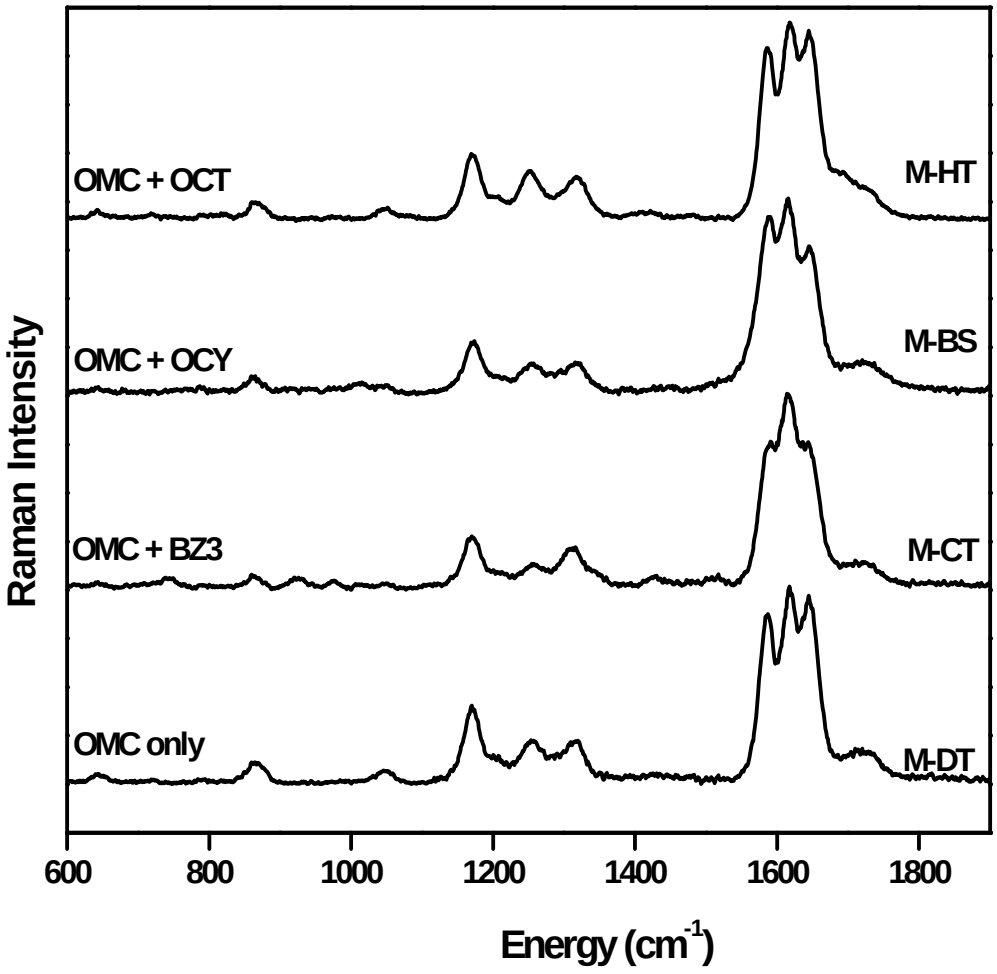

Figure 2.15: UVRR spectra of sunscreen AI mixtures in methanol excited at 257 nm. For these mixtures the compositions of Table 1 in methanol were used. Spectra have been scaled to the height of the largest peak in each spectrum and offset along the ordinate for clarity. The "M" prefix means that the samples here are mixtures of the AIs corresponding to the sunscreen formulations shown in Table 2.1. The constituent AIs in each mixture are also shown on the left of each spectrum.

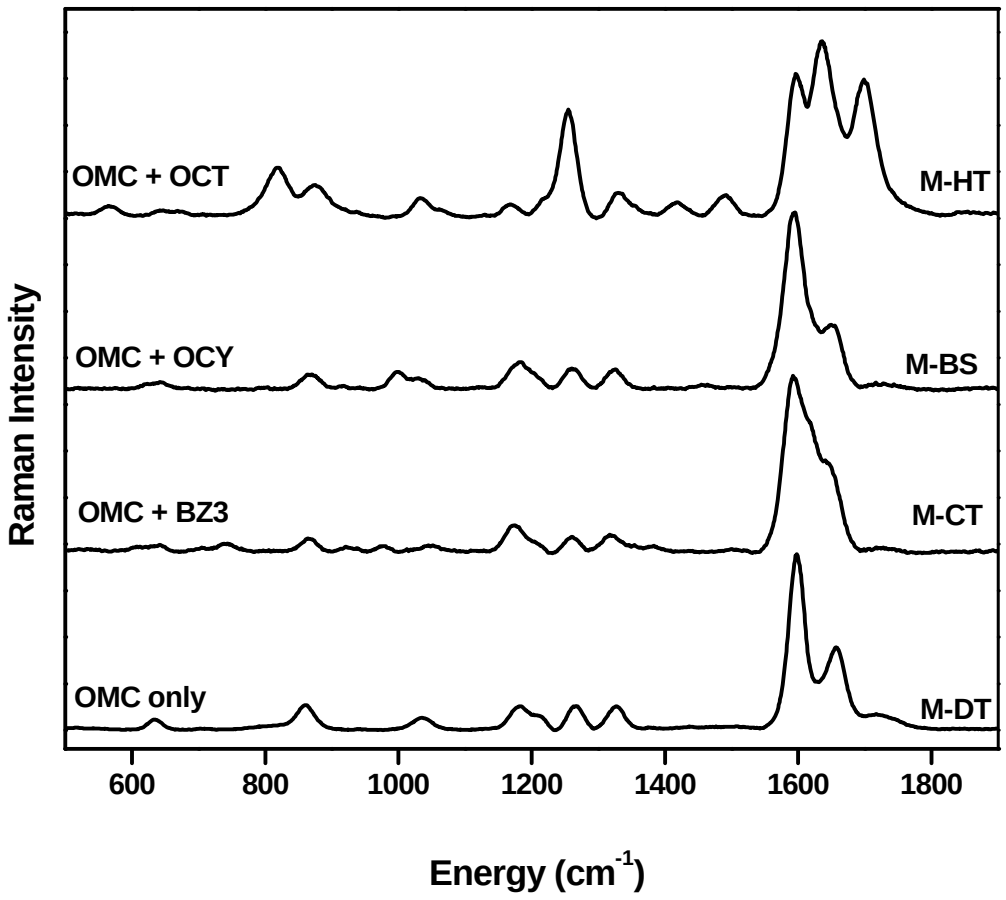

Figure 2.16: UVRR spectra of sunscreen AI mixtures in methanol excited at 244 nm. For these mixtures the compositions of Table 1 in methanol were used. Spectra have been scaled to the height of the largest peak in each spectrum and offset along the ordinate for clarity. The "M" prefix means that the samples here are mixtures of the AIs corresponding to the sunscreen formulations shown in Table 2.1. The constituent AIs in each mixture are also shown on the left of each spectrum.

As for M-BS (containing OMC and OCY), the convolution of the OCY C=O stretch band around 1605 cm^{-1} with the two bands of OMC around 1600 cm^{-1} may result in the less resolved two bands observed in this region at 244 nm excitation. However, this is not conclusive considering that M-DT, which contains only OMC, has essentially the same spectral pattern as M-BS. The weak band around 1000 cm^{-1} observed in M-BS which is absent in M-DT serves to conclusively discriminate OCY from OMC. M-CT has both OMC and BZ3 as the AIs and the spectral pattern is indicative of the presence of these two components, especially the rather broad band with weak shoulders around 1581 cm^{-1} which may be seen as a convolution of the corresponding bands in OMC and BZ3 (Figure 2.7). Since M-DT has a single component (OMC), the spectral pattern is unambiguous and does not require further analysis. The sum of the two bands observed between 1590 and 1690 cm^{-1} in OCT with the three bands between 1550 and 1700 cm^{-1} in OMC (Figure 2.7) give rise to the resultant three bands observed in M-HT near 1600 cm^{-1}. Also, the strong salicylate C-O stretch around 1250 cm^{-1} in M-HT is typical of OCS or OCT,[7,44] since the corresponding band at this position in OMC is weaker (see Figure 2.7). In addition, there is a band in the spectrum of M-HT around 811 cm^{-1} which is observed only in OCS and OCT but not in OMC at 244 nm excitation (Figure 2.7). This band is also indicative of the presence of OCS or OCT.

The wavelength-dependent subtle differences between the spectra of each binary mixture can be seen in Figures 2.17-2.20. From these figures, it can be discerned that discrimination between the components of each mixture is difficult at 257-275 nm, as the spectral signatures are similar. However at 244 nm, the signatures are uniquely different such that each component in a given binary mixture can be identified. The spectral evolution observed for the mixtures here is consistent with the rationalization given in the previous section that the spectral signatures are similar at 257-275 nm because resonance is observed from the ca. 300 nm band (Figure 2.1A). This corresponds to a lower-lying excited-state which is sensitive to only the phenyl rings. And since all the sunscreen AIs have phenyl rings, the spectra

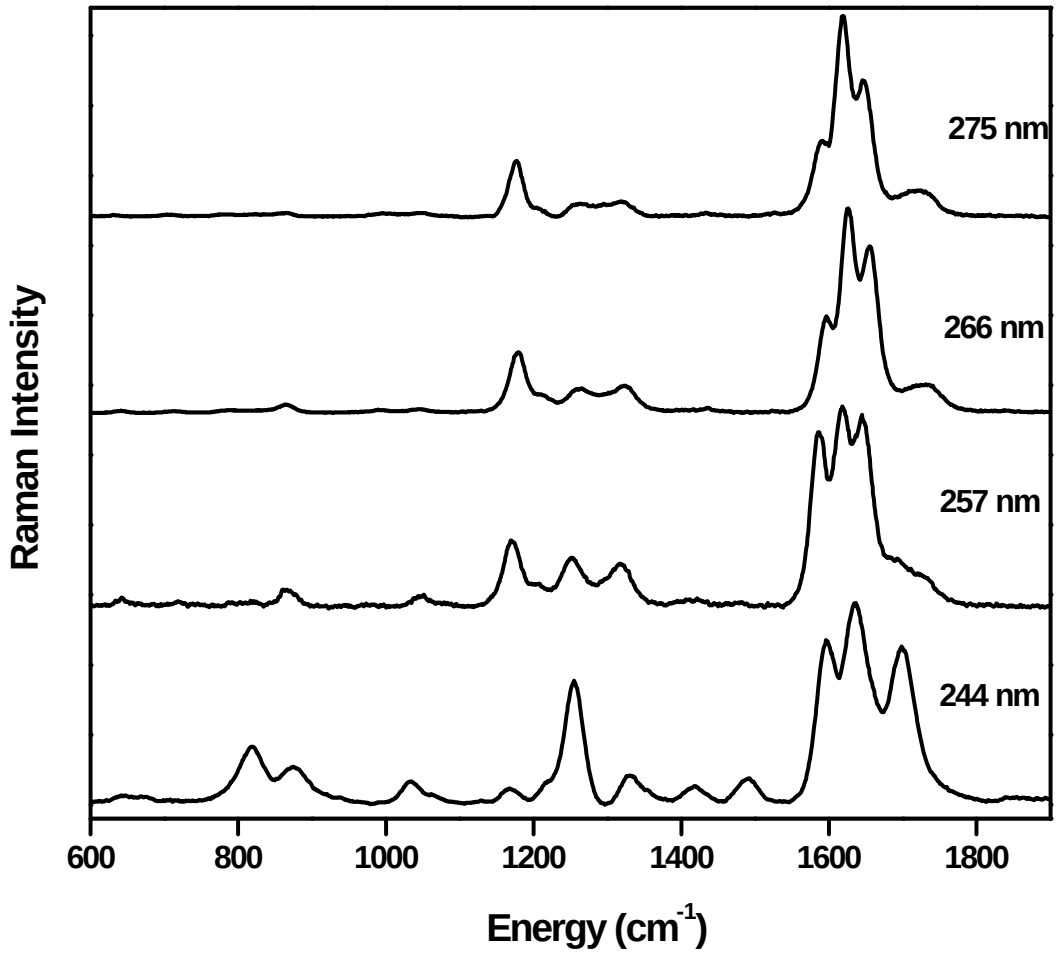

Figure 2.17. UVRR spectra of binary mixture M-HT in methanol excited at different excitation wavelengths. This mixture contains OMC (7.5% w/w) and OCT (5% w/w) as shown in Table 2.1 for the real sunscreen it mimics. Spectra have been scaled to the height of the largest peak in each spectrum and offset along the ordinate for clarity.

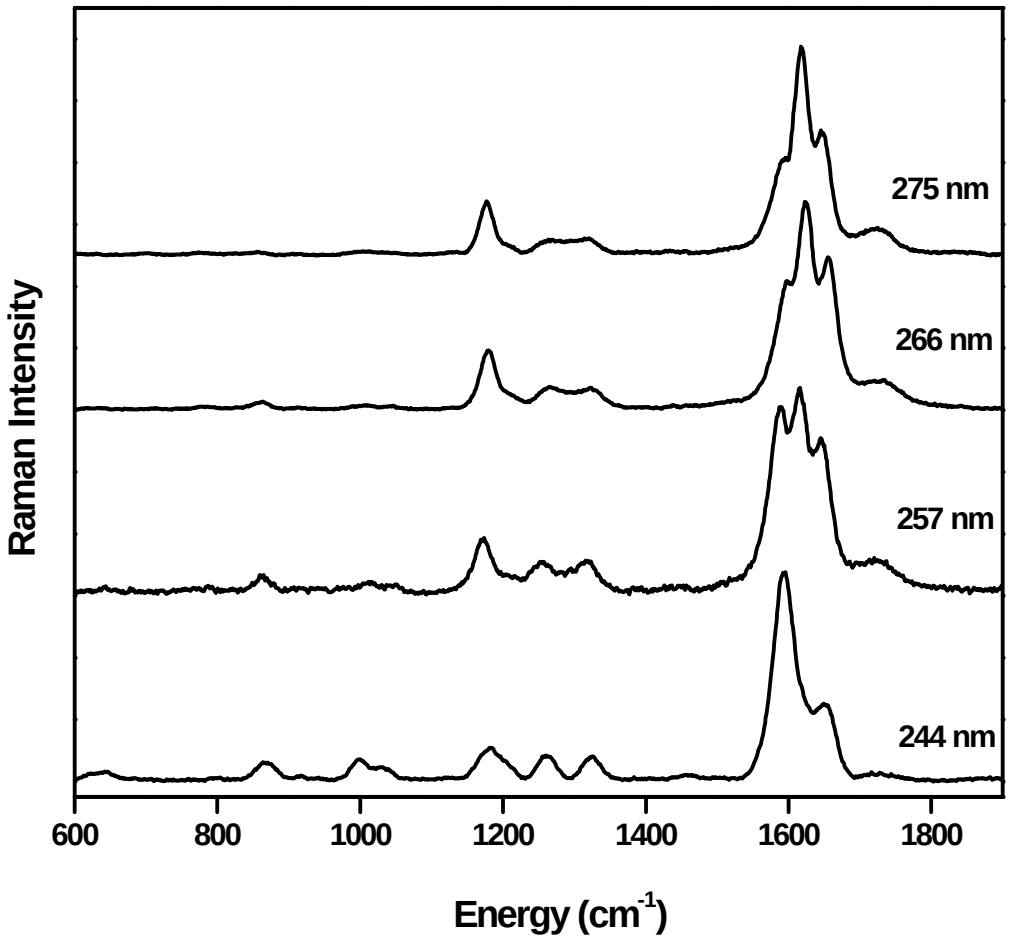

Figure 2.18. UVRR spectra of binary mixture M-BS in methanol excited at different excitation wavelengths. This mixture contains OMC (7.5% w/w) and OCY (10% w/w) as shown in Table 2.1 for the real sunscreen it mimics. Spectra have been scaled to the height of the largest peak in each spectrum and offset along the ordinate for clarity.

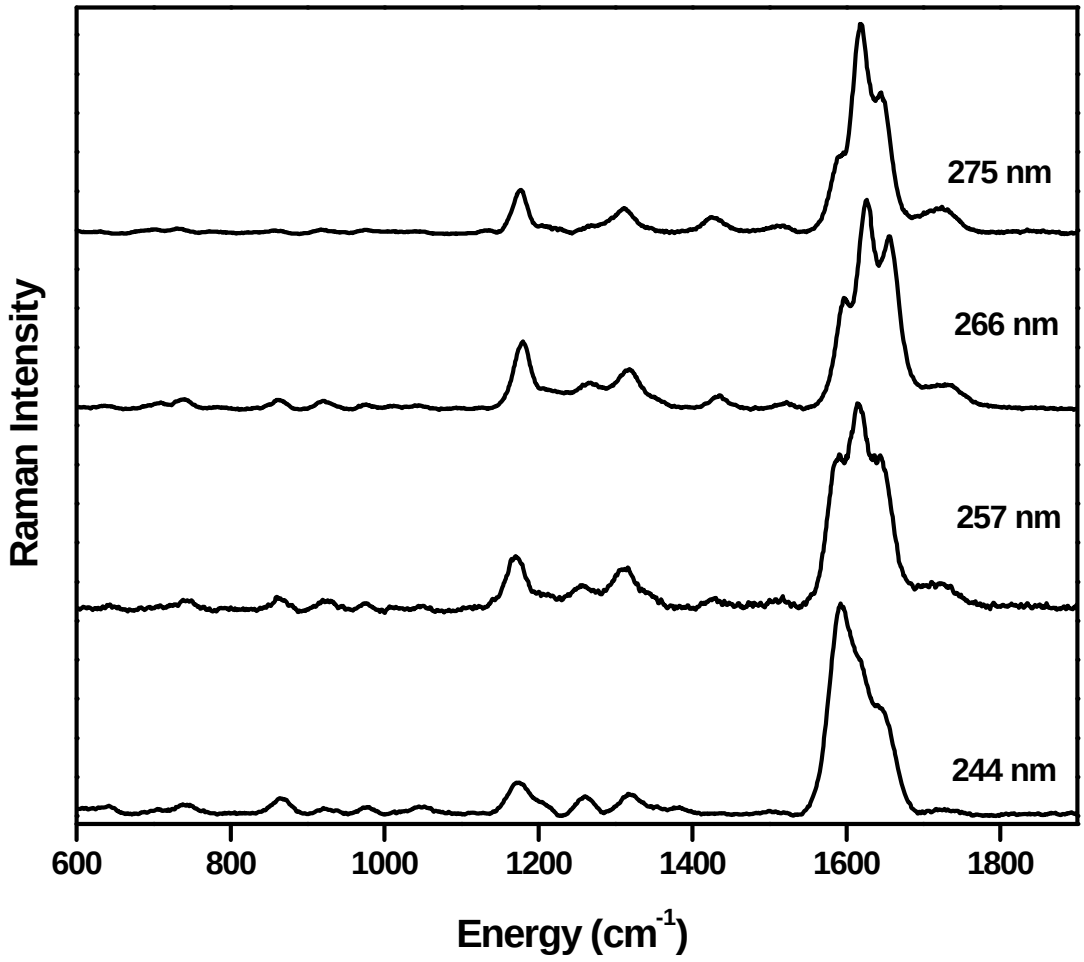

Figure 2.19. UVRR spectra of binary mixture M-CT in methanol excited at different excitation wavelengths. This mixture contains OMC (7.5% w/w) and BZ3 (4% w/w) as shown in Table 2.1 for the real sunscreen it mimics. Spectra have been scaled to the height of the largest peak in each spectrum and offset along the ordinate for clarity.

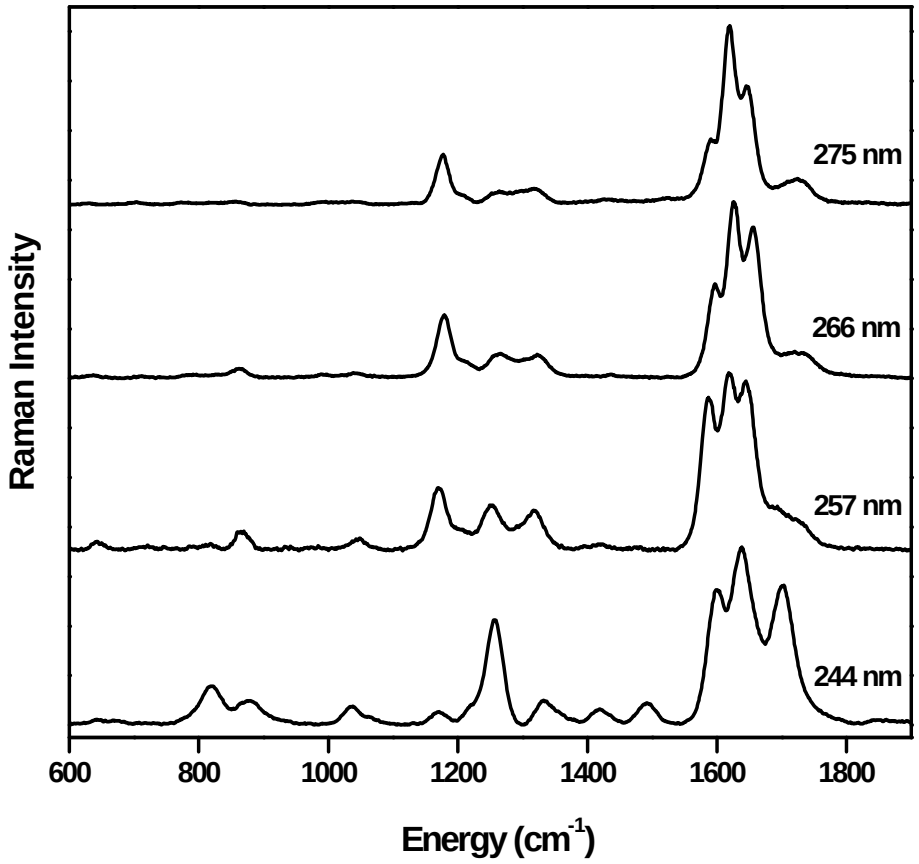

Figure 2.20. UVRR spectra of binary mixture M-BZ in methanol excited at different excitation wavelengths. This mixture contains OMC (7.5% w/w) and OCS (5% w/w), though the actual sample contains four components (see Table 2.1). The 4-component mixture for this sample is shown in the next section (see Figure 2.25). Spectra have been scaled to the height of the largest peak in each spectrum and offset along the ordinate for clarity.

are similar at these three wavelengths of excitation. In contrast, at 244 nm excitation, the spectral signatures of the AIs are different because resonance is observed for the ca. 230 nm band. (Figure 2.1A). This band corresponds to a higher-lying excited-state which is sensitive to both the phenyl rings and the substituents, hence the observed spectral differences at 244 nm. Note that the spectra corresponding to M-DT have not been included in the following set of figures (Figure 2.17-2.20) because the spectra are already shown as Figure 2.12 and because it contains only OMC which mimics the real sunscreen L-DT (Table 2.1).

2.3.5 UVRRS of sunscreen formulations

Based on the robustness of UVRRS, the technique was applied to the direct *in situ* analysis of the sunscreen formulations given in Table 2.1. Because the 244 nm excitation wavelength gave the best possible discrimination in the AI mixtures, this wavelength is expected to give best discrimination for the sunscreen formulations too. The results for the sunscreen formulations are shown in Figures 2.21-2.25. It is interesting to see that despite the complex nature of the matrix in which the sunscreen AIs are suspended, good quality spectra were obtained for each of the sunscreen formulations at all excitation wavelengths. This is an indication of the good selectivity that can be obtained with UVRRS. Using Figures 2.24 and 2.25 as reference since 244 nm excitation gives the best discrimination, one can see that in all cases, spectral signatures corresponding to the constituent AIs are discernible. This is more obvious especially when one compares these figures with the corresponding ones for the AI mixtures (Figures 2.13-2.16). It is also impressive to note that there is essentially no interference from the wide variety of other additives present in the complex matrix or from fluorescence. The minor differences between the spectra of M-BS, M-CT and M-DT in Figures 2.13-2.16, and the corresponding spectra of L-BS, L-CT and L-DT in Figures 2.21-2.25 are ascribed to other components in the sunscreen formulation. For instance, the higher intensity peak at ~1750 cm^{-1} observed in the spectra of these three lotions is ascribed to perturbations by other

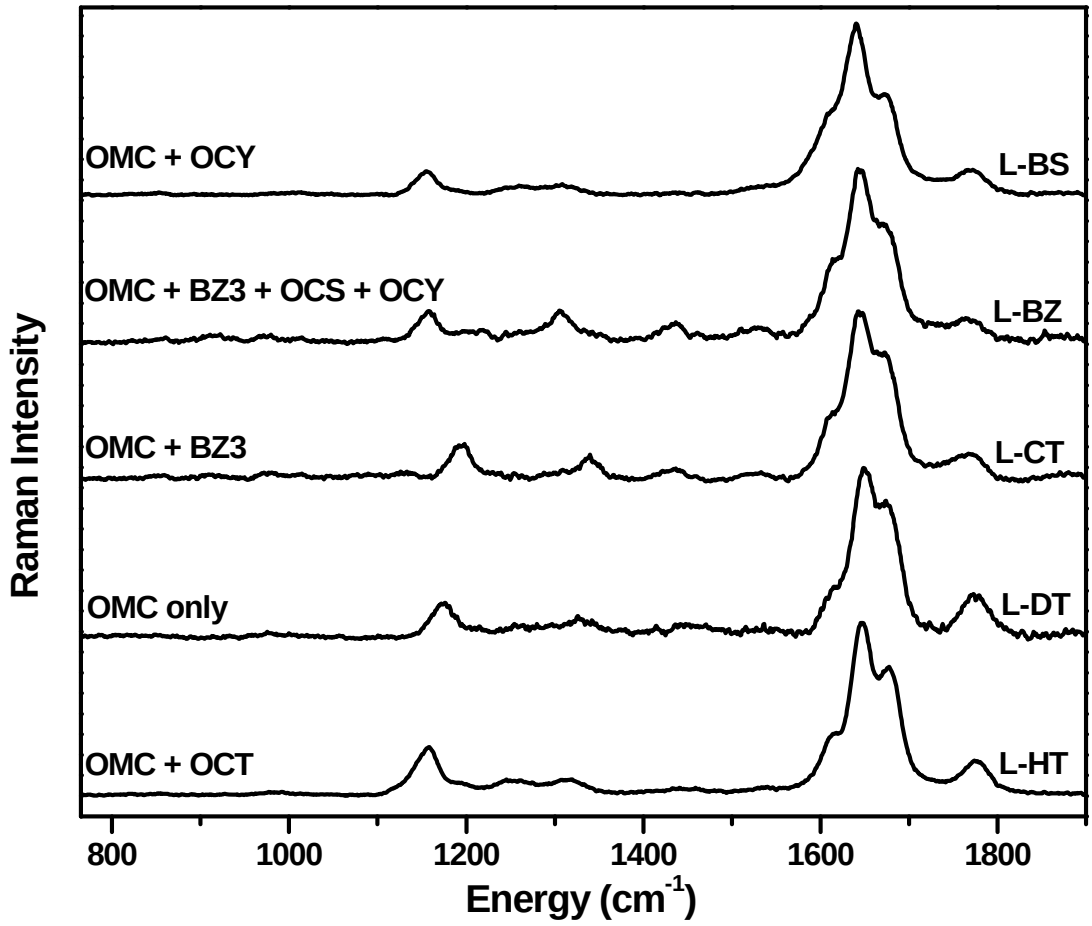

Figure 2.21. UVRR spectra of neat sunscreen formulations (Table 2.1) excited at 275 nm. The constituent AIs in each case are shown. Spectra have been scaled to the height of the largest peak in each spectrum and offset along the ordinate for clarity. The "L" prefix means that the spectra are for neat sunscreen formulations shown in Table 2.1. Raman data below 800 cm^{-1} were obscured by intense stray light and are not shown.

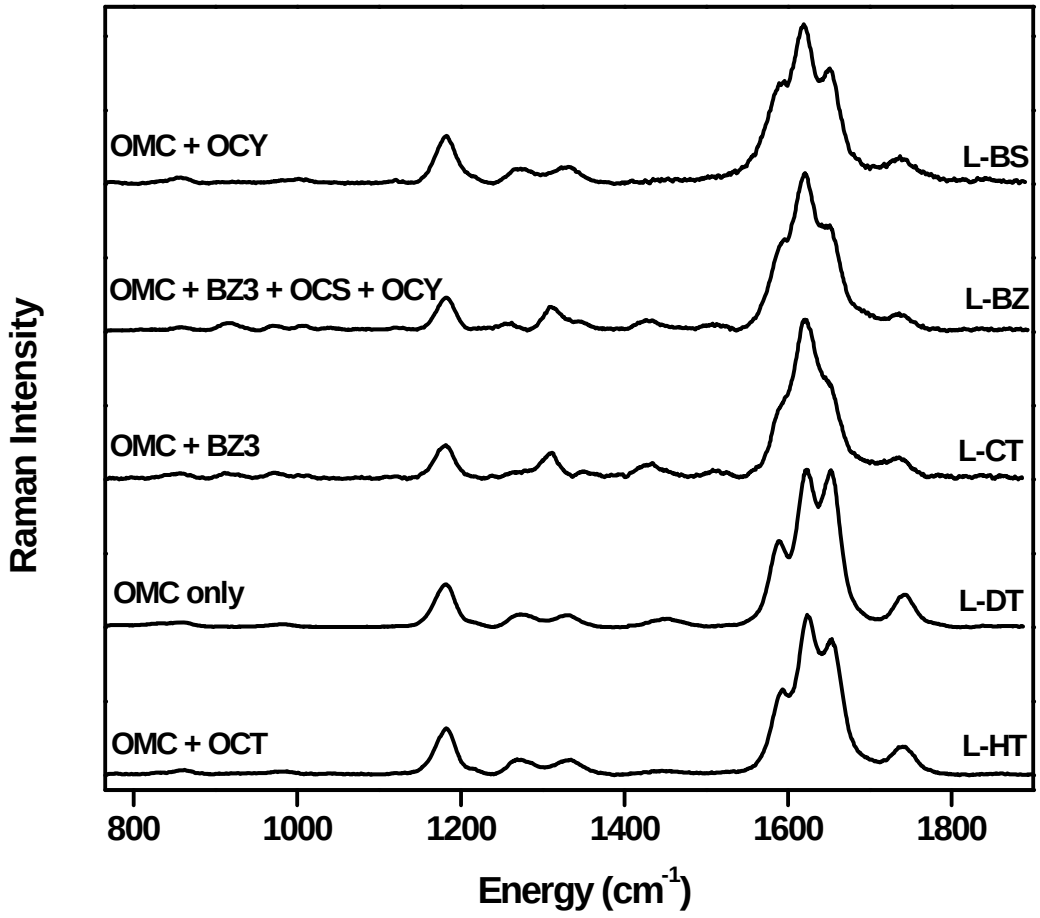

Figure 2.22. UVRR spectra of neat sunscreen formulations (Table 2.1) excited at 266 nm. The constituent AIs in each case are shown. Spectra have been scaled to the height of the largest peak in each spectrum and offset along the ordinate for clarity. The "L" prefix means that the spectra are for neat sunscreen formulations shown in Table 2.1. Raman data below 800 cm^{-1} were obscured by intense stray light and are not shown.

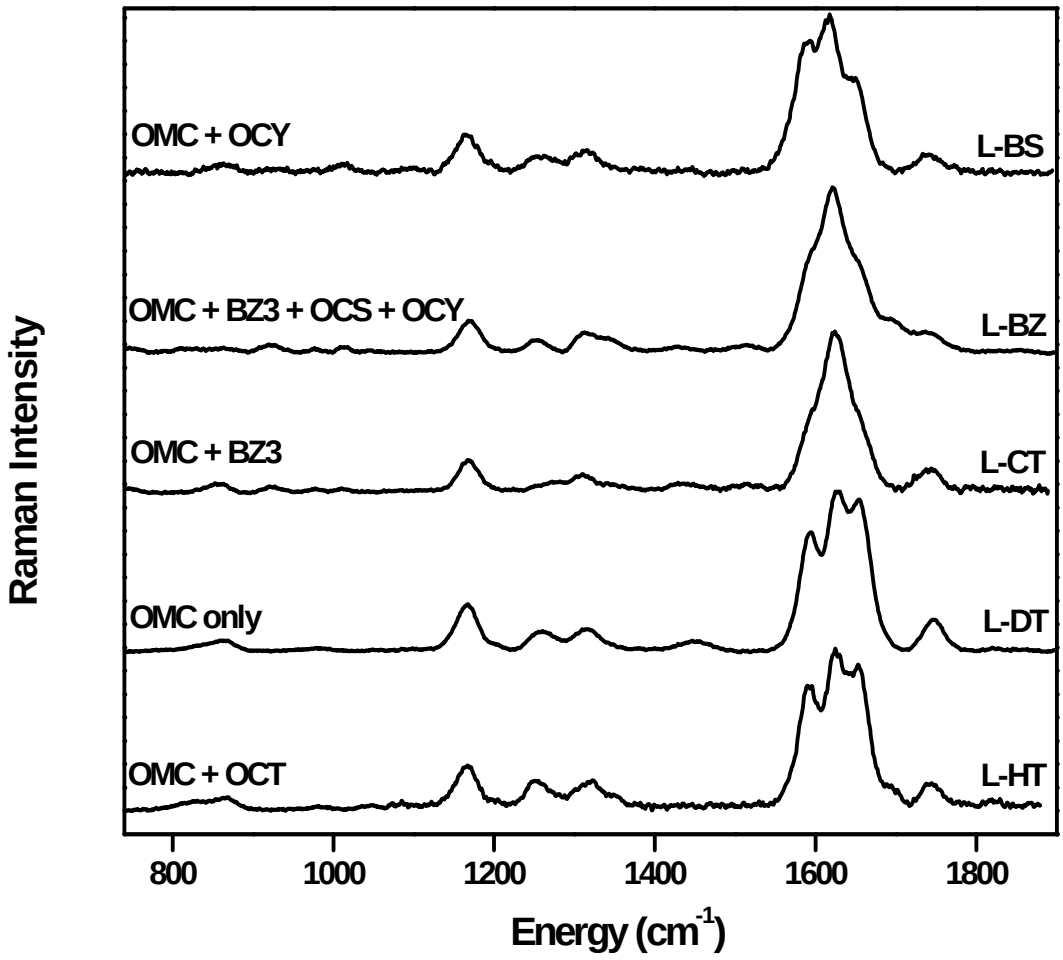

Figure 2.23. UVRR spectra of neat sunscreen formulations (Table 2.1) excited at 257 nm. The constituent AIs in each case are shown. Spectra have been scaled to the height of the largest peak in each spectrum and offset along the ordinate for clarity. The "L" prefix means that the spectra are for neat sunscreen formulations shown in Table 2.1. Raman data below 800 cm^{-1} were obscured by intense stray light and are not shown.

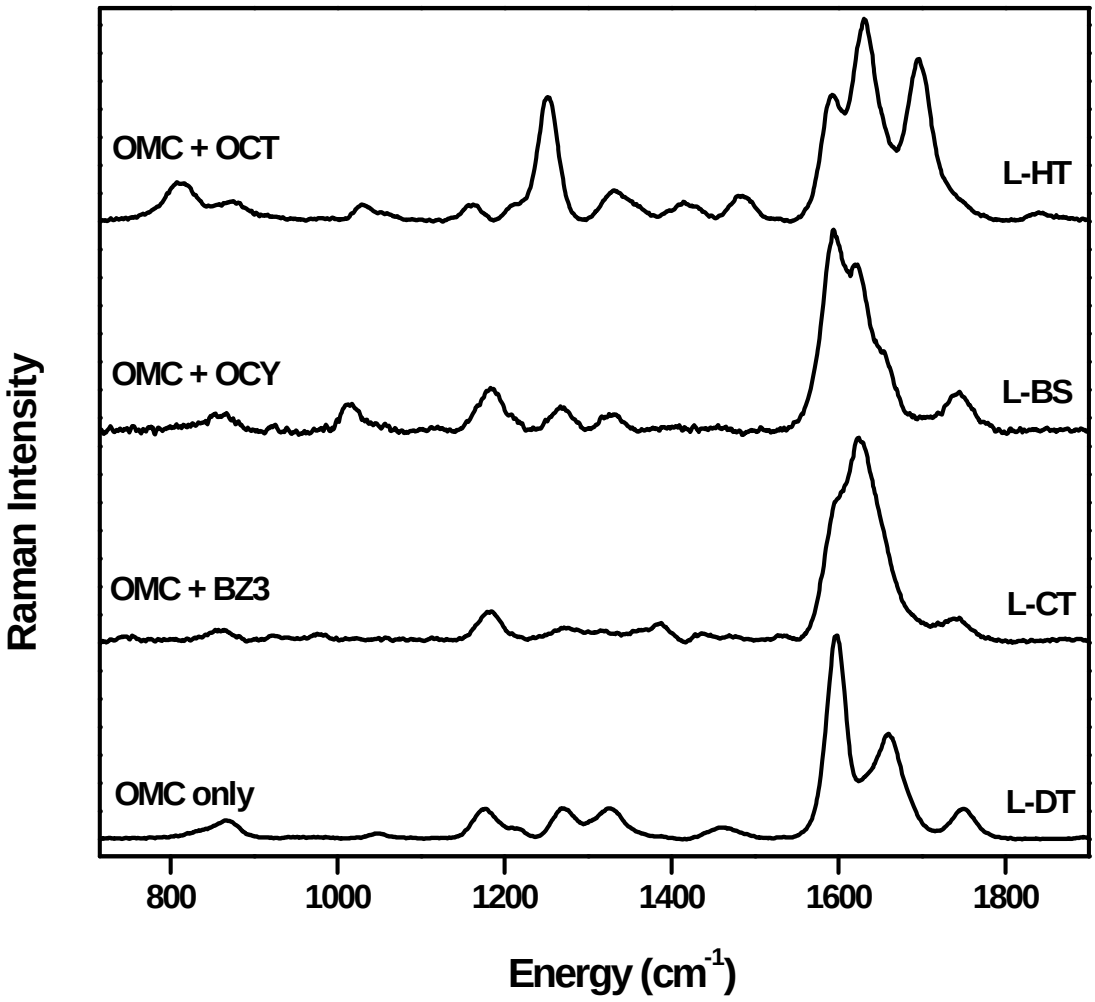

Figure 2.24. UVRR spectra of neat sunscreen formulations (Table 2.1) excited at 244 nm. The constituent AIs in each case are shown. Note that the spectrum of L-BZ is not included here, it is shown in Figure 2.25 below. Spectra have been scaled to the height of the largest peak in each spectrum and offset along the ordinate for clarity. The "L" prefix means that the spectra are for neat sunscreen formulations shown in Table 2.1. Raman data below 800 cm^{-1} were obscured by intense stray light and are not shown.

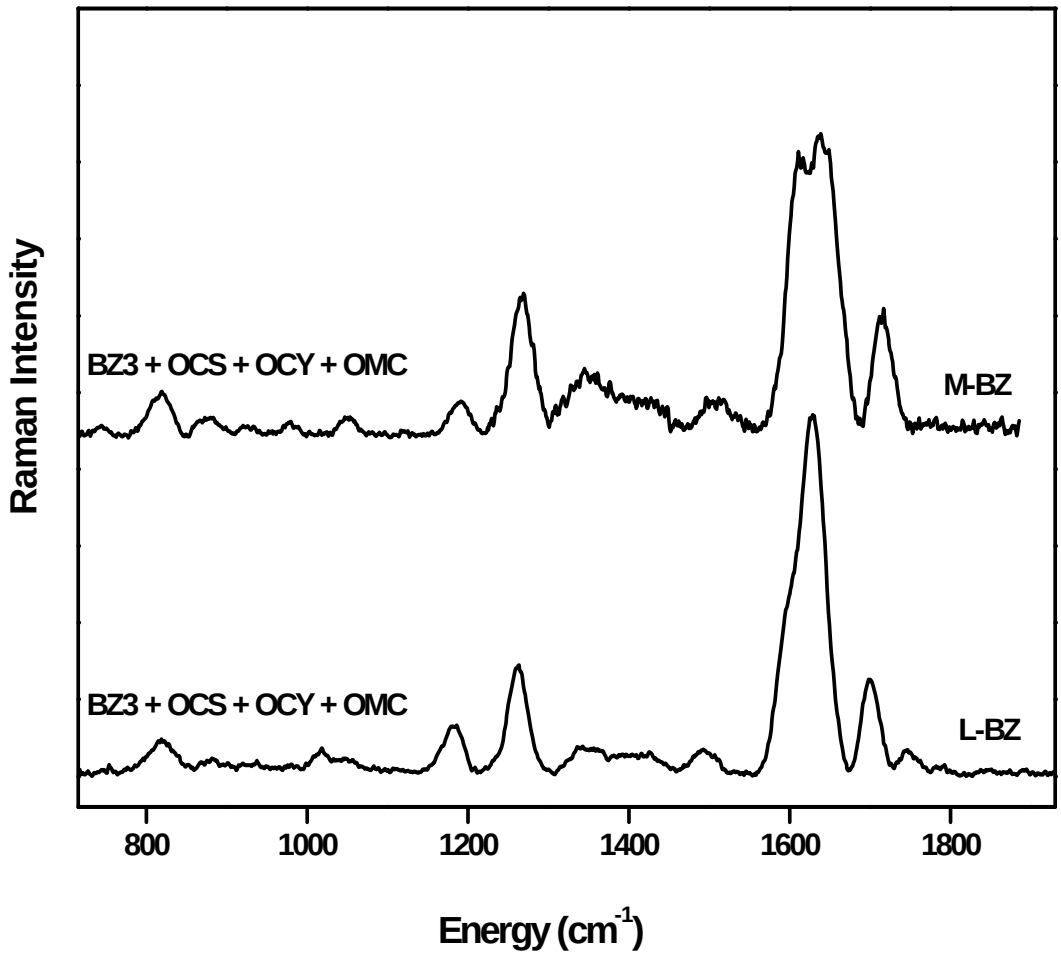

Figure 2.25. UVRR spectra of complete M-BZ containing all four AIs in the amounts indicated in Table 2.1 in methanol. The spectrum for the corresponding sunscreen formulation L-BZ is also shown for comparison. Both spectra were acquired at 244 nm excitation. Spectra have been scaled to the height of the largest peak in each spectrum and offset along the ordinate for clarity. Raman data below 800 cm^{-1} were obscured by intense stray light and are not shown.

components in the sunscreen matrix. The examination of these perturbations is outside the scope of my interest and so it is not discussed further here. However, it could be a subject of further study. In the case of L-HT, the spectral pattern of the AI mixture M-HT is very similar to that of its corresponding formulation L-HT, hence the presence of both OMC and OCT is clearly evident.

The UVRRS of the 4-component mixture and sunscreen formulation for BZ are compared in Figure 2.25. As shown in the figure, the spectra are very similar. However, the spectrum for the mixture is somewhat noisier, and the low energy shoulder around 1590 cm^{-1} is more intense in the mixture. The spectral pattern observed for L-BZ in Figure 2.25 is similar to that of L-CT in Figure 2.24 except for the band at ~1260 cm^{-1}. This band is indicative of the presence of OCS in L-BZ, which is absent in L-CT (Table 2.1).

As can be seen in Figures 2.21-2.25, the technique is sensitive enough to determine the concentrations and identities of sunscreen AIs present in sunscreen formulations due to the differential signal enhancement that can be achieved as a result of resonance. This differential signal enhancement significantly reduces any interference from the complex sunscreen matrix. It should also be mentioned that despite the fluorescence of some of the AIs (see Figure 2.2A & B), high-quality spectra were still obtained from the sunscreen formulations without interference from fluorescence. The low fluorescence of OCS, OCT and OMC does not interfere with the UVRRS measurements, thus, the fluorescence yield must be very low. This observation is in agreement with previous results that show UV resonance Raman spectra with little fluorescence interference when a deep UV excitation wavelength is used.[47,48]

The wavelength-dependent spectral evolution of the real sunscreen formulations are also presented (Figures 2.26-2.30). Again, the distinction between spectra at 244 nm excitation and the ones at the three other wavelengths is apparent. The noisy background seen in many of the spectra is ascribed to the complex matrix.

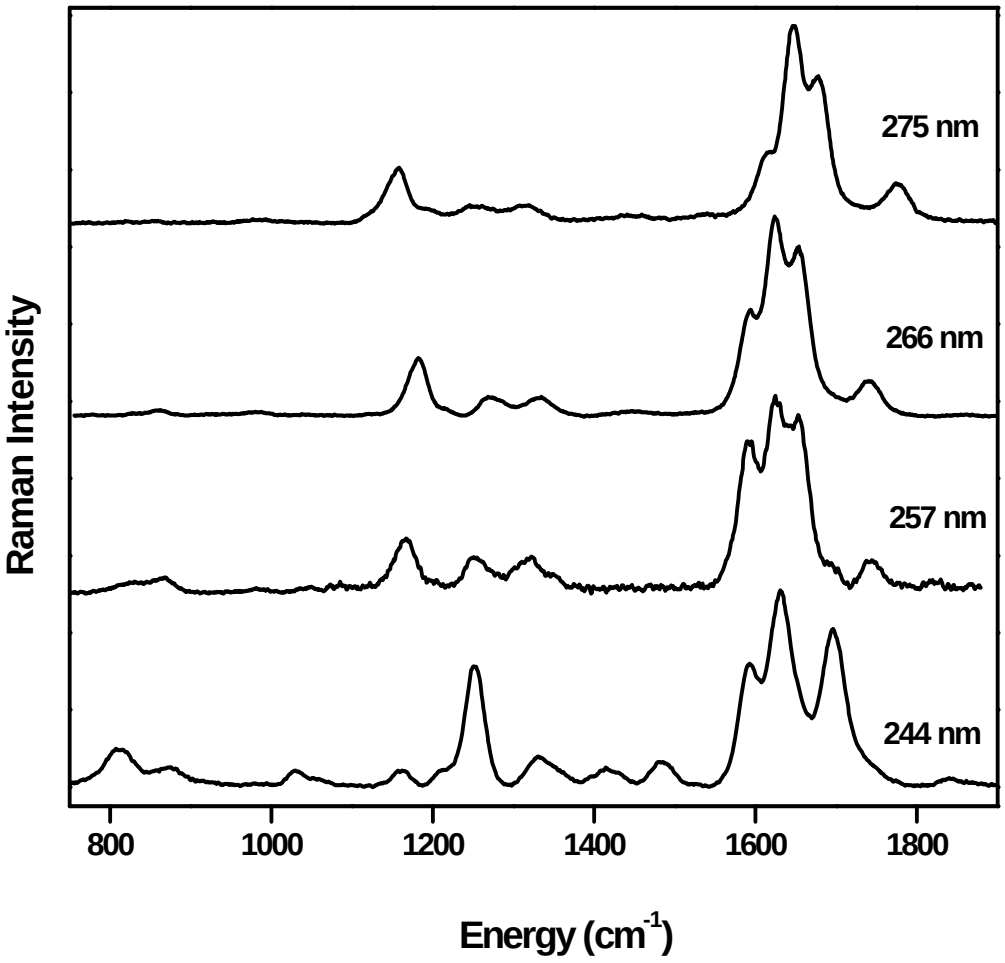

Figure 2.26: UVRR spectra of L-HT excited at different excitation wavelengths. The composition of this sample and its SPF value are as shown in Table 2.1. Spectra have been scaled to the height of the largest peak in each spectrum and offset along the ordinate for clarity.

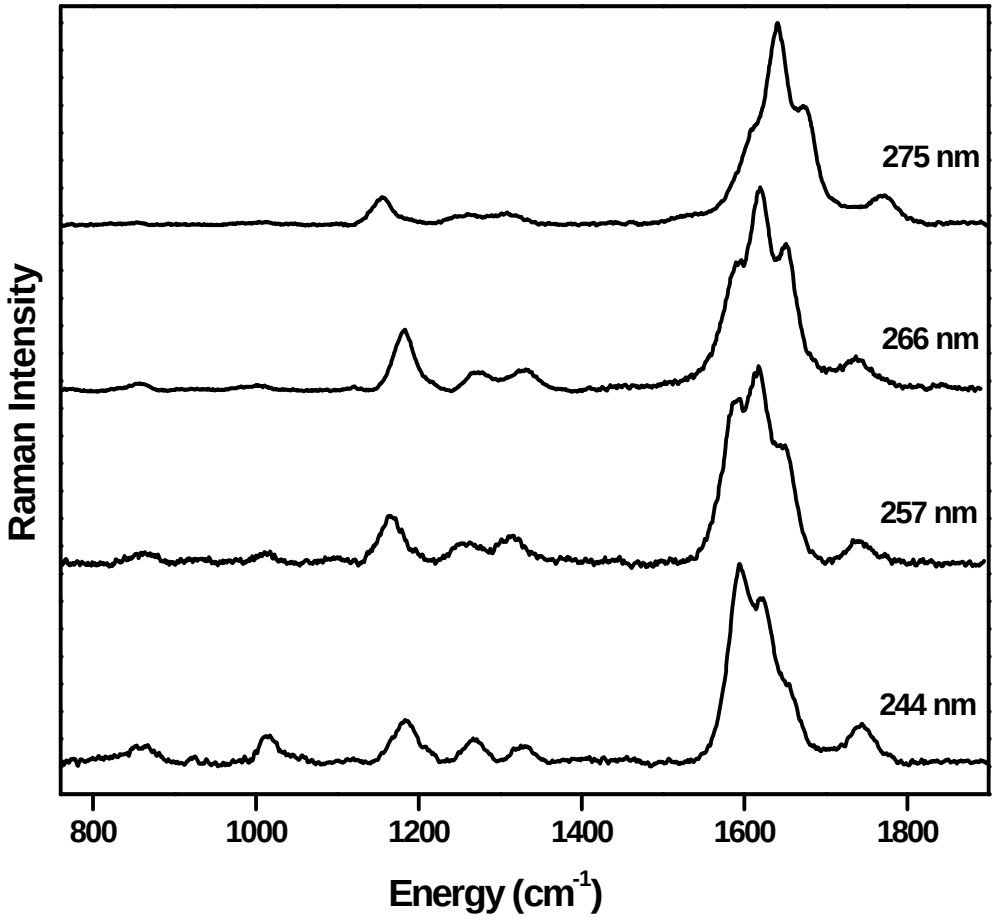

Figure 2.27: UVRR spectra of L-BS excited at different excitation wavelengths. The composition of this sample and its SPF value are as shown in Table 2.1. Spectra have been scaled to the height of the largest peak in each spectrum and offset along the ordinate for clarity.

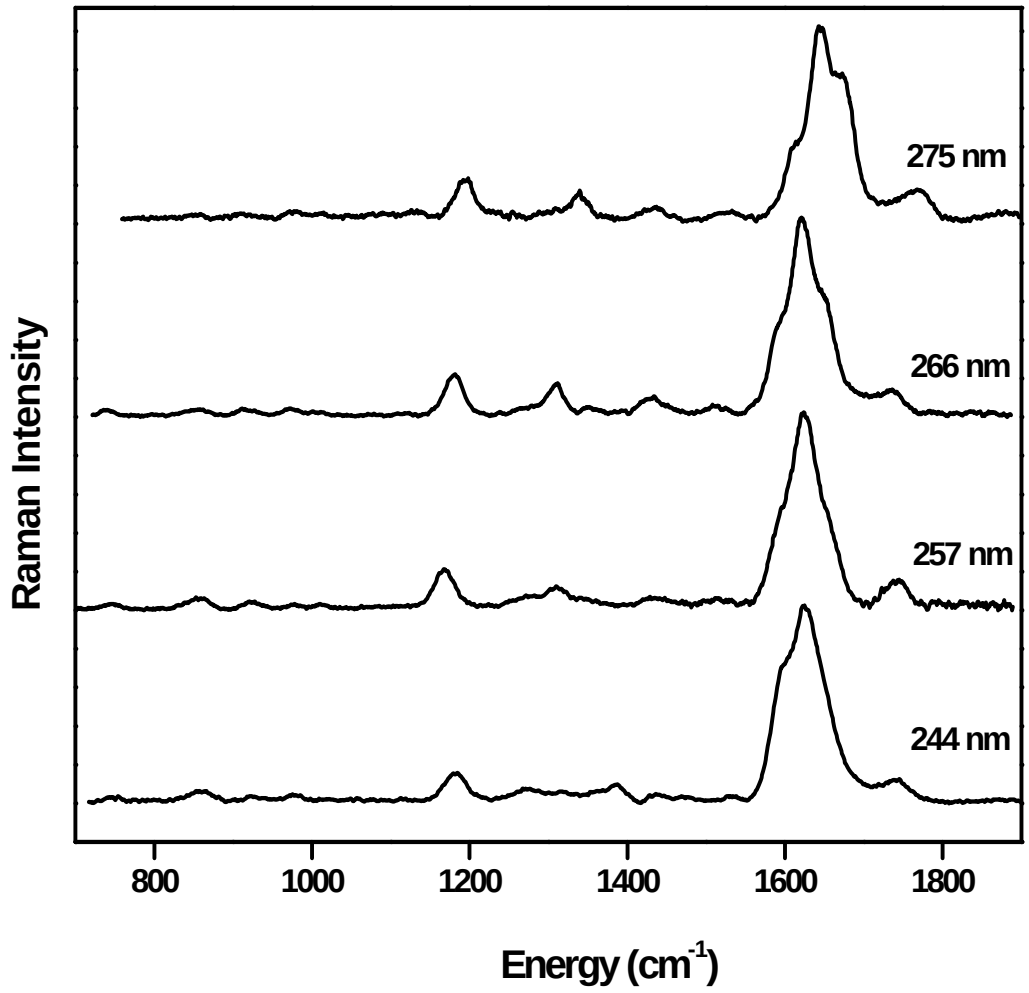

Figure 2.28: UVRR spectra of L-CT excited at different excitation wavelengths. The composition of this sample and its SPF value are as shown in Table 2.1. Spectra have been scaled to the height of the largest peak in each spectrum and offset along the ordinate for clarity.

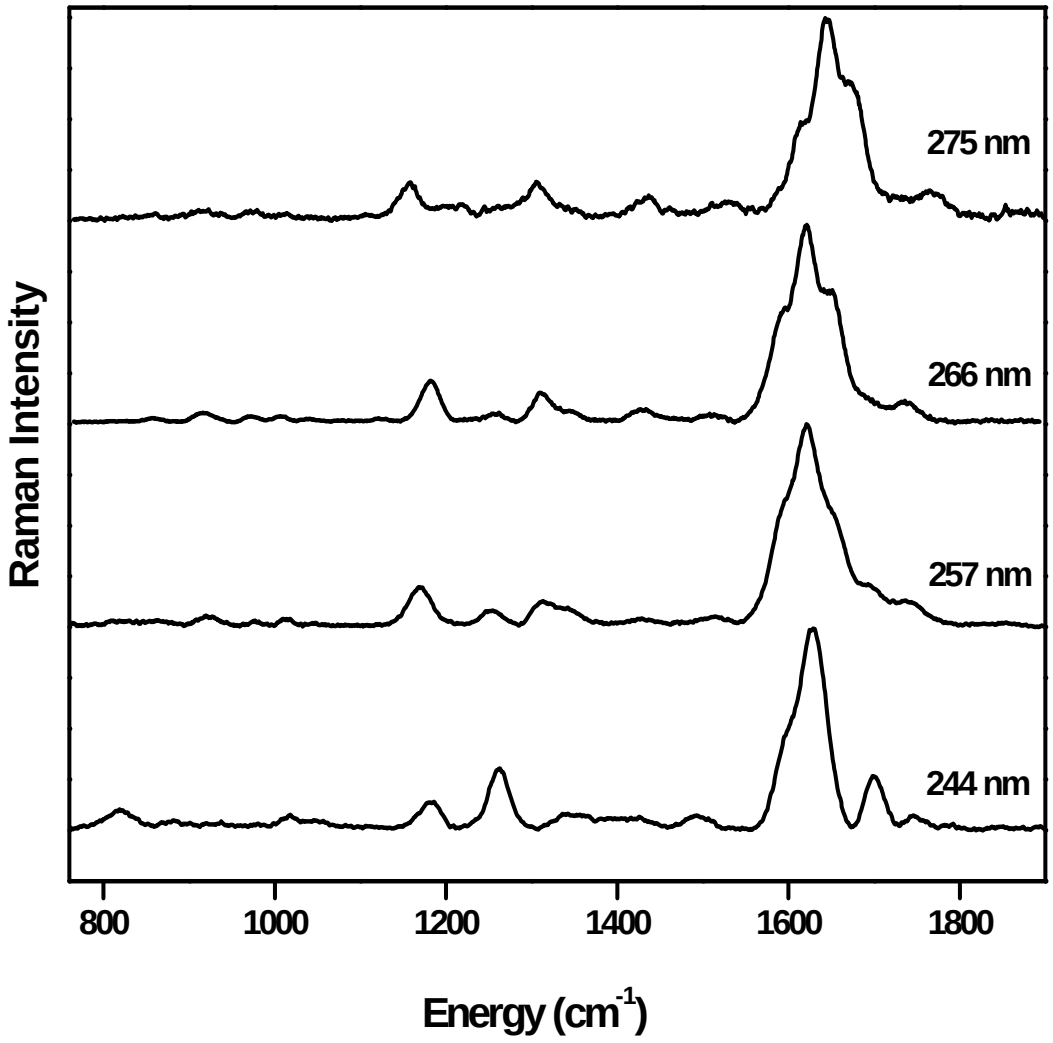

Figure 2.29: UVRR spectra of L-BZ excited at different excitation wavelengths. The composition of this sample and its SPF value are as shown in Table 2.1. Spectra have been scaled to the height of the largest peak in each spectrum and offset along the ordinate for clarity.

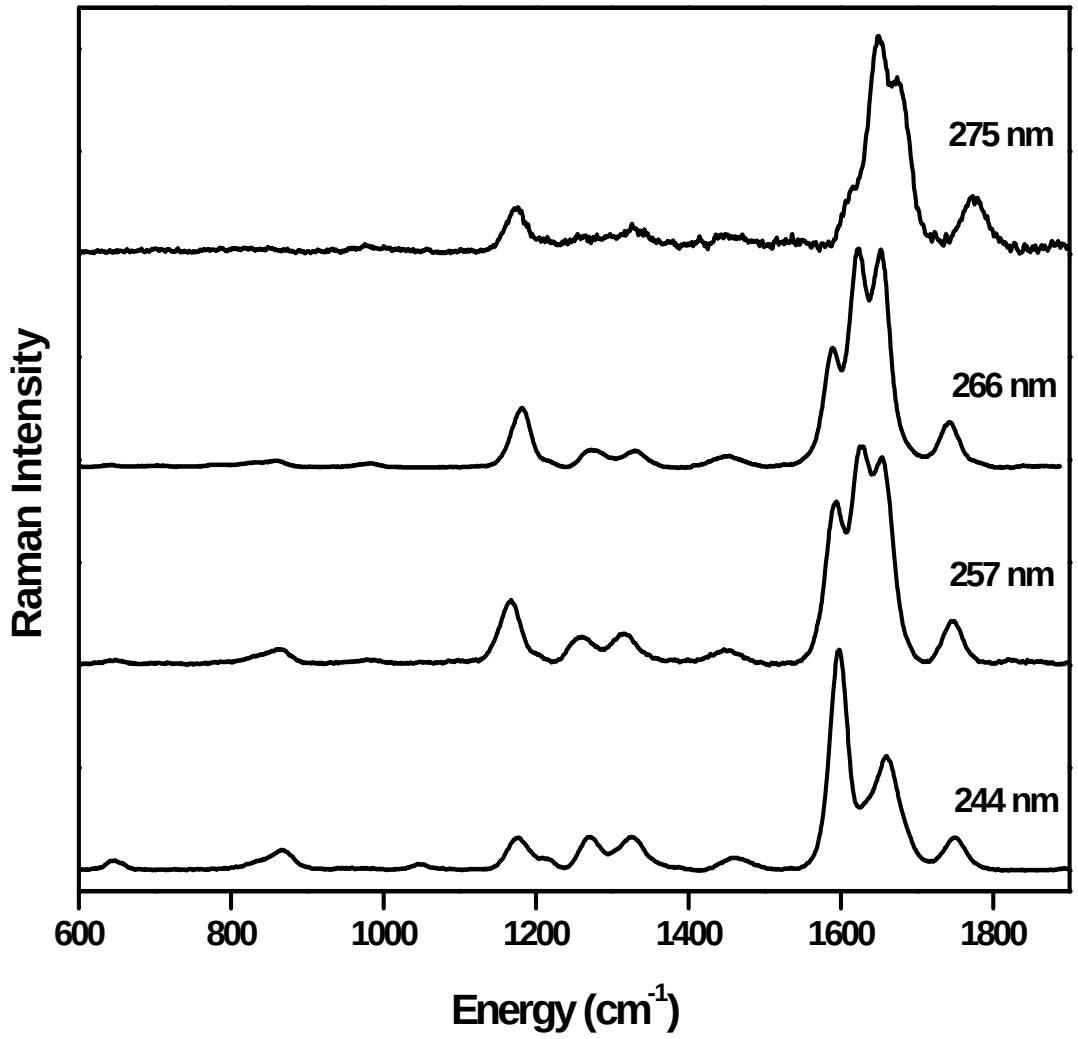

Figure 2.30: UVRR spectra of L-DT excited at different excitation wavelengths. The composition of this sample and its SPF value are as shown in Table 2.1. Spectra have been scaled to the height of the largest peak in each spectrum and offset along the ordinate for clarity.

2.3.6 Limit of detection for OMC

UVRR spectra of a sunscreen formulation L-OB spiked with OMC were acquired to assess the capability of this technique for quantitative analysis of sunscreen AIs in real-world sunscreen samples. This sunscreen product originally contains no OMC (see Table 2.1). This set of experiments was performed following successful quantitation of OMC in methanol solvent (see Table 2.2). The reason for selecting OMC for this set of experiments is because this AI is common to most sunscreen formulations and it has the strongest resonance Raman scattering among the sunscreen AIs considered in this work. The L-OB sunscreen lotion was spiked with different concentrations of OMC to give final formulations containing OMC in the range of 0% w/w – 30% w/w. Three replicate runs were performed on fresh portions of each sample. As shown in Figure 2.31, the intensity of UVRR bands from OMC increases with its concentration in the sunscreen product.

The calibration curve was obtained by dividing OMC band at 1580 cm^{-1} by matrix band at 1620 cm^{-1}. The plot is linear (Figure 2.32) over this concentration range. The regression equation is given by $y = (0.027 \pm 0.002)x + (0.29 \pm 0.03)$, while the R^2 value is 0.99. As shown in Table 2.2, the LOD was found to be 0.23% w/w, which is far less than the typical concentrations of OMC in sunscreen formulations (Table 2.1).[6,8] Although the usual concentration of sunscreen AIs in cosmetics is from 0.1 - 10% w/w,[8] the concentration of the AIs found in actual sunscreen formulations is rarely less than 1%. Thus, this method has the capability of quantifying OMC and other active ingredients in sunscreen formulations. The LOQ was determined to be 0.78% w/w, which also falls below the typical concentrations of OMC found in sunscreen formulations. The dynamic range was found to be about two orders of magnitude. The LOD was determined as $3\sigma_{bl}/m$ and the LOQ was determined as $10\sigma_{bl}/m$, where σ_{bl} is the standard deviation of the baseline noise level in the absence of the AI and m is the slope of the calibration curve. For OMC in methanol, the LOD and LOQ were found to be 0.001% w/w and 0.003% w/w respectively, with a linear dynamic range that spans three orders of magnitude (Table 2.2). Hence, this method has the capability of quantifying

Table 2.2. Comparison of figures of merit of HPLC and UVRRS

Figure of merit	Method			
	HPLC		UVRRS	
	AI in methanol[b]	AI in sunscreen lotion[c]	AI in methanol	AI in sunscreen lotion
Limit of detection (LOD)[d] (10^{-4} / % w/w)	0.038	Not applicable	7.8	2300
Limit of quantitation (LOQ)[c] (10^{-4} / % w/w)	Not stated	Not applicable	26	7800
Linear dynamic range[e]	> 1 order of magnitude	Not applicable	> 3 orders of magnitude	≥ 2 order of magnitude
Sensitivity[f] (% w/w)$^{-1}$	Not stated	Not applicable	6.4	0.027

[a] This comparison is based on the HPLC method of reference 17. [b]The concentration values in reference 17 were converted to % w/w for direct comparison. [c]To the best of our knowledge, HPLC has not been used for direct *in situ* sunscreen analysis. [d]The LOD was determined as $3\sigma_{bl}/m$, LOQ was determined as $10\sigma_{bl}/m$, σ_{bl} is the standard deviation of the baseline noise level and m is the slope of the calibration curve. [e]This is the linear portion of the calibration curve starting from the LOQ. [f]This is taken as the slope of the calibration curve.

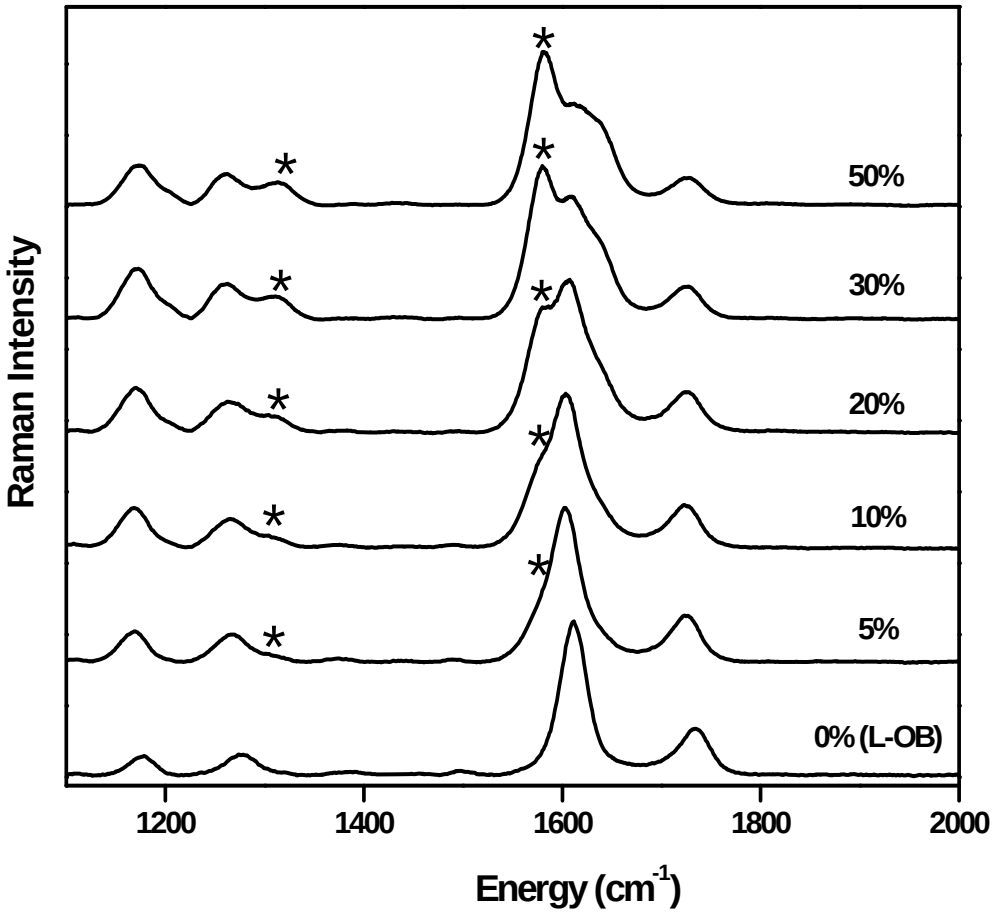

Figure 2.31: UVRR spectra of different concentrations of OMC in a sunscreen formulation L-OB excited at 244 nm. The spectrum of pure (unspiked) L-OB is also shown for comparison. The composition of each sample by weight of OMC is also indicated (in units of % w/w). The bands due to the OMC active ingredient are indicated by asterisks (*). These bands increase as a function of OMC concentration in the sunscreen formulation. Spectra have been scaled to the height of the largest peak in each spectrum and offset along the ordinate for clarity. Data extracted from these and the replicate spectra were used for plotting the calibration curve shown in Figure 2.32.

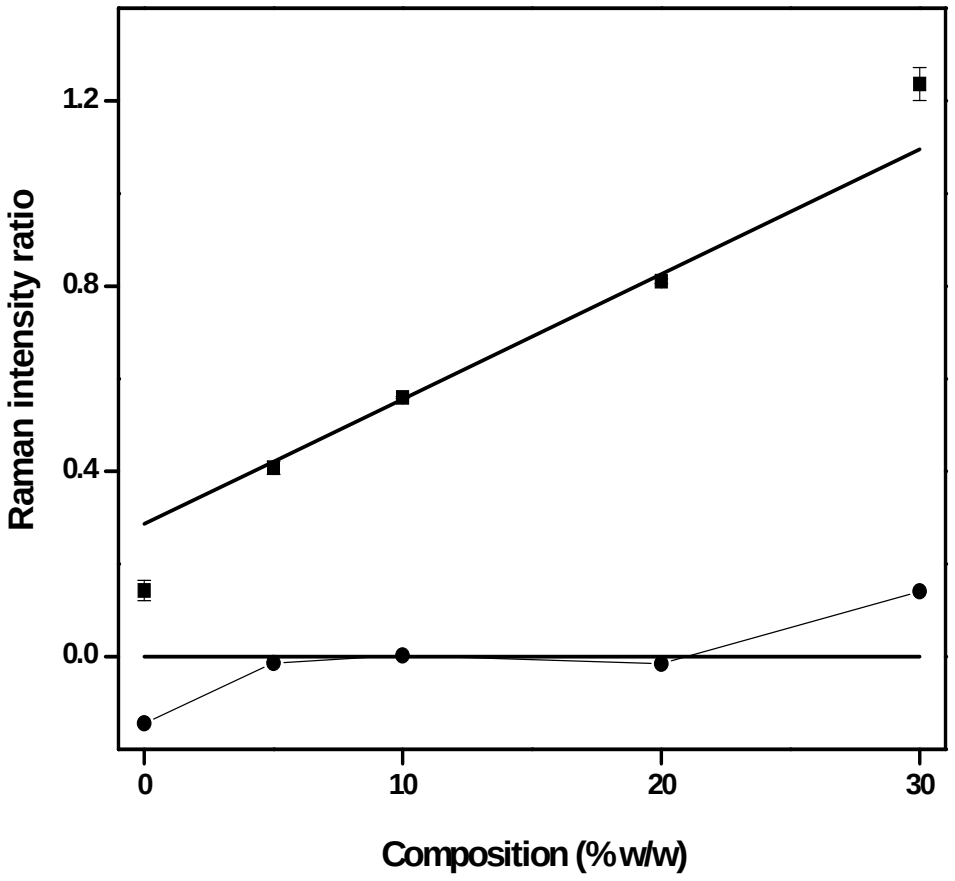

Figure 2.32: Calibration curve for OMC at different concentrations in the sunscreen formulation L-OB. The sunscreen formulation was spiked with different amounts of OMC to determine the LOD for OMC in actual sunscreen matrix. Data points represent the intensity of the highest peak in OMC relative to the neighbouring matrix peak. Each data point is an average of three replicate runs. The error bar representing the standard deviations of each data point is also shown. Data points centred around zero on the y-axis represent the residual plot. The regression equation is given by $y = (0.027 \pm 0.002)x + (0.29 \pm 0.03)$, while the R^2 value is 0.99. Shown below the calibration graph are the residuals, which are centred around zero.

OMC, and possibly other active ingredients in sunscreen formulations.

The differential signal enhancement capability of this technique for different sunscreen AIs at different concentrations, as demonstrated by the fluorescence-free, high signal-to-noise ratio spectra obtained from real sunscreen formulations, makes it suitable for routine sunscreen analysis without prior sample separation and pretreatment. Therefore, analyses can be carried out rapidly and *in situ*, a desirable feature of online quality control. This is in contrast to the HPLC technique which involves rigorous sample pretreatment steps,[9-10,17,28] and which, because of the complex matrix of the sunscreen formulations, is incapable of *in situ* sunscreen analysis as indicated in Table 2.2. In addition, the method being presented here is universal to all real-world sunscreen formulations and so does not require any modifications if a new set of sunscreen formulations are to be analyzed. Conversely, HPLC is less universal in that a set of chromatographic conditions optimal for the analysis of a certain group of AIs, may be unsuitable for another group, thereby leading to unnecessary continuous optimization of conditions as new formulations are made. UVRRS is sensitive enough to determine sunscreen AIs at the levels in which they are present in actual sunscreen formulations and is less time-consuming and less labour-intensive than HPLC. Hence, UVRRS has the capability for direct *in situ* determinations of the AIs in sunscreen formulations.

As shown in Table 2.2, a few of the analytical figures of merit of HPLC are better than UVRRS in the determination of OMC in methanol, but HPLC is incapable of direct *in situ* analysis of sunscreen formulations without prior sample pretreatment. On the other hand, UVRRS has the capability of direct quantitative determination of AIs in sunscreen formulations. Therefore, it is better suited for routine on-line quality control in the sunscreen industry.

Since a tunable picosecond laser was used in this work, one important factor to consider is the potentially higher costs of UVRRS, compared to HPLC. However, cheaper alternative UV laser sources are available, such as doubled argon ion lasers, metal vapour hollow cathode lasers and LED lasers. The overall costs of Raman systems with these cheaper light sources can

compare favourably with the costs of a complete HPLC system including the detector. In addition, the costs associated with sample pretreatments and separations are saved when using UVRRS. Thus, the method is feasible for the direct analysis of sunscreen formulations.

2.4 Conclusions

It has been demonstrated in this chapter that UVRRS has the capability of analyzing sunscreen formulations *in situ* for their constituent AIs. Good-quality, fluorescence-free UV resonance Raman spectra were obtained for all samples. The spectral patterns of all the five AIs are distinct from one another at all the excitation wavelengths used. In the AI mixtures, 244 nm excitation gives the best discrimination between the AIs. With excitation of the sunscreen formulations at 244 nm, the AIs were easily identified with essentially no interference from the sample matrix. In addition, despite the fluorescence of some AIs, good quality and fluorescence-free UV resonance Raman spectra were obtained for all AIs, mixtures and sunscreen formulations. For OMC, LOD and LOQ that were found are far below the typical concentrations of the AI in sunscreen formulations, with a linear calibration curve. These results indicate that UVRRS is unique and unrivalled by HPLC in its capability for direct *in situ* qualitative and quantitative determinations of AIs in real-world sunscreen formulations without prior sample separation or pretreatment. Therefore, this proposed technique combines speed, robustness, wide applicability and flexibility which make it a suitable spectroscopic method for routine online quality control analysis in the sunscreen industry.

2.5 References

(1) Martincigh, B. S.; Allen, J. M.; Allen, K. S. In *Sunscreen Photobiology. Molecular, Cellular and Physiological Aspects;* Gasparro, F. P. Ed., Springer, 1997; pp 11-45.

(2) Urbach, F. *Photochem. Photobiol.* **1989,** *49,* 507-513.

(3) Brown, M. W.; Galley, E. *Cosme. Toiletries* **1990,** *105,* 69-73.

(4) Drobetsky, E. A.; Turcotte, J.; Châteauneuf, A. *Proc. Natl. Acad. Sci. USA* **1995,** *92,* 2350-2354.

(5) Norval, M.; Cullen, A. P.; de Gruijl, F. R.; Longstreth, J.; Takizawa, Y.; Lucas, R. M.; Noonan, F. P.; van der Luen, J. C. *Photochem. Photobiol. Sci.* **2007,** *6,* 232-251.

(6) Lowe, N. J.; Shaath, N. A.; Pathak, M. A. *Sunscreens Development, Evaluation and Regulatory Aspects,* Cosmetic Science and Technology Series; Marcel Dekker: New York, 1997; Vol. 15.

(7) Beyere, L.; Yarasi, S.; Loppnow, G. R. *J. Raman Spectrosc.* **2003,** *34,* 743-750.

(8) Salvador, A.; Chisvert, A. *Anal. Chim. Acta* **2005,** *537,* 1-14.

(9) Salvador, A.; Chisvert, A. *Anal. Chim. Acta* **2005,** *537,* 15-24.

(10) Chisvert, A.; Pascual-Martí, M. C.; Salvador, A. *J. Chromatogr. A* **2001,** *921,* 207-215.

(11) Chisvert, A.; Salvador, A.; Pascual-Martí, M. C. *Anal. Chim. Acta* **2001,** *428,* 183-190.

(12) Imanaka, N.; Masui, T.; Hirai, H.; Adachi, G. *Chem. Mater.* **2003,** *15,* 2289-2291.

(13) Broadbent, J. K.; Martincigh, B. S.; Raynor, M. W.; Salter, L. F.; Moulder, R.; Sjöberg, P.; Markides, K. E. *J. Chromatogr. A* **1996,** *732,* 101-110.

(14) Cheng, J.; Li, Y. S.; Roberts, R. L.; Walker, G. *Talanta* **1997,** *44,* 1807-1813.

(15) Chisvert, A.; Pascual-Martí, M. C.; Salvador, A. *Fresenius J. Anal. Chem.* **2001,** *369,* 638-641.

(16) Rastogi, S. C.; Jensen, G. H. *J. Chromatogr. A* **1998,** 828, 311-316.

(17) Sarveiya, V.; Risk, S.; Benson, H. A. E. *J. Chromatogr. B* **2004,** *803,* 225-231.

(18) Potard, G.; Laugel, C.; Baillet, A.; Schaefer, H.; Marty, J.-P. *Int. J. Pharm.* **1999,** *189,* 249-260.

(19) Gaspar, L. R.; Maia Campos, P. M. B. G. *Int. J. Pharm.* **2006,** 307, 123-128.

(20) Fernandez, C.; Marti-Mestres, G.; Ramos, J.; Maillols, H. *J. Pharm. Biomed. Anal.* **2000,** *24,* 155-165.

(21) Huang, H.-Y.; Chiu, C.-W.; Chen, Y.-C; Yeh, J.-M. *Electrophoresis* **2005,** *26,* 895-902.

(22) Vanquerp, V.; Rodriguez, C.; Coiffard, C.; Coiffard, L. J. M.; De Roeck-Holtzhauer, Y. *J. Chromatogr. A* **1999,** *832,* 273-277.

(23) Balaguer, A.; Salvador, A.; Chisvert, A.; Meliá, M.; Herráez, M.; Díez, O. *Anal. Bioanal. Chem.* **2006,** *385,* 1225-1232.

(24) Westgate, E.; Sherma, J. *J. Liq. Chrom. & Rel. Technol.* **2000,** *23,* 609-615.

(25) Granger, K. L.; Brown, P. R. *J. Liq. Chrom. & Rel. Technol.* **2001,** *24,* 2895-2924.

(26) Chisvert, A.; Izquierdo, J. V.; Salvador, A. *Anal. Bioanal. Chem.* **2002,** *374,* 963-967.

(27) Salvador, A.; Chisvert, A.; Camarasa, A.; Pascual-Martí, M. C.; March, J. G. *Analyst* **2001,** *126,* 1462-1465.

(28) Jiang, R.; Hayden, C. G. J.; Prankerd, R. J.; Roberts, M. S.; Benson, H. A. E. *J. Chromatogr. B* **1996,** *682,* 137-145.

(29) Schmitz-Masse, M.-O.; Herpol-Borremans, M.; Parmentier, F. *Int. J. Cosmet. Sci.* **1979,** *1,* 101-110.

(30) Masse, M. O.; Herpol-Borremans, M. *Int. J. Cosmet. Sci.* **1991,** *13,* 303-315.

(31) Azevedo, J. S.; Viana, N. S.; Soares, C. D. V. *Il Farmaco* **1999,** *54,* 573-578.

(32) Whiteman, D. C.; Brown, R. M.; Xu, C.; Paterson, C. L.; Miller, D.; Parsons, P. G. *J. Photochem. Photobiol. B: Biol.* **2003,** *69,* 59-63.

(33) Masse, M-O.; Herpol-Borremans, M.; Grimee, R.; Gleviczky, S. *Int. J. Cosmet. Sci.* **1982,** *4,* 235-246.

(34) Masse, M.-O.; Delporte, C.; Bervelt, E. *Int. J. Cosmet. Sci.* **2001,** *23,* 259-279.

(35) Narayanan, V. A.; Bello, J. M.; Stokes, D. L.; Vo-Dinh, T. *Analusis* **1991,** *19,* 307-310.

(36) Laserna, J. J.; Berthod, A.; Winefordner, J. D. *Talanta* **1987,** *34,* 745-747.

(37) Berthod, A.; Laserna, J. J.; Winefordner, J. D. *Appl. Spectrosc.* **1987,** *41,* 1137-1141.

(38) Pelletier, M. J. *Analytical Applications of Raman Spectroscopy;* Blackwell Science Ltd.: Oxford, 1999.

(39) Billinghurst, B. E.; Loppnow, G. R. *J. Phys. Chem. A* **2006,** *110,* 2353-2359.

(40) Billinghurst, B. E.; Yeung, R.; Loppnow, G. R. *J. Phys. Chem. A* **2006,** *110,* 6185-6191.

(41) De Orsi, D.; Giannini, G.; Porrà, R.; Berri, S.; Bolasco, A.; Carpani, I.; Tonelli, D. *Chromatographia* **2006**, *64,* 509-515.

(42) McHale, J. L. In *Handbook of Vibrational Spectroscopy;* Chalmers, J. M.; Griffiths, P. R. Eds.; John-Wiley & Sons Ltd.: 2002; Vol. 1, pp 534-556.

(43) Krishnan, R.; Carr, A.; Blair, E.; Nordlund, T. M. *Photochem. Photobiol.* **2004,** *79,* 531-539.

(44) Colthup, N. B.; Daly, L. H.; Wiberley, S. E. In *Introduction to Infrared and Raman Spectroscopy;* Academic Press Inc.: 1990; pp 387-481.

(45) Lee, S.-H.; Tang, K.-C.; Chen, I.-C.; Schmitt, M.; Shaffer, J. P.; Schultz, T.; Underwood, J. G.; Zgierski, M. Z.; Stolow, A. *J. Phys. Chem. A* **2002,** *106,* 8979-8991.

(46) Padma Malar, E. J.; Jug, K. *J. Phys. Chem.* **1984,** *88,* 3508-3516.

(47) Asher, S. A.; Johnson, C. R. *Science* **1984,** *225,* 311-313.

(48) Asher, S. A; In *Handbook of Vibrational Spectroscopy;* Chalmers, J.

M., Griffiths, P. R., Eds., John-Wiley & Sons Ltd.: 2002; Vol. 1, pp 557-571.

Chapter 3

Initial Excited-state Structural Dynamics of a Sunscreen Active Ingredient, Benzophenone-3, from UV Resonance Raman Spectroscopy*

3.1 Introduction

An overexposure of human skin to ultraviolet (UV) radiation may lead to sunburn, premature skin aging and an increased risk of skin cancers.[1-3] The steady increase in the incidence of melanoma, non-melanoma cutaneous neoplasia and preneoplastic disorders has contributed to the demand for more effective protection from the sun.[3] With the increase in incidence of skin cancer, sunscreens have been more strongly recommended in recent years to protect the skin from the harmful effects of UV radiation.[4,5] In order to be effective, sunscreens must absorb UV radiation and dissipate the acquired energy in a manner that does not lead to the destruction of the absorbers themselves (photodegradation), nor to the formation of toxic products.[6] Photodegradation of the sunscreen active ingredients (AIs) may lead to the reduction in the efficacy of the sunscreen product, formation of stable photoproducts or formation of reactive intermediates, such as free radicals. The formation of stable photoproducts and reactive intermediates also are of major concern because they may be toxic.[6] For example, formation of photoadducts between sunscreen AIs and thymine nucleobases have been reported.[7,8] In addition, some sunscreen AIs generate free radicals,[9] and reactive oxygen species, which can produce toxic effects.[6,10-12]

Until recently, the photochemical stabilities of sunscreen AIs and resulting

---

* This work was done in collaboration with Dr. Sarah Schmidtke of Chemistry Department, Wooster College, Ohio, USA. She provided the resonance Raman and absorbance data at 275 nm excitation.

sunscreen formulations were not of interest, due in part to the lack of established standards.[13] However, recent studies of the toxicological implications of sunscreen photochemical instability have started to provide sufficient evidence that sunscreen photostability should be studied further.[13] Consequently, studies are beginning to take place to establish the photostability of common sunscreen AIs.[13] In some of these studies, a sunscreen AI widely used for many years, para-amino benzoic acid (PABA) was clearly shown to have harmful side effects, such as photosensitization, formation of singlet molecular oxygen and subsequent reaction with such reactive species.[6,8-12] Despite these harmful side effects, which have in fact reduced the use of products containing this sunscreen AI, it continues to appear on the list of approved AIs in the US.[8] However, the harmful effects of PABA has been reportedly reduced by zeolite encapsulation.[14] All these reports necessitate further studies into the photostability of other sunscreen AIs.

The fact that sunscreen formulations contain other additives apart from the AIs must also be accounted for in photostability studies.[5] This means that chemical interactions may take place when different sunscreen AIs are mixed together and mixed with other additives. These interactions may be difficult to predict from the individual ingredients, as the chemical interactions in the real sunscreen formulations are complex.[13,15] For example, "destabilization", or loss of optical density in the UV, can occur when two UV absorbers undergo a chemical reaction after absorption of UV radiation. This destabilization may be countered by adding triplet quenchers to the sunscreen formulation to remove reactive intermediates. This is the case with the unexpected photolysis of octyl methoxycinnamate (OMC) in the presence of another AI, avobenzone.[13] A similar photodegradation was observed in Benzophenone-3 (BZ3) in the presence of a physical sunscreen titanium (IV) oxide (TiO_2).[8] For all these reasons, besides assessment of the properties of the single sunscreen AIs, it may be necessary to investigate photostabilities of at least binary AI combinations[5].

BZ3 (Figure 3.1) is one of the more common approved sunscreen active ingredients (AIs) in the US.[16,17] It is a broad-range UVA/UVB filter with absorbance maxima at 288 and 325 nm.[18] It is also one of the few photostable common sunscreen AI and it has been in use for many years.[4,6,8,10,19,20] The 288 nm band in BZ3 corresponds to a $\pi\pi^*$ transition, while the band at 325 nm is the $n\pi^*$ transition.[8] Its reactivity is solvent-dependent, as it was reported to be very stable in acetonitrile, less stable in both n-hexane and water compared to acetonitrile, but unstable in methanol.[8] A number of studies have been conducted on this sunscreen AI, including studies of photostability, solvent interactions and quality control analysis studies.[4,8,16,21,22] It has been found that the photochemical quantum yield and photochemical rate constant of BZ3 are zero.[6,10] However, none of these studies have examined the excited-state structural dynamics of BZ3, or any other common sunscreen AI for that matter. Such studies are important for a detailed understanding of the structural factors responsible for the photochemical stability of BZ3. Such studies will also provide insight on the possible structural changes that take place in the excited state of this molecule, affording an opportunity to determine the structural determinants of the inherent stability of different sunscreen molecules. This can aid in more effective design of sunscreen molecules which are photostable, which do not generate reactive intermediates and which do not form toxic photoproducts.

Resonance Raman spectroscopy is a powerful tool for exploring the excited-state structural dynamics of molecules.[23-29] Tuning the exciting laser wavelength into the absorption band of a given molecule gives rise to resonant enhancement of those vibrational modes coupled to the molecular electronic excitation.[16,24,25] The resonance Raman vibrational band intensity is directly proportional to the slope of the excited-state potential energy surface along that vibrational coordinate – the greater the change in molecular structure along the vibrational coordinate, the more intense the resulting resonance Raman band. Thus, the intensities of the resonance Raman bands reflect the conformational distortion of the molecule along each normal mode upon excitation to an electronic excited state.

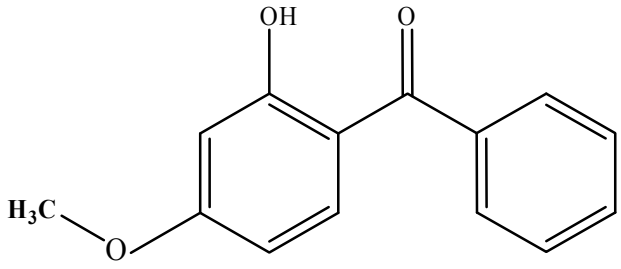

Figure 3.1. Structure of BZ3

In this chapter, we used UV resonance Raman spectroscopy to probe the initial excited-state structural dynamics of methanol solutions of BZ3 within its intense, ππ* absorption band at 288 nm. The results obtained demonstrate the capability of resonance Raman spectroscopy to distinguish the important structural and environmental determinants of excited-state dynamics. The resulting initial excited-state structural dynamics parameters correlate with the structural changes in the molecule, thereby providing a strong molecular basis for its photostability. To our knowledge, this is the first report of the initial excited-state structural dynamics of a sunscreen AI from UV resonance Raman spectroscopy.

3.2 Experimental

3.2.1 Materials and methods

Benzophenone-3 (BZ3) was generously donated by ISP Van Dyk (Belleville, NJ, USA). ACS grade methanol and acetonitrile were obtained from Fisher Scientific (Ottawa, ON, Canada), and Caledon Laboratories Ltd. (Georgetown, ON, Canada), respectively. All solutions were prepared in methanol. Methanol and the BZ3 were used as received without further purification.

The spectrometer and the laser system are the same as those described in Chapter 2. Excitation wavelength of 266, 275 and 290 nm were used here. Typical UV laser powers were 6-14 mW at the sample. The resulting laser beam was spherically focused on an open, wire-guided stream of flowing solution in a 135º backscattering geometry. Cold air was blown onto the sample reservoir to minimize solvent evaporation from the flowing BZ3 solution. Multichannel detection of the resonance Raman scattering was obtained with a piezoelectric-cooled diode array detector (Princeton Instruments, Trenton, NJ, USA) connected to a double-grating spectrometer model 5222 (Spex Industries, Metuchen, NJ, USA) with 3600 g/mm gratings, as described in Chapter 2. Spectral slit widths were 5-7 cm^{-1}. For each

spectrum, the total accumulation time was 15 minutes. All resonance Raman spectra were obtained using 5-15 mM BZ3 containing neat methanol as solvent and internal standard. The collection of the resonance Raman spectra and determination of intensities were repeated three times on each sample of BZ3 at each wavelength. Absorbance spectra were collected before and after each Raman scan with a diode array spectrometer (Hewlett-Packard, model HP 8452A, Sunnyvale, CA, USA). Observed changes in absorbance were due to solvent evaporation and the resulting concentration of BZ3 at each stage was properly corrected for in the data analysis.[30,31] Frequency calibration was performed by measuring the Raman scattering of solvents for which the peak positions are known (cyclohexane, N,N-dimethylformamide, methanol, acetonitrile, chloroform and acetic acid). Wavenumbers are accurate to ±2 cm^{-1}.

3.2.2 Data analysis

Analysis of the data were performed as described previously.[30,32,33] Briefly, the resonance Raman spectra were analyzed by first correcting for the wavelength dependence of the spectrometer efficiency by dividing these spectra by the measured spectrum of a standard lamp (Oriel Corporation, Stanford, CT, USA) and multiplying the resulting spectra by the standard lamp spectral output. The spectral baselines were leveled by subtracting multiple joined line segments from each spectrum. No smoothing was performed on the spectra. Overlapping peaks were separated by fitting regions of the spectra to sums of Gaussian (or Gaussian/Lorentzian) peaks. Possible bleaching of the sample was corrected by measuring the absorbance spectra before and after each scan, and the average absorbance was used in each case to determine the concentration of BZ3.

The differential resonance Raman cross-sections were found from the relative integrated intensities using[30,32-34]

$$\frac{d\sigma_{BZ3}}{d\Omega} = \frac{d\sigma_{MeOH}}{d\Omega} \frac{I_{BZ3}[MeOH]E_{MeOH}}{I_{MeOH}[BZ3]E_{BZ3}} 10^{dC(\varepsilon_{BZ3}-\varepsilon_{MeOH})} \qquad (3.1)$$

where $\frac{d\sigma}{d\Omega}$ is the differential Raman cross-section, I is the resonance Raman intensity, E is the spectrometer efficiency, C is the absorbing species concentration, and ε is the molar extinction coefficient. The subscripts BZ3 and MeOH refer to the BZ3 and MeOH internal standard, respectively, present in solution at concentrations [BZ3] and [MeOH]. The $10^{dC(\varepsilon_{BZ3}-\varepsilon_{MeOH})}$ term represents the correction for the differential self-absorption by the sample and d is the path length for the incident laser power to decrease by half (d = -(log 0.5/$C\varepsilon_{laser}$)), where ε_{laser} is the extinction coefficient at the laser frequency. In this method, relative differential cross-sections for methanol were measured by using known values of the acetonitrile differential cross-sections.[32] Relative intensities of the 918 cm^{-1} acetonitrile line and the 1045 cm^{-1} methanol line were measured by recording Raman spectra of a mixture of 9.58 M acetonitrile and 12.28 M methanol. The methanol intensity ratios were converted to differential cross-sections by using Eq. 3.1. These methanol cross-sections were then fit to the A-term fit expression in Eq. 3.2[32,34,35] using the four methanol cross-sections data points,

$$\frac{d\sigma_R}{d\Omega} = K\upsilon_o\upsilon^3\left[\frac{\upsilon_e^{\,2}+\upsilon_o^{\,2}}{(\upsilon_e^{\,2}-\upsilon_o^{\,2})^2}\right]^2 \qquad (3.2)$$

where $\frac{d\sigma_R}{d\Omega}$ is methanol's differential cross-section, υ_e is the resonant electronic transition energy, υ_0 is the incident photon energy, υ is the scattered photon energy and *K* is a scaling constant. Using this equation and the A-term parameters K = 2.10 x10^{-10}Å^2/(molecule sr), υ_e = 201,000 cm^{-1}, we obtained the differential cross-sections for methanol as 3.14 x 10^{-13}, 7.68 x 10^{-14}, 4.93 x 10^{-14}, and 2.90 x 10^{-14} Å^2/(molecule sr) at 266, 351, 400, and 457.9 nm, respectively. Although the resonant electronic transition energy, υ_e, found for methanol is rather high, it is less than that previously found for acetonitrile.[35] The experimental cross-sections and A-term fit are shown in Figure 3.2.

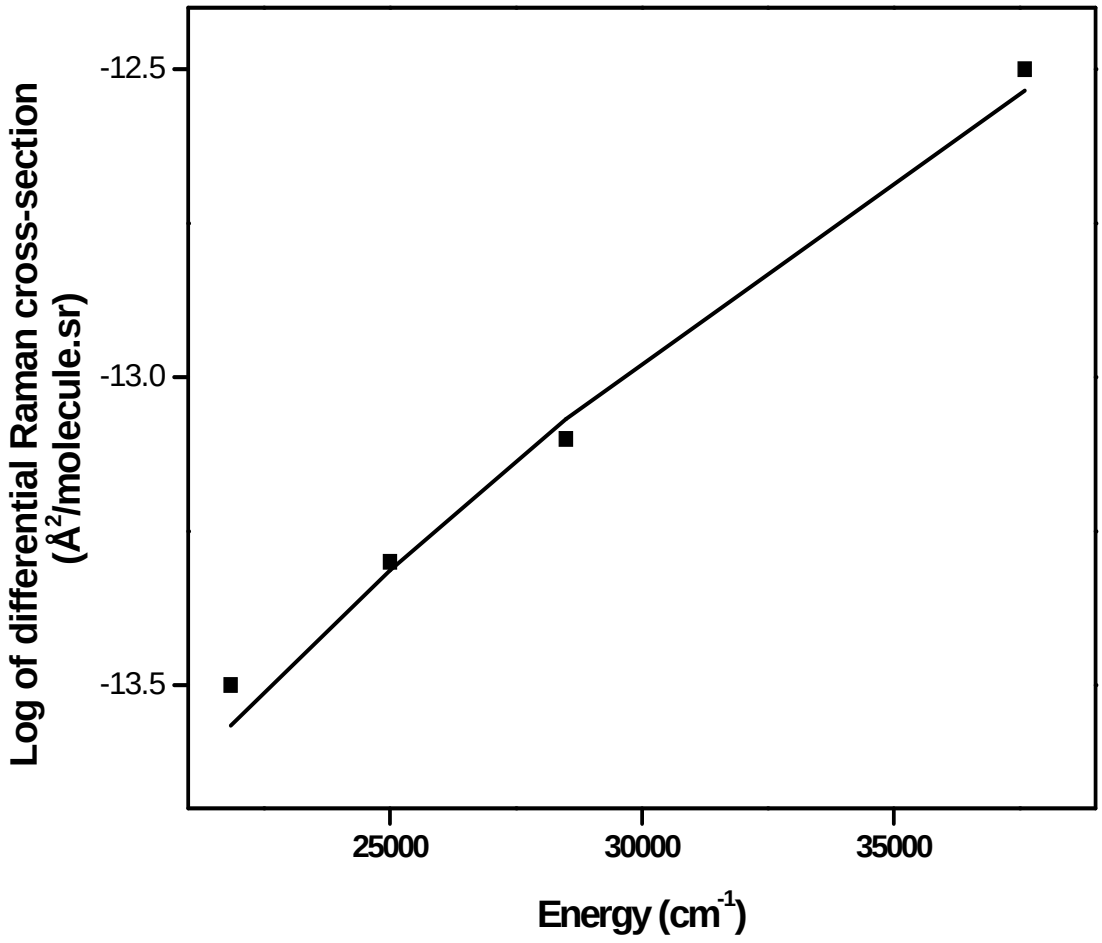

Figure 3.2. A-term fit to the methanol differential cross-sections. The solid line was calculated with Eq. 3.2 using K= 2.10 x10^{-10}Å^2/(molecule sr), υ_e = 201,000 cm^{-1}. The estimated errors are on the order of the point size.

3.2.3 Theory

The resonance Raman excitation profiles were simulated with the time-dependent wave packet formalism expressed by Eqs. 1.8 and 1.10.[26-29] We used initial guesses for the displacements along each normal coordinate (Δ) that were based on the assumption that the average relative resonance Raman intensities are proportional to Δ^2, with the intensity of the 1627 cm^{-1} mode set arbitrarily to 1. We then scaled the relative Δ's to reproduce the experimentally observed absorption and resonance Raman excitation profile bandwidths. All 12 observed fundamental vibrational modes in BZ3 were used in the time-dependent calculations, until the best possible agreement was obtained between the calculated and experimental absorption spectra and resonance Raman excitation profiles.

3.3 Results and Discussion

3.3.1 Resonance Raman spectra

The wavelength-dependent UV resonance Raman spectra of BZ3 are shown in Figure 3.3. Twelve bands (614, 703, 744, 924, 972, 1128, 1179, 1241, 1326, 1367, 1506 and 1627 cm^{-1}) are observed between 600 and 1700 cm^{-1} at 266, 275 and 290 nm. All the 12 bands have been assigned based on the vibrational assignment of Beyere, et al.[21] These assignments are shown in Table 3.1. The UVRR spectra do not exhibit any significant differences in relative intensity as the wavelength is tuned throughout the 288 nm absorption band. This is an indication that we are in resonance with a single electronic transition, despite the proximity of the 290 nm excitation wavelength to the BZ3 S1 state at 325 nm.

BZ3 shows a single intense band at 1627 cm^{-1}, in addition to a number of medium and weak bands at lower energies. The 1627 cm^{-1} band is assigned to the C=O stretch, based on previous assignments.[16,18,19,21] The peak at 1506 cm^{-1} is ascribed to the CH_3 deformation mode. The medium intensity bands from 1367 cm^{-1} and 1241 cm^{-1} are ascribed to C-O stretches, while the band at 1179 cm^{-1} is assigned as a C-O-C bend (Table 3.1). Phenyl ring breathing modes

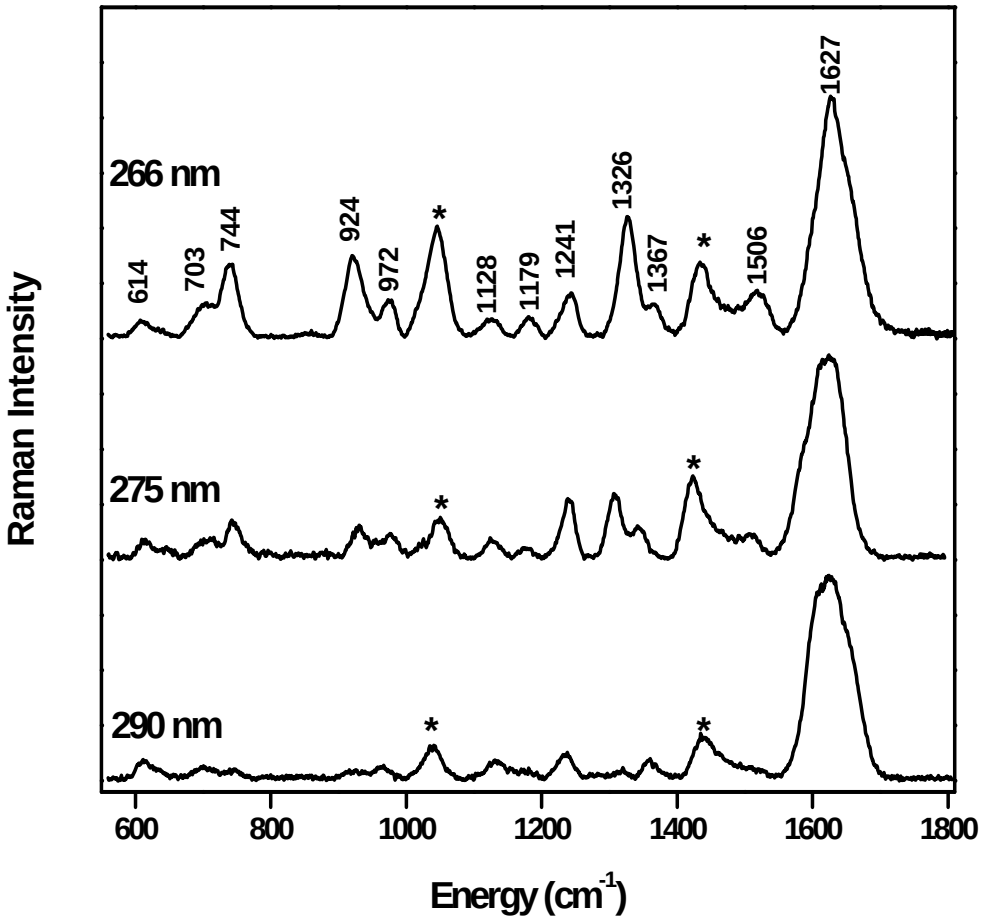

Figure 3.3. Wavelength-dependent UV resonance Raman spectra of 5-15 mM BZ3 in methanol. The asterisks (*) mark the methanol internal standard bands. The spectra have been scaled to the height of the largest peak in each spectrum and offset along the ordinate axis for clarity.

Table 3.1. Resonance Raman frequencies, assignments and harmonic parameters for BZ3.

Mode (cm^{-1})[a]	Mode Assignment[b]	$\|\Delta\|$[c]	E[d]
1627	ν(C=O)	0.63	320
1506	CH_3 def	0.16	19
1367	ν(C-O)	0.14	13
1326	ν(C-O)	0.20	27
1241	ν(C-O)	0.20	25
1179	(C-O-C) be	0.11	7.1
1128	C-H bend	0.16	14
972	Phenyl ring breathing	0.16	12
924	Phenyl ring breathing	0.17	13
744	6-mem. ring def	0.19	13
703	6-mem. ring def	0.22	17
614	Ring tor	0.27	22

[a]Frequencies listed are the experimental frequencies reported here. [b]Abbreviations: ν is stretching, tor is torsion, def deformation and be is bending. Assignments are from ref. 21. [c]Displacements (Δ) are in units of dimensionless normal coordinates and were obtained by fitting Eqs. 1.8 and 1.10 with the following parameters: temperature T = 298 K, Brownian oscillator line shape $\kappa = \lambda/D = 0.1$, Gaussian homogeneous line width Γ_G = 1550 cm^{-1}, inhomogeneous line width θ = 800 cm^{-1}, zero-zero energy E_o = 33550 cm^{-1}, and transition length M = 0.84 Å. The estimated errors in the parameters used in our calculations are as follows: $E_o \pm 1\%$, $M \pm 1\%$, $\Gamma \pm 5\%$, $\Delta \pm 5\%$. [d]E is the reorganization energy, in wavenumbers, calculated using $E = \bar{\upsilon}\Delta^2/2$, where E is the reorganization energy of a particular mode in cm^{-1}, $\bar{\upsilon}$ is the wavenumber of that vibration, and Δ is the excited-state equilibrium geometry displacement in dimensionless normal coordinates.

are represented by the bands at 972 and 924 cm^{-1}, while the bands 744 and 703 cm^{-1} are assigned as six-membered ring deformations. The weak band at 614 cm^{-1} is ascribed to a ring torsion (Table 3.1).

3.3.2 Excitation profiles and absorption spectra

The experimental and simulated absorption spectra of BZ3 are shown in Figure 3.4, while Figures 3.5-3.6 show the experimental and simulated resonance Raman excitation profiles, which are obtained by quantitative measurements of the resonance Raman cross-section of each fundamental vibration as a function of excitation wavelength within the 288 nm absorption band. The simulated absorption spectrum and UV resonance Raman excitation profiles (RREPs) in these figures are modeled with Eqs. 1.8 and 1.10, as well as the parameters in Table 3.1. Figures 3.4 - 3.6 show reasonably good agreement between the experimental and simulated absorption spectra and resonance Raman excitation profiles. The deviations observed between the simulated and experimental absorption spectra in Figure 3.4 below 35,000 cm^{-1} and above 37,000 cm^{-1} are attributed to lower and higher energy electronic transitions, respectively, which are not included in the model used here. Similar deviations have been observed before in the simulated and experimental absorption spectra of other molecules. [23-25] The different relative resonance Raman intensities of the observed vibrational modes in Figure 3.3 are directly reflected in the different experimental Raman differential cross-sections (Figure 3.5) and excited-state geometry displacements (Table 3.1).

3.3.3 Photochemical structural dynamics

To date, there has been no previous report on the initial excited-state structural dynamics of BZ3, nor has there been any on its photochemistry. The only available information on BZ3 are from photostability experiments.[4,8] The absence of photochemistry data on this molecule makes it difficult to interpret the observed structural change on the basis of possible photochemistry. However, because the molecule is photostable,[4,6,8,10,19,20] and has extremely

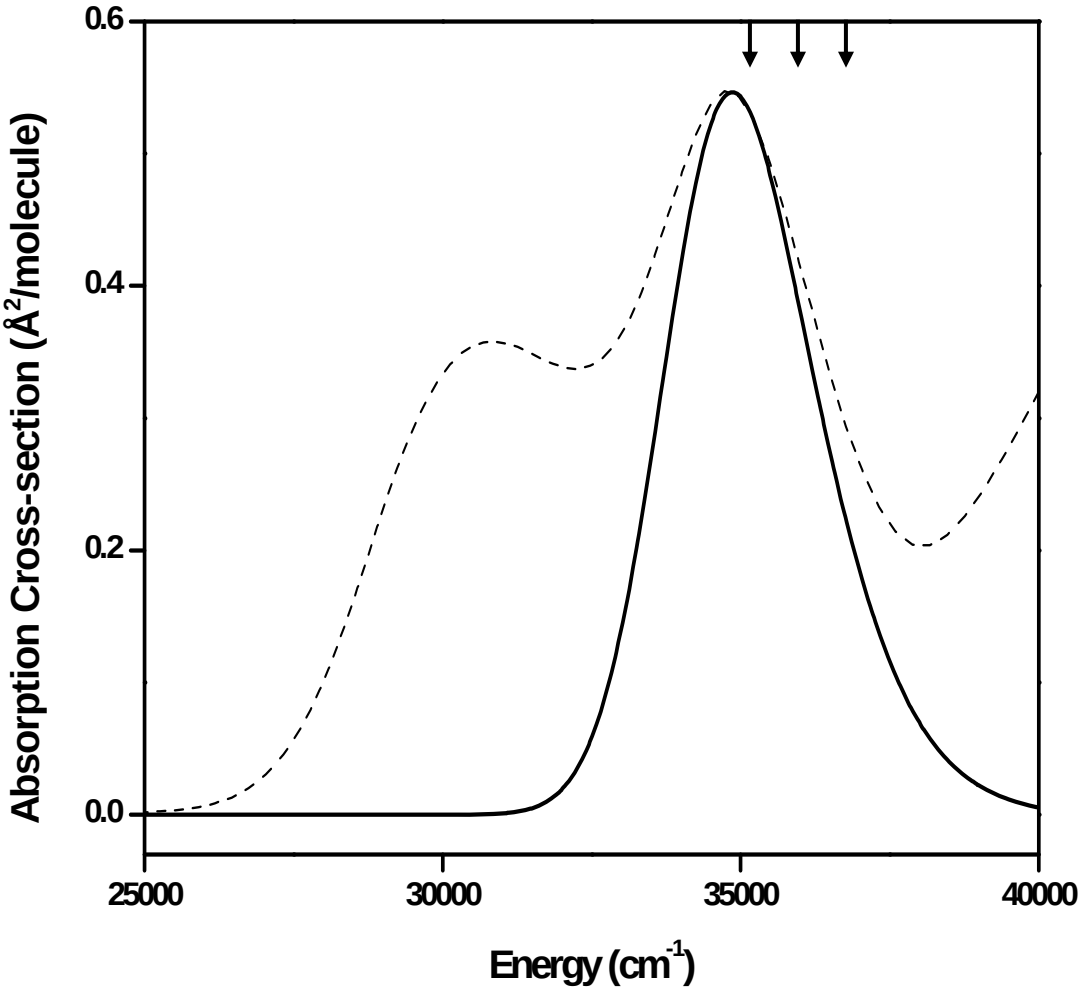

Figure 3.4. Experimental (dotted line) and simulated (solid line) absorption spectra of BZ3 in methanol in the S2 energy state. The simulated absorption spectrum was simulated using Eq. 1.10 with the parameters in Table 3.1. The arrows indicate the UV resonance Raman excitation wavelengths.

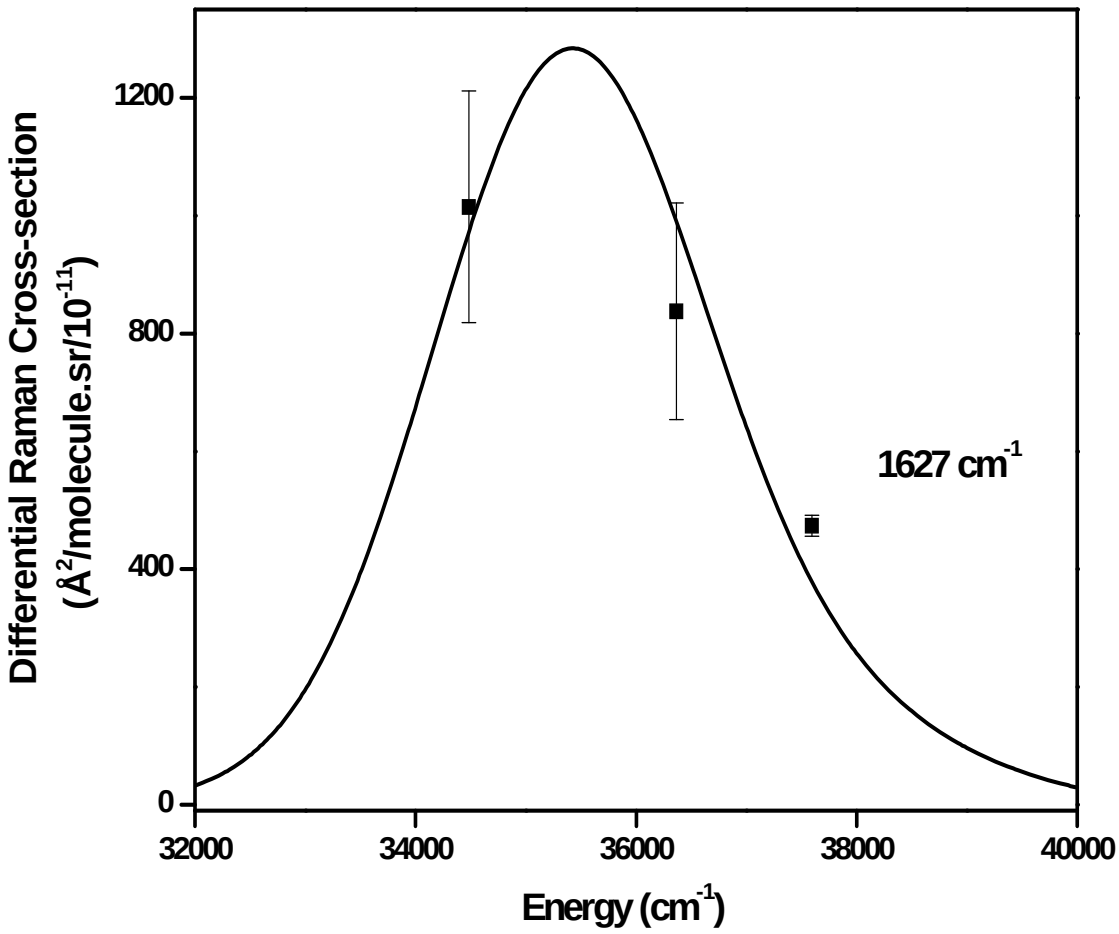

Figure 3.5. Experimental (points) and calculated (solid lines) resonance Raman excitation profile for the 1627 cm^{-1} band. Error bars represent the standard deviations of the data. Note that errors in the differential cross-section data points may range from 0-20%.

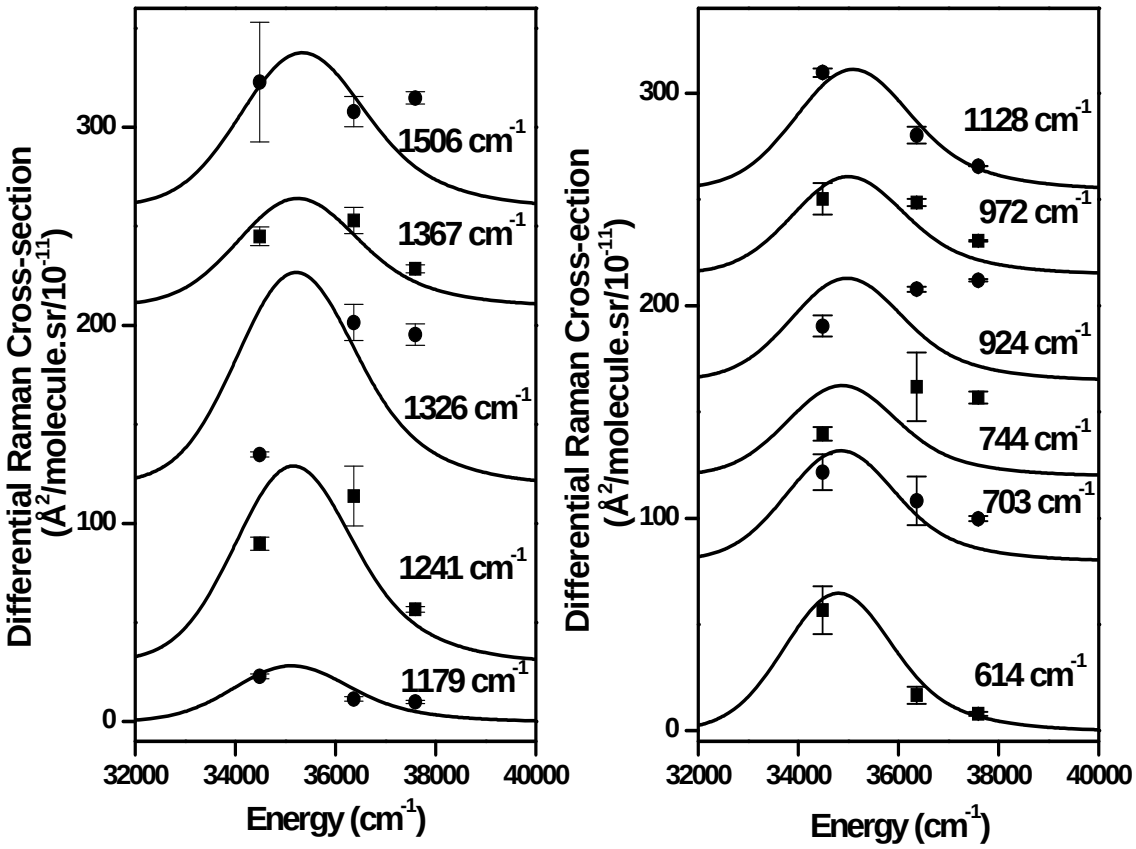

Figure 3.6. Experimental (points) and calculated (solid lines) resonance Raman excitation profiles for all bands except the 1627 cm^{-1} band. The spectra have been offset along the ordinate axis for clarity. Error bars are the standard deviations of the data points and are on the order of the point size unless otherwise shown. Note that errors in the differential cross-section data points may range from 0-20%.

low quantum yields,[6,10] it may be suggested that most of its initial excited-state structural dynamics will lie along dissipative modes.

On the basis of Δ values previously obtained for pyrimidine bases (0.11-0.85),[23-25,36,37] the Δ values obtained here for BZ3 (Table 3.1) are mostly low, suggesting an inherently photostable sunscreen molecule. For example, the total reorganization energy for BZ3 is 502 cm^{-1}, while it is 721, 1442, 1004 and 1384 cm^{-1} for thymine, cytosine, uracil and 5-fluorouracil, respectively. This observation is consistent with previous reports on the photostability of this molecule, compared to other sunscreen AIs.[4,6,8,10,19,20] However, the Δ value is high for the C=O stretch. This observation can be explained considering the methanol solvent in which this molecule is dissolved. This result suggest a significant interaction between the methanol solvent and the BZ3 molecules. This is possible since it has been reported that unlike in many solvents, this sunscreen AI is not photochemically stable in methanol.[4,8] Although it remains to be seen what the impact of different solvents will be on the initial excited-state structural dynamics of BZ3, earlier experiments on solvent interactions with sunscreen AIs indicated Raman intensities are sensitive to hydrogen-bonding and polarizability properties of solvents, thereby reflecting a differential stabilization of sunscreens resonance structures.[21,22] The structural displacement observed for the carbonyl group in this otherwise photostable molecule may be a result of a significant interaction with the methanol solvent. The fact that the carbonyl group also shows the largest Δ value is a strong indication for solvent interaction. This strong interaction may therefore provide a pathway for either the dissipation of the absorbed energy or for facilitating the reactivity of the BZ3 sunscreen.

3.3.4 Excited-state photophysics

Self-consistent analysis of the absorption and resonance Raman excitation profiles with Eqs. 1.8 and 1.10 allows the partitioning of the spectral breadth into homogeneous and inhomogeneous components. These two factors are known to affect the observed absorption and resonance Raman excitation profile differently.[23-25] The inhomogeneous component arises from ensemble

site effects and only broadens the absorption spectrum and resonance Raman excitation profiles, while the homogeneous line width represents solvent-solute coupling, which dampens out the resonance Raman scattering intensity and broadens both. From the footnote of Table 3.1, it can seen that both homogeneous and inhomogeneous line widths used need to be fairly large in order to reproduce both absolute Raman intensities and absorption band shape. The homogeneous line width is fairly consistent with previously reported values for thymine and uracil,[37,38] but higher than for cytosine and 5-fluorouracil (5-FU).[24,25] The inhomogeneous line width is also fairly consistent with the values previously reported for the nucleobases.[24,25,37,38]

In the condensed phase, solvent dynamics may contribute significantly to the breadth of the absorption spectrum, either through homogeneous or inhomogeneous mechanisms.[23-25] These two factors affect the absorption spectrum and the resonance Raman excitation profiles differently. For BZ3, the homogeneous line width must be relatively large to reproduce the experimental absorption spectrum and resonance Raman excitation profiles. To accurately model the magnitude of the resonance Raman cross-sections and the diffuse absorption spectrum, a Gaussian homogeneous line width of 1550 cm^{-1} was required. This large homogeneous line width for BZ3 represents the contributions from solute-solvent coupling. Non-radiative decay processes, primarily internal conversion, are known to be the primary population decay mechanism for nucleobases because of their low quantum yield for fluorescence and photochemistry.[23,24] This fact is thought to be true for BZ3 since a zero quantum yield of photochemistry has been reported.[6,10] Thus, it can be rationalized that internal conversion dominates the excited-state relaxation dynamics of the second excited-state of BZ3.

The inhomogeneous broadening arises because there can be a number of different solvation structures in solution, leading to a distribution of electronic transition energies.[23-25] Inhomogeneous broadening is considered static on the resonance Raman time scale. The inhomogeneous line width used to fit the data for BZ3 is fairly high (800 cm^{-1}) and consistent with the values obtained for the nucleobases already studied.[23-25,36,37] A previous report on the

calculations of the solvated structures of BZ3 interacting with methanol molecules has described the nature of its molecular structure and the solvation complex.[22] According to this study, there is a favourable formation of H-bonds with methanol and negligible BZ3 molecular structural change accompanying the solute-solvent complexation. Because of the interaction between BZ3 and methanol, fluctuation or transitions between different BZ3-methanol complexes can account for the inhomogeneous line width obtained here, when such fluctuations or transitions occur on a slower time scale than the resonance Raman scattering. A stronger interaction is expected for the water-soluble pyrimidines compared to sparingly-soluble BZ3 in methanol, hence the slightly smaller inhomogeneous line width obtained for BZ3 here.

3.4 Conclusions

Self-consistent analysis of the resonance Raman spectra of BZ3 and its absorption spectrum provide insight into the initial excited-state structural dynamics of the molecule. We observed Δ values, which reflect the excited-state structural dynamics, that are small, except for a large Δ value for the carbonyl stretch. This large carbonyl Δ value is ascribed to an interaction with the methanol solvent, which may result in a dissipation of the excitation energy and/or a pathway for reactive facilitation of the BZ3 molecule. Based on these results, we propose that solvent determines whether BZ3 is photochemically stable or not, depending on the pathway of interaction with solvent. The lack of significant structural dynamics along other modes suggest a photochemically stable sunscreen AI. This means that the mostly low Δ values obtained for BZ3 indicate that sunscreen formulations containing BZ3 as an AI may not quickly loose their efficacy following absorption of UV light.

3.5 References

(1) Martincigh, B. S.; Allen, J. M.; Allen, S. K. In *Sunscreens: The Molecules and their Photochemistry;* Gasparro, F. P., Ed.; Sunscreen Photobiology. Molecular, Cellular and Physiological Aspects; Springer-Verlag: New York, 1997; pp 11-45.

(2) Urbach, F. *Photochem. Photobiol.* **1989,** 50, 507-513.

(3) Couteau, C.; Faure, A.; Fortin, J.; Paparis, E.; Coiffard, L. J. M. *J. Pharm. Biomed. Anal.* **2007**, *44*, 270-273.

(4) Tarras-Wahlberg, N.; Stenhagen, G.; Larko, O.; Rosen, A.; Wennberg, A.-M.; Wennerstro O. *J. Invest. Dermatol.* **1999**, *113*, 547-553.

(5) Herzog, B.; Wehrle, M.; Quass, K. *Photochem. Photobiol.* **2009**, *85*, 869-878.

(6) Allen, J. M.; Allen, S. K.; Lingg, B. In *Photostabilities of several chemical compounds used as active ingrediaents in sunscreens;* Albini, A., Fasani, E., Eds.; Drugs: Photochemistry and Photostability; Royal Society of Chemistry: Cambridge, UK, 1998; Vol. 2, pp 171-181.

(7) Shaw, A. A.; Wainschell, L. A.; Shetlar, M. D. *Photochem. Photobiol.* **1992**, *657*, 663.

(8) Serpone, N.; Salinaro, A.; Emeline, A. V.; Horikoshi, S.; Hidaka, H.; Zhao, J. *Photochem. Photobiol. Sci.* **2002**, *1*, 970-981.

(9) Xu, C.; Green, A.; Parisi, A.; Parsons, P. G. *Photochem. Photobiol.* **2001**, *73*, 600-604.

(10) Allen, J. M.; Gossett, C. J.; Allen, S. K. *Chem. Res. Toxic.* **1996**, *9*, 605-609.

(11) Allen, J. M.; Gossett, C. J.; Allen, S. K. *J. Photochem. Photobiol. B: Biol.* **1996**, *32*, 33-37.

(12) Gulston, M.; Knowland, J. *Mutation Res.* **1999**, *444*, 49-60.

(13) Sayre, R. M.; Dowdy, J. C.; Gerwig, A. J.; Shields, W. J.; Lloyd, R. V. *Photochem. Photobiol.* **2005**, *81*, 452-456.

(14) Chretien, M. N.; Migahed, L.; Scaiano, J. C. *Photochem. Photobiol.* **2006**, *82*, 1606-1611.

(15) Maier, H.; Schauberger, G.; Brunnhofer, K.; Honigsmann, H. *J. Invest. Dermatol.* **2001**, *117*, 256-262.

(16) Oladepo, S. A.; Loppnow, G. R. *Anal. Chim. Acta* **2008**, *628*, 57-66.

(17) Oladepo, S. A.; Loppnow, G. R. In *UV resonance Raman spectroscopy as a tool for probing complex samples;* Withnall, R.; Chowdhry, B. Z., Eds.; Proceedings of the 21st international conference on Raman spectroscopy (ICORS); IMPublications: Chichester, UK, 2008; Vol. 21, pp 1028-1029.

(18) Scahllreuter, K.; Wood, J. M.; Farwell, D. W.; Moore, J.; Edwards, H. G. M. *J. Invest. Dermatol.* **1996**, *106*, 583-586.

(19) Rapp, C.; Heinsohn, G.; Hintze, U. *J. Invest. Dermatol.* **1998**, *110*, 97-98.

(20) Roscher, N. M.; Lindemann, M. K. O.; Kong, S. B.; Cho, C. G.; Jiang, P. *J. Photochem. Photobiol. A: Chem.* **1994**, *80*, 417-421.

(21) Beyere, L.; Yarasi, S.; Loppnow, G. R. *J. Raman Spectrosc.* **2003**, *34*, 743-750.

(22) Baughman, B. M.; Stennett, E.; Lipner, R. E.; Rudawsky, A. C.; Schmidtke, S. J. *J. Phys. Chem. A* **2009**, *113*, 8011-8019.

(23) Yarasi, S.; Brost, P.; Loppnow, G. R. *J. Phys. Chem. A.* **2007**, *111*, 5130-5135.

(24) Billinghurst, B. E.; Loppnow, G. R. *J. Phys. Chem. A* **2006**, *110*, 2353-2359.

(25) Billinghurst, B. E.; Yeung, R.; Loppnow, G. R. *J. Phys. Chem. A* **2006**, *110*, 6185-6191.

(26) Myers, A. B.; Mathies, R. A. In *Resonance Raman spectra of polyenes and aromatics;* Spiro, T. G., Ed.; Biological Applications of Raman Spectroscopy; Wiley-Interscience: New York, 1987; Vol. 2, pp 1-58.

(27) Myers, A. B. In *Excited electronic state properties from ground-state resonance Raman intensities;* Myers, A. B., Rizzo, T. R., Eds.;

Laser Techniques in Chemistry; Wiley: New York, 1995; pp 325-384.

(28) Kelley, A. M. *J. Phys. Chem. A* **1999**, *103*, 6891-6903.

(29) Lee, S.-Y.; Heller, E. J. *J. Chem. Phys.* **1979**, *71*, 4777-4788.

(30) Webb, M. A.; Kwong, C. M.; Loppnow, G. R. *J. Phys. Chem. B* **1997**, *101*, 5062-5069.

(31) Fraga, E.; Loppnow, G. R. *J. Phys. Chem. B* **1998**, *102*, 7659-7665.

(32) Fraga, E.; Webb, M. A.; Loppnow, G. R. *J. Phys. Chem.* **1996**, *100*, 3278-3287.

(33) Loppnow, G. R.; Fraga, E. *J. Am. Chem. Soc.* **1997**, *119*, 896-905.

(34) Loppnow, G. R.; Mathies, R. A. *Biophys. J.* **1988**, *54*, 35-43.

(35) Dudik, J. M.; Johnson, C. R.; Asher, S. A. *J. Chem. Phys.* **1985**, *82*, 1732-1740.

(36) Loppnow, G. R.; Billinghurst, B. E.; Oladepo, S. A. In *Excited-state Structural Dynamics of Nucleic Acids and Their Components;* Shukla, M. K. Leszczynski, J., Eds.; Radiation Induced Molecular Phenomena in Nucleic Acids. A Comprehensive Theoretical and Experimental Analysis Series: Challenges and Advances in Computational Chemistry and Physics; Springer: Netherlands, 2008; Vol. 5, pp 237-263.

(37) Yarasi, S.; Ng, S.; Loppnow, G. R. *J. Phys. Chem. B* **2009**, *113*, 14336-14342.

(38) Ng, S.; Yarasi, S.; Brost, P.; Loppnow, G. R. *J. Phys. Chem. A* **2008**, *112*, 10436-10437.

Chapter 4

Initial Excited-state Structural Dynamics of 9-Methyladenine from UV Resonance Raman Spectroscopy

4.1 Introduction

Generally, DNA is considered to have intrinsic stability towards harmful UV radiation.[1-5] This stability is believed to be one means by which nature preserves the genetic code from photochemical damage.[3,4,6] The UV photostability of DNA is generally determined by the excited-state relaxation processes occurring in its nucleobases, which are believed to involve primarily non-radiative decay back to the electronic ground state.[1,2,6] In contrast to the pyrimidine nucleobases, the purine nucleobases are more photostable,[7,8] due to the ultrafast electronic relaxation of their excited-states.[2-4] When compared to the pyrimidines, the few number of reports on the excited-state dynamics of purines,[8-10] is probably due to lack of photoreactivity of the purines.

However, there have been some previous work that explored the electronic excited-state dynamics of guanine (G) and adenine (A) nucleobases.[1,4,11-17] A number of these reports have attempted to elucidate the underlying factors responsible for the observed ultrafast relaxation mechanism of A and its analogs.[1-4,14,16,18] For instance, femtosecond time-resolved photoelectron spectroscopy has shown that A and 9-MeA (Figure 4.1) show almost identical time scales for the processes involved in the deactivation of their electronic excited-states,[3] although the decay pathways for these two molecules appear to be quite different.[2,3] These reports[2,3] and others[1,14,16] identified the presence of an N9-H dissociative $\pi\sigma^*$ state in A, which does not appear to play any role in the relaxation of 9-MeA, in addition to the $\pi\pi^*$ and $n\pi^*$ states that are present in both molecules. The significance of the N9 position, the position at

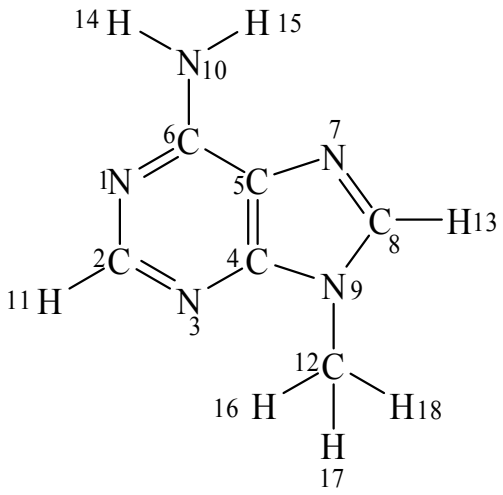

Figure 4.1. The structure of 9-MeA with the numbering scheme. This structure may be compared with that of adenine shown in Figure 1.4.

which the nucleobases attach to the sugar, and the fact that the πσ* state is absent in 9-MeA suggests that the photochemistry of these two molecules may be different. While all these reports have increased our understanding of the molecular mechanisms for the fast relaxation of the electronic excited-state in A, few have focused on the electronic dynamics of 9-MeA.[2,3] In addition, none of these studies explored the excited-state structural dynamics of either A or 9-MeA. Subpicosecond transient absorption experiments have estimated the excited-state lifetime of A, adenosine (Ade) and adenosine monophosphate (AMP) to be about 2 ps;[19] the lifetime for 9-MeA could be longer, due to the absence of the πσ* state decay channel.[3,20] This value however represents only the electronic relaxation, giving little insight into the structural changes that take place in the photochemically-active excited-state. Thus, a probe of the initial excited-state structural dynamics of 9-MeA is crucial for understanding the possible molecular distortions that take place, which may be important in its photochemistry.

The capability of resonance Raman spectroscopy for exploring the excited-state structural dynamics of molecules and the resulting resonance enhancement of vibrational modes coupled to the molecular electronic excitation have been stated in Chapter 3.[21-28] There have been previous resonance Raman studies on several deoxyribonucleotides[29-33] as well as 9-MeA,[33,34] but there appears to be no previous report on the initial excited-state structural dynamics of 9-MeA from resonance Raman spectroscopy, though other nucleobases and analogues have been previously studied.[8] Such information is needed to obtain a complete picture of the dynamics of this molecule in the excited-state. Exploration of the excited-state structural dynamics of 9-MeA will reveal details of molecular distortion that takes place in the nucleobase directly upon photoexcitation, and yield insight into the photoreaction which takes place. In adenine deoxyribodinucleotide dApdA (Figure 4.2), the primary event in the photodimerization of A involves cycloaddition of the N7/C8 double bond of the 5'-A with the C6/C5 single bond of the 3'-A.[35] Two distinct photoproducts of A have been reported upon the formation of the unstable A photodimer, the A=A and AA* photoproducts

(Figure 4.2).[7,35-37] The A molecule blocked at the N9 position by a methyl group provides a good model for DNA, and many of the characteristic vibrations in 9-MeA differ little from those of the corresponding nucleosides and nucleotides.[33,38,39] Thus, a thorough understanding of the excited-state structural dynamics of 9-MeA should lead to a good understanding of the photochemistry of DNA.

In this work, we determine the initial excited-state structural dynamics of 9-MeA from its UV resonance Raman spectra, within the intense, longest-wavelength absorption band at 262 nm. The results obtained demonstrate the capability of resonance Raman spectroscopy to distinguish the important structural and environmental determinants of excited-state dynamics. The results give the initial excited-state structural dynamics, which correlate with the expected photochemical structural changes in the molecule, thereby providing a strong molecular basis for its photoreaction.

4.2 Experimental

4.2.1 Materials and methods

9-Methyl adenine (6-amino-9-methylpurine, 97%) (Sigma, Oakville, Ontario, Canada) and sodium nitrate (99%, EM Science, Darmstadt, Germany) were used without further purification. All samples were prepared using nanopure water from a Barnstead (Boston, MA, USA) water filtration system.

The laser system, the harmonic generation system, sample flow, Raman scattering collection geometry, as well as the spectrometer used in this work re as described previously (Chapter 3). However, typical UV laser powers were 6-14 mW at the sample and 244, 257, 266, 275 and 290 nm excitation wavelengths were used here. For each spectrum, the total accumulation time was 15 minutes. All resonance Raman spectra were obtained using 0.6-0.9 mM 9-MeA containing 0.067 M sodium nitrate as internal standard. The addition of sodium nitrate as an intensity internal standard did not have any

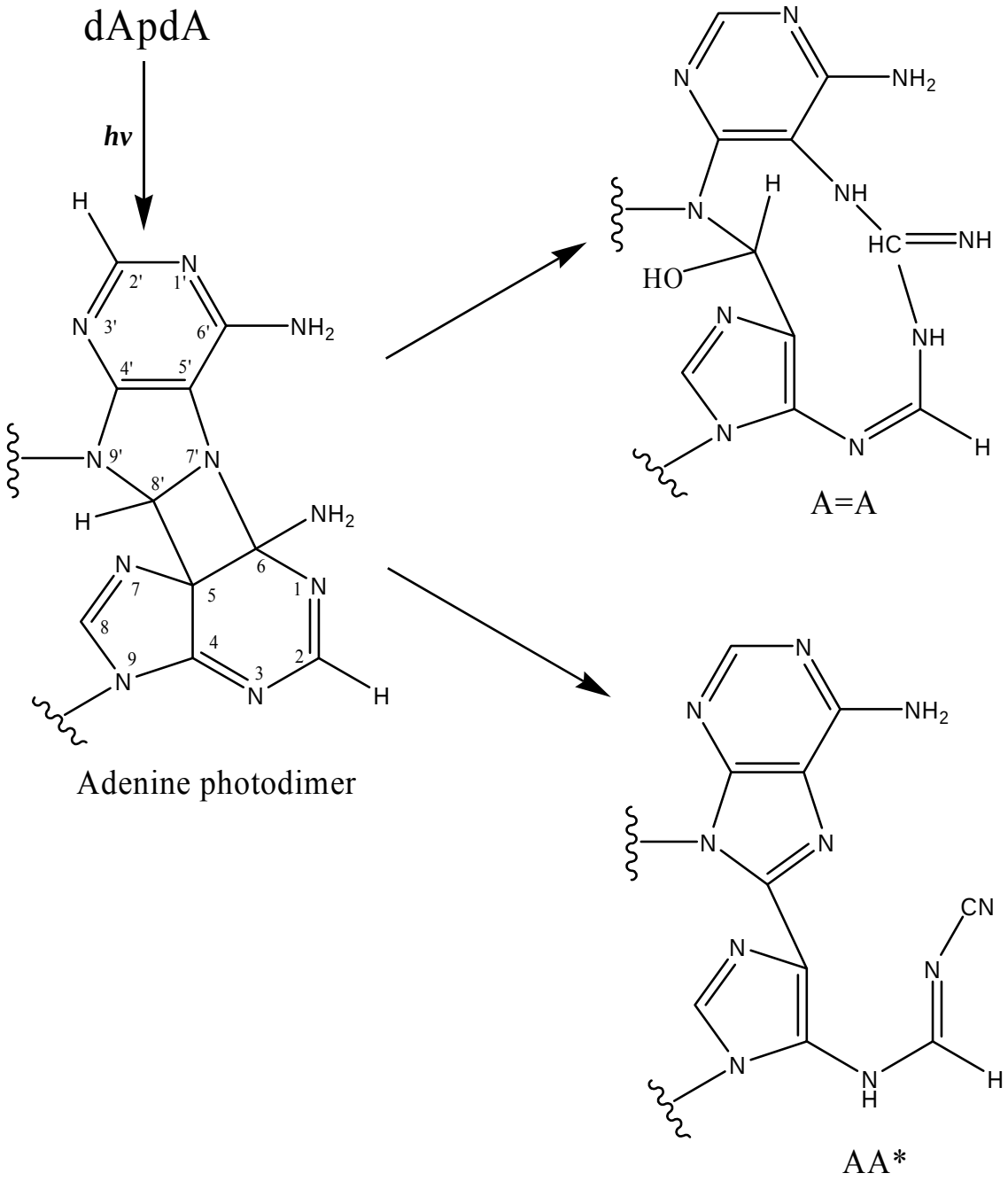

Figure 4.2. The formation of adenine photodimer from adenine deoxyribodinucleotide. The fate of the unstable photodimer is also shown.

noticeable effect on the resonance Raman spectra of 9-MeA. The collection of the resonance Raman spectra and determination of intensities were repeated three times on a fresh sample of 9-MeA at each wavelength. Absorbance spectra were collected before and after each Raman scan with a diode array spectrometer (Hewlett-Packard, model HP 8452A, Sunnyvale, CA). No significant change in absorbance was observed, suggesting that the bulk photoalteration parameter is below 5%.[40,41] Frequency calibration was performed by measuring the Raman scattering of solvents for which the peak positions are known (cyclohexane, N,N-dimethylformamide, methanol, acetonitrile, dimethyl sulfoxide and acetic acid). Wavenumbers are accurate to ±2 cm^{-1}.

4.2.2 Data analysis

Analysis of the data were performed as described previously.[40,42,43] Briefly, the resonance Raman spectra were analyzed by subtracting a water background from all spectra. The resulting spectra were then corrected for the wavelength dependence of the spectrometer efficiency as stated in Chapter 3. The spectral baselines were leveled by subtracting multiple joined line segments from each spectrum. No smoothing was performed on the spectra. Overlapping peaks were separated by fitting regions of the spectra to sums of Gaussian (or Gaussian/Lorentzian) peaks. Possible bleaching of the sample was corrected by measuring the absorbance at 262 nm before and after each scan, and the average absorbance was used in each case to determine the concentration of 9-MeA.

The differential resonance Raman cross-sections, $\frac{d\sigma}{d\Omega}$ were found from the relative integrated intensities using[40,42-44]

$$\frac{d\sigma_{9-MeA}}{d\Omega} = \frac{d\sigma_{NO_3^-}}{d\Omega} \frac{I_{9-MeA}[NO_3^-]E_{NO_3^-}}{I_{NO_3^-}[9-MeA]E_{9-MeA}} 10^{dC(\varepsilon_{nuc}-\varepsilon_{ustd})} \qquad (4.1)$$

where I is the resonance Raman intensity, E is the spectrometer efficiency, d is the Raman sample pathlength, C is the absorbing species concentration, and ε is the molar extinction coefficient. The subscripts "nuc" and "std$^-$" refer to the 9-MeA and NO_3^- internal standard, respectively, present in solution at concentrations [9-MeA] and [NO_3^-]. The $10^{dC(\varepsilon_{nuc}-\varepsilon_{std})}$ term represents the correction for the differential self-absorption by the sample and d is the path length for the incident laser power to decrease by half ($d = -(\log 0.5/C\varepsilon_{laser})$), where $\varepsilon_{nuc}, \varepsilon_{std}$ and ε_{laser} are the extinction coefficients at the nucleobase, internal standard and laser energies, respectively. In this method, a nitrate internal standard is used whose cross-section was measured using the A-term fit[42,44,45] of Eq. 3.2. We obtained the experimental differential cross-sections for nitrate internal standard as 5.50 x 10^{-11}, 2.43 x 10^{-11}, 1.53 x 10^{-11}, 1.02 x 10^{-11}, and 0.579 x 10^{-11} Å^2/(molecule sr) at 244, 257, 266, 275, and 290 nm, respectively.

4.2.3 Theory

The resonance Raman excitation profiles were simulated with the time-dependent wave packet formalism expressed by Eqs. 1.8 and 1.10.[24-27] However, in this case, we used initial guesses for the Δ by arbitrarily setting the intensity of the 1343 cm^{-1} mode to 1. We then scaled the relative Δ's to reproduce the experimentally observed absorption and resonance Raman excitation profile bandwidths. All 12 observed fundamental vibrational modes in 9-MeA were used in the time-dependent calculations. The parameters were then iteratively optimized as previously described[46] until the best possible agreement was obtained between the calculated and experimental absorption spectra and resonance Raman excitation profiles.

4.3 Results and Discussion

4.3.1 Resonance Raman and absorption spectra

The wavelength-dependent UV resonance Raman spectra of 9-MeA are shown in Figure 4.3. Twelve bands (535, 601, 728, 1010, 1208, 1254, 1343, 1437, 1498, 1537, 1603 and 1680 cm^{-1}) are observed between 500 and 1700 cm^{-1} at 257, 266 and 275 nm, while eleven bands (all but the 1010 cm^{-1} band) are observed at 244 and 290 nm. All of these bands have been previously assigned.[34,39,47-50] The absence of the weak 1010 cm^{-1} band at the latter two wavelengths may be due to lack of enhancement of this vibrational mode, as a result of lower absorption of the molecule at these wavelengths (Figure 4.4) or due to overlap with the nitrate band at 1040 cm^{-1}. The twelve bands have been assigned based primarily on the vibrational assignments of Xue, et al., derived from DFT calculations at B3LYP level of theory using 6-31G* basis set.[47] These assignments are shown in Table 4.1.

The UVRR spectra exhibit subtle differences in intensity at 275 – 290 nm for the 1498 and 1537 cm^{-1} bands, but there are no frequency shifts in any of the bands at any excitation wavelength. This is an indication that we are in resonance with a single electronic transition. 9-MeA exhibits a single intense band at 1343 which is assigned to the $C_8N_9/C_5N_7/C_4C_5$ stretches (Table 4.1). This band is close to a similarly-assigned band found at 1340 cm^{-1} for adenine.[51] There is a number of medium intensity bands found at 1208, 1254, 1437, 1498, 1537 and 1603 cm^{-1}, while weak bands in 9-MeA occur at 535, 601, 728, 1010, and 1680 cm^{-1}.

4.3.2 Excitation profiles

The experimental and simulated absorption spectra of 9-MeA are shown in Figure 4.4. Figure 4.5 shows the experimental and simulated resonance Raman excitation profiles, which are obtained by quantitative measurements of the resonance Raman cross-section of each fundamental vibration as a function of excitation wavelength within the absorption band. The UV resonance Raman excitation profiles (RREPs) and simulated absorption

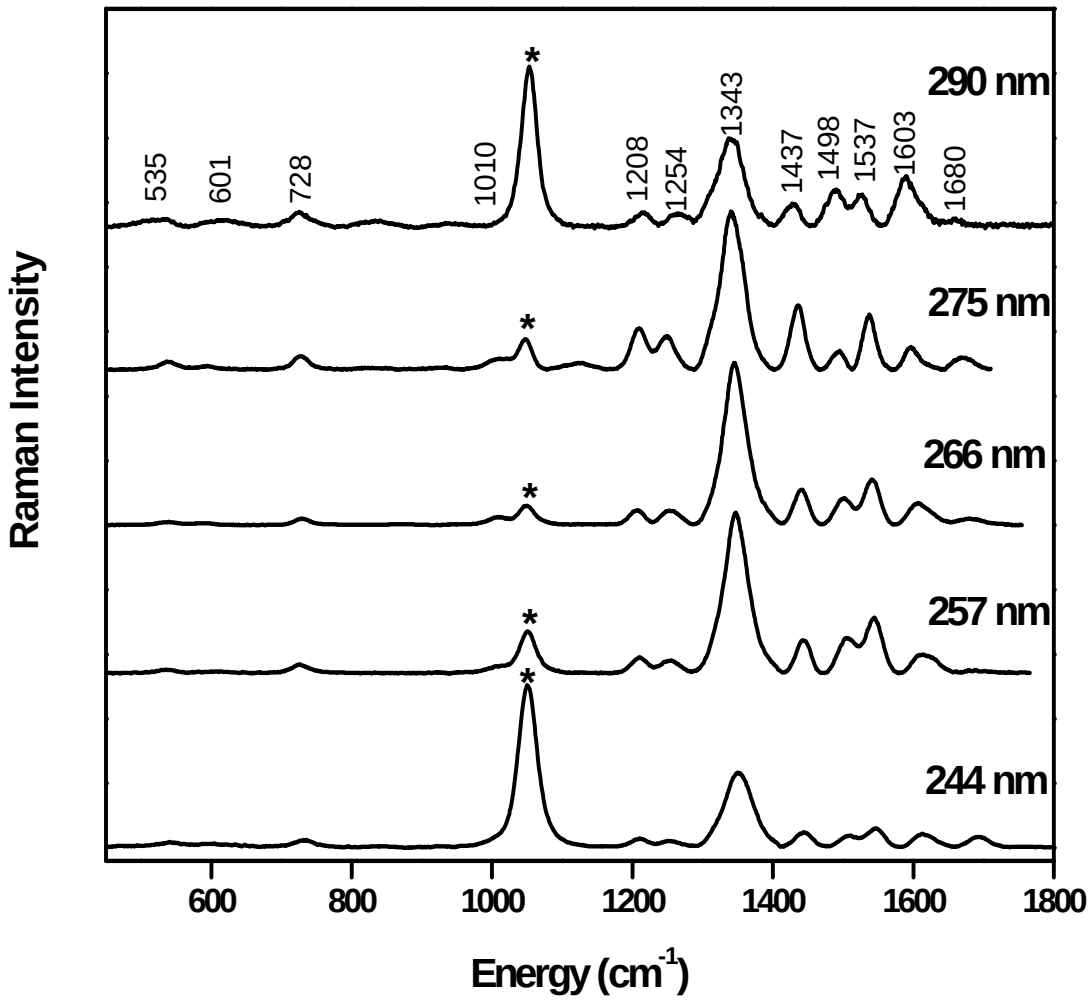

Figure 4.3. Wavelength-dependent UV resonance Raman spectra of 0.7 mM 9-MeA. The asterisks (*) mark the sodium nitrate internal standard band. The spectra have been scaled to the height of the largest peak in each spectrum and offset along the ordinate axis for clarity.

Table 4.1. Resonance Raman Frequencies, Assignments and Harmonic Parameters for 9-MeA.

Mode (cm^{-1})[a]	Mode assignment and PED%[b]	$\|\Delta\|$[c]	E[d]
1680	$\delta(NH_2)$ [91]	0.07	4.12
1603	exocyclic NH_2 be [53], $\nu(C_6N_{10})$ [25], ν (C_5C_6) [14]	0.11	9.70
1537	**$\nu(C_4C_5)$ [25], exocyclic NH_2 be [25], $\nu(N_3C_4)$ [21]**	**0.14**	**15.1**
1498	CH_3 bend [79]	0.12	10.8
1437	**CH_3 be [84], $\nu(N_7C_8)$ [14]**	**0.14**	**14.1**
1343	**$\nu(C_8N_9)$ [22], $\nu(C_5N_7)$ [21], $\nu(C_4C_5)$ [16]**	**0.35**	**82.3**
1254	exocyclic NH_2 be [20], $\nu(N_9C_{12})$ [12], pyrimidine ring be [11]	0.115	8.30
1208	indole ring be [33], $\nu(N_7C_8)$ [14]	0.12	8.70
1010	Bicyclic ring def [31], CH_3 be [20]	0.09	4.09
728	6-mem. Ring def [26], $\nu(N_9C_{12})$ [24], bicyclic ring def [15]	0.115	4.81
601	Ring tor [100]	0.08	1.92
535	6-mem. Ring tor [43], bicyclic ring τ [20]	0.12	3.85

Photochemically-relevant modes are in bold. [a]Frequencies listed are the experimental frequencies reported here. [b]Abbreviations: ν is stretching, δ is scissoring, def. is deformation, τ is torsion and be is bending. Assignments are from ref. 47. Numbers in square parentheses represent the percentage potential energy distribution (PED) of the listed internal coordinate(s) to the normal mode. Only the internal coordinates with percentage contribution greater than 10% are listed. [c]Displacements (Δ) are in units of dimensionless normal coordinates and were obtained by fitting Eqs. 1.8 and 1.10 of Chapter 1 with the following parameters: temperature T = 298 K, Brownian oscillator line shape $\kappa = \Lambda/D = 0.1$, Gaussian homogeneous line width $\Gamma_G = 1200$ cm^{-1}, inhomogeneous line width $\theta = 1000$ cm^{-1}, zero-zero energy $E_o = 37200$ cm^{-1}, and transition length M = 0.87 Å. The estimated errors in the parameters used in our calculations are as follows: $E_o \pm 1\%$, $M \pm 1\%$, $\Gamma \pm 5\%$, $\Delta \pm 5\%$. [d]E is the reorganization energy, in wavenumbers, calculated using $E = \bar{\upsilon}\Delta^2/2$, where E is the reorganization energy of a particular mode in cm^{-1}, $\bar{\upsilon}$ is the wavenumber of that vibration, and Δ is the excited-state equilibrium geometry displacement in dimensionless normal coordinates.

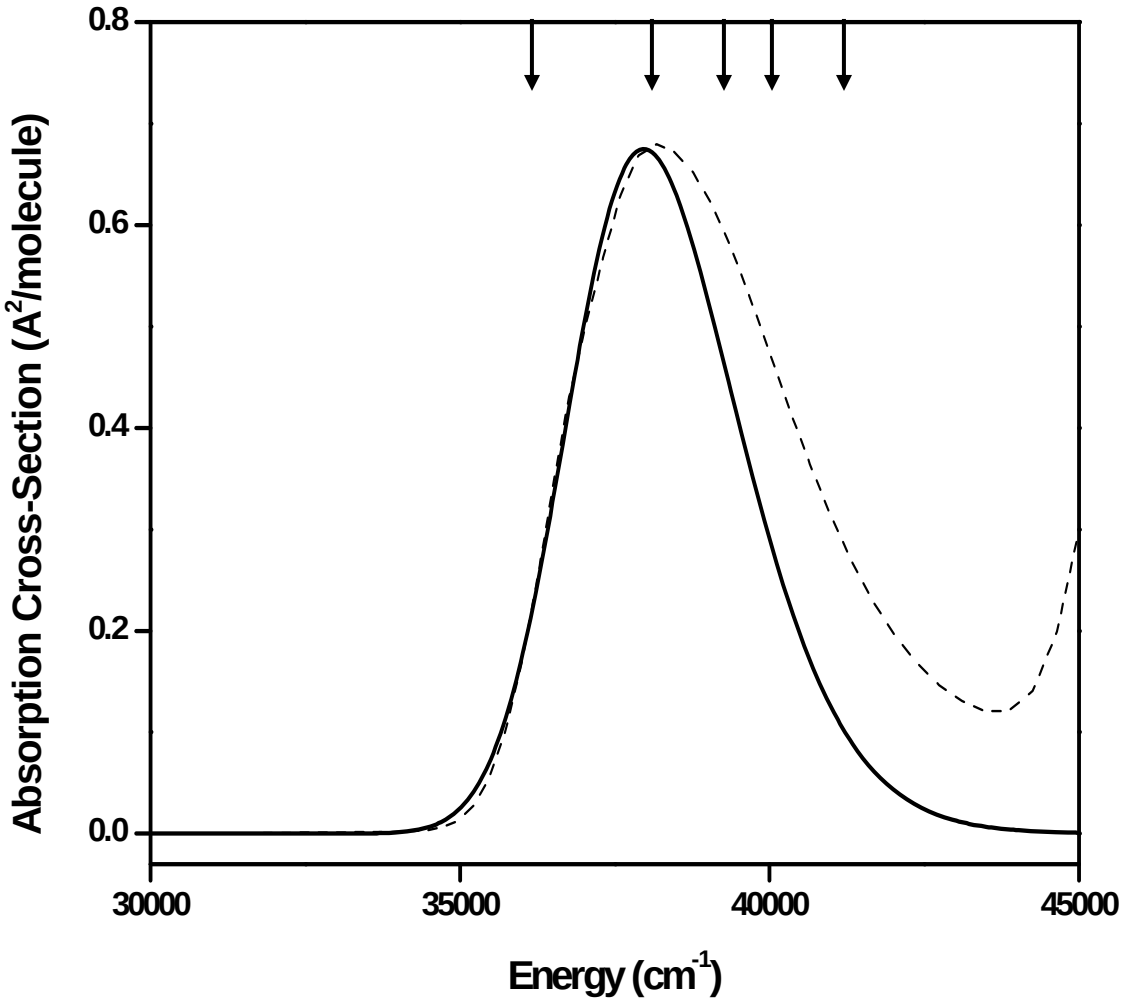

Figure 4.4. Experimental (dotted line) and simulated (solid line) absorption spectra of 9-MeA. The simulated absorption spectrum was simulated using Eq. 1.10 of Chapter 1 with the parameters in Table 4.1. The arrows indicate the UV resonance Raman excitation wavelengths. Discrepancies observed at energies greater than 38 000 cm^{-1} are due to higher energy electronic transitions which were not modeled in our simulation.

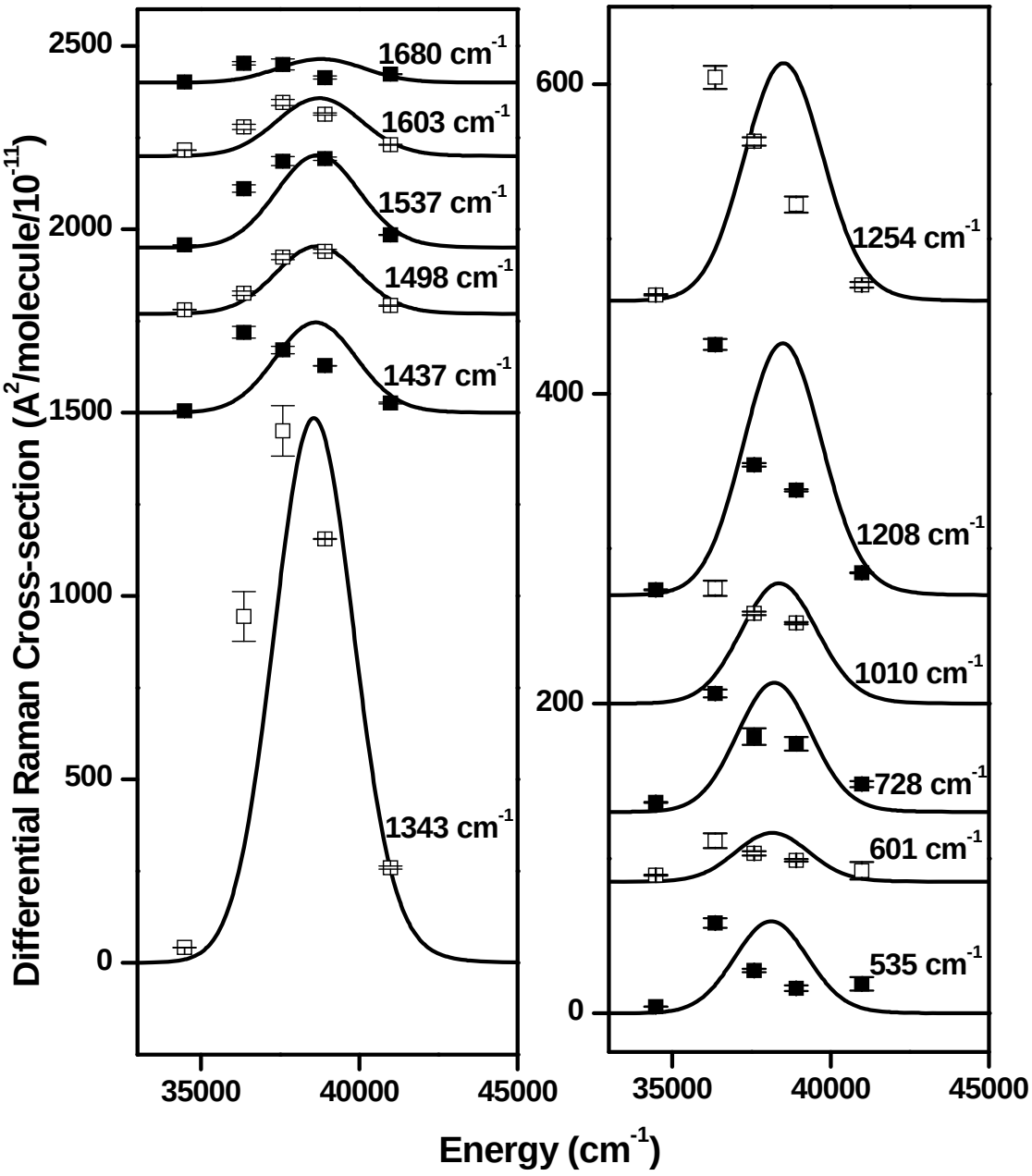

Figure 4.5. Experimental (points) and calculated (solid lines) resonance Raman excitation profiles of 9-MeA. These excitation profiles were calculated with Eq. 1.8 (Chapter 1) by using the parameters in Table 4.1. The excitation profiles have been offset along the ordinate axis for greater clarity. Error bars are the standard deviations of the data points and are on the order of the point size unless otherwise shown. Note that errors in the differential cross-section data points may range from 0-20%.

spectra in these figures are modeled with Eqs. 1.8 and 1.10, respectively, as well as the parameters in Table 4.1. Figures 4.4 and 4.5 show good agreement between the experimental and simulated absorption spectra and resonance Raman excitation profiles. The deviations observed between the simulated and experimental absorption spectra in Figure 4.4 above 38,000 cm^{-1} are attributed to higher energy electronic transitions which are not included in the model used here. Similar deviations have been observed in the absorption spectra of other nucleobases.[21-23] The different relative resonance Raman intensities of the observed vibrational modes in Figure 4.3 are directly reflected in the different experimental Raman cross-sections (Figure 4.5) and excited-state geometry displacements (Table 4.1).

4.3.3 Photochemical structural dynamics

Previous work has examined the excited-state electronic dynamics of 9-MeA.[2,3] We present here a discussion of 9-MeA's initial excited-state structural dynamics, which accompany those electronic dynamics. The initial structural dynamics presented here involve the very early stage of the excited-state, i.e. the first ≤50 fs of structural evolution from the Franck-Condon region.

Assuming the methyl at the N9 position plays no role in the photochemistry of 9-MeA, one can predict from Figure 4.2, which vibrational bands in the resonance Raman spectrum of 9-MeA will have intensity, if the initial excited-state structural dynamics lie along the photochemical reaction coordinate. For 9-MeA, the formation of the photodimer results in significant lengthening of the C5=C6 and N7=C8 bonds as a result of the change from double-bond character to more single-bond character. Because of resonance, all the bonds in the 6-membered rings, and C6-N7 and N7=C8 bonds in the 5-membered rings have some double-bond character in the original 9-MeA molecules. Therefore, in the photodimer, C6-N1 and C4-C5 bonds only experience secondary shortening effects in one of the 9-MeA molecules due to loss of resonance. Similarly, N1-C2, C2-N3 and N3-C4 bonds all change in one of the A molecules (Figure 4.2) because of resonance changes upon

photodimer formation. Therefore, one would expect significant intensity in the C4=C5 and N7=C8 stretching modes, and probably some intensity in the N1-C2, C2-N3, N3-C4 and C6-N1 stretching modes in the resonance Raman spectrum for 9-MeA. In addition to these, because of the change in hybridization from sp^2 to sp^3 at C5, C6, N7 and C8, modes involving bending, deformation and wagging on these atoms would be expected to have significant intensity.

To understand the excited-state structural dynamics of a molecule,. The mode assignments given in this work (Table 4.1) are based primarily on the most recent literature report on the vibrational modes assignment and the potential energy distribution (PED) on 9-MeA.[47] Using the predicted intense vibrational modes in the resonance Raman spectra of 9-MeA and the assignments given in Table 4.1, three bands may be identified as being photochemically relevant (bold entries in Table 4.1). The most intense of these is the 1343 cm^{-1} mode (C8-N9 + C5-N7 + C4=C5 stretch). The other bands are the 1537 cm^{-1} (C4-C5 stretch, NH_2 bend and N3-C4 stretch) and 1437 cm^{-1} (CH_3 bend and N7=C8 stretch). Because most of the initial excited-state structural dynamics occur along these photochemically relevant modes, it is therefore suggested that the 9-MeA UV photoproduct may be the same photodimer shown in Figure 4.2. These bands also have relatively high Δ values (Table 4.1). This is not unexpected, since resonance Raman intensity is roughly proportional to Δ^2.[22,23] We also observed a weaker but significant peak at 1498 cm^{-1}, which is assigned to CH_3 deformation. Similarly, weaker but relatively significant bands at 1208 cm^{-1} (indole ring bend and N7=C8 stretch), and 1603 cm^{-1} (NH_2 bend, C6-N10 + C5-C6 stretch) were seen in the resonance Raman spectra. The fact that the CH_3 deformation mode (1498 cm^{-1}) has relatively significant intensity and Δ value, and that another more intense band (1437 cm^{-1}) contain internal modes with significant CH_3 deformation component, confirm the involvement of the methyl group in the initial excited-state structural dynamics of 9-MeA. The other structural changes observed in this molecule are listed in Table 4.1 and their respective significance can be rationalized from the Δ values; the higher this value, the

more significant the mode will be in the initial excited-state structural dynamics of the molecule. Accordingly, the N3-C4, C4=C5, C5-C6, C5-N7, N7=C8 and C8-N9 bonds, and CH_3 bonds angles show the most structural changes in the excited-state of 9-MeA. Thus, we conclude that most of the initial excited-state structural dynamics of 9-MeA lie along these internal coordinates.

The primary photochemical intermediate formed is a cyclobutyl photodimer of the two interacting adenine molecules, forming new bonds between the N7 of one adenine and C6 of the other, and between C8 of one adenine and C5 of the other (Figure 4.2).[35] The unstable adenine photodimer intermediate subsequently breaks down into two distinct isolatable photoproducts A=A and AA* (Figure 4.2), which on acid hydrolysis forms 4,6-diamino-5-guanidinopyrimidine and 8-(5-amino-imidazol-4-yl)adenine, respectively.[35] These acid hydrolysis products are usually not observed in DNA or RNA.[35] Resonance Raman spectroscopy should not be sensitive to these products, unless significant amounts accumulate in our sample. We see no evidence of these products.

We expect the photochemistry of 9-MeA to be similar to that of A, considering that the initial unstable intermediate that is formed in adenine does not involve the N9-C12 bond in either of the two reacting A molecules (Figure 4.2).[35] As stated above, based on the A photodimer photoproduct of Figure 4.2, most of the vibrational modes that are predicted to have intense bands in the resonance Raman spectra of 9-MeA are in fact found to have significant intensity in the resonance Raman spectra. Indeed, the UVRR spectrum of 9-MeA reported here is similar to that of adenine, reported previously.[8,49] Therefore, we propose that, at least, some of the photochemically-relevant modes in the initial excited-state structural dynamics of A would be similar to that of 9-MeA, i.e. the initial structural dynamics of A would lie mostly along the photochemical coordinate. Such studies are currently on-going in our group.

The mode corresponding to the photochemically irrelevant methyl group deformation was not expected to have a significant intensity, if the

photochemical dynamics lay along the photochemical coordinate. The fact that this mode does in fact have significant intensity in the resonance Raman spectra of 9-MeA is an indication that it is involved in the initial excited-state structural dynamics. Our observation of the involvement of the methyl group in the structural dynamics of 9-MeA is consistent with the significant role played by it in 9-MeA's electronic dynamics when compared to A, which is responsible for the difference in decay pathways between these two molecules (vide infra).[2, 3] But according to Figure 4.2, there should be no involvement of the methyl group in the photochemistry of 9-MeA. This is more evident when one considers the fact that the sugar moiety in adenosine plays no role in the dimerization of A (Figure 4.2). However, it has been established in previous studies[21,52] that vibrational modes of substituents like amino groups show significant intensity in the resonance Raman spectra because of their proximity to photochemically active modes. The results presented here for 9-MeA are therefore consistent with the N-H bend seen in uracil and thymine initial excited-state structural dynamics. The N-H bond is not photochemically active in itself, but its proximity to the C5=C6 site of thymine and uracil photochemistry makes its bending vibration observable in the UV resonance Raman spectrum. In this case, it is the proximity of the methyl group to the photochemically relevant N7-C8 bond that is responsible for the significant resonance Raman intensity observed for this substituent.

The results found in the work presented here can be compared with *ab initio* computation studies on the radiationless decay mechanisms of adenine.[1] In that work, two photochemical pathways were found, which involve out-of-plane deformations of the 6-membered ring via the twisting of the C2N3 and N1C6 bonds. Our results are consistent with this report since we also report a change in the hybridization of the C6 carbon centre, based on all the assigned internal coordinates (Table 4.1). We also see some twisting of the C2N3 and N1C6 bonds in bicyclic ring deformations and torsion modes. In the same vein, the 6-membered ring deformations found in our analysis (Table 4.1) is consistent with this earlier report.

Another interesting way to quantify our results is to calculate the reorganization energy along each vibrational mode.[21,23] The reorganization energies obtained for all vibrational modes are shown in Table 4.1. Summing up these reorganization energies for the three most intense bands, whose modes are obviously photochemically active as discussed earlier, and expressing the sum as a percentage of the total reorganization energy for all the modes observed for 9-MeA (Table 4.1), we see that 66% of the excited-state structural reorganization energy is in the photochemically relevant modes.

4.3.4 Comparison with pyrimidines

Our group has previously reported on the excited-state structural dynamics of cytosine, 5-fluorouracil (5-FU), thymine, and uracil.[22,23,52,53] In all these reports, the differences in the resonance Raman spectral intensities between these similar nucleobases were highlighted, as well as the implication on their structural dynamics and photochemistry. For example, thymine only differs from uracil by the presence of a methyl group at the C5 position. However, their photochemistry is different. The origin of the differences have been rationalized based on their UVRR spectra, which are also different. It was found that in thymine, the dynamics lie primarily along the C5=C6 bond lengthening coordinate, while in uracil, most of the structural dynamics occur along a C5 and C6 pyramidalization coordinate. These differences in initial excited-state structural dynamics are one factor responsible for the different photoproducts observed for these two similar nucleobases.[21,52,53] It was therefore suggested that the observed differences in the excited-state structural dynamics of thymine and uracil arises from the methyl group in thymine acting as a mass barrier, thereby localizing the vibrations at the photochemical active site. The resonance Raman spectra obtained for the related analogue of these two, 5-FU, shows intensity that are more similar to thymine than uracil, thereby supporting the mass barrier hypothesis.[23]

The Δ values and total reorganization energies obtained for the vibrational modes in 9-MeA (Table 4.1) are lower than those of pyrimidines.[22,23,54] This points to the relative photochemical stability of purines compared to pyrimidines. It therefore demonstrates the relevance and validity of the results obtained here. The value for the photochemical component of the reorganization energy for 9-MeA (66%) is lower than for 5-fluorouracil (81%) and thymine (73%),[23,54] but it is more than those reported for cytosine and uracil.[22] Therefore, less of cytosine's and uracil's reorganization energy are directed along the photochemical coordinate, compared to 9-MeA, 5-fluorouracil and thymine. The quantum yield of dimerization for these nucleobases are in the order cytosine (0.04) > thymine (0.013) > 5-FU = U (0.007) > 9-MeA (0.003).[21-23,35,52,54] By scaling the reorganization energy in the photochemically active modes by the percentage of the mode which is localized along a photochemically relevant coordinate, a lower limit for the percentage of the reorganization energy along the photochemically relevant coordinate of 36% is obtained. This compares with 38% for thymine and 46% for 5-fluorouracil, but it is significantly different from 7% reported for cytosine.[23]

A significant outcome of this study may be the low Δ values obtained for the vibrational modes in 9-MeA. As seen in Table 4.1, the Δ values obtained for the photochemically relevant modes are between 0.14 and 0.35. These Δ values are mostly lower than Δ values obtained for the photochemically relevant modes of pyrimidine bases (0.11-0.85).[21-23,52] Since Δ is a measure of geometry displacements and of course, structural change that a molecule experiences in the excited-state, low Δ values indicate a rather stable molecule whose structure does not significantly change. The Δ values obtained here therefore suggest a stable molecule. This provides a strong support for the photochemical stability of 9-MeA, and therefore the photostability of purines as compared to pyrimidines. To our knowledge, this represents the first proof of the photostability of purines compared to pyrimidines, based on initial excited-state structural dynamics studies.

4.3.5 Excited-state photophysics

Self-consistent analysis of the resonance Raman excitation profiles and absorption with Eqs. 1.8 and 1.10 allows the partitioning of the spectral breadth into homogeneous and inhomogeneous components. These two factors are known to affect the observed absorption and resonance Raman excitation profiles differently.[21-23] The inhomogeneous component arises from ensemble site effects and only broadens the absorption spectrum and resonance Raman excitation profiles, while the homogeneous line width represents solvent-solute coupling, which dampens out the resonance Raman scattering intensity and broadens both. From Table 4.1, it can seen that both homogeneous and inhomogeneous line widths used need to be fairly large in order to reproduce both absolute Raman intensities and absorption band shape. The homogeneous line width is fairly consistent with previously reported values for thymine and uracil (1450-1700 cm^{-1}),[52,53] but higher than for cytosine and 5-fluorouracil (185-650 cm^{-1}).[22,23] The inhomogeneous line width is however consistent with the values previously reported for all four nucleobases (1000-1300 cm^{-1}).[22,23,52,53]

In the condensed phase, solvent dynamics may contribute significantly to the breadth of the absorption spectrum, either through homogeneous or inhomogeneous mechanisms.[21-23] These two factors affect the absorption spectrum and the resonance Raman excitation profiles differently. For 9-MeA, both homogeneous and inhomogeneous line widths must be relatively large to reproduce the experimental absorption spectrum and resonance Raman excitation profiles. To accurately model the magnitude of the resonance Raman cross-sections and the diffuse absorption spectrum, a Gaussian homogeneous line width of 1200 cm^{-1} was required. This large homogeneous line width for 9-MeA represents the contributions from solute-solvent coupling. Non-radiative decay processes, primarily internal conversion are known to be the primary population decay mechanism for nucleobases because of their low quantum yield for fluorescence and photochemistry.[21,22] This fact is thought to be true for 9-MeA since a low quantum yield of photochemistry (3.8×10^{-4}) has also been reported for A, which is expected to

be photochemically similar to 9-MeA.[35] Thus, it can be rationalized that internal conversion dominates the excited-state relaxation dynamics of the first excited-state of 9-MeA. Since the excited-state lifetime of 9-MeA is 2 ps,[19] a Gaussian homogeneous line width in energy of 4.4 cm^{-1} would be obtained.[21,22] Since this Gaussian line width is too low to account for the width of the absorption spectrum and the magnitude of the resonance Raman cross-sections, compared to the 1200 cm^{-1} used here, it follows therefore that solvent-induced dephasing is the primary contributor to the homogeneous line width.

Although, no previous calculations are available on the interaction of 9-MeA with water molecules, similar work on pyrimidine bases indicate significant differences in the interactions with hydrophobic part of the nucleobases.[21] The inhomogeneous broadening arises because there can be a number of different solvation structures in solution, leading to a distribution of electronic transition energies.[21-23] Inhomogeneous broadening is considered static on the resonance Raman experiment time scale. The inhomogeneous line width used to fit the data for 9-MeA is quite high (1000 cm^{-1}). Since there is no previous calculations on the solvated structures of 9-MeA interacting with water molecules, the nature of its molecular structure and the probable size of the solvation complex is unclear. Our high inhomogeneous line width however is comparable with those reported for thymine, cytosine and uracil, and based on calculations on the structures of these nucleobases interacting with water molecules,[21,22] we speculate that the room for minor structural changes is large, thus accounting for the large inhomogeneous line width obtained. However, our value is somewhat smaller than for thymine and cytosine. Thus, these results show relatively stronger interactions between these pyrimidines and water, compared to that between 9-MeA and water. This is reasonable and expected, when, from a practical standpoint, one considers the relative solubility of pyrimidine and purine nucleobases. A stronger interaction is expected for the more soluble pyrimidines compared to the less soluble purines, hence the relatively high inhomogeneous line width

for the pyrimidines. The relative hydrophobicity of 9-MeA compared to these nucleobases buttresses this point.

4.4 Conclusions

Self-consistent analysis of the resonance Raman spectra of 9-MeA and its absorption spectrum provide insight into the initial excited-state structural dynamics and photochemistry of the molecule. The photochemically relevant resonance Raman bands are the 1537, 1437 and 1343 cm^{-1} bands. Therefore, the more significant excited-state structural dynamics occur along these modes, since they give the highest Δ values. Since the methyl group is not involved in the photochemistry, we propose that the photochemical structural dynamics of A would be similar to that of 9-MeA found in this work. The Δ values obtained for the vibrational modes of 9-MeA are lower than those of pyrimidines, thereby pointing to the relative photochemical stability of purines compared to pyrimidines. 66% of the total excited-state reorganization energy of 9-MeA lies along these photochemically relevant modes. The results also provide insight into the initial structural changes that takes place in 9-MeA, suggesting that the photochemistry is primed in the purines for the initial excitation. The presence of the methyl group at N9 is seen to be involved in the initial excited-state structural dynamics of 9-MeA, but based on the structure of adenine photodimer, it does not seem to play any role in the photochemistry of 9-MeA.

4.5 References

(1) Perun, S.; Sobolewski, A. L.; Domcke, W. *J. Am. Chem. Soc.* **2005**, *127*, 6257-6265.

(2) Bisgaard, C. Z.; Satzger, H.; Ullrich, S.; Stolow, A. *ChemPhysChem* **2009**, *10*, 101-110.

(3) Satzger, H.; Townsend, D.; Zgierski, M. Z.; Patchkovskii, S.; Ullrich, S.; Stolow, A. *Proc. Natl. Acad. Sci. USA* **2006**, *103*, 10196-10201.

(4) Cohen, B.; Hare, P. M.; Kohler, B. *J. Am. Chem. Soc.* **2003**, *125*, 13594-13601.

(5) Gador, N.; Samoylova, E.; Smith, V. R.; Stolow, A.; Rayner, D. M.; Radloff, W.; Hertel, I. V.; Schultz, T. *J. Phys. Chem A.* **2007**, *111*, 11743-11749.

(6) Perun, S.; Sobolewski, A. L.; Domcke, W. *J. Phys. Chem. A* **2006**, *110*, 9031-9038.

(7) Poerschke, D. *J. Am. Chem. Soc.* **1973**, *95*, 8440-8446.

(8) Loppnow, G. R.; Billinghurst, B. E.; Oladepo, S. A. In *Excited-state Structural Dynamics of Nucleic Acids and Their Components;* Shukla, M. K. Leszczynski, J., Eds.; Radiation Induced Molecular Phenomena in Nucleic Acids A Comprehensive Theoretical and Experimental Analysis Series: Challenges and Advances in Computational Chemistry and Physics; Springer: Netherlands, 2008; Vol. 5, pp 237-263.

(9) Nishimura, Y.; Tsuboi, M.; Kubasek, W. L.; Bajdor, K.; Peticolas, W. L. *J. Raman Spectrosc.* **1987**, *18*, 221-227.

(10) Lagant, P.; Vergoten, G.; Peticolas, W. L. *J. Raman Spectrosc.* **1999**, *30*, 1001-1007.

(11) Saigusa, H. *J. Photochem. Photobiol. C: Photochem. Rev.* **2006**, *7*, 197-210.

(12) Crespo-Hernandez, C. E.; Cohen, B.; Hare, P. M.; Kohler, B. *Chem. Rev.* **2004**, *104*, 1977-2019.

(13) Sobolewski, A. L.; Domcke, W.; Dedonder-Lardeux, C.; Jouvet, C. *Phys. Chem. Chem. Phys.* **2002**, *4*, 1093-1100.

(14) Serrano-Andres, L.; Merchan, M.; Borin, A. C. *Proc. Natl. Acad. Sci. USA* **2006**, *103*, 8691-8696.

(15) Plutzer, Chr.; Kleinermanns, K. *Phys. Chem. Chem. Phys.* **2002**, *4*, 4877-4882.

(16) Nix, M. G. D.; Adam, L. D.; Cronin, B.; Ashfold, M. N. R. *J. Chem. Phys.* **2007**, *126*, 124312.

(17) Wells, K. L.; Roberts, G. M.; Stavros, V. G. *Chem. Phys. Lett.* **2007**, *446*, 20-24.

(18) Serrano-Andres, L.; Merchan, M.; Borin, A. C. *Chem. Eur. J.* **2006**, *12*, 6559-6571.

(19) Nikogosyan, D. N.; Angelov, D.; Soep, B.; Lindqvist, L. *Chem. Phys. Lett.* **1996**, *252*, 322-326.

(20) Luhrs, D. C.; Viallon, J.; Fischer, I. *Phys. Chem. Chem. Phys.* **2001**, *3*, 1827-1831.

(21) Yarasi, S.; Brost, P.; Loppnow, G. R. *J. Phys. Chem. A.* **2007**, *111*, 5130-5135.

(22) Billinghurst, B. E.; Loppnow, G. R. *J. Phys. Chem. A* **2006**, *110*, 2353-2359.

(23) Billinghurst, B. E.; Yeung, R.; Loppnow, G. R. *J. Phys. Chem. A* **2006**, *110*, 6185-6191.

(24) Myers, A. B.; Mathies, R. A. In *Resonance Raman spectra of polyenes and aromatics;* Spiro, T. G., Ed.; Biological Applications of Raman Spectroscopy; Wiley-Interscience: New York, 1987; Vol. 2, pp 1-58.

(25) Myers, A. B. In *Excited electronic state properties from ground-state resonance Raman intensities;* Myers, A. B., Rizzo, T. R., Eds.; Laser Techniques in Chemistry; Wiley: New York, 1995; pp 325-384.

(26) Kelley, A. M. *J. Phys. Chem. A* **1999**, *103*, 6891-6903.

(27) Lee, S.-Y.; Heller, E. J. *J. Chem. Phys.* **1979**, *71*, 4777-4788.

(28) Oladepo, S. A.; Loppnow, G. R. *Anal. Chim. Acta* **2008**, *628*, 57-66.

(29) Perno, J. R.; Grygon, C. A.; Spiro, T. G. *J. Phys. Chem.* **1989**, *93*, 5672-5678.

(30) Fodor, S. P. A.; Rava, R. P.; Hays, T. R.; Spiro, T. G. *J. Am. Chem. Soc.* **1985**, *107*, 1520-1529.

(31) Grygon, C. A.; Spiro, T. G. *Biopolymers* **1990**, *29*, 707-715.

(32) Fodor, S. P. A.; Spiro, T. G. *J. Am. Chem. Soc.* **1986**, *108*, 3198-3205.

(33) Lord, R. C.; Thomas Jr., G. J. *Spectrochim. Acta* **1967**, *23A*, 2551-2591.

(34) Wiorkiewicz-Kuczera, J.; Karplus, M. *J. Am. Chem. Soc.* **1990**, *112*, 5324-5340.

(35) Clingen, P. H.; Davies, R. J. H. *J. Photochem. Photobiol. B* **1997**, *38*, 81-87.

(36) Kumar, S.; Joshi, P. C.; Sharma, N. D.; Bose, S. N.; Davies, R. J. H.; Takedal, N.; McCloskey, J. A. *Nucleic Acids Res.* **1991**, *19*, 2841-2847.

(37) Kumar, S.; Sharma, N. D.; Davies, R. J. H.; Phillipson, D. W.; McCloskey, J. A. *Nucleic Acids Res.* **1987**, *15*, 1199-1216.

(38) Harada, I.; Lord, R. C. *Spectrochim. Acta* **1970**, *26*, 2305-2318.

(39) Savoie, R.; Poirier, D.; Prizant, L.; Beauchamp, A. L. *J. Raman Spectrosc.* **1981**, *11*, 481-486.

(40) Webb, M. A.; Kwong, C. M.; Loppnow, G. R. *J. Phys. Chem. B* **1997**, *101*, 5062-5069.

(41) Fraga, E.; Loppnow, G. R. *J. Phys. Chem. B* **1998**, *102*, 7659-7665.

(42) Fraga, E.; Webb, M. A.; Loppnow, G. R. *J. Phys. Chem.* **1996**, *100*, 3278-3287.

(43) Loppnow, G. R.; Fraga, E. *J. Am. Chem. Soc.* **1997**, *119*, 896-905.

(44) Loppnow, G. R.; Mathies, R. A. *Biophys. J.* **1988**, *54*, 35-43.

(45) Dudik, J. M.; Johnson, C. R.; Asher, S. A. *J. Chem. Phys.* **1985**, *82*, 1732-1740.

(46) Shoute, L. C. T.; Loppnow, G. R. *J. Chem. Phys.* **2002**, *117*, 842-850.

(47) Xue, Y.; Xie, D.; Yan, G. *Int. J. Quant. Chem.* **2000**, *76*, 686-699.

(48) Stephanian, S. G.; Sheina, G. G.; Radchenko, E. D.; Blagoi, Yu, P. *J. Mol. Struct.* **1985**, *131*, 333-346.

(49) Majoube, M. *J. Raman Spectrosc.* **1985**, *16*, 98-110.

(50) Dhaouadi, Z.; Gbomi, M.; Austin, J. C.; Girling, R. B.; Hester, R. E.; Mojzes, P.; Chinsky, L.; Turpin, P. Y.; Coulombeau, C.; Jobic, H.; Tomkinson, J. *J. Phys. Chem.* **1993**, *97*, 1074-1084.

(51) Tsuboi, M.; Hirakawa, A. Y.; Nishimura, Y.; Harada, I. *J. Raman Spectrosc.* **1974**, *2*, 609-621.

(52) Yarasi, S.; Ng, S.; Loppnow, G. R. *J. Phys. Chem. B* **2009**, *113*, 14336-14342.

(53) Ng, S.; Yarasi, S.; Brost, P.; Loppnow, G. R. *J. Phys. Chem. A* **2008**, *112*, 10436-10437.

(54) Faichuk, M.; Mah, A.; Loppnow, G. R. *Photochem. Photobiol.* **2007**, *83*, 1491-1496.

Chapter 5
The Effect of Tryptophan on UV-induced DNA Photodamage*

5.1 Introduction

UV radiation is a known genotoxic agent.[1,2] Therefore, when DNA is exposed to solar UV radiation, photochemical products such as cyclobutane pyrimidine dimers (CPDs), [6-4] pyrimidine-pyrimidinone photoproducts and photohydrates can form.[3-5] These photoproducts have been implicated in mutagenesis, carcinogenesis and cell death.[3] Therefore, the identification of mechanisms for protection, both endogenous and exogenous, is critical for human health. Tryptophan (Trp) is an aromatic amino acid (Figure 5.1) that absorbs in the same region of the UV as DNA.[6-8] The similarity of the absorption spectra of Trp and DNA (Figure 5.2) demonstrate that both photochemical damage or sacrificial absorption can occur. Thus, when DNA solutions are irradiated with UV light in the presence of Trp, there could be biologically-relevant interactions between the Trp and DNA.

There have been a number of studies on the photochemistry of nucleic acids and their components in the presence of Trp.[6,9-12] Reeve and Hopkins[6,9,10] and Saito et al.[11,12] irradiated the pyrimidine bases, and later the polynucleotides,[12] in the presence of Trp with UV light in the range 270-310 nm. They putatively isolated two classes of photoproducts, the reduced base dihydrothymine and the Trp-thymine adducts. Products were identified on the basis of chromatography with photoproduct standards and absorption spectroscopy,[6,9-12] leading to some ambiguity in the nature of the products. Although these studies measured preliminary quantum yields and kinetics, they did not discriminate between Trp-induced damage and inherent DNA damage. Indeed, the quantum yields obtained were the same as those

---

* A version of this chapter has been submitted. Oladepo, S. A., Loppnow, G. R. (Photochemistry and Photobiology, 2010)

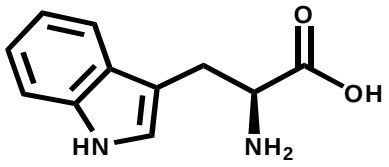

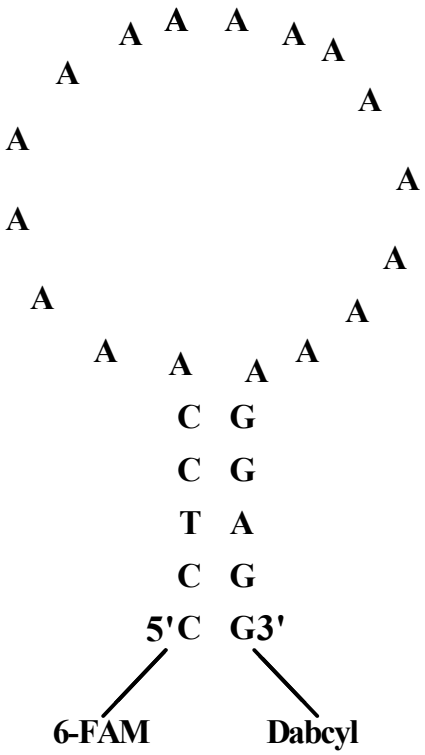

Trp

MB

Figure 5.1. Structure of Trp and the molecular beacon (MB) used in this work.

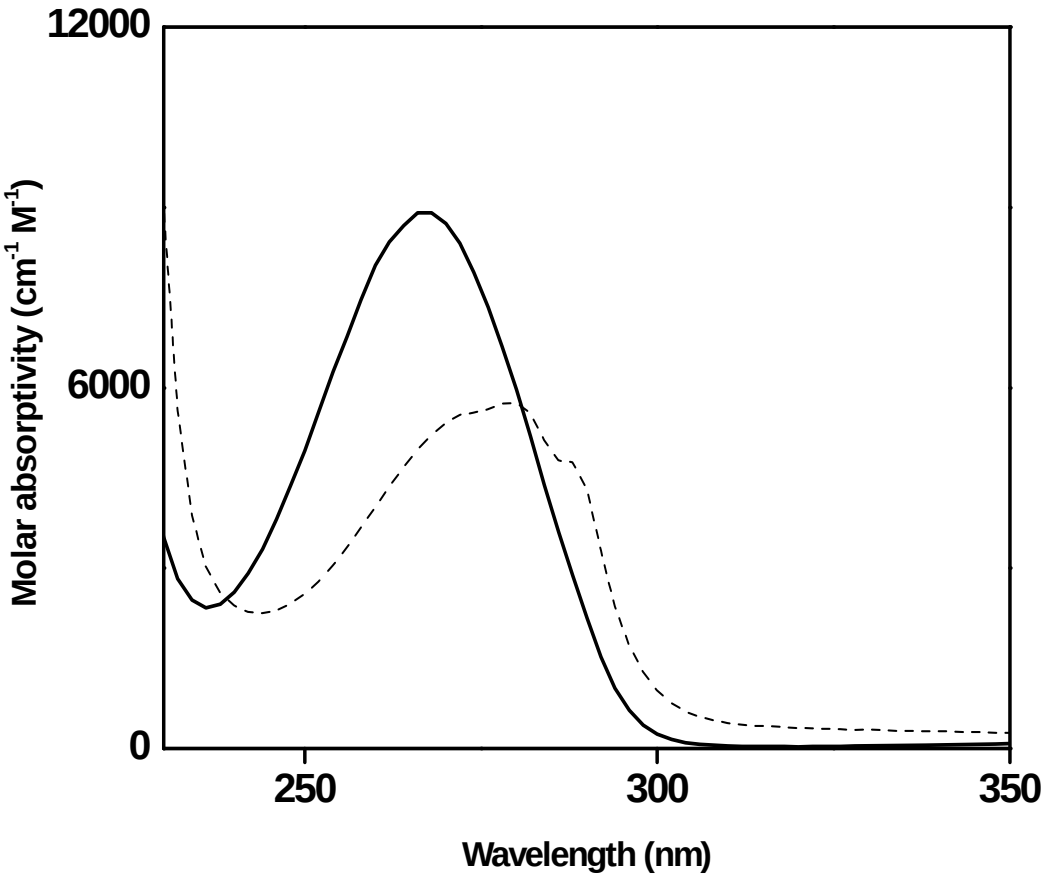

Figure 5.2. UV-Vis absorption spectra of separate solutions of 4 μM poly-dT oligonucleotide target (solid line) and 30 μM Trp (dashed line). For poly-dT, the oligonucleotide spectrum has been divided by 17 to yield the extinction coefficient of a single nucleotide in the 17-mer oligonucleotide, including hypochromicity.

reported for DNA damage.[3] Finally, these studies used a UV light source filtered with 1 mm thick Corex, which blocks wavelengths ≤265 nm. The lack of well-designed controls has prompted us to re-examine the photochemistry of DNA in the presence of tryptophan.

The absorption of UV light by different chromophores as a means of protecting living organisms from photodamage is well-documented.[13-24] For example, carotenoid pigments present in addition to the visual pigment in the photoreceptors of flies *Calliphora, Musca* and *Drosophila* prevent the photoreceptors from destruction by absorbing the harmful short wavelengths of light.[13-15] Similarly, chromophores like anthocyanins and carotenoids present in photosynthetic tissues of plants have been reported to offer effective protection for these tissues against photodestruction.[16-24] To this end, it has been reported that the reduction in the risk of photo-inhibition, without photosynthetic limitation, explains why anthocyanin-rich plant species thrive in high altitudes or in northern latitudes.[20] The photoprotection offered by this chromophore via absorption of harmful radiation allows the plants to withstand such environments. Trp may assume a similar photoprotective role when it is present with DNA in the same medium. It is therefore important to understand the kinetics of light absorption by Trp and elucidate the relative significance of both damage and protective processes.

Recently, molecular beacon (MB) probes[25-28] have been utilized for the detection of UV-induced DNA damage.[5] This study demonstrated that sensitive and accurate measurements of DNA damage can be achieved by this method, and that these probes can be useful for detecting all types of nucleic acid damage (A. Mah, S. Sparling and G. R. Loppnow, manuscript in preparation). MBs are oligonucleotide probes with a stem-loop structure (Figure 5.1), containing a fluorescent dye on one end and a quencher on the other. In the absence of target DNA, the fluorophore and the quencher are in close proximity, so there is minimal fluorescence. However, in the presence of the complementary target sequence, the MB hybridizes with the target, resulting in a significant increase in fluorescence. In the presence of DNA damage, the hybrid formed between the MB and the damaged DNA is less

stable since the DNA target is no longer perfectly complementary to the loop of the MB. Thus, the fluorescence is lower for this hybrid compared to that formed between the undamaged DNA and the MB. The difference in fluorescence intensity in these two cases is observable for a single damage site in the DNA.[5] These inherent properties make the MBs highly sensitive and very selective probes for DNA damage.

In this chapter, we report the photochemical kinetics of Trp-containing DNA solutions, which is essential for a better understanding of *in vivo* DNA photodamage and photoprotection. Given the high sensitivity and specificity of MB probes for monitoring DNA damage,[5,26] fluorescence-based MB detection was used to assay the UV-induced photodamage of oligonucleotide solutions in the absence and presence of Trp. Fluorescence curves obtained from the MBs in our experiments show that the fluorescence intensity decreases more slowly in the presence of Trp than when this amino acid is absent, indicating slower damage kinetics in the presence of Trp. The Trp concentration-dependent rate constants suggest a mechanism of sacrificial absorption of UV light by the Trp, which is then dissipated non-photochemically. These results are discussed in the context of inherent protection mechanisms which mediate the possible UV-induced DNA damage in cells.

5.2 Experimental

5.2.1 Materials and methods

The single-strand target oligonucleotide, dT_{17} and the MB, 5'-(6-FAM)-CCTCC$[A]_{17}$GGAGG-(Dabcyl)-3' (where 6-FAM is 6-carboxyfluorescein and Dabcyl is 4-(4'-dimethylaminophenylazo)-benzoic acid), were obtained from Integrated DNA Technologies Inc. (Coralville, IA, USA). The fluorophore (6-FAM) and the quencher (Dabcyl) are attached to the 5' and 3' end of the MB, respectively (Figure 5.1). The dT_{17} was purified by standard desalting and the MB was purified by HPLC, both by the vendor. The sodium hydroxide (NaOH), sulfuric acid (H_2SO_4) and hydrochloric acid (HCl) were

obtained from BDH Inc. (Toronto, ON, Canada), Caledon Laboratories Ltd. (Georgetown, ON, Canada) and Anachemia (Montreal, QC, Canada), respectively. The magnesium chloride ($MgCl_2$), Tris, Trp and ethylenediamine-tetraacetic acid (EDTA) were obtained from EM Science (Gibbstown, NJ, USA), ICN Biomedicals, (Aurora, OH, USA), Sigma Chemical Company (St. Louis, MO, USA) and BDH Inc. (Toronto, ON, Canada), respectively. All chemicals were used as received. Nanopure water from a Barnsted Nanopure (Boston, MA, USA) system was used for all solutions.

The MB was first annealed before dissolution in nanopure water, to ensure that all the MB molecules are in the correct conformation when used. The annealing was performed by rapidly heating the MB contained in the sample vial to a temperature of about 70 ^{o}C in a water bath, followed by gradual cooling to room temperature in the same bath. The sample vial was carefully wrapped in aluminium foil and sealed with parafilm.

Oligonucleotide samples and MB were each dissolved in nanopure water and kept frozen at -20 ^{o}C until needed. Upon thawing, they were diluted in buffer (10 mM Tris, 1 mM EDTA pH 7.5) to give the desired concentrations. The concentrations of the oligonucleotide solutions were confirmed by UV absorbance measurements.

5.2.2 Irradiation

Samples were irradiated in a Luzchem (Ottawa, ON, Canada) DEV photoreactor chamber with UV light from UVC lamps emitting principally at 254 nm. 5 mL of 4 μM nitrogen-purged solutions of dT_{17} were irradiated in the presence of 0 – 10 mM Trp contained in sealed, UV-transparent, 1-cm pathlength cuvettes. For some experiments, the DNA solution was placed alone in a cuvette which would then be placed in a larger UV-transparent cuvette containing a Trp solution of known concentration. The pathlength of this outer layer of Trp solution is about 0.5 cm. The cuvettes were placed in a water bath contained also in a UV-transparent water dish. The temperature, which was monitored by means of a Cole-Parmer DiGi-SENSE thermocouple

(Niles, IL, USA), was kept constant throughout the irradiation by the water bath. The samples were constantly stirred during irradiation and the photoreactor was purged with nitrogen throughout the irradiation to flush out oxygen and any ozone generated from the lamps. Control samples were handled identically but were not exposed to UV radiation. However, a sample containing only Trp in aqueous solution was also irradiated. The UVC lamps were turned on about 20 minutes before the start of irradiation to stabilize the lamp output. Absorption spectra were recorded at intervals throughout the irradiation period.

5.2.3 Absorption and fluorescence measurements

Absorption spectra of the irradiated samples were recorded on a Hewlett-Packard 8452A diode array spectrophotometer (Sunnyvale, CA, USA). A 20-μL aliquot of each irradiated solution was taken at various time intervals, and was later mixed with appropriate amounts of MB and the buffer solution to give final concentrations of 200 nM DNA and 200 nM MB. These solutions were then incubated in the dark at room temperature for at least 24 hours. Fluorescence spectra of the incubated samples were measured using a Photon Technologies International (Birmingham, NJ, USA) fluorescence system. The spectra were recorded between 490 and 700 nm with excitation at 480 nm and using 4 nm slits. A 10-mm pathlength, Suprasil quartz, fluorescence cuvette was used for these measurements. The spectra were recorded at room temperature on a 200-μL aliquot of the DNA-MB hybridization mixture.

The MBs were characterized by thermal denaturation profile experiments, in which temperature-dependent fluorescence measurements were carried out on buffer solutions of MB incubated in the absence or presence of the target DNA or Trp. The temperature was varied from 20 – 68 ^{o}C at 4 ^{o}C increment, a heating rate of 1 ^{o}C/min and 5 min settling time (for proper equilibration at set temperatures) for the heating cycle, and 68 – 20 ^{o}C for the reverse cooling cycle. 200 nM MB and 10 times excess DNA were used for this set of measurements.

5.3 Results and Discussion

Both pure DNA solutions and Trp-containing DNA solutions were irradiated in a similar manner, and the UV-induced photodamage was progressively monitored by incubating aliquots of these solutions with MBs. The enhanced selectivity of the MB probes was exploited in this work for detecting UV-induced DNA damage, and in exploring the possibilities of Trp-DNA adducts formation and the preferential absorption of UV light by Trp. It should be emphasized here that the MB was not irradiated, it was only incubated with aliquots of pure DNA and Trp-containing DNA solutions following their irradiation.

5.3.1 Thermal denaturation profiles of the MB

The MB probe used in this work was carefully designed to optimize its performance in detecting DNA damage. The factors affecting MB hybridization, such as electrostatic effects, relative melting temperatures of the loop and the stem, and probe-to-target concentration have been discussed in detail previously.[5] The temperature-dependent conformational changes characteristic of MBs as well as the thermodynamic basis of the enhanced specificity of MBs, both in the absence and presence of DNA target have also been described elsewhere.[25-29] To ensure the correct design of the MB, thermal denaturation profiles of the MB were measured. Figure 5.3 shows the melting curves derived from the heating cycle for the MB and DNA-MB hybrid samples. The melting temperature for the MB in the absence of DNA target, as reflected in the inflection point on the curve was found to be 56 ^{o}C. The melting temperature for the MB-DNA hybrid (Figure 5.3) was 44 ^{o}C. The shape of the thermal denaturation profiles and the difference in melting temperatures (12 ^{o}C) between MB only and MB-DNA hybrid are similar to those found for different MB/target hybrids in earlier reports.[5,26] It is clear from Figure 5.3 that the dissociation of the MB stem occurs at a higher temperature than that of the MB-DNA hybrid, an important criterion for the optimal performance of the MB in the detection of DNA damage.[5,26] The relatively low concentration of the MB used here (200 nM) reflects the

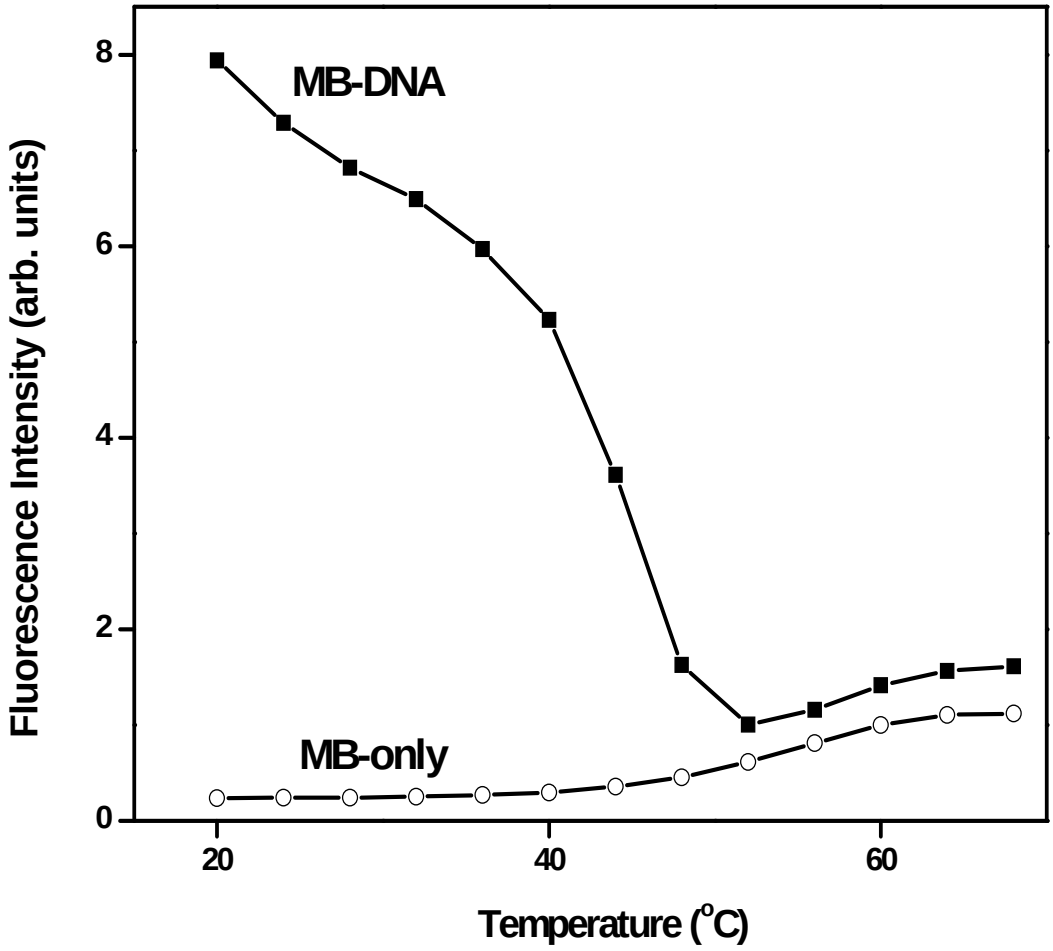

Figure 5.3. Thermal denaturation profile curves for 200 nM MB alone (open circles) and 200 nM MB in the presence of a 10-fold excess of target oligonucleotide (filled squares). Fluorescence intensity of each data point is the peak height in the 500-540 nm range. Both curves were generated at a heating rate of 1 ^{o}C/min, in 4 ^{o}C increments and 5 minutes holding time per increment. The curves shown are the heating cycles. The corresponding cooling cycle for each curve (not shown) is identical to the heating cycle shown here, indicating that no hysteresis was observed.

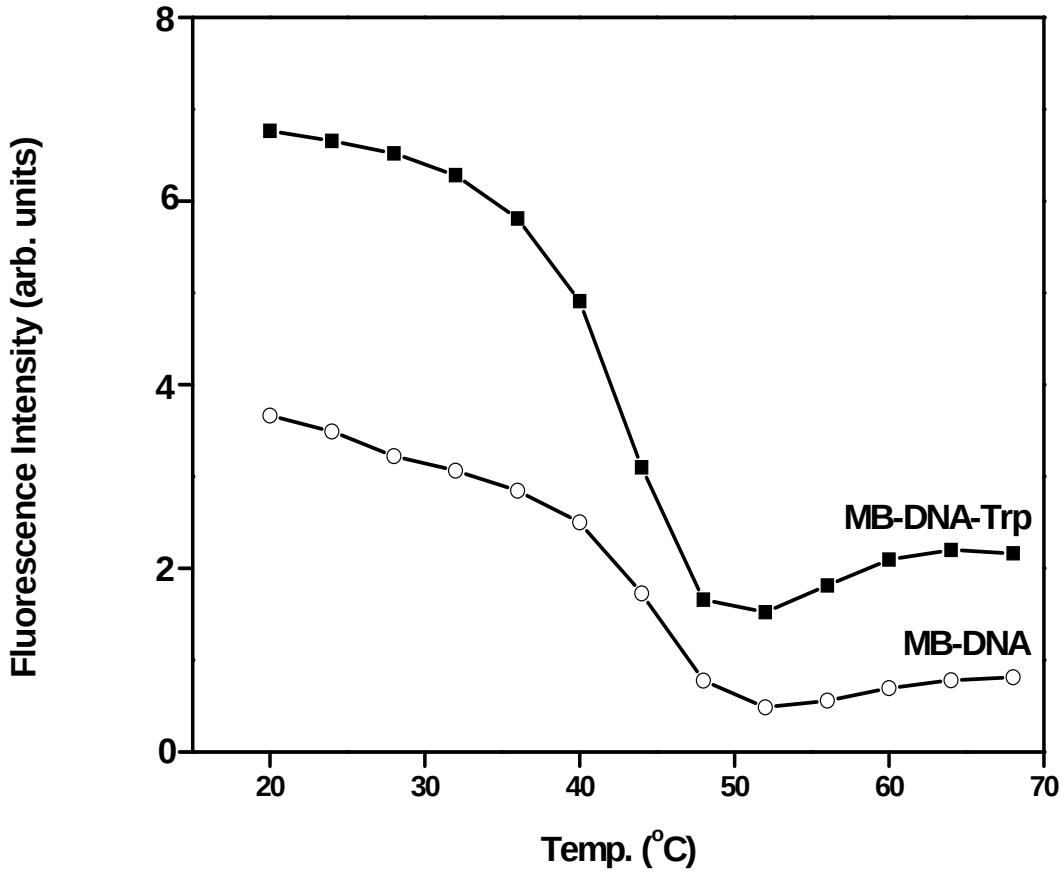

Figure 5.4. Heating curves for 200 nM MB in the presence of a 10-fold excess of target oligonucleotide and 5 mM Trp (upper curves). Heating curves for 200 nM MB in the presence of a 10-fold excess of target oligonucleotide (lower curves). Fluorescence intensity of each data point is the peak height in the 500-540 nm range. Both curves were generated at a heating rate of 1 ^{o}C/min, in 4 ^{o}C increments and 5 minutes holding time per increment. The corresponding cooling cycle for each curve (not shown) is identical to the heating cycle shown here, indicating that no hysteresis was observed. In both cases, the melting temperature of the MB-DNA hybrid is essentially constant (melting temperature difference is within experimental error) despite the presence of Trp. The fluorescence signal levels are different because the fluorescence measurements were carried out in different experiments, with different fluorescent lamp intensities.

exquisite sensitivity of these probes. Since the MB only recognizes intact DNA, the presence of Trp must not interfere with the performance of the MB. To prove this, we also performed thermal denaturation profile experiments in the presence of Trp. We found that the presence of Trp does not change the melting temperature of the MB significantly (Figure 5.4). These MB probes are very specific and the presence of other components (such as Trp in the case of this study) does not appear to impact their sensitivity and specificity.

5.3.2 UV irradiation of Trp-containing DNA solutions

Oligonuclotide solutions with and without Trp were irradiated at constant temperature, and the subsequent damage was detected by both absorption and fluorescence measurement of incubated solutions of MB with aliquots of the irradiated solutions. The absorption measurements (data not shown) were not very informative, as the Trp absorption masks any changes in the absorbance of the DNA which would indicate damage. It has been demonstrated previously that MB probes are capable of detecting single base mismatches and damage sites in DNA[5,26,28] Shown in Figure 5.5A are the fluorescence emission spectra of MB-DNA solutions at different irradiation times in the absence of Trp, while Figure 5.5B are the fluorescence emission spectra of MB-DNA solutions in the presence of 10 mM Trp under identical irradiation conditions and at similar irradiation time intervals. It can be seen from these figures that the fluorescence intensity decreases much faster in the pure DNA solution than in the Trp-containing DNA solutions. These results suggest that Trp inhibits damage to the DNA. These results also suggest that Trp-induced DNA damage products (i.e. Trp-DNA adducts) are not as significant, since it would be expected that this would make the observed decrease in fluorescence intensity much faster than that of the pure DNA solution. In other words, if Trp-DNA adducts are being significantly formed compared to preferential Trp absorption of the UV light, then much less DNA should be available for hybridization with the MB, leading to a much faster decrease in fluorescence. However, the results indicate that more DNA remains intact when Trp is present in solution.

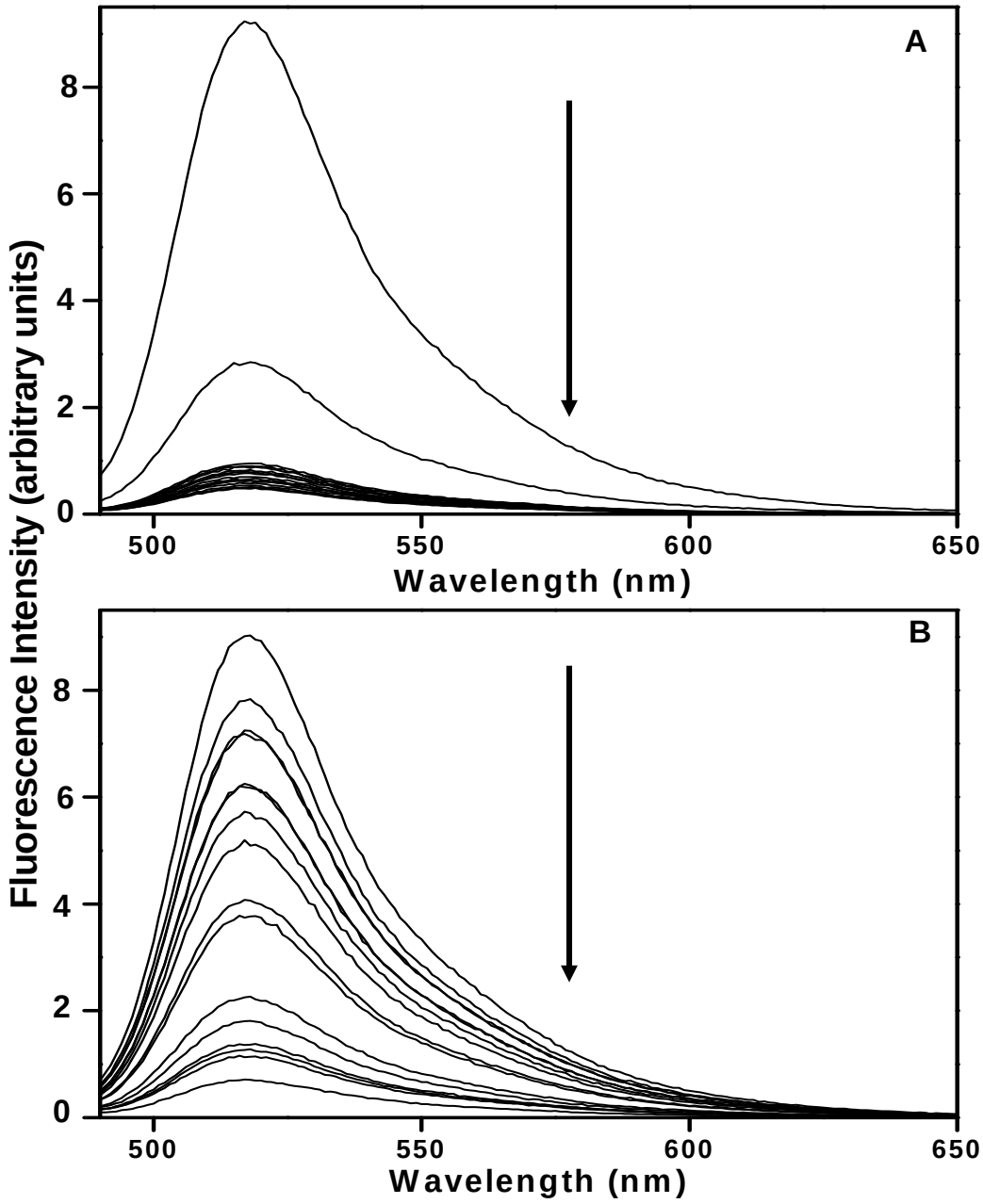

Figure 5.5. (A) Fluorescence emission spectra of MB with target DNA excited at 480 nm at different target DNA irradiation times in the absence of Trp. Direction of the arrow indicates the direction of fluorescence intensity change with increasing irradiation time from 0 to 240 minutes. (B) Fluorescence emission spectra of MB with target DNA excited at 480 nm at different target DNA irradiation times in the presence of 10 mM Trp. Direction of the arrow indicates the direction of fluorescence intensity change with increasing irradiation time from 0 to 240 minutes. Note that the irradiation time points in both figures are the same.

Shown in Figure 5.6 are the fluorescence curves for the DNA solutions in the presence of different concentrations of Trp. A closer look at the bottom curve in this figure, which represents the pure DNA solution, reveals that the fluorescence has decreased to about 25% of its original intensity after 2 minutes of irradiation, and that the intensity has decreased to about 10% of its original value after 4 minutes. In the presence of 10 mM Trp (topmost curve), it took 30 minutes for the DNA to decrease to 25% of its original intensity and about 4 hours to decrease to 10% of its original value. These results indicate that in the absence of Trp, UV-induced damage to the target DNA is very rapid under these irradiation conditions, i.e. about 90% of the target has at least single-site damage within 4 minutes of irradiation. However, in the presence of 10 mM Trp, it takes about 4 hours of UV irradiation to damage at least a single site in 90% of the target DNA, about 60 times longer. We also found that the observed photodamage is not thermally induced because the temperatures of all samples were kept constant throughout the irradiation time, and an unirradiated Trp-containing DNA solution at the same temperature shows no damage.

The fluorescence spectral data were fit to a single-exponential decay function (Figure 5.6 and Table 5.1). From these curves, we obtained time constants which vary from 1.2 ± 0.09 min to 29 ± 2.8 min for Trp concentrations between 0 and 10 mM Trp, respectively. The corresponding first-order rate constants for DNA photodamage therefore vary from 0.82 min^{-1} for 0 mM Trp, to 0.03 min^{-1} for 10 mM Trp. These results indicate that the DNA damage rate constant has reached a limiting value at 5 mM Trp concentration, such that the rate constant is not very different with further concentration increase (Figure 5.17 *vide infra*). This result is interesting, when one considers the fact that the physiological concentration of Trp is in the 10 mM range, twice the concentration at which the DNA photodamage rate constant assumes a limiting value.[30-32]

The decrease in MB fluorescence is more prolonged as the amount of Trp present increases (Figure 5.6). These results support preferential absorption of UV light by Trp, thereby reducing the DNA damage and making more intact

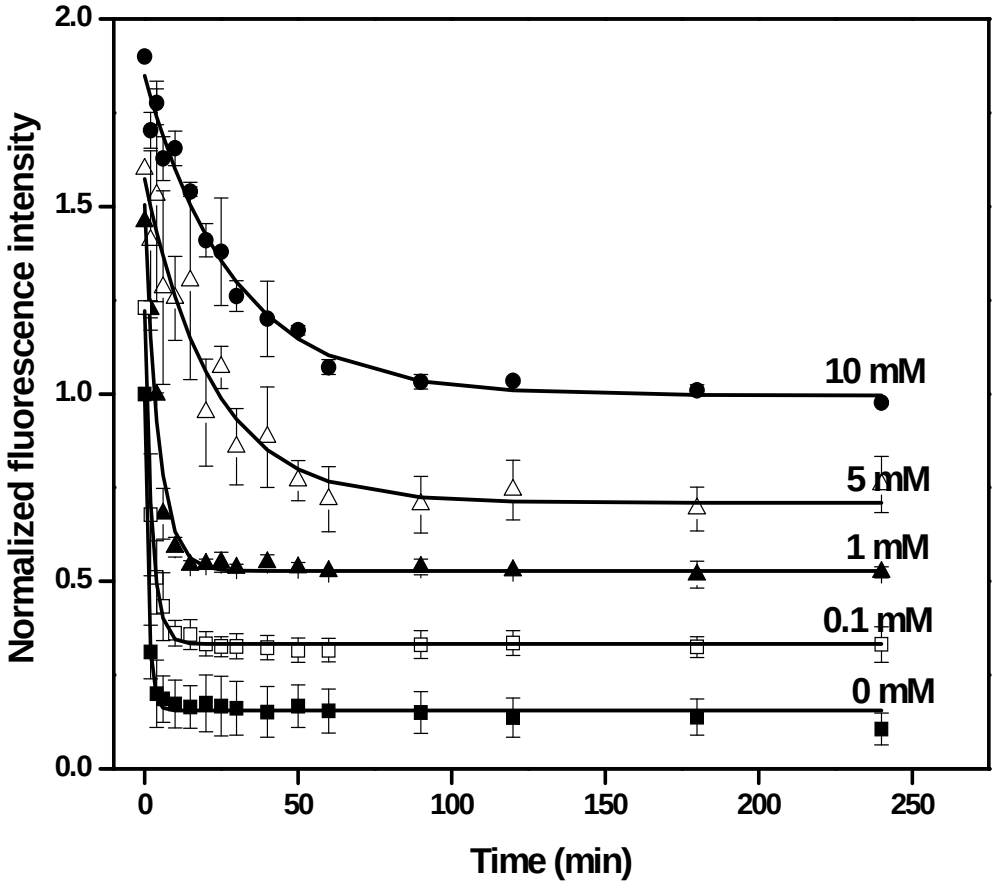

Figure 5.6: Normalized fluorescence intensity of hybridization mixtures of 200 nM oligonucleotide targets and 200 nM MB as a function of target DNA irradiation time. The MB was excited at 480 nm and the fluorescence emission was monitored at 520 nm. The irradiation of the DNA was carried out in the presence of different concentrations of Trp: 0 mM (filled squares), 0.1 mM (open squares), 1 mM (filled triangles), 5 mM (open triangles), and 10 mM (filled circles). The curves have been offset along the ordinate for clarity. The solid line through the points on each curve is the fit to an offset, single-exponential decay function, $y = y_o + Ae^{-t/\tau}$. Each data point is an average of four replicate measurements and the error bars correspond to the standard deviation of the measurements. The fluorescence time constants, τ, [y_o, A] for the different concentrations of Trp are 1.2 ± 0.1 min [0.16 ± 0.01, 0.84 ± 0.02], 2.3 ± 0.1 min [0.10 ± 0.01, 0.89 ± 0.02], 4.5 ± 0.4 min [0.07 ± 0.01, 1.0 ± 0.04], 22 ± 4 min [0.11 ± 0.04, 0.9 ± 0.1], and 29 ± 3 min [0.1 ± 0.02, 0.9 ± 0.03], for 0, 0.1, 1, 5 and 10 mM Trp, respectively.

DNA available for binding to the MB, hence the prolonged decrease in fluorescence. If Trp-induced DNA damage were the predominant effect, we should see a faster decrease in fluorescence when Trp is present. The individual curves of Figure 5.6 are shown in Figures 5.7 to 5.12, including that of DNA in the presence of 1.5 mM Trp, which was not shown in Figure 5.6, for clarity.

We conducted a set of experiments in which Trp of varying concentrations are placed in an outer cuvette, into which an inner cuvette of DNA solution was immersed. This was to further test this preferential absorption model and to justify the existence or otherwise of Trp-induced DNA damage product in the irradiated solutions. This assembly was irradiated at the same time as were the other cuvettes containing DNA and Trp in the same cuvette. For Trp concentrations between 0.1 and 1.5 mM, the time constants obtained are 2.3 ± 0.1 min to 29 ± 2 min. The results (Figures 5.13-5.16 and Table 5.1) indicate that at low Trp concentrations (0 - 0.1 mM), the kinetics of fluorescence loss are essentially the same, whether the Trp and DNA are kept together in the same cuvette or kept in separate cuvettes. However, at Trp concentrations of 1 and 1.5 mM, the kinetics are significantly different between these two scenarios. The time constant for the DNA-Trp in the same medium is lower than that of DNA/Trp in concentric cuvettes. For example, these results indicate that when the DNA is present with 0.1 mM Trp concentration in the same medium, the DNA can compete well with Trp molecules for incoming UV photons, given the low number of Trp molecules in solution. In the concentric-cuvette arrangement, this low concentration Trp means that little absorption of the UV light by the outer solution of Trp occurs, and significant damage to the inner DNA solution results. The similarity of the kinetics at 0.1 mM Trp also suggests little Trp-induced DNA damage. If such damage occurred, kinetics for the Trp-containing DNA solution would indicate a faster decrease in fluorescence compared to the concentric-cuvette arrangement.

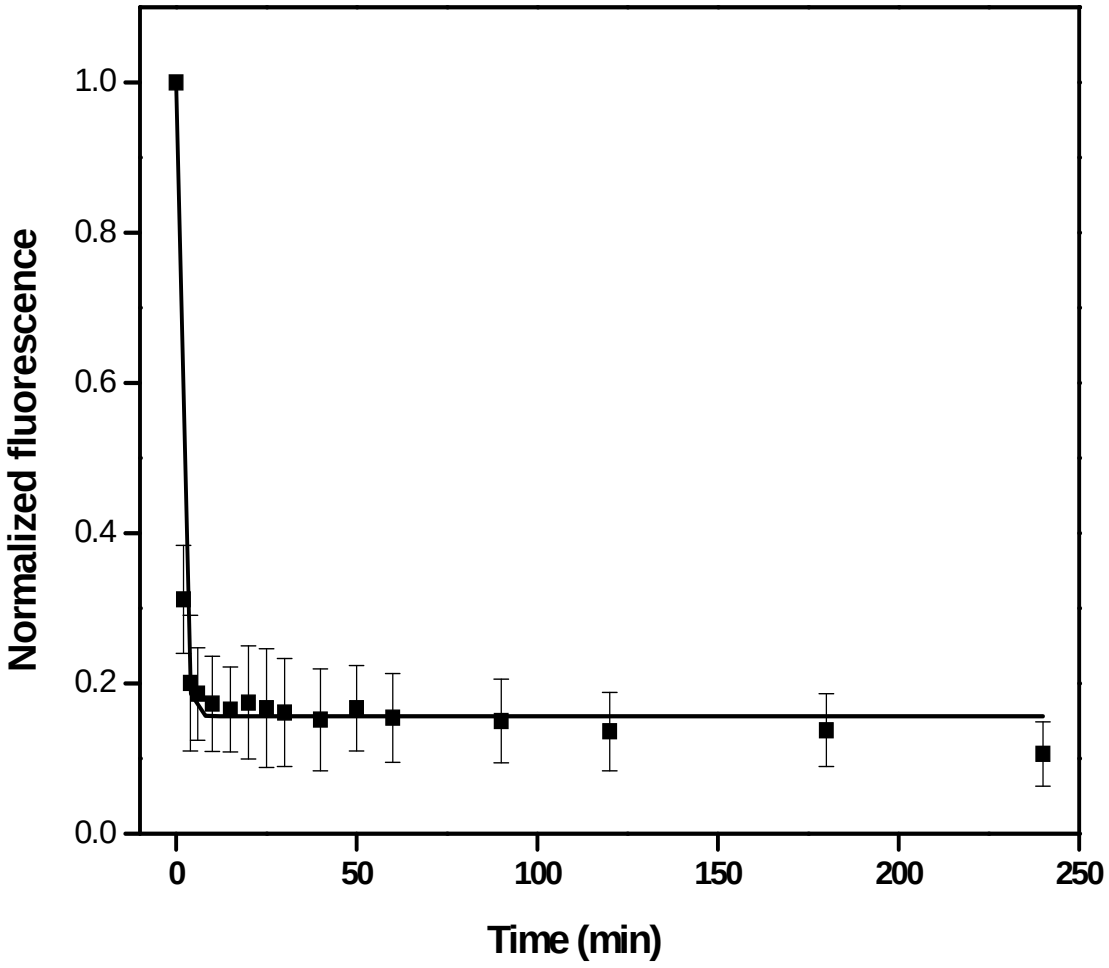

Figure 5.7. Plot of normalized fluorescence intensity vs irradiation time for a solution of target DNA containing no Trp. The plot is the same as that shown in Figure 5.6, but is individually shown here for clarity. The fluorescence time constant, y_o (offset) and A (amplitude) for this DNA only sample are 1.2 ± 0.1 min, 0.16 ± 0.01 and 0.84 ± 0.02, respectively. Error bars representing the standard deviations are shown.

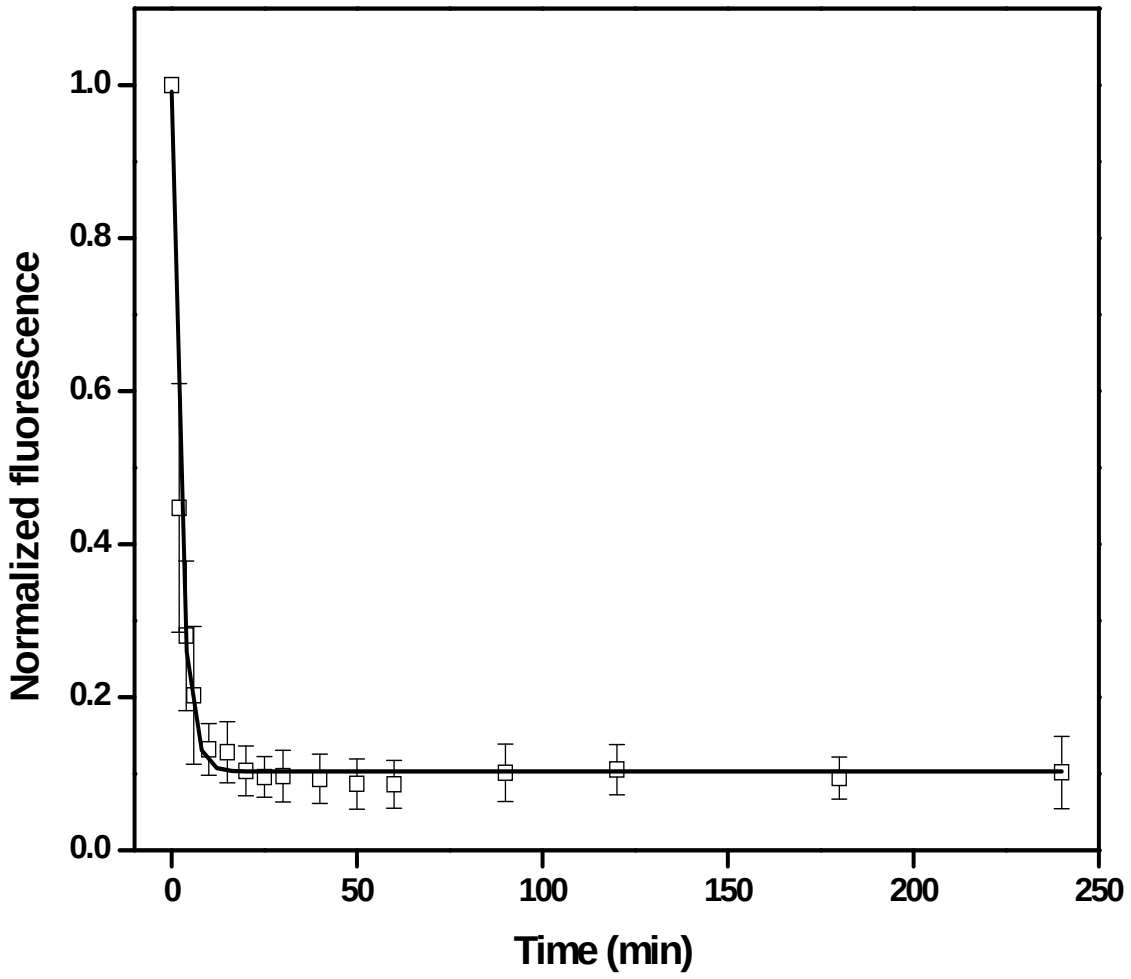

Figure 5.8. Same as Figure 5.7 but for DNA in the presence of 0.1 mM Trp. The fluorescence time constant, y_o (offset) and A (amplitude) for this sample are 2.3 ± 0.1 min, 0.10 ± 0.01 and 0.89 ± 0.02, respectively. Error bars representing the standard deviations are shown.

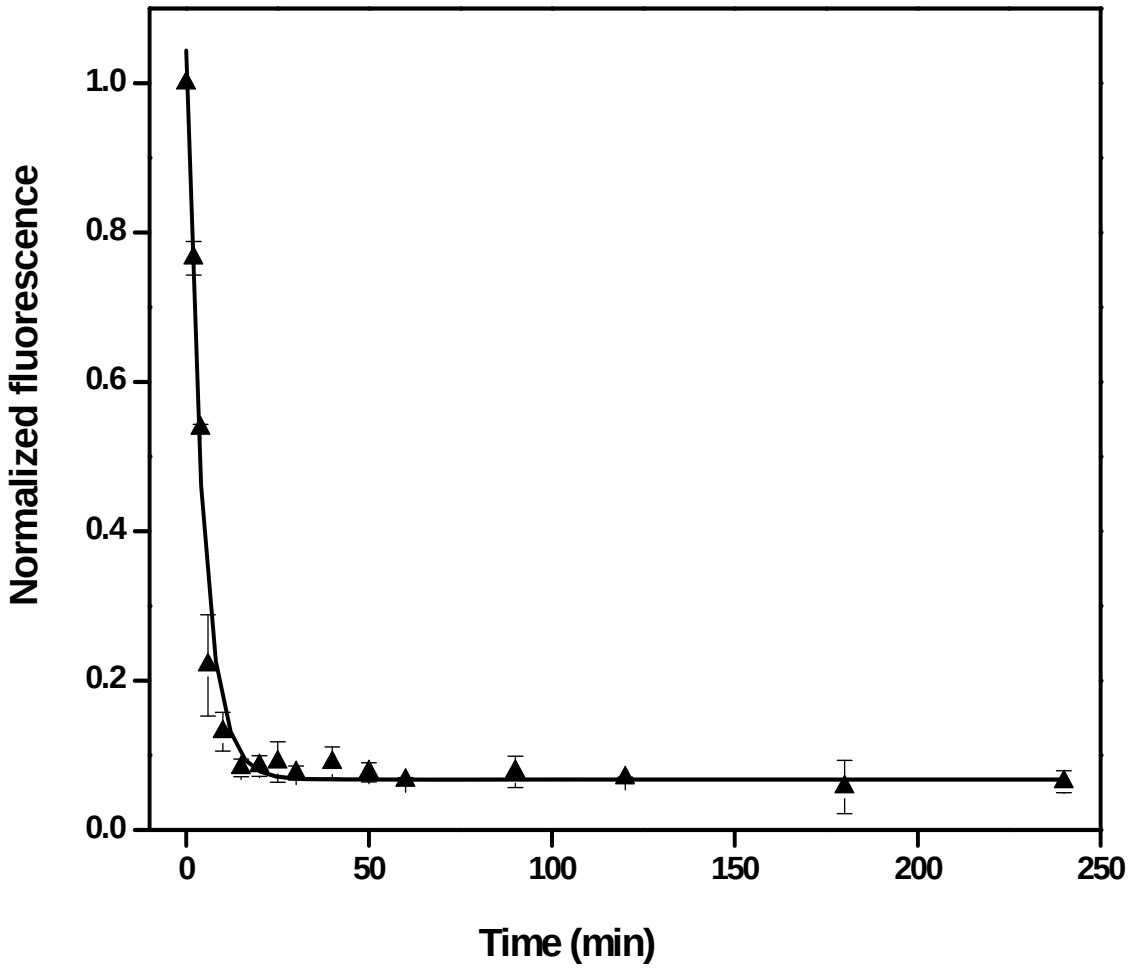

Figure 5.9. Same as Figure 5.7 but for DNA in the presence of 1 mM Trp. The fluorescence time constant, y_o (offset) and A (amplitude) for this sample are 4.5 ± 0.4 min, 0.07 ± 0.01 and 1.0 ± 0.04, respectively. Error bars representing the standard deviations are shown.

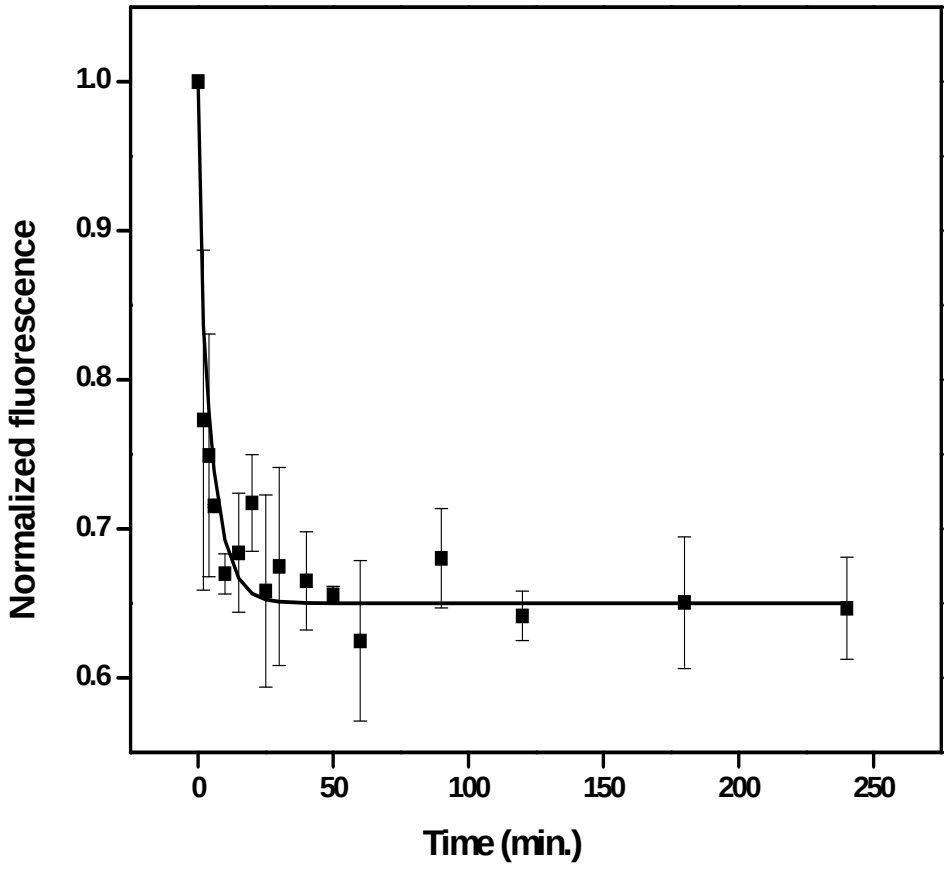

Figure 5.10 Same as Figure 5.7 but for DNA in the presence of 1.5 mM Trp. The fluorescence time constant, y_o (offset) and A (amplitude) for this sample are 5.4 ± 0.1 min, 0.65 ± 0.01 and 0.27 ± 0.03, respectively. Error bars representing the standard deviations are shown.

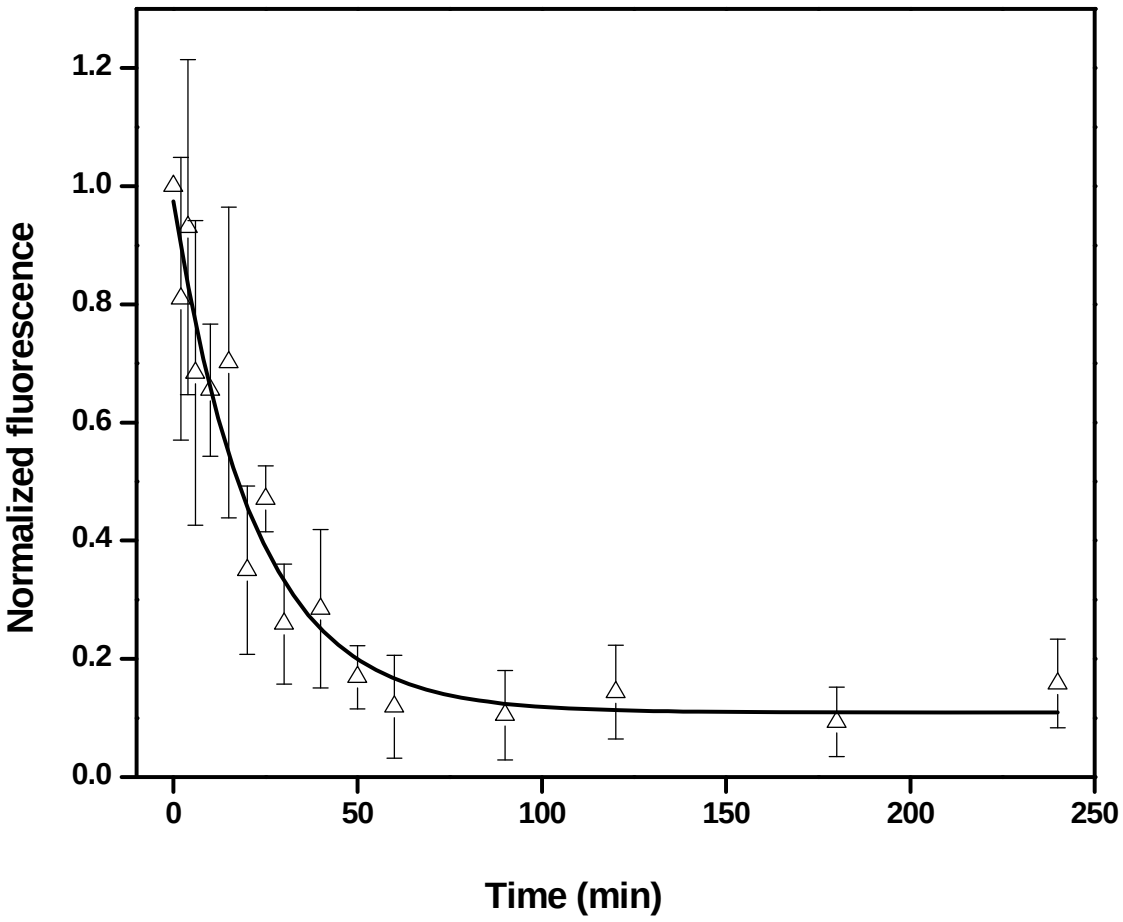

Figure 5.11. Same as Figure 5.7 but for DNA in the presence of 5 mM Trp. The fluorescence time constant, y_o (offset) and A (amplitude) for this sample are 22 ± 4 min, 0.11 ± 0.04 and 0.9 ± 0.1, respectively. Error bars representing the standard deviations are shown.

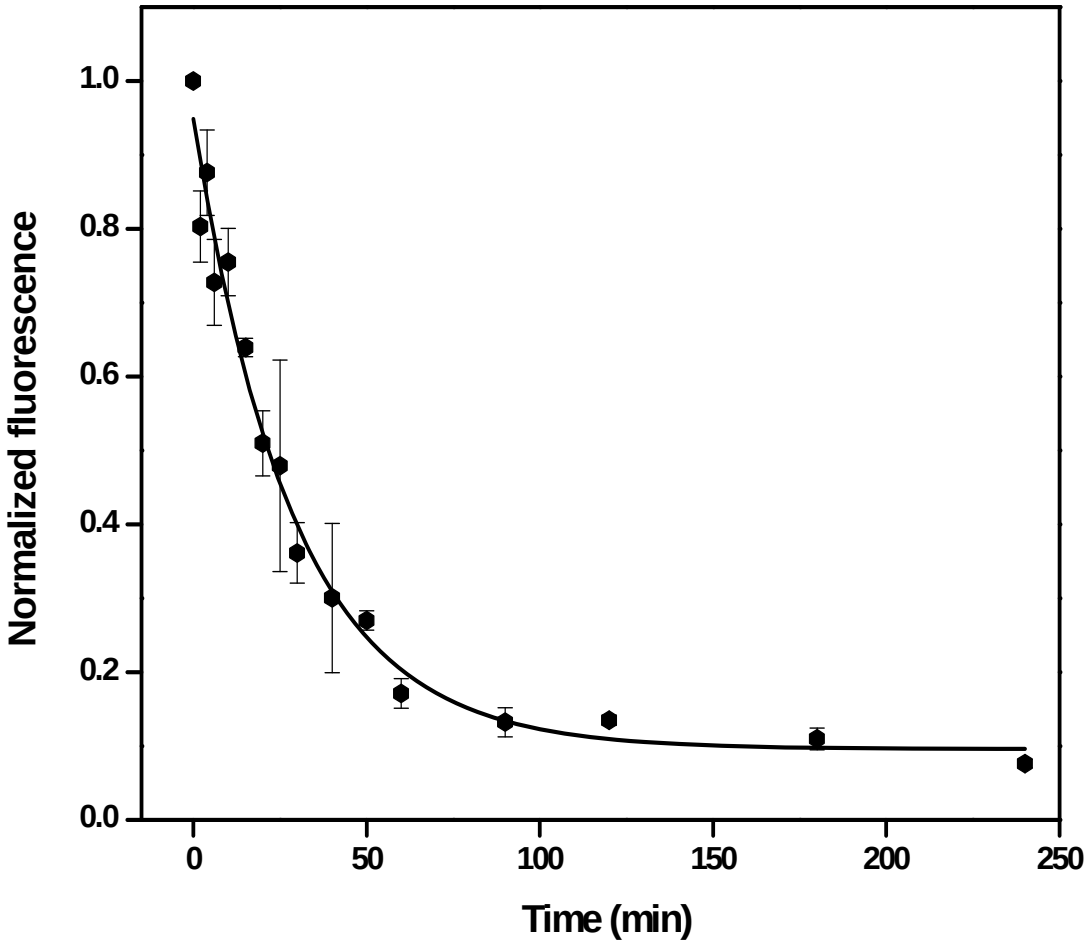

Figure 5.12 Same as Figure 5.7 but for DNA in the presence of 10 mM Trp. The fluorescence time constant, y_o (offset) and A (amplitude) for this sample are 29 ± 3 min, 0.10 ± 0.02 and 0.85 ± 0.03, respectively. Error bars representing the standard deviations are shown.

Table 5.1. Time constants and DNA photodamage rate constants for DNA irradiation experiments at different concentrations of Trp.

[Trp] (mM)	[Trp]/[DNA]	Time constant/min. (DNA photodamage rate constant/min.$^{-1}$)	
		DNA-Trp (same medium)	DNA-Trp (different media)
0	0	1.2 ± 0.1 (0.83)	1.2 ± 0.1 (0.83)
0.1	50	2.3 ± 0.1 (0.43)	2.3 ± 0.1 (0.43)
1	250	4.5 ± 0.4 (0.22)	12 ± 0.5 (0.08)
1.5	375	5.4 ± 0.1 (0.19)	29 ± 2 (0.03)
5	1250	22 ± 4 (0.05)	-
10	2500	29 ± 3 (0.03)	-

[Trp/[DNA] is the concentration ratio of Trp to DNA. Trp-DNA (same medium) represents a mixture of Trp and DNA kept together in the same medium. Trp-DNA (different media) is the concentric cuvette arrangement, where the cuvette containing the DNA is immersed in another UV-transparent cuvette containing Trp of specified concentration. The dash (-) indicates that no experiment was conducted at the indicated Trp concentration.

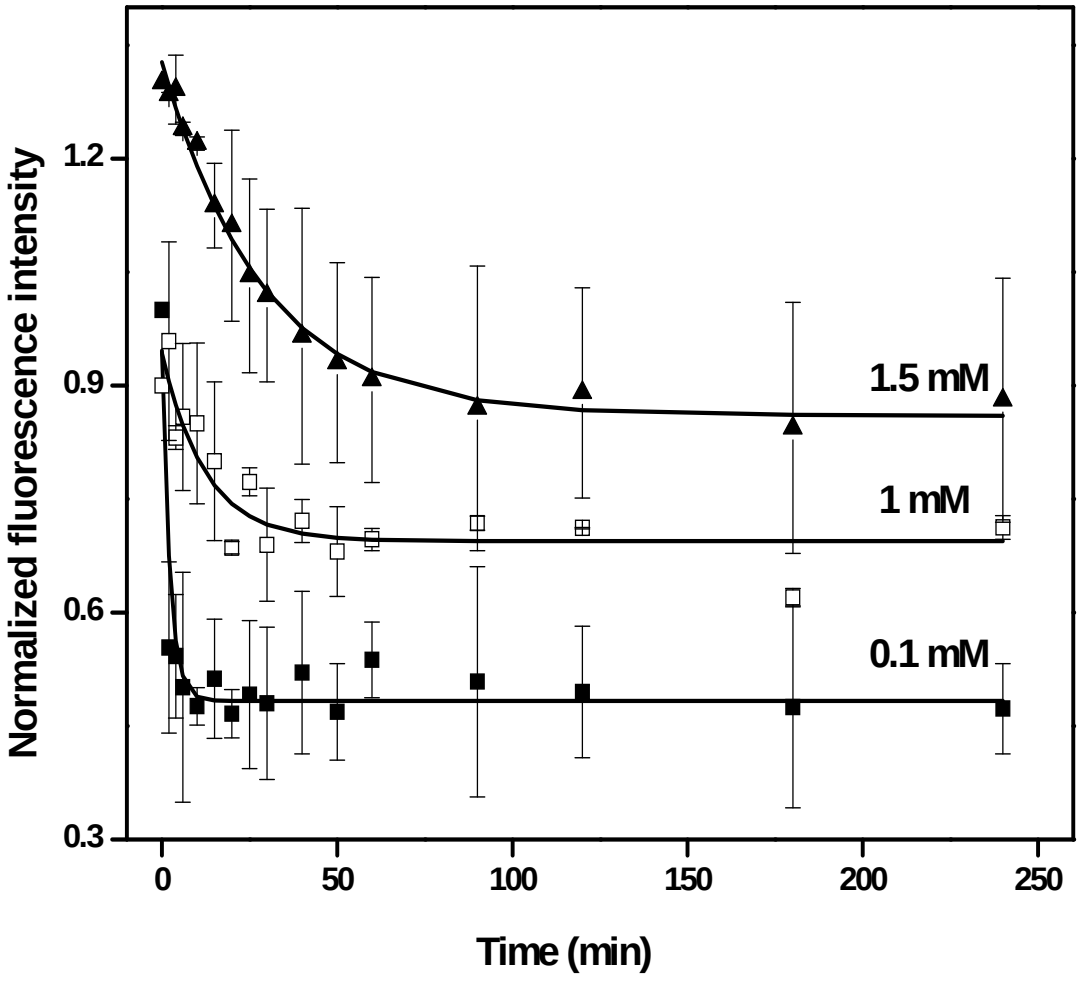

Figure 5.13. Same as Figure 5.6 but for different concentrations of Trp placed in an outer cuvette, i.e. concentric-cuvette arrangement. 0.1 mM (filled squares), 1 mM (open squares), 1.5 mM (filled triangles). The curves have been offset along the ordinate for clarity. The solid line through the points on each curve is the fit to an offset, single-exponential decay function, $y = y_o + Ae^{-t/\tau}$. Each data point is an average of three replicate measurements and the error bars correspond to the standard deviation of the measurements. The fluorescence time constants, τ, [y_o, A] for the different concentrations of Trp are 2.3 ± 0.1 min [0.48 ± 0.01, 0.46 ± 0.04], 12 ± 0.5 min [0.79 ± 0.01, 0.25 ± 0.03], and 29 ± 2 min [0.56 ± 0.01, 0.47 ± 0.01] for 0.1, 1 and 1.5 mM Trp, respectively. The individual curves are shown in Figures 5.14 to 5.16. Higher offset seen in these plot is due to residual fluorescence from the MB.

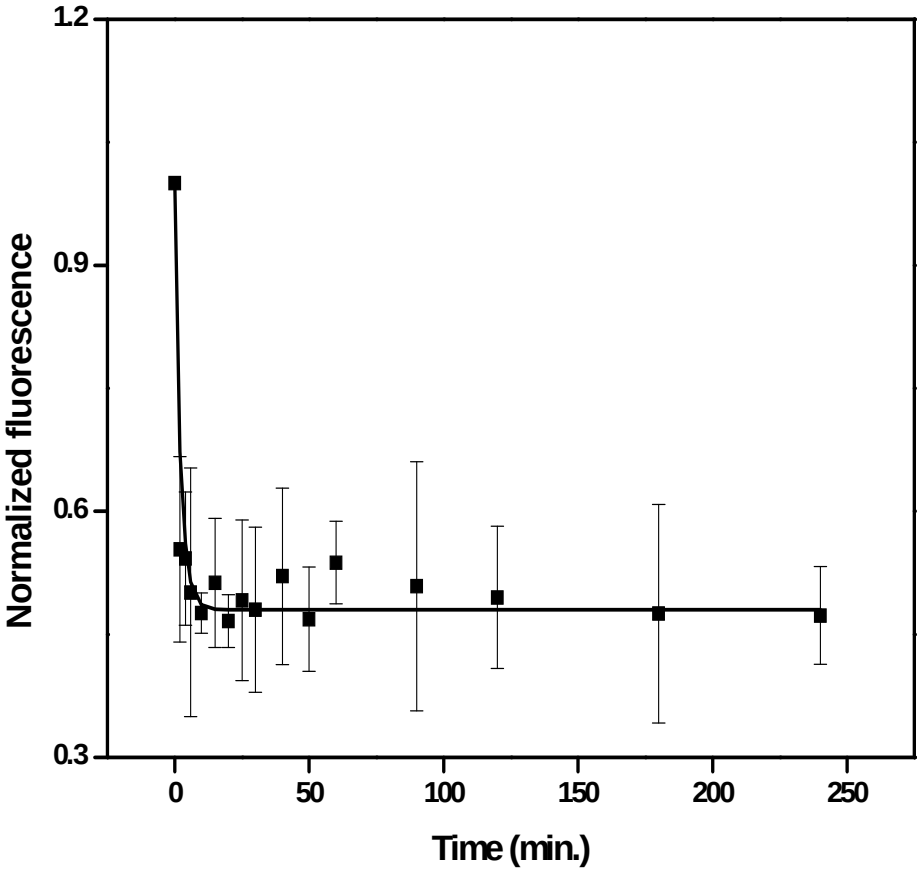

Figure 5.14 Plot of normalized fluorescence intensity vs irradiation time for a solution of target DNA solution immersed in a cuvette of 0.1 mM Trp. The fluorescence time constant, y_o and A for this DNA/Trp "sandwich" solutions are 2.3 ± 0.1 min, 0.48 ± 0.01 and 0.46 ± 0.04, respectively. Error bars representing the standard deviations are shown. Higher offset seen in this plot is due to residual fluorescence from the MB.

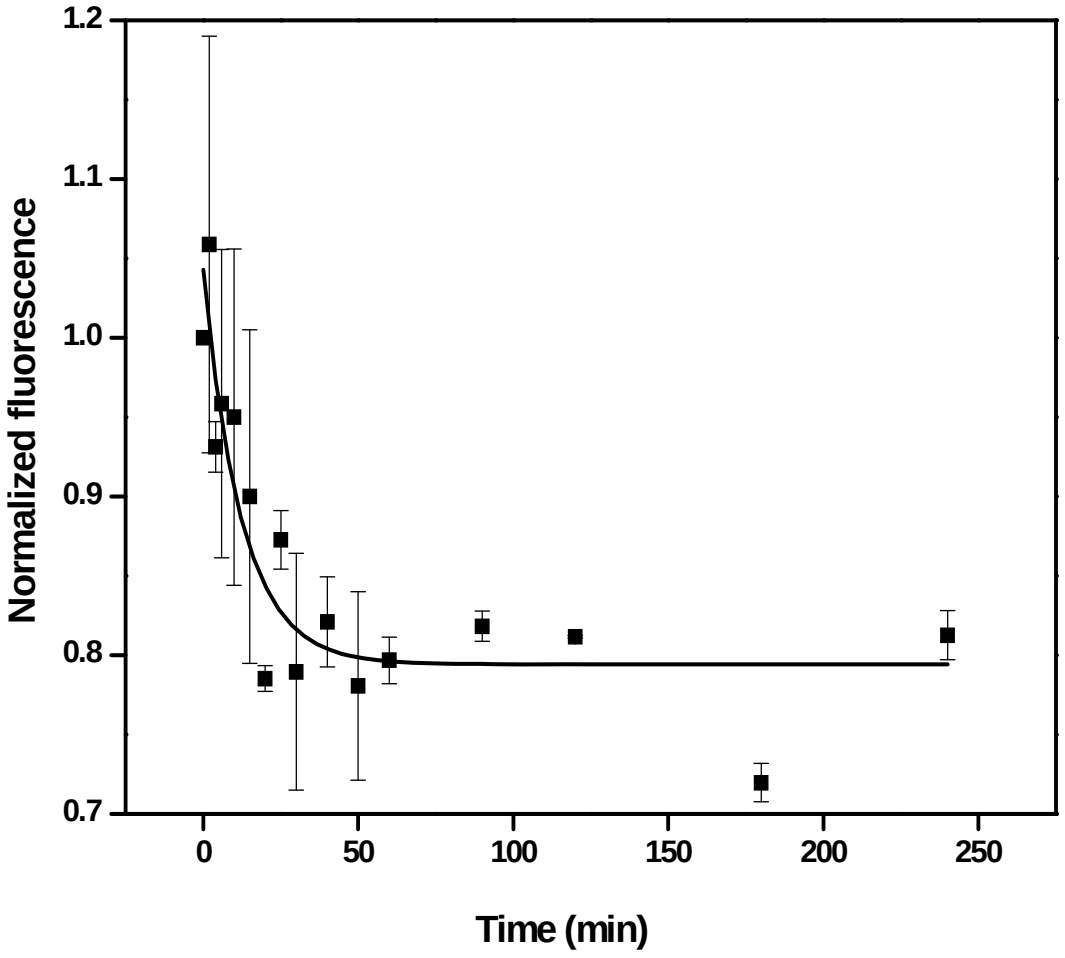

Figure 5.15 Same as Figure 5.14 but for a solution of 1 mM Trp. The fluorescence time constant, y_o and A for this DNA/Trp "sandwich" solutions are 12 ± 0.5 min, 0.79 ± 0.01 and 0.25 ± 0.03, respectively. Error bars representing the standard deviations are shown. Higher offset seen in this plot is due to residual fluorescence from the MB.

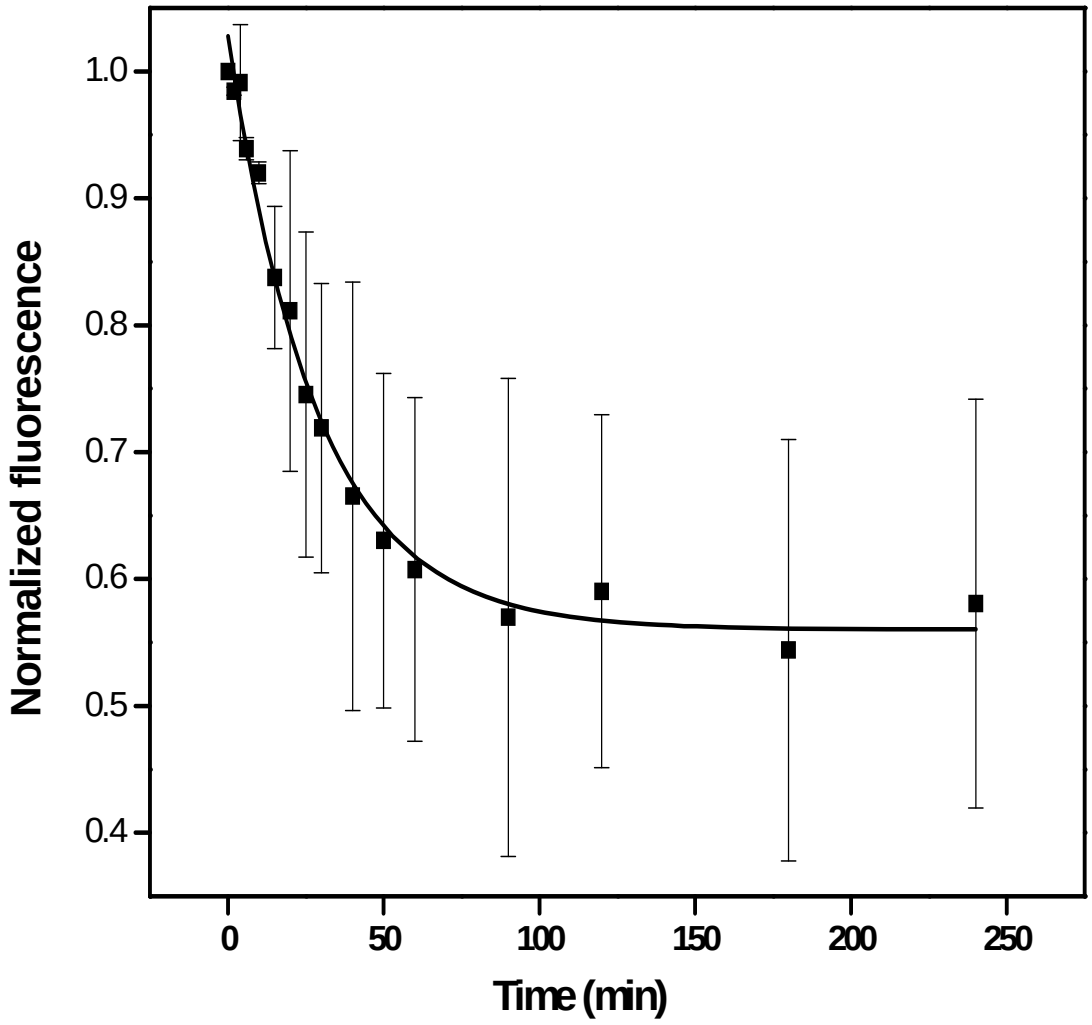

Figure 5.16. Same as Figure 5.14 but for a solution of 1.5 mM Trp. The fluorescence time constant, y_o and A for this DNA/Trp "sandwich" solutions are 29 ± 2 min, 0.56 ± 0.01 and 0.47 ± 0.01, respectively. Error bars representing the standard deviations are shown. Higher offset seen in this plot is due to residual fluorescence from the MB.

At higher Trp concentrations however, the kinetics are different for DNA/Trp kept in the same medium and in the concentric cuvettes. When the DNA-Trp are kept together, they both can compete for the incoming UV light, even though the Trp molecules are significantly more populous than the DNA molecules (250-375 Trp molecules per DNA molecule per unit volume). This simultaneous 'competition' leads to more DNA damage. But when the Trp is in the outer cuvette and the DNA is in the inner one, the large number of Trp molecules exclusively present in the outer layer would significantly absorb most of the incoming light, with the significantly attenuated light transmitted to the inner layer of DNA solution. This means that the rate of DNA damage in this concentric arrangement is much smaller and the damage is much less compared to the same medium DNA-Trp case (see Table 5.1).

The fact that the kinetics of fluorescence loss for irradiated solutions of DNA with 0.1 mM Trp present either in the same cuvette or in an outer cuvette are essentially the same suggests that the contribution of Trp-induced DNA damage products (Trp-DNA adducts) to *in vivo* DNA damage are insignificant (Table 5.1). If Trp-DNA adducts are significant, then we would expect to see a difference in kinetics when Trp is not present together with the DNA in the same cuvette, as there is no way a Trp-DNA cross-link can be formed in this case. But since preferential absorption by Trp is the predominant process, it does not matter if the Trp solution is placed together with the DNA or in an outer cuvette, because the preferential absorption by Trp in these two cases are similar, hence the observed similar kinetics of fluorescence loss. The results therefore corroborate our argument that the DNA is involved in competitive absorption with the Trp in the homogeneous solutions in which they are both present. In addition, this preferential absorption process and the attendant screening of DNA are much more significant than the formation of Trp-induced DNA damage products.

5.3.3 Mechanism and confirmation of Trp preferential absorption

In order to ascertain the mechanism by which Trp confers protection on DNA, we consider the following kinetic expressions. In the absence of Trp

$$\text{DNA} \xrightarrow{h\nu} \text{damaged DNA} \quad (5.1)$$

and the corresponding rate is

$$\frac{-d[DNA]}{dt} = k_1[DNA] \quad (5.2)$$

In the presence of Trp however, we have

$$\text{DNA + Trp} \xrightarrow{h\nu} \text{damaged DNA + Trp-DNA adducts + Trp photoproducts} \quad (5.3)$$

with the corresponding rate given by

$$\frac{-d[DNA]}{dt} = k_2[DNA][Trp] + k_1[DNA] \approx k_2'[DNA] \quad (5.4)$$

$$\text{where} \quad k_2' \approx k_2[Trp] + k_1 \quad (5.5)$$

since [Trp] >> [DNA]. In the absence of Trp ([Trp] = 0), k_2 reduces to k_1. Note that this mechanism predicts that the rate of any Trp-induced DNA damage should depend linearly on [Trp].

Alternatively, the mechanism through which Trp protects the DNA may be explained using the photochemical relation $k_{photochem} \propto I$ (where I is transmitted intensity). According to Beer's law, $I = I_o * 10^{-\varepsilon l[\text{Trp}]}$, where l is the pathlength, ε is the extinction coefficient and I and I_o are the transmitted and incident light intensities, respectively.[33] If Trp-induced protection occurs by preferential absorption of the UV light, then the rate constant k should be exponentially dependent on Trp concentration. Since we are detecting DNA damage, the rate constant for that damage should decrease exponentially with increasing [Trp]. Therefore,

$$k \propto e^{-\alpha l[Trp]} \quad (5.6)$$

where α represents the absorptivity of Trp. To test this proposed model, we plotted the observed rate constant *k* vs [Trp] (Figure 5.17). The data have been fitted with Eq. 5.6 and clearly show an exponential dependence on [Trp] .

The proportionality constant of 0.69 min^{-1} obtained from this fit is consistent with the experimentally observed value for k_1 (i.e. the [Trp] = 0 rate constant) of 0.82 $min.^{-1}$ and this shows the validity of our model. The effective pathlength obtained from this fit is the distance from the cuvette wall to the nearest Trp molecule on average. This argument is consistent with the rationale given for the *l* value in a previous study of the photodegradation of quinoline, where the photodegradation rate is affected by humic acid through the process of the inner-filter effect.[34] In this study, the authors used UV irradiation to remove the quinoline pollutant from water. They monitored the rate of removal of quinoline and found the kinetics of removal to be affected in a concentration-dependent manner by humic acid, which is co-present in the reactor. The plot of rate constant vs humic acid concentration gave an exponential curve similar to what is observed here. These authors ascribed the observed reduction in rate of quinoline removal to the absorption of the UV light by humic acid (inner- filter effect).

The implication of our results is that, similar to previous studies on the chromophoric absorption of harmful UV light as a means of protection for living organisms,[13-24] cellular nucleic acids may have a natural protection mechanism from UV photodamage in the associated amino acids and proteins, which are more significant and of course, beneficial to the cells, compared to the rather deleterious Trp-DNA adducts. This suggestion is reasonable, given the fact that the highest Trp concentration (10 mM) used in this study is in the same order of magnitude as the physiological concentration of Trp.[30-32] This may imply that the inherent protection mechanisms in living systems, by way of associated amino acids and proteins, regulate or minimize the extent of damage to cellular DNA. Moreover, an analogy can be drawn between the UV protective effect of Trp found in this study and the UV protective effects of

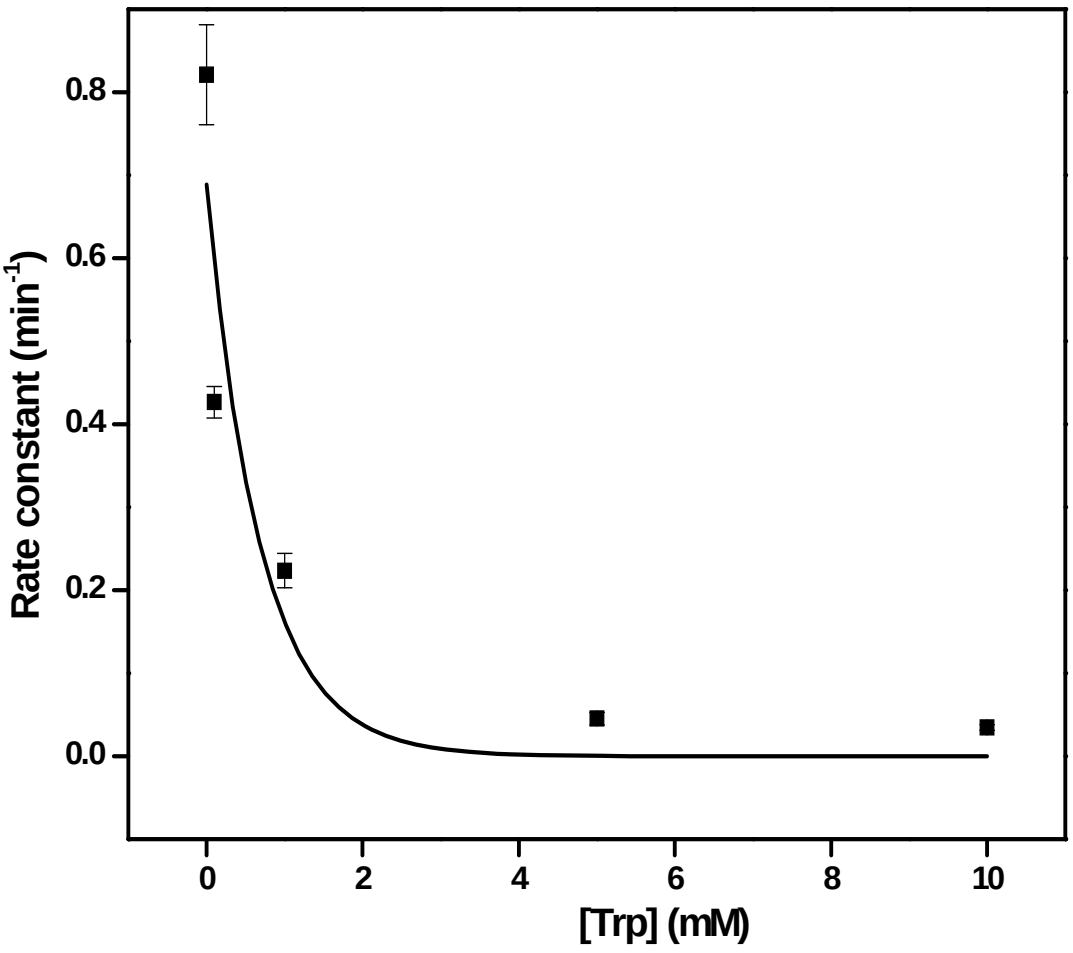

Figure 5.17: Plot of DNA photodamage rate constant as a function of Trp concentration. Each data point is an average of four measurements and the error bars representing the standard deviations are shown. The data points were fit to Eq. 5.6 in the text, with $\alpha = 3365 \pm 0$ min^{-1}, $l = 0.0004 \pm 0$ cm, a proportionality constant of 0.69 ± 0.08 min^{-1} and $R^2 = 0.88$.

DNA repair enzymes and RNA fragments recently reported.[35] Using topical formulations containing either DNA repair enzymes or RNA fragments, this recent report suggested that RNA fragments may be useful as a photoprotective agent with *in vivo* effects comparable to DNA repair enzymes.[35] Although, the mechanism of the observed protection is not yet fully understood.[35] it may be possible that the UV protective effects of Trp found in this study and that of DNA repair enzymes and RNA fragments earlier reported are synergistic mechanisms naturally established in living systems for reducing the extent of UV photodamage in cellular DNA. This suggestion indicates that further investigation is required to fully elucidate the processes that are at play *in vivo*, and of course, their underlying mechanisms.

5.4 Conclusions

This study demonstrates the significance and relevance of preferential or sacrificial absorption of UV light by Trp when Trp-containing DNA solutions are exposed to UV light. Our results suggest that the preferential absorption has an overriding effect when these solutions are irradiated and that Trp-induced DNA damage is comparatively negligible. We utilized the sensitivity and specificity afforded by MB probes to show that UV-induced DNA damage is reduced in a Trp concentration-dependent manner. We also found the DNA photodamage rate constants to be an exponential function of the Trp concentration, consistent with a sacrificial or preferential absorption/screening of UV light by Trp molecules. These results suggest that cellular nucleic acids may have a natural protection mechanism from UV-induced damage in the associated amino acids and proteins.

5.5 References

(1) Douki, T.; Cadet, J. *Biochemistry* **2001**, *40,* 2495-2501.

(2) Ravanat, J.-L.; Douki, T.; Cadet, J. *J. Photochem. Photobiol. B: Biol.* **2001,** *63,* 88-102.

(3) Ruzsicska, B. P.; Lemaire, D. G. E. In *DNA Photochemistry;* Horspool, W. M.; Song, P.-S. Eds.; CRC Handbook of Organic Photochemistry and Photobiology; CRC Press, New York. 1995, pp. 1289-1317.

(4) Wagner, D. M.; Loppnow, G. R. *Spectrum* **2004,** *17,* 26-29.

(5) Yarasi, S.; McConachie, C.; Loppnow, G. R. *Photochem. Photobiol.* **2005,** *81,* 467-473.

(6) Reeve, A. E.; Hopkins, T. R. *Photochem. Photobiol.* **1980,** *31,* 297-304.

(7) Wetlaufer, D. B. *Adv. Protein Chem.* **1962,** *17,* 303-390.

(8) Voet, D.; Gratzer, W. B.; Cox, R. A.; Doty, P. *Biopolymers* **1963,** *1,* 193-208.

(9) Reeve, A. E.; Hopkins, T. R. *Photochem. Photobiol.* **1979,** *30,* 677-681.

(10) Reeve, A. E.; Hopkins, T. R. *Photochem. Photobiol.* **1980,** *31,* 413-415.

(11) Saito, I.; Sugiyama, H.; Matsuura, T. *Tetrahedron Lett.* **1984,** *25,* 3243-3246.

(12) Saito, I.; Matsuura, T. *Acc. Chem. Res.* **1985,** *18,* 134-141.

(13) McIntyre P.; Kirschfeld, K. *J. Comp. Physiol.* **1981,** *143,* 3-15.

(14) Zhu, H.; Kirschfeld, K. *J. Comp. Physiol. A.* **1984,** *154,* 153-156.

(15) Kirschfeld, K.; Feiler, R.; Franceschini, N. *J. Comp. Physiol.* **1978,** *125,* 275-284.

(16) Burger J.; Edwards, G. E. *Plant Cell Physiol.* **1996,** *37,* 395-399.

(17) Chalker-Scott, L. *Photochem. Photobiol.* **1999,** *70,* 1-9.

(18) Nishio, J. N. *Plant Cell Environ.* **2000,** 23, 539-548.

(19) Feild, T. S.; Lee, D. W.; Holbrook, N. M. *Plant Physiol.* **2001,** *127,* 566-574.

(10) Pietrini, F.; Iannelli, M. A.; Massacci, A. *Plant Cell Environ.* **2002,** *25,* 1251-1259.

(21) Neil, S. O.; Gould, K. *Funct. Plant. Biol.* **2003,** *30,* 865-873.

(22) Wiliams, E. L.; Hovenden, M. J.; Close, D. C. *Funct. Plant. Biol.* **2003,** *30,* 1205-1218.

(23) Hormaetxe, K.; Hernández, A.; Becerril, J. M.; García-Plazaola, J. I. *Plant Biology.* **2004,** *6,* 325-332.

(24) Manetas, Y.; Petropoulou, Y.; Psaras, G. K.; Drinia, A. *Funct. Plant. Biol.* **2003,** *30,* 265-270.

(25) Sokol, D. L.; Zhang, X.; Lu, P.; Gewirtz, A. M. *Proc. Natl. Acad. Sci. USA* **1998,** *95,* 11538-11543.

(26) Bonnet, G.; Tyagi, S.; Libchaber, A.; Kramer, F. R. *Proc. Natl. Acad. Sci. USA* **1999,** *96,* 6171-6176.

(27) Leone, G.; van Schijndel, H.; van Gemen, B.; Kramer, F. R.; Schoen, C. D. *Nucleic Acids Res.* **1998,** *26,* 2150-2155.

(28) Tyagi, S.; Kramer, F. R. *Nature Biotechnol.* **1996,** *14,* 303-308.

(29) Kundu, L. M.; Burgdorf, L. T.; Kleiner, O.; Batschauer, A.; Carell, T. *ChemBioChem.* **2002,** *3,* 1053-1060.

(30) Guyton, A. C.; Hall, J. E. (2006) In *Textbook of Medical Physiology*, Eleventh edition, W. B. Saunders Company, Philadelphia, 2006, pp. 11-26.

(31) Guyton, A. C. Hall, J. E. In *Textbook of Medical Physiology*, Eleventh edition, W. B. Saunders Company, Philadelphia, 2006, pp. 865-880.

(32) Laich, A.; Neurauter, G.; Widner, B.; Fuchs, D. *Clin. Chem.* **2002,** *48,* 579-581.

(33) Tinoco Jr., I.; Sauer, K.; Wang, J. C. Physical Chemistry: principles and applications in biological sciences. Prentice-Hall Inc., Englewood Cliffs, 1985.

(34) Enriquez, R.; Pichat, P. *Langmuir* **2001,** *17,* 6132-6137.

(35) Ke, M. S.; Camouse, M. M.; Swain, F. R.; Oshtory, S.; Matsui, M.; Mammone, T.; Maes, D.; Cooper, K. D.; Stevens, S. R.; Baron, E. D. *Photochem. Photobiol.* **2008,** *84,* 180-184.

Chapter 6

Self-quenching Smart Probes as a Platform for Multiplex Detection of Specific DNA Sequences and UV-Induced DNA Photodamage

6.1 Introduction

Molecular beacon probes[1,2] are hairpin oligonucleotides with a fluorophore on one end and a quencher on the other. They display minimal fluorescence in the absence of target DNA sequence, but they give significant increase in fluorescence in the presence of the complementary target sequence. These probes have been used for a large number of DNA sequence applications due to their excellent sensitivity and specificity.[3-6] The built-in signaling property of molecular beacons (MBs), which is now well-established[1,2] is due to the hairpin conformation of these probes and distance-dependent fluorescence energy transfer (FRET) between a fluorophore and a quencher on each end of the probe.

In MBs, the loop sequence is designed to be complementary to the target DNA sequence, or at least, to the portion of the target sequence to be detected. In the absence of target DNA, they exist in the stem-loop structure and so the fluorophore is in close proximity to the quencher. Therefore, there is minimal fluorescence as a result of FRET. However, in the presence of the complementary target sequence, the loop sequence of MBs hybridizes with the target. The stem unwinds thereby forcing the fluorophore and the quencher far apart, resulting in a significant increase in fluorescence. In the presence of a single base mismatch, the hybrid formed between the probe and the mismatch sequence is less stable since this target is not perfectly complementary to the loop of the probe. Thus, the fluorescence is lower for this hybrid compared to that formed between the perfectly complementary sequence and the probe. These inherent properties make MBs very sensitive and specific.[1-6]

However, despite the wide applications and the exquisite sensitivity and selectivity of MBs, they have limitations.[7-12] For instance, MBs require site-specific labelling of each terminus of the hairpin with a fluorophore and a quencher, respectively. This dual labelling makes their synthesis and purification difficult and expensive.[7,8,10,12] The high cost of MBs makes their use for multiplex analysis of a large number of different specific DNA sequences unattractive. Since the two termini of the hairpin are already occupied by the donor and acceptor, any further modification, for example, for attachment to a solid support, would require the incorporation of an additional modified nucleotide into the stem.[7,10] Furthermore, due to incomplete attachment of the quencher, some hairpins may only be labelled with the fluorophore. In this case, highly sensitive assays would be interfered with by a high background due to unquenchable probe molecules.[7,8]

Instead of using FRET between two extrinsic labels, FRET between a fluorophore with intrinsic nucleobases can be used for the specific detection of DNA or RNA sequences.[10] Recently, hairpin probes that take advantage of the selective quenching of fluorophores by neighbouring guanosine residues were introduced.[7-10,12-14] These novel hairpin probes, called smart probes (SPs), are oligonucleotide probes just like MBs (Figure 6.1). However, with these probes, quenching is achieved via photoinduced intramolecular electron transfer upon contact between the fluorophore and the guanosine residues.[10,13] Thus, these self-quenching smart probes contain a fluorescent dye on one end and a set of guanosine residues on the other (Figure 6.1). The quenching can be made substantially more efficient by the attachment of additional overhanging guanosine residues at the end opposite to the fluorophore (Figure 6.1).[10]

SPs are designed in a similar fashion to MBs, with consecutive guanosine residues replacing the extrinsic quencher. They are also sensitive and specific in recognizing target DNA sequences. As demonstrated with confocal fluorescence microscopy, these probes are capable of single-molecule level detection.[8] By careful design and selection of the appropriate fluorophore, these probes have been shown to give a fluorescence increase of up to 20-fold

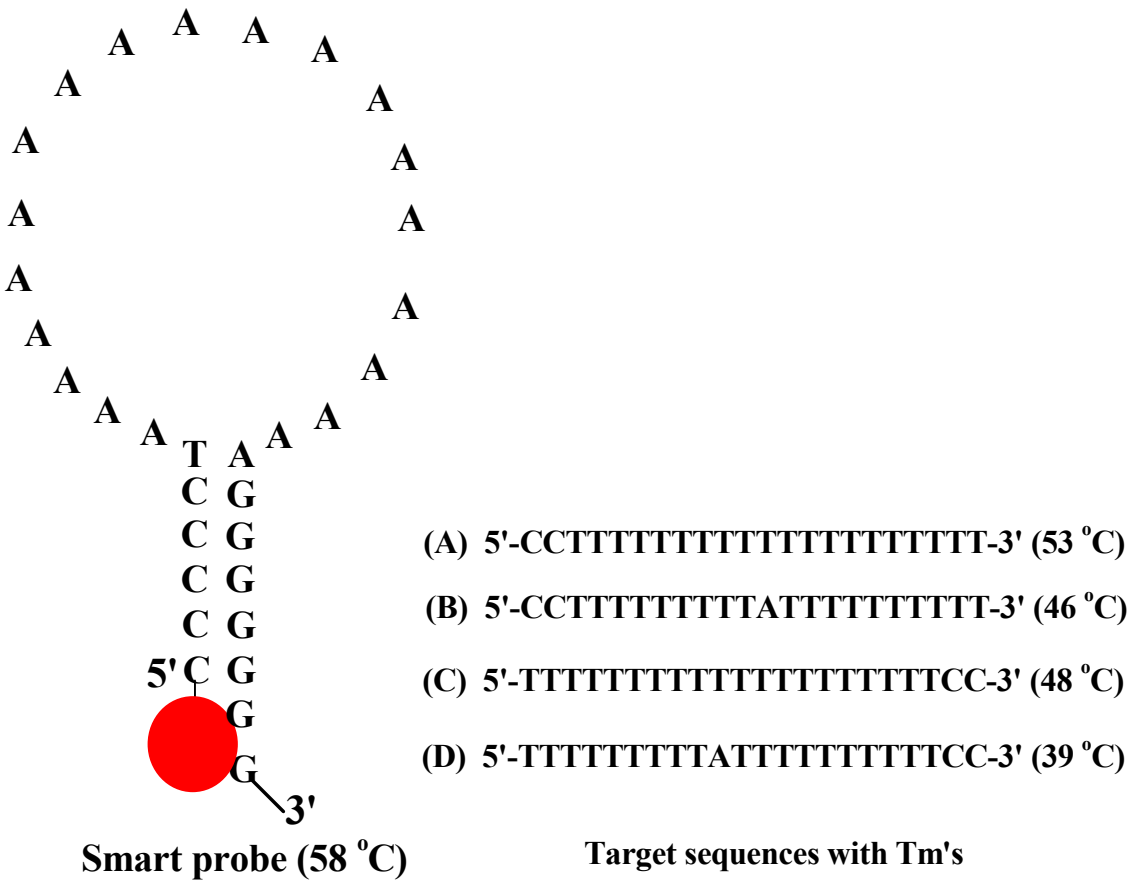

Figure 6.1. The hairpin structure of the smart probe used in this work. The contact between the GG overhangs and the melting temperature of the SP are shown. All four target and mismatch sequences with their respective melting temperatures are also shown**.**

upon hybridization to the target sequence.[7,9,10]

In SPs, intramolecular fluorescence quenching via photoinduced intramolecular electron transfer is achieved by the low oxidation potential of guanosine.[7,10,15,16] Depending on the reduction potential of the fluorophore on the hairpin, efficient fluorescence quenching occurs upon contact between the fluorophore and guanosine.[7,10,17] In contrast to MBs, SPs are relatively easy to synthesize (single labelling step), they are less expensive and they have a free terminus at the poly-guanosine end for further modifications.[7] Thus, these probes represent cost-effective alternatives to MBs and constitute an ideal platform for multiplex homogeneous and heterogeneous DNA sequence analysis.

The deleterious effects of the UV radiation of DNA on the health of organisms has been well-documented.[18] Therefore, the sensitive and precise measurement of DNA damage and repair is essential for understanding the lethal and mutagenic effects of UV-induced DNA photoproducts.[6] Although SPs have been used for specific DNA sequence applications, they have not been tested as probes for UV-induced DNA photodamage. In this chapter, we report the careful design and characterization of a SP and its use for monitoring UV-induced photoproduct formation in DNA model oligonucleotides. The specificity of this probe is also demonstrated by its ability to discriminate between closely similar target oligonucleotide sequences which only differ by a single base. The conditions for best performance of these probes based on our experimental findings are also highlighted. The low cost of synthesis of these probes compared to MBs make them a suitable candidate for multiplex DNA sequence analysis.

6.2 Experimental

6.2.1 Materials and methods

The single-strand target oligonucleotide, 5'-CCTTTTTTTTTTTTTTTTTTT-3' (target sequence A), the mismatch target oligonucleotide, 5'-CCTTTTTTTTTATTTTTTTTTT-3' (with one non-complementary base, henceforth called single mismatch sequence B), 5'-TTTTTTTTTTTTTTTTTTTCC-3' (with two non-complementary bases, henceforth called double mismatch sequence C) and 5'-TTTTTTTTTATTTTTTTTTCC-3' (with three non-complementary bases, henceforth called triple mismatch sequence D), and the SP, 5'-(6-FAM)-CCCCCTAAAAAAAAAAAAAAAAAAGGGGGGG-3' (where 6-FAM is 6-carboxyfluorescein), were custom-synthesized by Integrated DNA Technologies Inc. (Coralville, IA, USA). The fluorophore (6-FAM) is attached to the 5' end of the SP (Figure 6.1). The target oligonucleotides were purified by standard desalting, while the SP was purified by HPLC. The sodium hydroxide (NaOH), sulfuric acid (H_2SO_4) and hydrochloric acid (HCl) were obtained from BDH Inc. (Toronto, ON, Canada), Caledon Laboratories Ltd. (Georgetown, ON, Canada) and Anachemia (Montreal, QC, Canada), respectively. The magnesium chloride ($MgCl_2$) and sodium chloride (NaCl) were both obtained from EMD Chemicals Inc. (Gibbstown, NJ, USA). Tris and ethylenediamine-tetraacetic acid (EDTA) were obtained from ICN Biomedicals, (Aurora, OH, USA), and BDH Inc. (Toronto, ON, Canada), respectively. All chemicals were used as received. Nanopure water from a Barnsted Nanopure (Boston, MA, USA) system was used for all solutions.

The SP was first annealed before dissolution in nanopure water, to ensure that all the SP molecules are in the correct conformation when used. The annealing was performed by rapidly heating the SP contained in the sample vial to a temperature of about 70 ^{o}C in a water bath, followed by gradual cooling to room temperature in the same bath. The sample vial was carefully wrapped in aluminium foil and sealed with parafilm.

Oligonucleotide samples and smart probes were each dissolved in nanopure water and kept frozen at -20 ^{o}C until needed. Upon thawing, they

were diluted in buffer (10 mM Tris, 1 mM EDTA, pH 7.5) in the presence of 5 mM $MgCl_2$ to give the desired concentrations. In solutions in which SPs are present, NaCl was also added to a final concentration of 20 mM. The concentrations of the target oligonucleotide solutions were confirmed by UV absorbance measurements at 266 nm.

6.2.2 UV irradiation

All irradiation experiments were carried out as described in Chapter 5. In this case however, 4 mL of 8 μM nitrogen-purged solutions of target sequence A, (5'-CCTTTTTTTTTTTTTTTTTTT-3') the mismatch sequence B (5'-CCTTTTTTTTATTTTTTTTT-3'), the double mismatch sequence C (5'-TTTTTTTTTTTTTTTTTTCC-3'), and the triple mismatch sequence D (5'-TTTTTTTTATTTTTTTTTCC-3'), were irradiated.

6.2.3 Absorption and fluorescence measurements

Absorption spectra of the irradiated samples were recorded on a Hewlett-Packard 8452A diode array spectrophotometer (Sunnyvale, CA USA), by placing the irradiated solutions contained in photochemistry cuvettes directly into the spectrophotometer. For fluorescence measurements, a 20-μL aliquot of each irradiated solution was taken at various time intervals, and was later mixed with appropriate amounts of SP and the buffer solution in the presence of 5 mM $MgCl_2$ and 20 mM NaCl to give final concentrations of 400 nM oligonucleotide and 100 nM SP. These solutions were then incubated in the dark at room temperature for about 24 hours. Fluorescence spectra of the incubated samples were measured using a Photon Technologies International (Birmingham, NJ, USA) fluorescence system. The spectra were recorded between 500 and 700 nm with excitation at 495 nm using 4 nm slits. A 10-mm pathlength, Suprasil quartz, fluorescence cuvette was used for these measurements. The spectra were recorded at room temperature on a 200- to 400-μL aliquot of the SP-oligonucleotide hybridization mixture.

The SPs were characterized by thermal denaturation profile experiments, in which temperature-dependent fluorescence measurements were carried out

on buffer solutions of SP incubated in the absence or presence of the target oligonucleotide sequence or the mismatch target sequences. The temperature was varied from 20 – 68 ^{o}C at 4 ^{o}C increment, a heating rate of 1 ^{o}C/min and 5 min settling time (for proper equilibration at set temperatures) for the heating cycle, and 68 – 20 ^{o}C for the reverse cooling cycle. SP concentrations of 200 nM in the presence of 20-fold excess target oligonucleotide sequence and 20 mM NaCl were used for this set of measurements.

6.3 Results and Discussion

6.3.1 Design of SP and target sequences

The SP was carefully designed to maximize its performance as a sensitive and specific probe. This was achieved by ensuring that the conformation of the probe was extremely sensitive to changes in temperature, by way of having the stem melting temperature reasonably higher than the probe-target hybrid melting temperature. The fluorophore is on the 5' end and the guanosine quenchers are on the 3' end. To optimize the quenching by the guanosine residues, 7 guanosine residues were put on the 3' end, five of which form part of the stem and are complementary to the cytosine residues on the 5' end of the probe, and the remaining two form an overhang to further enhance the quenching efficiency.[10] As for the target and mismatch sequences, two sequences (A and C) are perfectly complementary to the loop of the SP, while two others (B and D) have a single base mismatch in the complementary loop sequence (Figure 6.1). Also, sequence C and D both have two base mismatches with the stem of the probe. Finally, to enhance the recognition and enhanced specificity of the SP, three residues in sequences A and B are made to be complementary to the stem on the 3'-end.

Previous reports on smart probes have also used various concentrations of NaCl, but the effect of this salt on the performance of the probe was never explained.[7-9,19,20] However, we believe the salt has the typical counterion effect of stabilizing dsDNA. For our experiments, the melting curve for the SP

has an atypical pattern (data not shown) in the absence of NaCl, probably because the guanine-rich 3' end forms guanine tetraplexes, also known as G-tetraplexes or cruciform structures.[21] However, when 20 mM NaCl is added, a melting curve with the proper shape was obtained (Figure 6.2). It has been previously reported that sodium ions do not stabilize G tetraplexes.[21-23] Thus, the formation of G-tetraplexes by this guanine-rich 3' end is probably prevented by the addition of 20 mM NaCl, which helps to better stabilize the hairpin structure of the probe and prevent it from forming G-tetraplexes.

6.3.2 Thermal characterization and stability of the SP

The intended use of the SP is for assaying specific DNA sequences and in discriminating between single base mismatches. Since they have essentially the same properties and conformational structures with MBs, the factors affecting SP hybridization and their temperature-dependent conformations, such as electrostatic effects, relative melting temperatures of the loop and the stem, and probe-to-target concentration are similar to those already discussed for MB.[1-5,24] To ensure the correct design and performance of the SP, thermal denaturation profiles of the SP were measured. Figure 6.2 shows the melting curves derived from the heating cycle for the SP and SP-target sequence hybrids for four specific oligonucleotide sequences.

For the SP alone (filled squares, Figure 6.2), at low temperatures, it exists in the hairpin form and so the fluorophore is in contact with the guanosine residues on the 3' end and there is minimal fluorescence due to photoinduced intramolecular electron transfer. When the temperature is increased to about 50 ^{o}C, the stem begins to melt and the fluorophore begins to separate from the quenching guanosine residues. This is indicated by the slight increase in fluorescence intensity beginning at about 52 ^{o}C. When the temperature is further increased, the fluorophore and the quencher are further separated, until the stem completely melts. This is evidenced by the increase in fluorescence intensity with temperature between 52 and 63 ^{o}C, at which point the fluorescence intensity becomes constant and the SP assumes a random coil conformation.

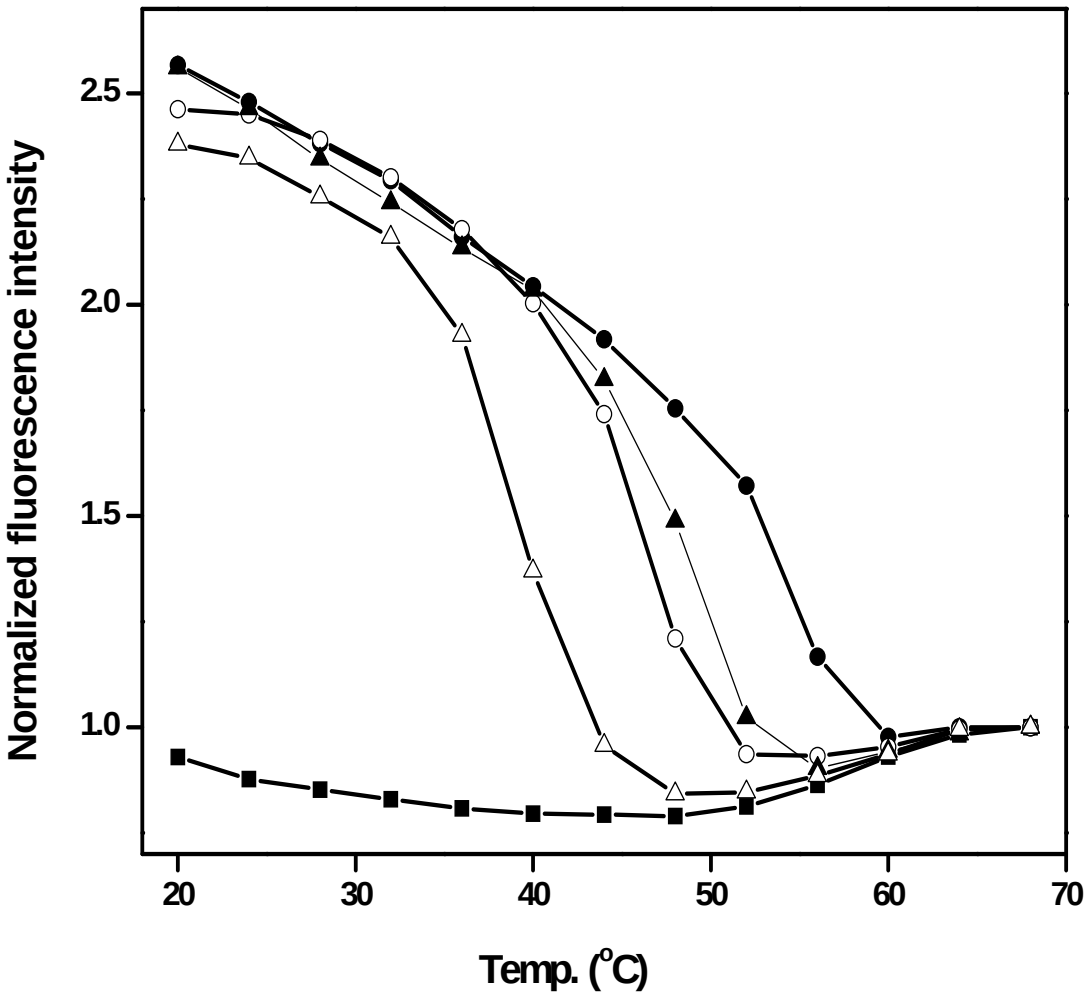

Figure 6.2. Thermal denaturation profile curves for 200 nM smart probe alone (filled squares), 200 nM smart probe in the presence of a 20-fold excess of perfectly complementary oligonucleotide target sequences with different stem-complementary overhangs (A, filled circles; C, filled triangles) and 200 nM smart probe in the presence of a 20-fold excess of mismatch oligonucleotide target sequences, also with different stem-complementary overhangs (B, open circles; D, open triangles). All these melting curves were generated at a heating rate of 1 ^{o}C/min, in 4 ^{o}C increments and 5 minutes holding time per increment. The curves shown are the heating cycles. The corresponding cooling cycle for each curve (not shown) is identical to the heating cycles shown here, indicating that no hysteresis was observed. The melting temperature for each sample is shown in Figure 6.1 and explained in the text.

In the presence of a 20-fold excess of perfectly complementary target (target sequence A), the fluorescence intensity starts out very high at low temperatures (Figure 6.2, filled circles), because the target hybridizes with the loop sequence of the SP, thereby forcing the fluorophore and the guanosine residues apart. Increasing the temperature gradually melts the stable hybrid and causes the fluorescence to decrease with temperature. This decrease continues with temperature until the target completely melts away from the probe and the SP assumes a hairpin conformation, when the fluorophore will be in contact with the guanosine residues. This is indicated by the lowest point on the curve, pointing to the minimal fluorescence observed when there is contact between the fluorophore and the quenching guanosine residues. As the temperature is further increased, the stem of the hairpin also gradually melts and the fluorescence intensity begins to increase again until the SP becomes a random coil when the fluorescence intensity also assumes a limiting value. There is about a 3-fold increase in fluorescence intensity at 20 ^{o}C when the curve for the SP alone is compared to the SP-target sequences curves. This increase is consistent with that reported previously for the oxazine dye MR121 in a smart probe.[7] Similar patterns are observed when there is a single (Figure 6.2, open circles), double (filled triangles) and triple (open triangles) base mismatches in the target. The same fluorescence intensity trend is followed by these more unstable hybrids but their melting temperatures are lower.

Target sequence A has three residues, CCT at the 5' end that are complementary to the probe stem (Figure 6.1), while double mismatch sequence C has only one residue, T that is complementary to the stem. As expected, target sequence A would require a higher temperature than the double mismatch sequence C, because of the extra two CC bases, which are absent in the double mismatch sequence C, for this target to completely separate from the probe. Therefore, the divergence observed in the melting curves of these two sequences is due to the difference in stem complementarity between them, since both sequences have perfect loop complementarity. A similar argument holds for the hybrids of single mismatch

sequence B and triple mismatch sequence D. The divergence in their melting curves must be due to the difference in stem complementarity, as they both have the same single base mismatch in the sequence that binds to the loop of the probe.

The melting temperature (T_m) for the probe and different probe-target sequence hybrids are shown in Figure 6.1. The T_m is in the order A>C~B>D. This result is expected, as the two extra G-C's present in sequences A and B hybrids makes their T_m's higher than for C and D, respectively. The effect of base complementarity to the stem of the probe is evident in the T_m's of targets which only differ in base complementarity with the stem. For instance, when target sequence A is compared with double mismatch sequence C, the difference in T_m is due to the extra CC present at the 5' end of target sequence A, which are absent in the double mismatch sequence C. This is true when we consider that the two CC mismatches at the 3' end of double mismatch sequence C makes no contribution to the thermodynamic stability of the hybrid, since reliable theoretical predictions gave the same T_m whether or not the two CC mismatches on the 3' end of double mismatch sequence C are present.[25-33] The results also show that the level of discrimination based on the loop mismatch (single base) is more than that due to lack of stem complementarity. For example, single mismatch sequence B, which differs from target sequence A by only a single base mismatch in the loop has a T_m of 46 ^oC, while double mismatch sequence C which differs from target sequence A (T_m of 53 ^oC) by the absence of CC complements at its 5' end has T_m of 48 ^oC. Only one base mismatch in the loop causes slightly more change in T_m, compared to two bases which are non-complementary in the stem. The lower T_m of single mismatch sequence B (one base mismatch in the loop) despite the absence of CC complements at the 5' end of double mismatch sequence C, is an indication that the recognition capability of these probes predominantly lies in the loop, as the lack of stem complementarity make only small difference to T_m. That the T_m of each specific oligonucleotide sequence is different from those of others is a direct result of the exquisite selectivity of the SP used in

this work. Thus, these novel probes have excellent specificity to be able to easily discriminate between DNA sequences that differ by only a single base.

The shape of the thermal denaturation profiles and the difference in melting temperatures between SP only and SP-target hybrids (5 ^{o}C for sequence A and 10 ^{o}C for sequence C) are similar to those found for different MB-target hybrids in earlier reports.[2,6] Similarly, the difference in melting temperatures between SP-target hybrids (A and C) and SP-mismatch hybrids (B and D) (7 ^{o}C between A and B, and 9 ^{o}C between C and D) are consistent with those previously found for SP-mismatch target hybrids.[20] Therefore, based on the hybrid melting temperatures, specific DNA sequences can be easily distinguished even down to the level of single base mismatches. The relatively low concentration of the SP used here (100 - 200 nM) reflects the exquisite sensitivity of these probes, while the specificity of this probe is evident from the T_m difference between the SP-target hybrids and SP-mismatch hybrids (Figure 6.2). Thus, these smart probes possess excellent sensitivity and specificity.

6.3.3 Detection of UV-induced DNA photodamage with SP

Target and mismatch oligonucleotide solutions (Figure 6.1, sequence targets A, B, C and D) were irradiated at constant temperature, and the resultant damage was detected in real-time by UV-Vis absorption measurements of the irradiated and control samples. In addition, we also carried out fluorescence measurements of incubated solutions of SP with aliquots of the irradiated samples of the oligonucleotide solutions. Aliquots of unirradiated samples of these solutions were also incubated with SP as controls. It must be noted that the SP was not irradiated, it was only incubated with aliquots of irradiated oligonucleotide solutions, as well as their unirradiated controls.

The absorption spectra of the irradiated target sequence A and the mismatch sequence B are shown in Figure 6.3 (A) and (B), respectively. In both spectra, the main absorption band in the oligonucleotides at 266 nm, which represents the $\pi\pi^*$ transitions of the nucleobases, is seen to decrease

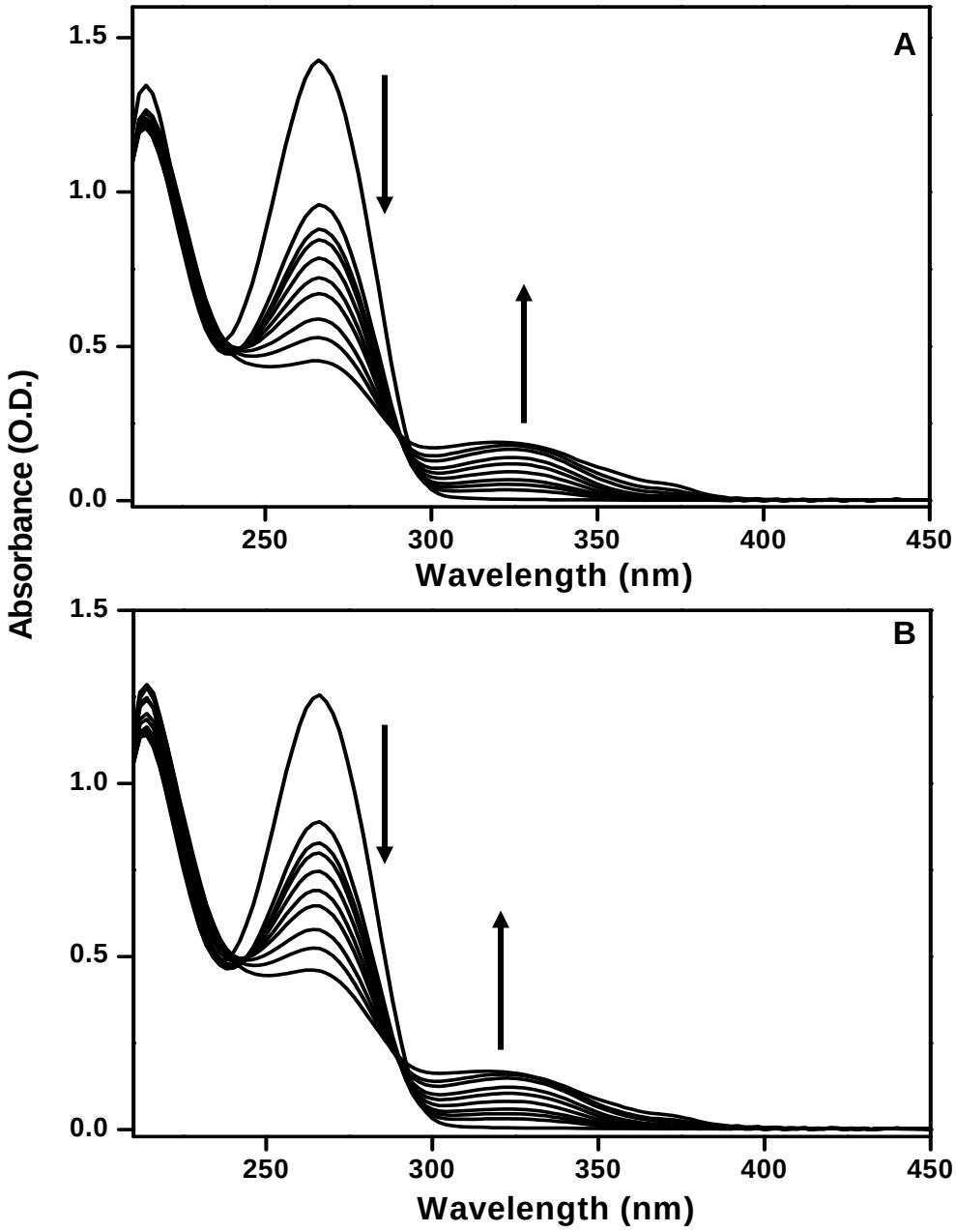

Figure 6.3. (A) UV-Vis absorption spectra of 8 μM target sequence A. The band at 266 nm represents the ππ* nucleobase transition and it decreases with irradiation time, while the band at 330 nm represents that of the pyrimidine-pyrimidinone [6-4] photoproduct and increases with irradiation time as shown. (B) Same as (A) but for single mismatch sequence B. Note that only the spectra for 0-60 min irradiation are shown here.

with time. These results are expected and indicate UV- induced damage to the oligonucleotides. The band at ca. 330 nm, which is an indicator of the pyrimidine-pyrimidinone [6-4] photoproduct being formed as a result of UV irradiation, is seen to increase with time. The spectra shown in Figure 6.3 (A) and (B) are for irradiation times between 0 and 60 min. From irradiation times of 0 to 240 min, the band at 266 nm continuously decreases with time. However, the band at 330 nm increases from 0 to 60 min (Figure 6.3), and then starts to decrease from 90 min onwards (Figure 6.4). This decrease indicates that the photoproduct starts to form secondary photoproducts at 90 min and later. The absorption spectra for the control samples show no change from 0 - 240 min (Figure 6.5), indicating that the decrease observed in the absorption spectra of irradiated samples is as a result of the exposure of these samples to UV radiation. Also, the trends in the absorption spectra for these two irradiated oligonucleotide samples (Figure 6.3) are indistinguishable from one another. The absorbance spectra for double mismatch sequence C and triple mismatch sequence D show similar trends (Figures 6.6-6.8) and there is little difference between the spectra. These results show that the photoproducts formed in these target sequences are similar and that the UV-Vis absorption spectra are insensitive to subtle differences in oligonucleotide sequences.

Shown in Figure 6.9A are the fluorescence emission spectra of SP in the presence of a 4-fold excess of target sequence A at different irradiation times, while Figure 6.9B shows the fluorescence emission spectra of SP in the presence of a 4-fold excess of target sequence B under identical irradiation conditions and at similar irradiation time intervals. It can be seen from these figures that the fluorescence intensity decreases with time in both cases. Similar spectra for the double mismatch and triple mismatch sequences C and D are shown in Figure 6.10. The fluorescence spectra of the unirradiated control samples show essentially no change in intensity with time (Figures 6.11 and 6.12), indicating that no damage took place in these unirradiated samples as indicated by the essentially constant fluorescence intensity. Although a 4-fold excess of target sequences were used here, these probes are

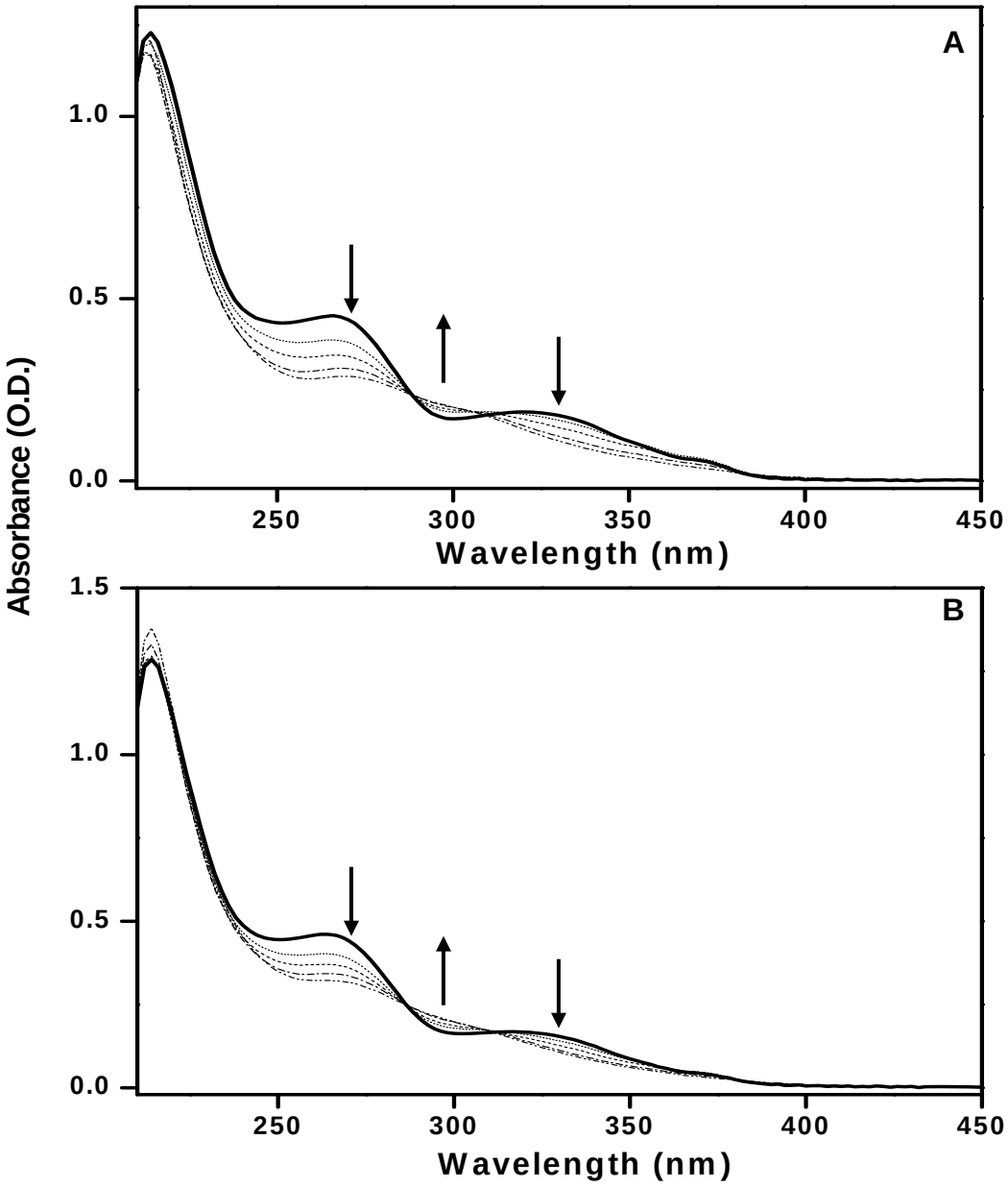

Figure 6.4. (A) UV-Vis absorption spectra of 8 μM target sequence A as a function of irradiation times for 60 min (solid line). 90 (short dot), 120 (short dash), 180 (dash dot) and 240 (dash dot dot) min irradiation times are shown to indicate that the photoproduct band at 330 nm starts decreasing at 90 min. of irradiation. Also, a new isosbestic point is formed at 315 nm as a result of the 330 nm band decrease. (B) Same as (A) but for the mismatch sequence B.

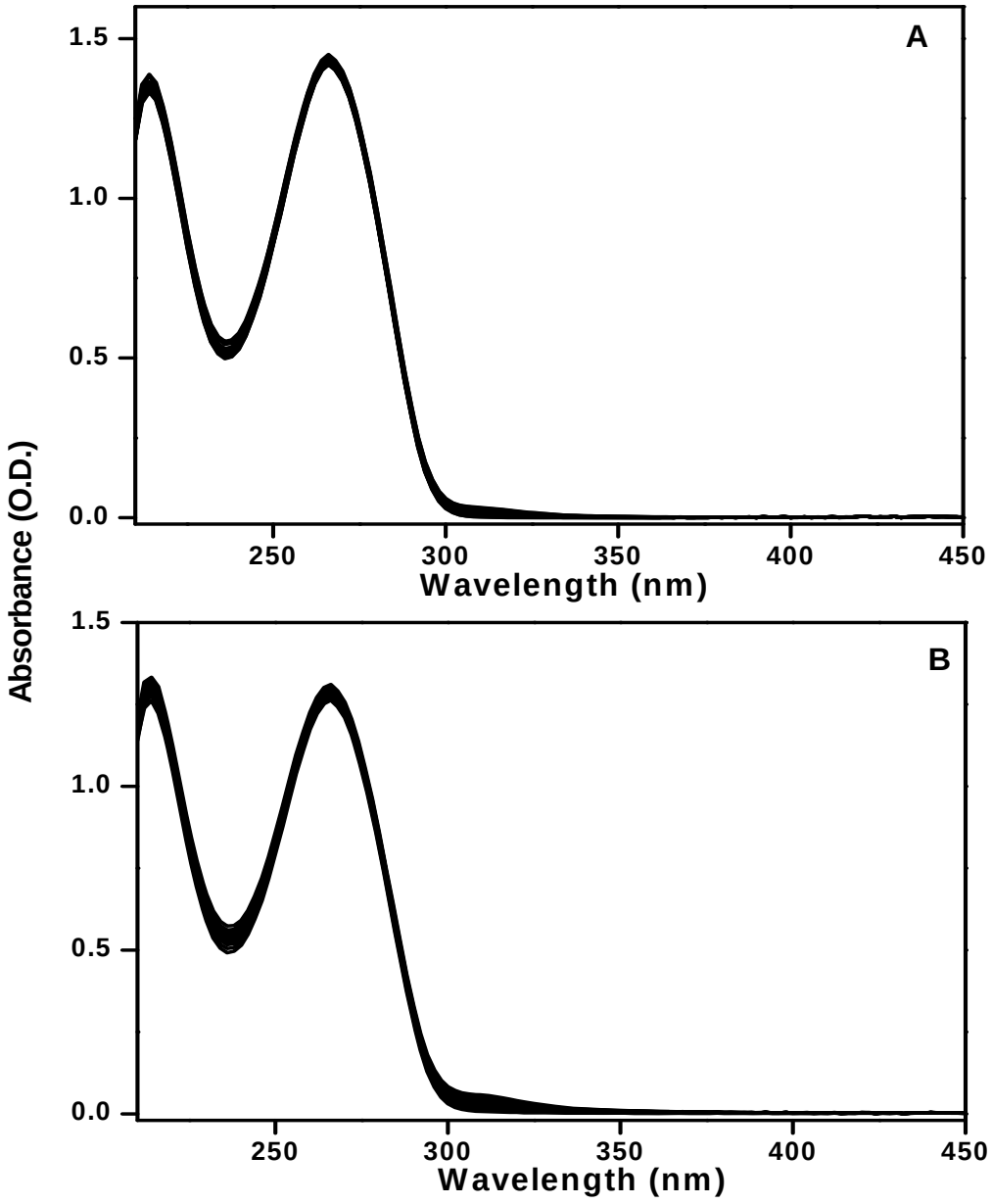

Figure 6.5. (A) Absorbance spectra of control sample of target sequence A. This sample was not exposed to UV radiation and therefore there is no damage to the DNA as indicated by the essentially constant absorbance as a function of time. (B) Same as (A) but for the mismatch sequence B.

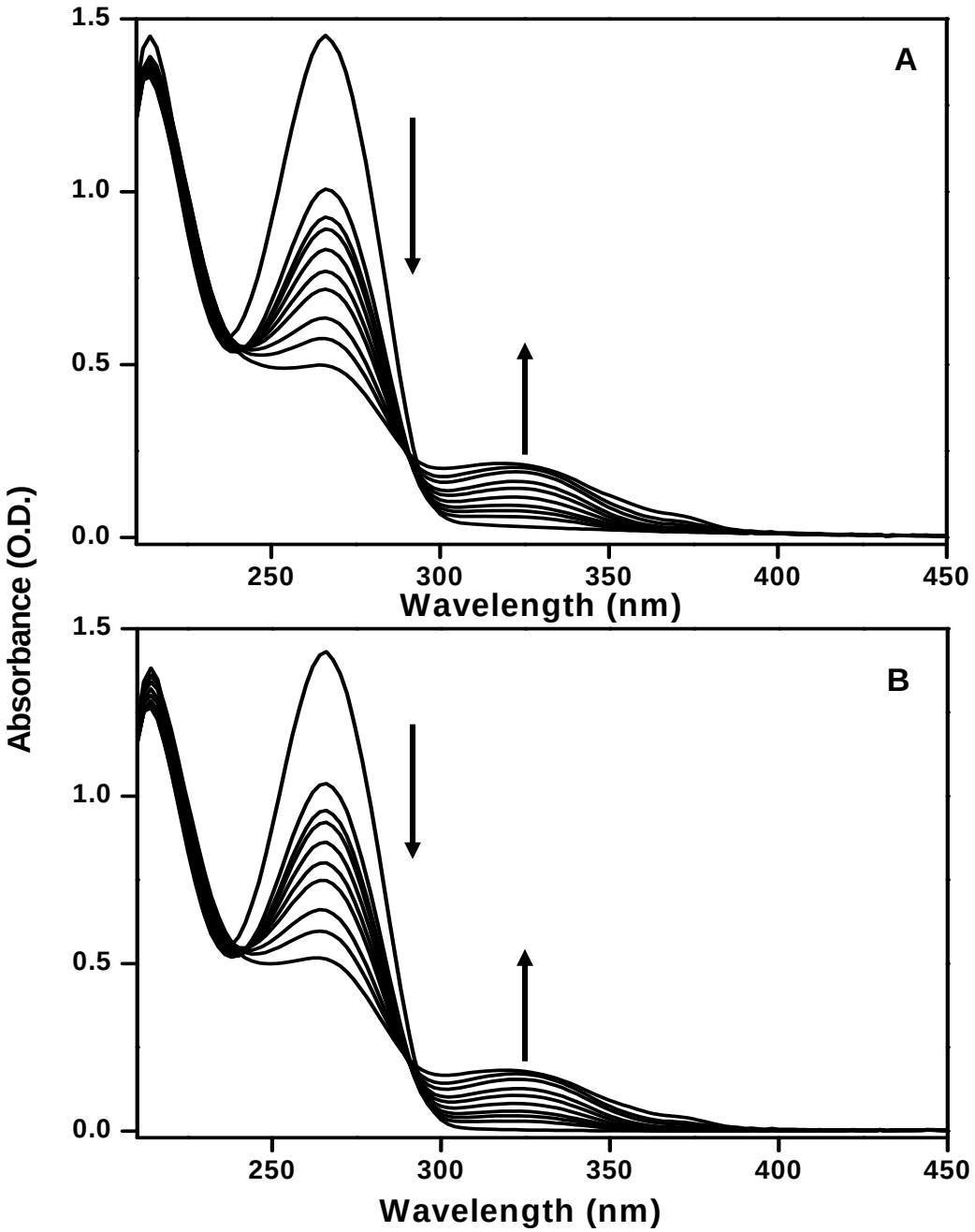

Figure 6.6. (A) UV-Vis absorption spectra of 8 μM double mismatch sequence C as a function of irradiation times 0-60 min. The band at 266 nm represents the ππ* transition and it decreases with irradiation time, while the band at 330 nm represents that of the pyrimidine-pyrimidinone [6-4] photoproduct and increases with irradiation time as shown. (B) Same as (A) but for triple mismatch target sequence D. Note that only the spectra for 0-60 min irradiation are shown here.

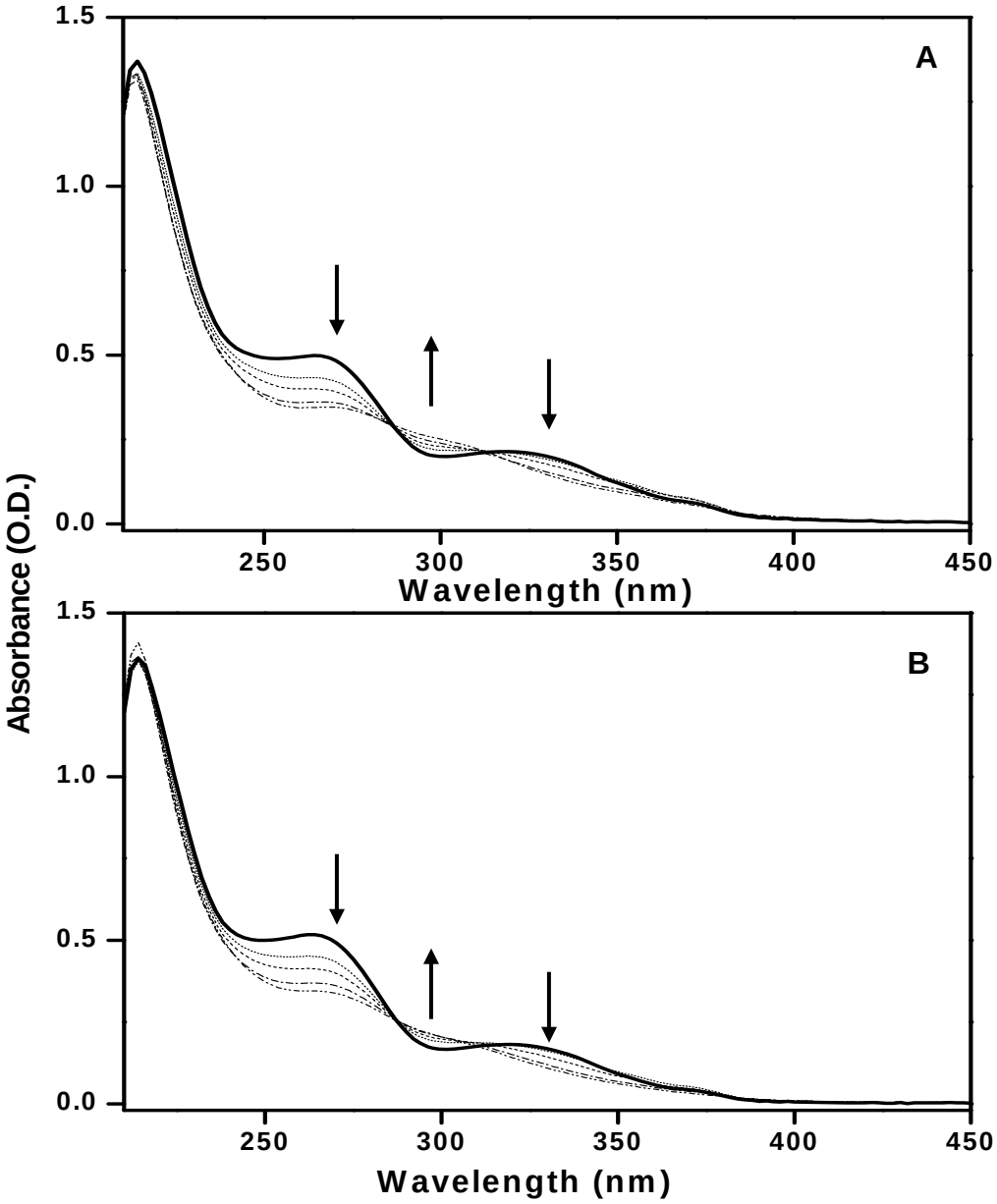

Figure 6.7. (A) UV-Vis absorption spectra of 8 μM double mismatch sequence C as a function of irradiation times for 60 min (solid line). 90 (short dot), 120 (short dash), 180 (dash dot) and 240 (dash dot dot) min irradiation times are shown to indicate that the photoproduct band at 330 nm starts decreasing at 90 min. of irradiation. Also, a new isosbestic point is formed at 315 nm as a result of the 330 nm band decrease. (B) Same as (A) but for the triple mismatch sequence D.

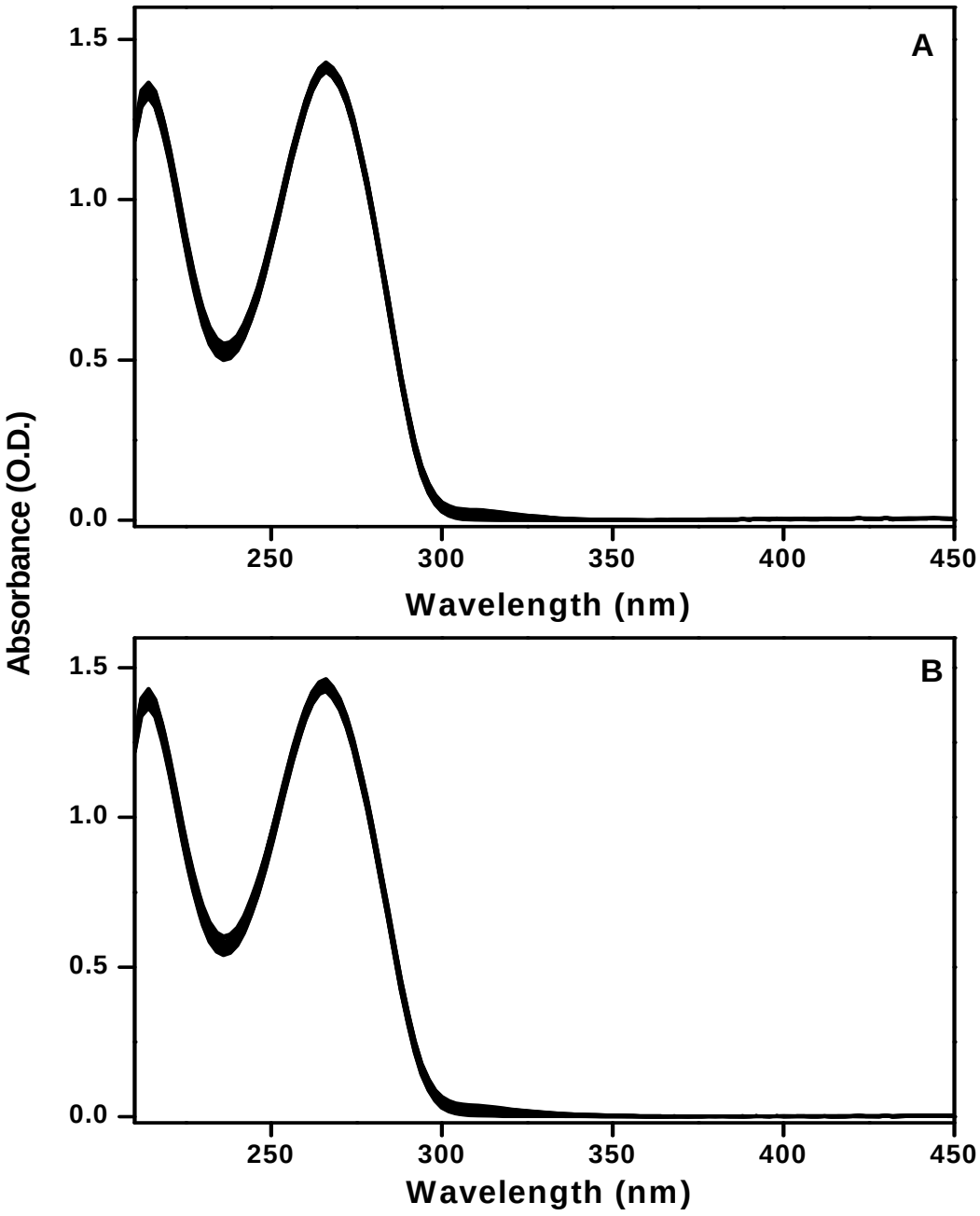

Figure 6.8. (A) Absorbance spectra of control sample of double mismatch sequence C. This sample was not exposed to UV radiation and therefore there is no damage to the DNA as indicated by the essentially constant absorbance as a function of time. (B) Same as (A) but for the triple mismatch sequence D.

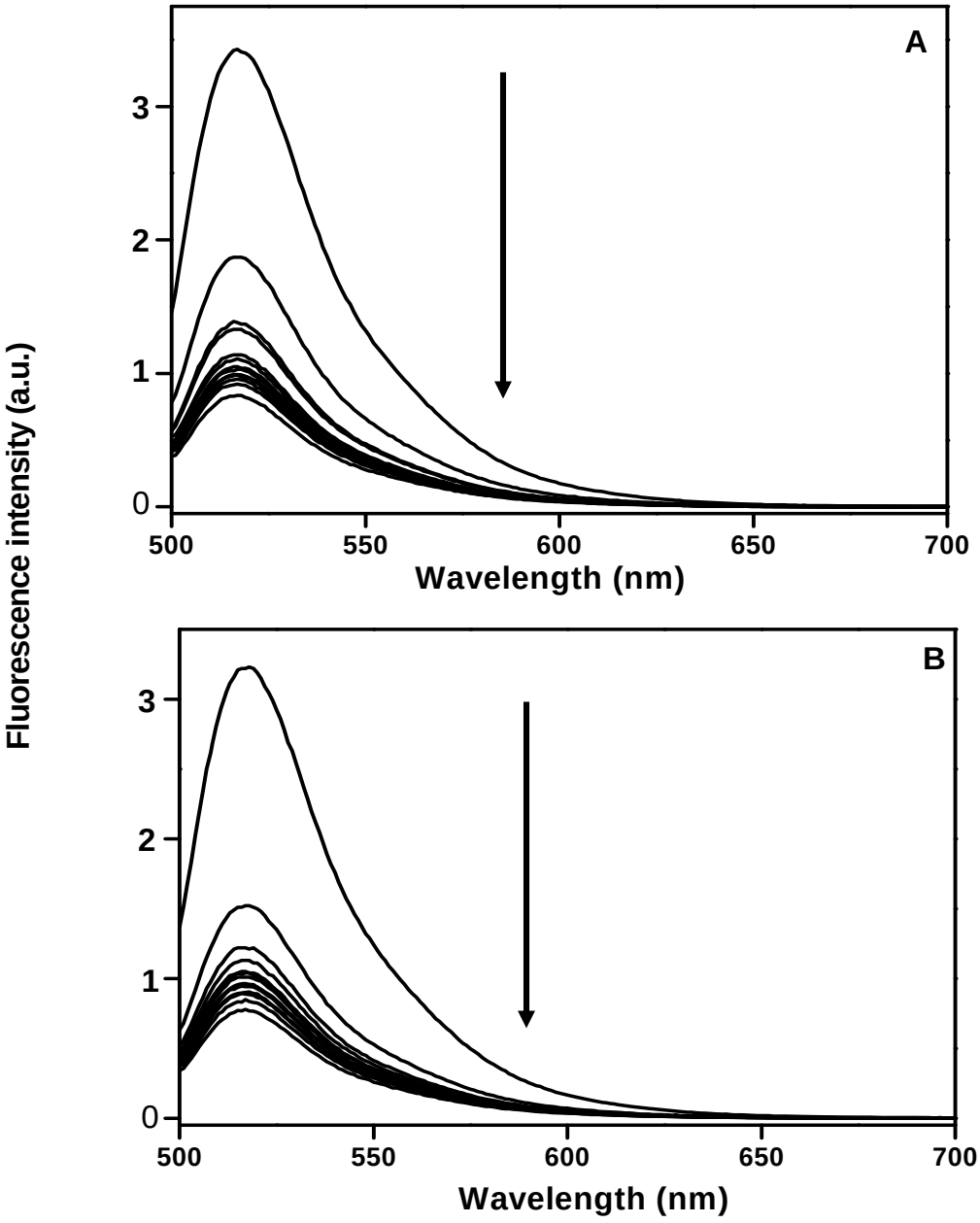

Figure 6.9. (A) Fluorescence emission spectra of 100 nM smart probe excited at 495 nm in the presence of 4-fold excess target sequence A at different irradiation times. The fluorescence emission from the SP was monitored at 520 nm. Direction of the arrow indicates the direction of fluorescence intensity change with increasing irradiation time from 0 to 240 minutes. (B) Same as (A) but for the single mismatch sequence B.

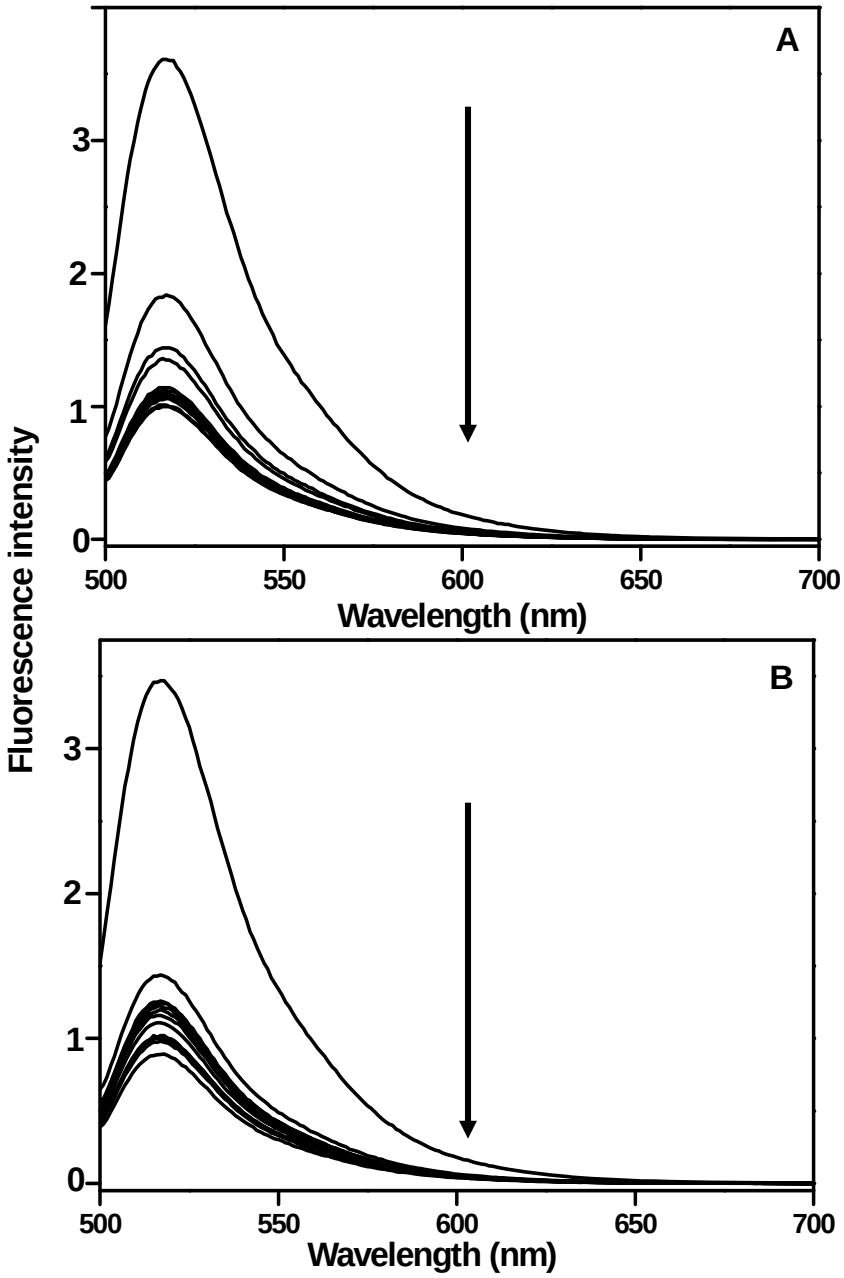

Figure 6.10. (A) Fluorescence emission spectra of 100 nM smart probe excited at 495 nm in the presence of 4-fold excess double mismatch sequence C at different irradiation times. The fluorescence emission from the SP was monitored at 520 nm. Direction of the arrow indicates the direction of fluorescence intensity change with increasing irradiation time from 0 to 240 minutes. (B) Same as (A) but for the triple mismatch sequence D.

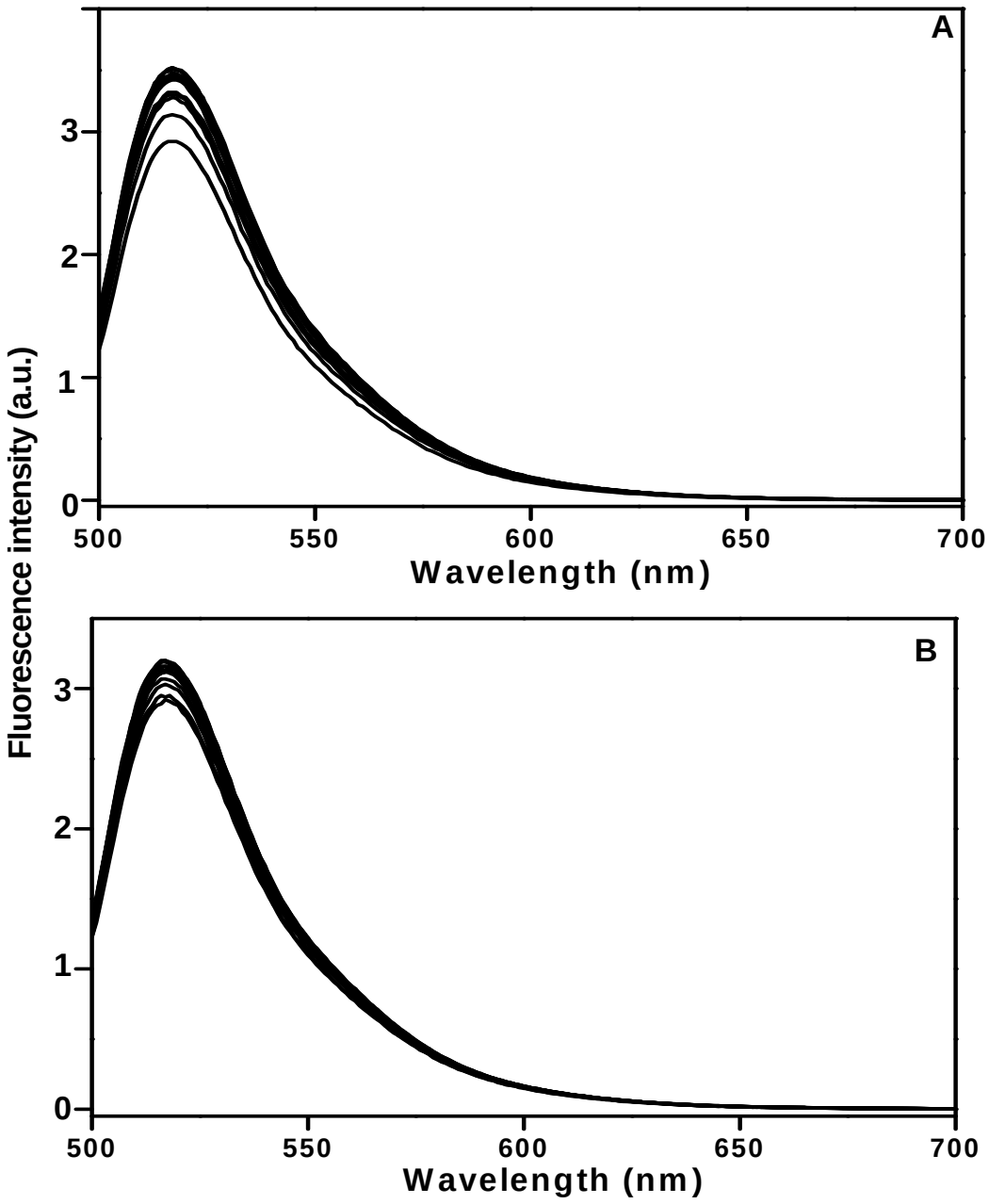

Figure 6.11. (A) Fluorescence spectra of 100 nM smart probe in the presence of 4-fold excess control sample of target sequence A. Aliquots taken at the same intervals of time as the irradiated samples were incubated with the smart probe in a similar manner as the irradiated samples. This sample was not exposed to UV radiation and therefore there is no damage to the DNA as indicated by the essentially constant fluorescence intensity as a function of time. The little hysteresis observed in the intensity may be ascribed to sampling error or lamp fluctuations. (B) Same as (A) but for the single mismatch sequence B.

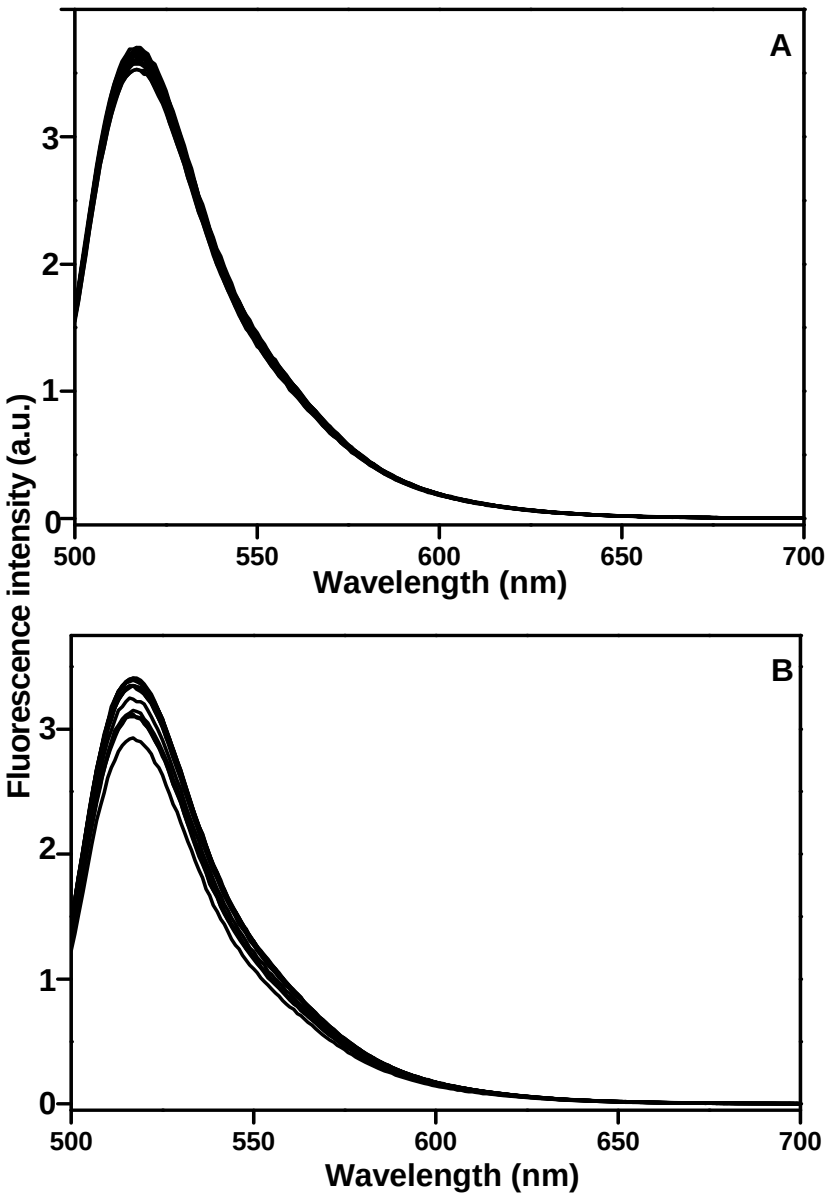

Figure 6.12. (A) Fluorescence spectra of 100 nM smart probe in the presence of 4-fold excess control sample of double mismatch sequence C. Aliquots taken at the same intervals of time as the irradiated samples were incubated with the smart probe in a similar manner as the irradiated samples. This sample was not exposed to UV radiation and therefore there is no damage to the DNA as indicated by the essentially constant fluorescence intensity as a function of time. The little hysteresis observed in the intensity may be ascribed to sampling error or lamp fluctuations. (B) Same as (A) but for the triple mismatch sequence D.

so sensitive that they can give 3-fold fluorescence signal increase even in the presence of 1 nM target sequence (data not shown). Therefore, these probes possess excellent sensitivity that they can give high fluorescence signal with very low concentrations of target sequences.

Shown in Figure 6.13 are the plots of absorbance and fluorescence as a function of irradiation time for oligonucleotide target sequence A and the single mismatch sequence B. These curves were obtained from the absorption spectra of Figure 6.3 and fluorescence spectra of Figure 6.9, respectively. The absorption spectral data were fit to a double exponential decay function, $y = y_o + A_1e^{-t/\tau 1} + A_2e^{-t/\tau 2}$, while the fluorescence spectral data were fit to a single-exponential decay function. As shown in this figure, the same absorbance decrease trend is observed for target sequence A and the single mismatch sequence B. Although the absorption curves are for specific oligonucleotide sequences which differ by at least a single base, the time constants for both curves (absorbance curves of Figures 6.13A and B) as well as other fitting parameters are essentially the same, indicating the insensitivity of absorption measurements to single base mismatch differences. For the perfectly complementary target sequence (target sequence A), the fluorescence time constant is found to be 2.13 ± 0.2 min, while that of the mismatch sequence B is 1.61 ± 0.2 min. Thus, the fluorescence intensity for the mismatch target sequence decreases faster than that of the perfectly complementary target sequence, as a result of the relative instability of its hybrid with the SP. This difference in the time constant again shows the exquisite specificity of the SP for single base mismatch discrimination.

Similarly, Figure 6.14 shows the plots of absorbance and fluorescence as a function of irradiation time for the double mismatch sequence C and the triple mismatch sequence D. Again, the same absorbance decrease trend is observed for both of these sequences. For target sequence C, the fluorescence time constant is found to be 1.87 ± 0.1 min, while that of the mismatch sequence D is 1.14 ± 0.2 min. The time constant for the triple mismatch sequence D is also lower than that of the double mismatch sequence C. The time constants for all four sequences also follow the same trend as the T_m, A>C~B>D.

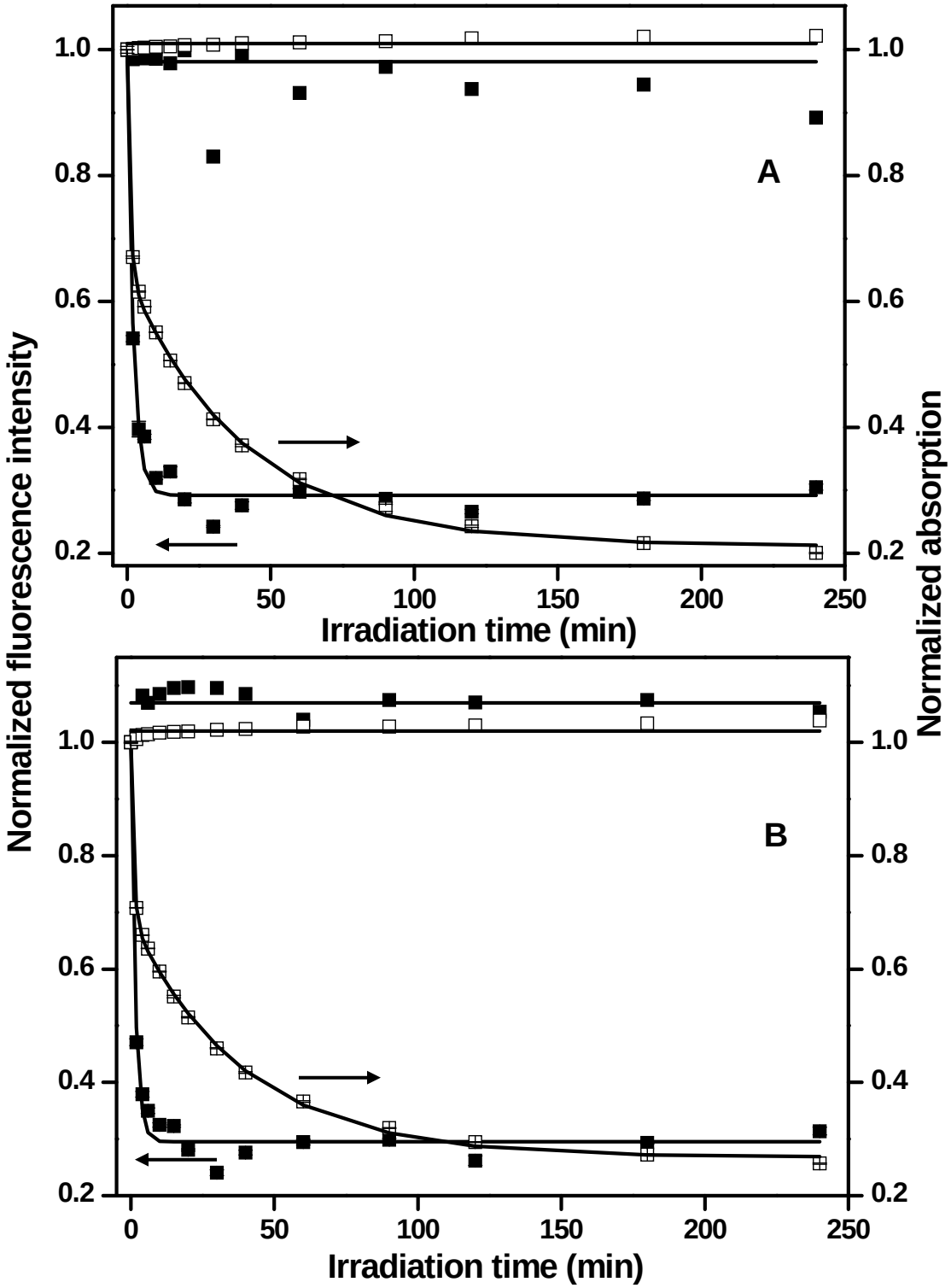
Normalized fluorescence intensity
Normalized absorption
Irradiation time (min)
A
B
1.0
0.8
0.6
0.4
0.2
0
50
100
150
200
250

Figure 6.13 (A) (open squares) Normalized absorbance spectra of irradiated target sequence A monitored at 266 nm as a function irradiation time, starting at 8 μM at zero irradiation time. The solid line through the points is the fit to an offset, double-exponential decay function, $y = y_o + A_1e^{-t/\tau 1} + A_2e^{-t/\tau 2}$. The absorbance time constants are 1.01 ± 0.1 min (t_1), 41.2 ± 2 min (t_2), A_1 = 0.36 ± 0.01 min^{-1}, A_2 = 0.43 ± 0.01 min^{-1} and y_o is 0.21. (filled squares) Normalized fluorescence of hybridization mixtures of 100 nM smart probe and 400 nM target sequence. The smart probe was excited at 495 nm and the fluorescence emission was monitored at 520 nm. The fluorescence time constant [y_o, A] for the target sequence is 2.13 ± 0.20 min [0.29, 0.70]. The controls are the flat lines centered around 1 at the top of both curves. In both cases, each data point is an average of three replicate measurements (except for the controls) and the error bars which are on the order of the data points, correspond to the relative standard deviation of the measurements. (B) Same as (A) but for the single mismatch sequence B. The absorbance (open squares) time constants are 0.99 ± 0.1 min (t_1), 39.3± 2 min (t_2), A_1 = 0.31 ± 0.01 min^{-1}, A_2 = 0.42 ± 0.01 min^{-1} and y_o is 0.25. The fluorescence (filled squares) time constant [y_o, A] in this case is 1.61 ± 0.2 min [0.29, 0.70].

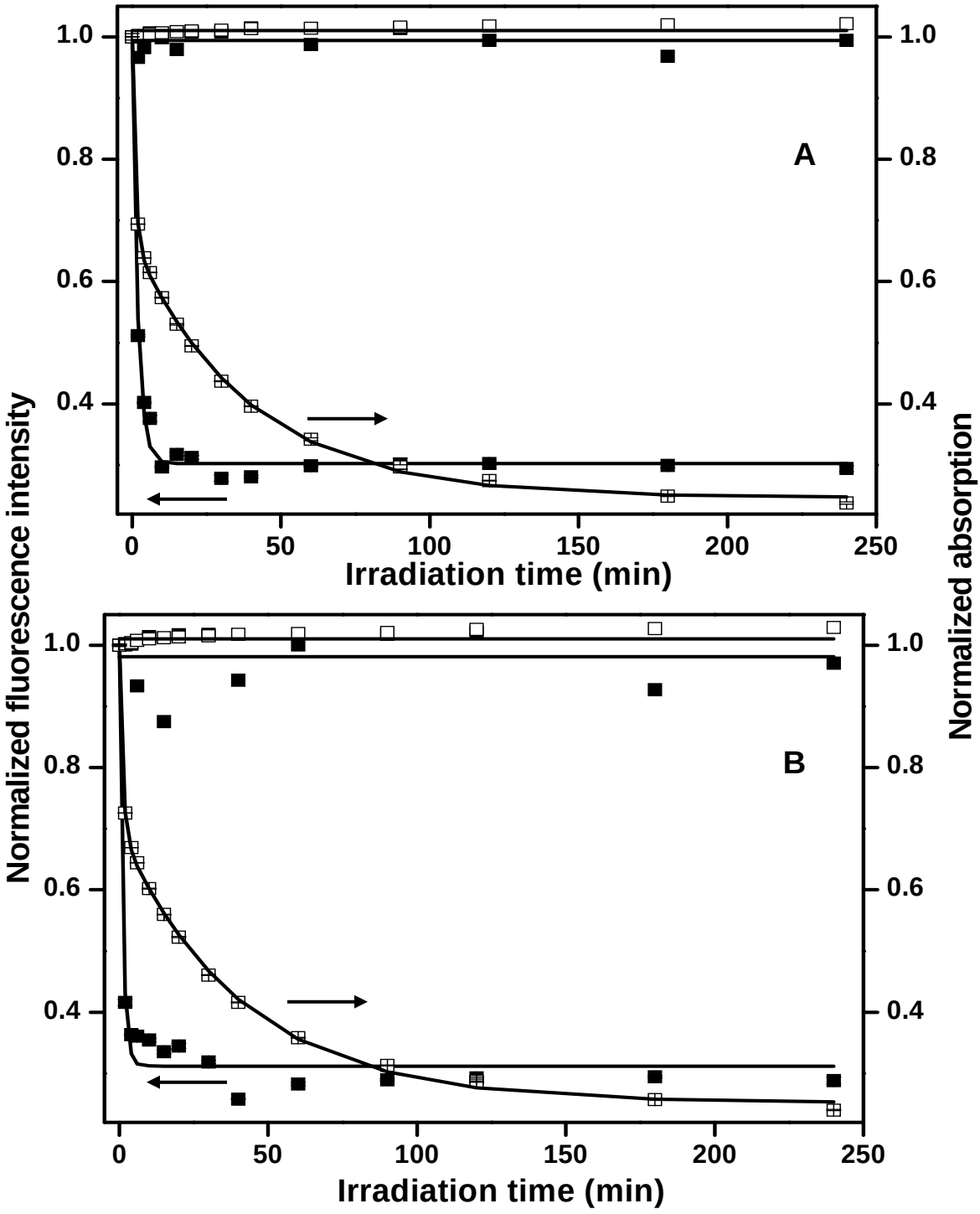
A
B
1.0
0.8
0.6
0.4
0
50
100
150
200
250
Irradiation time (min)
Normalized fluorescence intensity
Normalized absorption

Figure 6.14. (A) (open squares) Normalized absorbance of irradiated double mismatch sequence C monitored at 266 nm as a function irradiation time, starting at 8 μM at zero irradiation time. The solid line through the points is the fit to an offset, double-exponential decay function, $y = y_o + A_1e^{-t/\tau1} + A_2e^{-t/\tau2}$. The absorbance time constants are 1.03 ± 0 min (t_1), 39.0 ± 2 min (t_2), A_1 = 0.33 ± 0.01 min^{-1}, A_2 = 0.42 ± 0.01 min^{-1} and y_o is 0.25. (filled squares) Normalized fluorescence of hybridization mixtures of 100 nM smart probe and 400 nM target sequence. The smart probe was excited at 495 nm and the fluorescence emission was monitored at 520 nm. The fluorescence time constant [y_o, A] for the target sequence is 1.87 ± 0.1 min [0.30, 0.69]. The controls are the flat curves centered around 1 at the top of both curves. In both cases, each data point is an average of three replicate measurements (except for the controls) and the error bars which are on the order of the data points, correspond to the relative standard deviation of the measurements. (B) Same as (A) but for the triple mismatch sequence D. The absorbance (open squares) time constants are 1.12 ± 0.1 min (t_1), 41.2 ± 2 min (t_2), A_1 = 0.30 ± 0.01 min^{-1}, A_2 = 0.45 ± 0.01 min^{-1} and y_o is 0.25. The fluorescence (filled squares) time constant [y_o, A] in this case is 1.14 ± 0.2 min [0.31, 0.69].

An important observation in Figures 6.13 and 6.14 is that the offset in the fluorescence curves is about 0.3 for all four fluorescence spectra. Although the targets are all distinct, the fluorescence curves show a constant offset for all four samples. This is residual fluorescence, probably due to inefficient quenching by the guanosine residues. It is an indication of the residual fluorescence that will be seen even in the absence of target sequences. The residual fluorescence due to inefficient quenching is somewhat consistent with residual fluorescence of about 0.2 seen with MBs (Chapter 5, Oladepo, S. A., Loppnow, G. R., manuscript submitted).

Considering these time constants, it can also be seen that the complementarity of the target to the stem sequence of the probe has a small effect compared to the mismatch in the loop sequence. As seen previously in the case of the T_m's, the difference in time constant between target sequence A and single mismatch sequence B (0.52 min) with a single base mismatch in the loop is 2 times that between target sequence A and double mismatch sequence C (0.26 min). Although, double mismatch sequence C has two CC non-complementarity to the stem at its 5' end, this did not give as much of a time constant difference as the loop single base mismatch present in mismatch sequence B. Thus, a single base mismatch in the loop gives twice the time constant difference as double base non-complementarity with the stem of the probe.

Another important advantage of SP over MBs apart from its exquisite sensitivity and specificity just demonstrated is its cheap price. Thus, multiplex DNA sequence-specific analysis can be done with less cost. In addition, the free poly-guanosine end of the probe can be further modified for attachment to surfaces for a host of different surface-based applications. Therefore, apart from being a suitable probe for detecting DNA damage, the SPs are a suitable candidate for homogeneous and heterogeneous DNA sequence-specific analyses.

6.4 Conclusions

We have designed and characterized a novel SP which possesses structure and properties similar to MBs, but does not suffer from their limitations and has wider applications. The SP has exquisite sensitivity and specificity, which makes it a suitable alternative to MBs. Our results show that this SP can give a fluorescence signal intensity increase of 3-fold when it is bound to a perfectly complementary target. It can detect target sequence concentrations of as low as 1 nM and can discriminate between specific DNA sequences that differ by a single base, based on the difference in T_m's and fluorescence time constants. We also demonstrate the ability of this probe to detect UV-induced DNA photodamage in different sequences of DNA. With the probe, we were able to detect the damage and also characterized the damage in each sequence by the fluorescence time constant. Thus, this probe represents a novel tool for detecting DNA damage. The cheap cost, the ease of synthesis, and the possibility of attaching this probe to surfaces also make it a suitable candidate for a host of other bioanalytical applications. Therefore, the SPs, unlike MBs, represent a unique platform for both homogeneous and heterogeneous multiplex DNA sequence analyses.

6.5 References

(1) Tyagi, S.; Kramer, F. R. *Nature Biotechnol.* **1996**, *14*, 303-308.

(2) Bonnet, G.; Tyagi, S.; Libchaber, A.; Kramer, F. R. *Proc. Natl. Acad. Sci. USA* **1999**, *96*, 6171-6176.

(3) Sokol, D. L.; Zhang, X.; Lu, P;. Gewirtz, A. M. *Proc. Natl. Acad. Sci. USA* **1998**, *95*, 11538-11543.

(4) Leone, G.; van Schijndel, H.; van Gemen, B.; Kramer, F. R.; Schoen, C. D. *Nucleic Acids Res.* **1998**, *26*, 2150-2155.

(5) Kundu, L. M.; Burgdorf, L. T.; Kleiner, O.; Batschauer, A.; Carell, T. *ChemBioChem* **2002**, *3*, 1053-1060.

(6) Yarasi, S.; McConachie, C.; Loppnow, G. R. *Photochem. Photobiol.* **2005**, *81*, 467-473.

(7) Stohr, K.; Hafner, B.; Nolte, O.; Wolfrum, J.; Sauer, M.; Herten, D.-P. *Anal. Chem.* **2005**, *77*, 7195-7203.

(8) Knemeyer, J.-P.; Marme, N.; Sauer, M. *Anal. Chem.* **2000**, *72*, 3717-3724.

(9) Misra, A.; Kumar, P.; Gupta, K. C. *Anal. Biochem.* **2007**, *364*, 86-88.

(10) Heinlein, T.; Knemeyer, J.-P.; Piestert, O.; Sauer, M. *J. Phys. Chem. B* **2003**, *107*, 7957-7964.

(11) Kim., Y.; Yang, C. J.; Tan, W. *Nucleic Acids Res.* **2007**, *35*, 7279-7287.

(12) Misra, A.; Shahid, M. *Bioorg. Med. Chem.* **2009**, *17*, 5826-5833.

(13) Marme, N. Knemeyer, J.-P. *Anal. Bioanal. Chem.* **2007**, *388*, 1075-1085.

(14) Nazarenko, I.; Pires, R.; Lowe, B.; Obaidy, M.; Rashtchian, A. *Nucleic Acids Res.* **2002**, *30*, 2089-2195.

(15) Steeken, S.; Jovanovic, S. V. *J. Am. Chem. Soc.* **1997**, *119*, 617-618.

(16) Seidel, C. A. M.; Schulz, A.; Sauer, M. *J. Phys. Chem.* **1996**, *100*, 5541-5553.

(17) Sauer, M.; Drexhage, K. H.; Lieberwirth, U.; Muller, R.; Nord, S.; Zander, C. *Chem. Phys. Lett.* **1998**, *284*, 153-163.

(18) Ruzsicska, B. P.; Lemaire, D. G. E. In *DNA Photochemistry;* Horspool, W. M., Song, P.-S., Eds.; CRC Handbook of Organic Photochemistry and Photobiology; CRC Press: New York, 1995; pp 1289-1317.

(19) Friedrich, A.; Habl, G.; Sauer, M.; Wolfrum, J.; Hoheisel, J.; Marme, N.; Knemeyer, J.-P. *Proc. of SPIE* **2007**, *6444*, 64440M-1-64440M-7.

(20) Misra, A.; Kumar, P.; Gupta, K. C. *Nucleic Acids Symposium Series* **2007**, *51*, 311-312.

(21) Poon, K.; Macgregor. Jr.; R. B. *Biopolymers* **1998**, *45*, 427-434.

(22) Sen, D.; Gilbert, W. *Nature* **1990**, *344*, 410-414.

(23) Hardin, C. C.; Watson, T.; Corregan, M.; Bailey, C. *Biochemistry* **1992**, *31*, 833-841.

(24) Yang, J.-H.; Lai, J.-P.; Douglas, S. D.; Metzger, D.; Zhu, X.-H.; Ho, W.-*Z. J. Virol. Methods* **2002**, *102*, 119-128.

(25) Schildhkraut, C.; Lifson, S. *Biopolymers* **1965,** *3,* 195-208.

(26) Breslaeur, K. J.; Frank, R.; Marky, L. A. *Proc. Natl. Acad. Sci. USA 1986, 83,* 3746-3750.

(27) Wetmur, J. G. *Crit. Rev. Biochem. Mol. Biol.* **1991,** *26,* 227-259.

(28) Sugimoto, N.; Nakano, S.; Katoh, M.; Matsumura, A.; Nakamuta, H.; Ohmichi, T.; Yoneyema, M.; Sakasi, M.; *Biochemistry* **1995,** *34,* 11211-11216.

(29) Sugimoto, N.; Nakano, S.; Yoneyama, M.; Honda, K.; *Nucleic. Acids Res.* **1996,** *24,* 4501-4505.

(30) Owczarzy, R.; Vallone, P. M.; Gallo, F. J.; Paner, T. M.; Lane, M. J.; Benight, A. S. *Biopolymers* **1997,** *44,* 217-239.

(31) SantaLucia, J. Jr. *Proc. Natl. Acad. Sci. USA* **1998,** *95,* 1460-1465.

(32) Xia, T.; SantaLucia, J. Jr.; Burkard, M. E.; Kierzek, R.; Schoeder, S. J.; Jiao, X.; Cox, C.; Turner, D. H. *Biochemistry* **1998,** *37,* 14719-14735.

(33) Owczarzy, R.; You, Y.; Moreira, B. G.; Manthey, J. A.; Huang, L.; Behlke, M. A.; Walder, J. A. *Biochemistry* **2004,** *43,* 3537-3554.

Chapter 7

General Conclusions and Future Work

7.1 Summary

The research endeavours described in this thesis involve developing new tools to probe the nucleic acid damage resulting from photoinduced chemical processes and probing the initial excited-state structural dynamics of nucleic acids and sunscreen agents undergoing such chemical processes. The importance of these studies, which is apparent throughout the thesis, is due to the fact that nucleic acids are the fundamental essence of life, as they carry the genetic potential of all organisms.[1]

The work presented in Chapters 2-4 demonstrate the unique capabilities of UVRR spectroscopy for direct *in situ* analysis of complex samples like sunscreens on one hand, and the measurement of the initial excited-state structural dynamics of sunscreens and nucleic acids on the other.[1-3] Chapter 5 of this thesis presents a novel and significant contribution to the understanding of DNA damage in the presence of an amino acid, tryptophan (Trp). It enriches our understanding of the factors influencing the photochemistry of pyrimidine bases found in nucleic acids and it is the first report of photoprotection by Trp. The kinetics of such photoprotection and a model based on sacrificial or preferential absorption was presented. The exquisite sensitivity and specificity of MBs were exploited in this chapter for the detection of UV-induced DNA damage in the presence of Trp. Chapter 6 demonstrates a successful attempt at developing a simple DNA damage detection method, based on novel fluorescent probes that are cheaper and adaptable to a larger number of bioanalytical applications than molecular beacons (MBs).

7.2 General Conclusions

7.2.1 Chapter 2

Resonance Raman spectroscopy is an information-rich probe of chemical composition in complex samples.[4] This capability is harnessed for the direct *in situ* analysis of real-world sunscreen formulations discussed in Chapter 2. The motivation for this work lies in the challenges associated with the current method of analysis which is HPLC-based. The procedure involves pre-fractionation steps, which are time-consuming to isolate the active ingredients from the matrix. Because UVRRS can selectively excite the active ingredients of interest, it can give distinct resonance Raman signals corresponding to the sunscreen active ingredients (AIs) with little or no interference from the complex matrix. This shows UVRRS as a powerful tool for probing such complex systems as sunscreens. To date, UVRRS appears to be the only spectroscopic technique whose capability for selective assay of analytes in complex mixtures has been unequivocally demonstrated.[2,5] The *in situ* analysis also means that the procedure is solvent-free, as demonstrated in Chapter 2. This saves a lot of cost associated with solvents, which is an integral part of HPLC method. Thus, the UVRRS-based method can be said to be environmentally-friendly, compared to the HPLC-based method. For HPLC to handle all kinds of sunscreens; lotions, creams and aerosols, a different separation method has to be developed, since the state of the samples are different. However, UVRRS is robust and can be applied with little or no modifications to sampling, to all kinds of sunscreen products. Thus, as stated in Chapter 2, UVRRS is unique and unrivalled by HPLC in its capability for direct *in situ* qualitative and quantitative determinations of AIs in real-world sunscreen formulations. Therefore, it combines speed, robustness, wide applicability and flexibility which make it a suitable spectroscopic method for routine online quality control analysis in the sunscreen industry.

7.2.2 Chapter 3

Resonance Raman spectroscopy is a powerful probe of excited-state structure and dynamics.[6, 7] Thus, in Chapter 3, this technique was used to study the initial excited-state structural dynamics of a sunscreen active ingredient (AI), BZ3. The work is the first report on the initial excited-state structural dynamics of any sunscreen agent. In the UVRR spectra, significant intensities corresponding to C=O, C=C and C-O stretches were seen. The Δ values for all the observed vibrational bands in BZ3 are mostly low, suggesting an inherently photostable sunscreen molecule. However, the high Δ values for the C=O bond is explained on the basis of strong interaction between the methanol solvent and the BZ3 molecule.[8,9] This interaction allows the BZ3 molecule to dissipate its absorbed energy, rather than undergo photochemistry. Hence, our results suggest a photochemically stable molecule. This observation is consistent with previous reports on the relative photostability of this molecule compared to other sunscreen AIs.[10,11] The lack of well-established photochemistry of this molecule may be explained by this inherent photostability. Thus, it is concluded that this sunscreen AI is one of the more photostable ones in the market. This work is significant in that it lays the groundwork for the initial excited-state structural dynamics of sunscreen AIs. It can be used as a powerful probe for screening sunscreen photostability, not only of those currently in use, but also those on which regulatory approval is pending. This same type of screening can be applied to those being currently designed as possible sunscreen agents.

7.2.3 Chapter 4

As stated earlier, nucleic acids are vulnerable to a plethora of environmental insults, principal among which is UV radiation. Being the carrier of genetic information, UV-induced photodamage can have far-reaching negative implications for humans. The first step in UV-induced damage is the absorption of light and the subsequent electronic and structural dynamics.[1] This sequence of events may lead to photochemical reactions,

which then lead to mutation in DNA and ultimately cancer. Since the main UV chromophores in nucleic acids are the nucleobases themselves, it is their photochemical reactions which determine nucleic acids photochemistry.[12] Consequently, Chapter 4 examined the initial excited-state structural dynamics of 9-MeA, an analog of adenine. This work presents an insight into the structural changes that take place in the excited-state of this molecule. A significant outcome of this work is that the Δ values for the vibrational modes in 9-MeA are lower than for pyrimidine bases. This provides a strong support for the photochemical stability of this molecule, and of course the photostability of purines as compared to pyrimidines. To our knowledge, this represents the first proof of the photostability of purines compared to pyrimidines, based on initial excited-state structural dynamics studies. In addition, the results show that the glycosidic bond, though not directly involved in photochemistry, was found to undergo some structural change, perhaps due to its proximity to the photochemically-active N7-C8. This is consistent with the N-H bend seen in uracil and thymine initial excited-state structural dynamics. The N-H bond is not photochemically active in itself, but its proximity to the C5=C6 site of thymine and uracil photochemistry makes its bending vibration observable in the UV resonance Raman spectrum.[13,14] Also, our results show that 66% of the total excited-state reorganization energy of 9-MeA lies along the photochemically relevant modes. The results presented here, combined with those already reported for different nucleobases and analogs,[1,6,13-15] constitute a library from which initial excited-state structural dynamics of similar nucleobases and analogs can be predicted. Overall, these results show the invaluable information that can be obtained from initial excited-state structural dynamics studies, using UV resonance Raman spectroscopy.

7.2.4 Chapter 5

Part of the challenges associated with understanding and characterizing UV-induced DNA photodamage is the capability to detect such damage. To do this, sensitive detection techniques are needed to be able to detect even

single base damage. One of the methods of choice for this single base damage detection is MB-based fluorescence detection. The utility of this technique for the detection of thymine and uracil UV-induced photodamage has been previously reported.[16] Because DNA does not exist in isolation in cells, we therefore explored the effects of an amino acid, tryptophan (Trp) on UV-induced DNA photodamage in Chapter 5. With this technique, we explored the kinetics of DNA damage protection in the presence of the amino acid. The results highlights the significance and relevance of preferential or sacrificial absorption of UV light by Trp. Earlier reports on the UV photochemistry of nucleic acids in the presence of Trp only considered Trp-induced nucleic acid damage,[17-21] ignoring the inherent UV-induced DNA damage. The experiments discussed in Chapter 5 were therefore designed to probe these two possible processes in Trp-containing DNA solutions, UV-induced DNA damage and Trp-induced DNA damage. Our results suggest that the preferential absorption has an overriding effect when these solutions are irradiated and that Trp-induced DNA damage earlier reported is comparatively negligible. To determine if the observed effect of Trp is truly preferential absorption of the UV light, we conducted concentration-dependent experiments and found that the observed effect increases with Trp concentration, pointing to absorption of the UV light by Trp. In addition, DNA photodamage rate constants that were obtained from fluorescence curves were found to be exponential functions of Trp concentration, consistent with a sacrificial or preferential absorption/screening of UV light by Trp molecules. This is the first report on the predominance of preferential absorption of UV light by Trp over Trp-induced DNA damage, and the kinetics of such preferential absorption. The results suggest that cellular nucleic acids may have a natural protection mechanism from UV-induced damage in the associated amino acids and proteins. Thus, the results are significant in enriching our understanding of the nature of interaction of UV light with DNA, in the presence of Trp and other similar UV chromophores in cells.

7.2.5 Chapter 6

As exemplified in Chapter 5, MBs are very sensitive probes with a high degree of sequence specificity. However, their high costs, difficulty in synthesis, unsuitability for heterogeneous and multiplex homogeneous assays, and incomplete coupling of the quencher preclude their use for several bioanalytical applications. All these limitations motivated a search for an alternative fluorescence-based detection platform, one that maintains the sensitivity and specificity of MBs. Thus, in Chapter 6, the development of a cheaper alternative DNA damage detection method, using self-quenching smart probes (SPs) is discussed. In the melting temperature experiments discussed in Chapter 6, the results show that these SPs can detect DNA sequences in the low nanomolar concentration range and can discriminate between specific DNA sequences that differ by a single base. The ability of these probes to detect UV-induced DNA photodamage in different sequences of DNA was also demonstrated. We recommend the use of SPs for future applications, such as homogeneous and heterogeneous multiplex DNA sequence analyses.

7.3 Future Work

7.3.1 Introduction

Although the significance of the results presented in the preceding chapters of this thesis cannot be overemphasized, there is room for further exploration on each topic discussed in those chapters. In this section, future work is suggested based on the conclusions stated above. The suggested future work will build on the conclusions made here and take the work to the next logical level. In addition, a few recommendations are suggested where necessary.

7.3.2 *In situ* analysis of sunscreen aerosols

All the sunscreen formulations considered in the work presented in Chapter 2 are lotions and creams. It will be interesting to see sunscreen aerosols similarly analyzed. This is important as this sample type also constitute a good percentage of sunscreen products currently being sold. However, the sampling system in the instrumentation described in Chapter 2 has to be modified to accommodate this kind of samples. The sample handling for this kind of analysis might involve trapping such samples in sealed quartz NMR tubes. However, based on my observations while working with creams and lotions, the signal from sunscreen samples placed in NMR tubes are very weak. This might be a technical challenge to work around when it comes to the direct *in situ* analysis of sunscreen aerosols. A suggested solution to this challenge will be the use of fibre optics for sampling and signal collection. Fibre optics are used especially for sampling in remote or harsh environments, where it is not feasible to locate an expensive Raman instrument. As a matter of fact, a small fibre optic spectrometer that can be held on a palm has already been reported.[22] Since the poor signal is a result of the quartz interface between the excitation laser and the sample, creating a contact point between the laser and the sample will significantly improve the signal. The fibre optic can be adapted for sampling sunscreen aerosols by carefully designing a sample reservoir with both entrance and exit ports for the excitation and Raman signal collection fibre optics. The fibre head will be inserted into the sample reservoir and another fibre which collects the Raman scattered photons will be passed on to the spectrophotometer. This way, the challenge with sampling sunscreen aerosols can be solved, and all the other aspects of the UVRRS experiments remain the same as described in Chapter 2.

7.3.3 Exploration of the photochemistry of sunscreen AIs

One of the challenges to the interpretation of our results on the initial excited-state structural dynamics of BZ3 is the lack of photochemistry data on this and other sunscreen AIs. To my knowledge, at the present time, there is

no published data on the photochemistry of sunscreen AIs currently approved for use in sunscreen formulations. This may be partly explained on the basis of the expected photostability of sunscreen AIs, which necessitate their choice as a sunscreen agent in the first place. However, there seem to be little or no interest in exploring the photochemistry of sunscreen molecules, and there appears to be no scientific impediments to such research. Consequently, an important future work is the exploration of the photochemistry of sunscreen AIs. This will undoubtedly lay the foundation for subsequent studies on the photochemical interactions these molecules undergo following absorption of UV radiation. It will also be a payoff for those involved in gaining a fundamental understanding of the initial excited-state structural dynamics of these molecules, as it will be a reference point for the photochemistry data needed for the complete interpretation of the initial excited-state structural dynamics data.

7.3.4 Initial excited-state structural dynamics of the S1 state of BZ3

Only the initial excited-state structural dynamics of the S2 state was considered in Chapter 3. Therefore, one important future experiment will be to consider the S1 state (the lower energy electronic transition) of BZ3. This is an important experiment to conduct because this sunscreen AI has two absorption bands spanning the UVA-UVB regions (Figure 2.2A), and therefore it should protect against both UVA (320-400 nm) and UVB (280-320 nm) regions. The initial excited-state structural dynamics presented in this thesis concerns the S2 state UVB only. However, since the photochemical reaction depends on the excitation wavelength, the photochemistry of this molecule at the S2 state may be different from that of the S1 state. Thus, for a complete picture of the excited-state potential energy surface of this molecule, the photochemistry and therefore the photostability of this molecule, the initial excited-state structural dynamics of the S1 state is equally important and must be explored. It will also be worthwhile to explore solvent-dependent initial excited-state structural dynamics of BZ3. The strong solvent interaction that

was observed in Chapter 3 may be absent in other solvents, and this may change the initial excited-state structural dynamics.

7.3.5 Initial excited-state structural dynamics of OMC and OCS

While the initial excited-state structural dynamics of BZ3 presented in Chapter 3 might be the first of such reports on sunscreen AIs, further research work is needed to conduct similar studies on other common sunscreen AIs such as o-methoxy cinnamate (OMC) and octyl salicylate (OCS). To this end, preliminary data of about two wavelengths have been acquired on these sunscreen AIs (OMC and OCS) in our group. Once the remaining wavelengths are completed for these AIs, a complete picture of the initial excited-state structural dynamics will be obtained and their photostability and photochemistry compared with those of BZ3. And when experimental data on the photochemistry of these AIs become available, definite conclusions about how much of the initial excited-state structural dynamics is projected along the photochemical coordinate can be reasonably made. Furthermore, analogs of these sunscreen AIs which are also being used should be studied. This will enable a scientific comparison of the data, just like it is being done for nucleobases.

7.3.6 Use of structural dynamics data by regulatory agencies

In the long term, when reliable experimental photochemistry data on these common sunscreen AIs become available, the initial excited-state structural dynamics of common sunscreen AIs data could be used to screen sunscreen AIs as excellent or poor candidates for use in sunscreen formulations. Although photochemistry does not necessarily make a molecule a bad candidate for sunscreen, possible sunscreen candidates can be discriminated based on their photochemical quantum yields. Also, structural modifications that may be necessary to improve the photostability of sunscreen AIs might be predictable based on the initial excited-state structural dynamics analysis of available sunscreen AIs. Such research findings should be recommended for

incorporation by FDA and other similar agencies in their scientific decision-making process for the approval of sunscreen AI candidates.

7.3.7 Dynamics of higher energy electronic transitions in nucleic acids

The results presented on the initial excited-state structural dynamics of 9-MeA in Chapter 4 only took into account the band centered at 262 nm. For instance, as shown in Figure 4.4, our analysis only includes the transition at ca. 38,000 cm^{-1}, and not higher energy transitions. This is responsible for the observed deviation of the theoretical spectrum from the experimental spectrum at energies greater than 38,000 cm^{-1}. Therefore, further experiments are required on the higher energy electronic transitions in 9-MeA. This is going to become possible with the use of laser wavelengths further in the deep UV. Results from such deep UV experiments might shed more light on the initial excited-state structural dynamics of not only 9-MeA, but also other nucleobases and their analogs, as well as other molecules of interest that have electronic transitions in the deep UV.

7.3.8 Initial excited-state structural dynamics of other purine bases and analogs

The results from the initial excited-state structural dynamics of 9-MeA provides a basis for further structural dynamics studies on purine bases and analogs. As stated in Chapter 4, the limited photochemistry of purines because of their relative photostability may be responsible for a lack of experimental data on their structural dynamics. The little available experimental data should allow further investigations into the structural dynamics of purine bases and analogs. The available data on the photochemistry of adenine, for example, provides a photochemical basis for the results presented in Chapter 4. The same data can provide a sound basis for the initial excited-state structural dynamics studies on adenine and adenosine. It will be interesting to see how the results of these two studies compare with those of 9-MeA, especially when

it was already found in our study that the methyl group at the N9 position in 9-MeA plays no role in the photochemistry.

7.3.9 Protective effects of tyrosine and phenylalanine

Chapter 5 examines the protective role played by Trp on UV-induced DNA damage. Other UV-absorbing amino acids are expected to play a similar role. Therefore, aromatic amino acids such as tyrosine and phenylalanine are recommended for future research. To this end, in our group, preliminary data have been obtained on UV irradiation of DNA in the presence of tyrosine. It must, however, be stated that both tyrosine and phenylalanine have lower solubility in water compared to Trp. This factor is going to play a role in the level of protection they can confer on DNA, since lower amounts will be present in solution due to their limited solubility. This will probably make it difficult to conduct concentration-dependent experiments with amino acid concentrations higher than about 2 mM. However, a possible way to examine the role of these less soluble amino acids is to make them more soluble by incorporating them in peptides and proteins.

7.3.10 Further refinement of the SPs for easier synthesis

The SPs sequence described in Chapter 6 has 7 guanosine residues. As stated in the chapter, consecutive G bases have a tendency to form G-tetraplexes.[23] The formation of these tetraplexes can make the synthesis of SPs a bit difficult. However, an equally good SP can be made with less number of G bases, which will perform equally well. For instance, SPs with guanosine residues of five or less have been used with comparable sensitivities or even better. Since in SPs, intramolecular fluorescence quenching is achieved because of the low oxidation potential of guanosine,[24-28] another alternative design of sensitive SPs will be to use sequences involving consecutive or intermittent incorporation of adenosine residues (e. g. …GGGAGGGAGG…), since adenosine also has low oxidation potential, albeit slightly higher than guanosine. [25-28] The presence of A's can also disrupt tetraplexes. Therefore,

this exploration is an area where future work is suggested. In addition, two G overhangs were used in the SPs presented here to enhance fluorescence quenching, but it will also be interesting to determine the minimum number of G overhangs that can enhance quenching.

7.3.11 Refinement of the SPs for higher sensitivity

In addition to making the synthesis of the SPs much easier, their sensitivity also needs to be increased. Therefore, future experiments should test other possible intramolecular fluorescence quenchers such as Trp and 7-deazaguanosine residues to ascertain if they can give better sensitivity than the SPs described in this thesis.[28,29] In the same vein, other fluorophores should be experimented with, to test if changing the fluorophore could enhance the sensitivity and recognition efficiency of the SPs.

The signal change accompanying the transition from probe to probe-target duplex for the SPs as mentioned in Chapter 6 is about 3-fold (Figure 6.2). This needs to be further optimized to a level that is comparable to MBs, which is about 20-fold. This could be easily realized because by careful design and selection of the appropriate fluorophore, SPs can give a fluorescence increase of up to 20-fold upon hybridization to the target sequence.[24,26,28] This optimization lies in refining the structure and sequence of the SPs. A suggested approach to this will be to try different fluorophores, following an optimization of the quenching provided by different sequences of guanosine residues or other similar quenchers. Depending on the fluorescence quantum yield of different fluorophores tried, a signal increase of greater than 3-fold can be obtained. The sensitivity of these probes can also be further increased by incorporating them into confocal fluorescence microscopy. This way, the inherent sensitivities of the probes and that of the confocal technique could give synergistic sensitivity of up to 20-fold or greater.

7.4 References

(1) Loppnow, G. R.; Billinghurst, B. E.; Oladepo, S. A. In *Excited-state Structural Dynamics of Nucleic Acids and Their Components;* Shukla, M. K.; Leszczynski, J., Eds.; Radiation Induced Molecular Phenomena in Nucleic Acids; A Comprehensive Theoretical and Experimental Analysis Series: Challenges and Advances in Computational Chemistry and Physics; Springer: Netherlands, 2008; Vol. 5, pp 237-263.

(2) Oladepo, S. A.; Loppnow, G. R. *Anal. Chim. Acta* **2008**, *628*, 57-66.

(3) Oladepo, S. A.; Loppnow, G. R. In *UV resonance Raman spectroscopy as a tool for probing complex samples;* Withnall, R., Chowdhry, B. Z., Eds.; Proceedings of the 21st international conference on Raman spectroscopy (ICORS); IMPublications: Chichester, UK, 2008; Vol. 21, pp 1028-1029.

(4) Pelletier, M. J. In *Analytical applications of Raman spectroscopy;* Pelletier, M. J., Ed.; Blackwell Science Ltd: Oxford, 1999; , pp 1-478.

(5) Asher, S. A. *Anal. Chem.* **1984**, *56*, 720-724.

(6) Billinghurst, B. E.; Loppnow, G. R. *J. Phys. Chem. A* **2006**, *110*, 2353-2359.

(7) Myers, A. B.; Mathies, R. A. In *Resonance Raman spectra of polyenes and aromatics;* Spiro, T. G., Ed.; Biological Applications of Raman Spectroscopy; Wiley-Interscience: New York, 1987; Vol. 2, pp 1-58.

(8) Beyere, L.; Yarasi, S.; Loppnow, G. R. *J. Raman Spectrosc.* **2003**, *34*, 743-750.

(9) Baughman, B. M.; Stennett, E.; Lipner, R. E.; Rudawsky, A. C.; Schmidtke, S. J. *J. Phys. Chem. A* **2009**, *113*, 8011-8019.

(10) Ricci, A.; Chretien, M. N.; Maretti, L.; Scaiano, J. C. *Photochem. Photobiol. Sci.* **2003**, *2*, 487-492.

(11) Rodil, R.; Moeder, M.; Altenburger, R.; Schmitt-Jansen, M. *Anal. Bioanal. Chem.* **2009**, *395*, 1513-1524.

(12) Satzger, H.; Townsend, D.; Zgierski, M. Z.; Patchkovskii, S.; Ullrich, S.; Stolow, A. *Proc. Natl. Acad. Sci. USA* **2006**, *103*, 10196-10201.

(13) Yarasi, S.; Brost, P.; Loppnow, G. R. *J. Phys. Chem. A.* **2007**, *111*, 5130-5135.

(14) Yarasi, S.; Ng, S.; Loppnow, G. R. *J. Phys. Chem. B* **2009**, *113*, 14336-14342.

(15) Billinghurst, B. E.; Yeung, R.; Loppnow, G. R. *J. Phys. Chem. A* **2006**, *110*, 6185-6191.

(16) Yarasi, S.; McConachie, C.; Loppnow, G. R. *Photochem. Photobiol.* **2005**, *81*, 467-473.

(17) Reeve, A. E.; Hopkins, T. R. *Photochem. Photobiol.* **1980**, *31*, 297-304.

(18) Reeve, A. E.; Hopkins, T. R. *Photochem. Photobiol.* **1979**, *30*, 677-681.

(19) Reeve, A. E.; Hopkins, T. R. *Photochem. Photobiol.* **1980**, *31*, 413-415.

(20) Saito, I.; Sugiyama, H.; Matsuura, T. *Tetrahedron Lett.* **1984**, *25*, 3243-3246.

(21) Saito, I.; Matsuura, T. *Acc. Chem. Res.* **1985**, *18*, 134-141.

(22) Smith, E.; Dent, G. In *Modern Raman Spectroscopy - A Practical Approach;* John Wiley & Sons, Ltd.: Chichester, England, 2005; , pp 1-210.

(23) Poon, K.; Macgregor. Jr., R. B. *Biopolymers* **1998**, *45*, 427-434.

(24) Stohr, K.; Hafner, B.; Nolte, O.; Wolfrum, J.; Sauer, M.; Herten, D.-P. *Anal. Chem.* **2005**, *77*, 7195-7203.

(25) Friedrich, A.; Habl, G.; Sauer, M.; Wolfrum, J.; Hoheisel, J.; Marme, N.; Knemeyer, J.-P. *Proc. of SPIE* **2007**, *6444*, 64440M-1-64440M-7.

(26) Misra, A.; Kumar, P.; Gupta, K. C. *Anal. Biochem.* **2007**, *364*, 86-88.

(27) Misra, A.; Kumar, P.; Gupta, K. C. *Nucleic Acids Symposium Series* **2007**, *51*, 311-312.

(28) Heinlein, T.; Knemeyer, J.-P.; Piestert, O.; Sauer, M. *J. Phys. Chem. B* **2003**, *107*, 7957-7964.

(29) Marme, N. K.; Knemeyer, J.-P. *Anal. Bioanal. Chem.* **2007**, *388*, 1075-1085.